

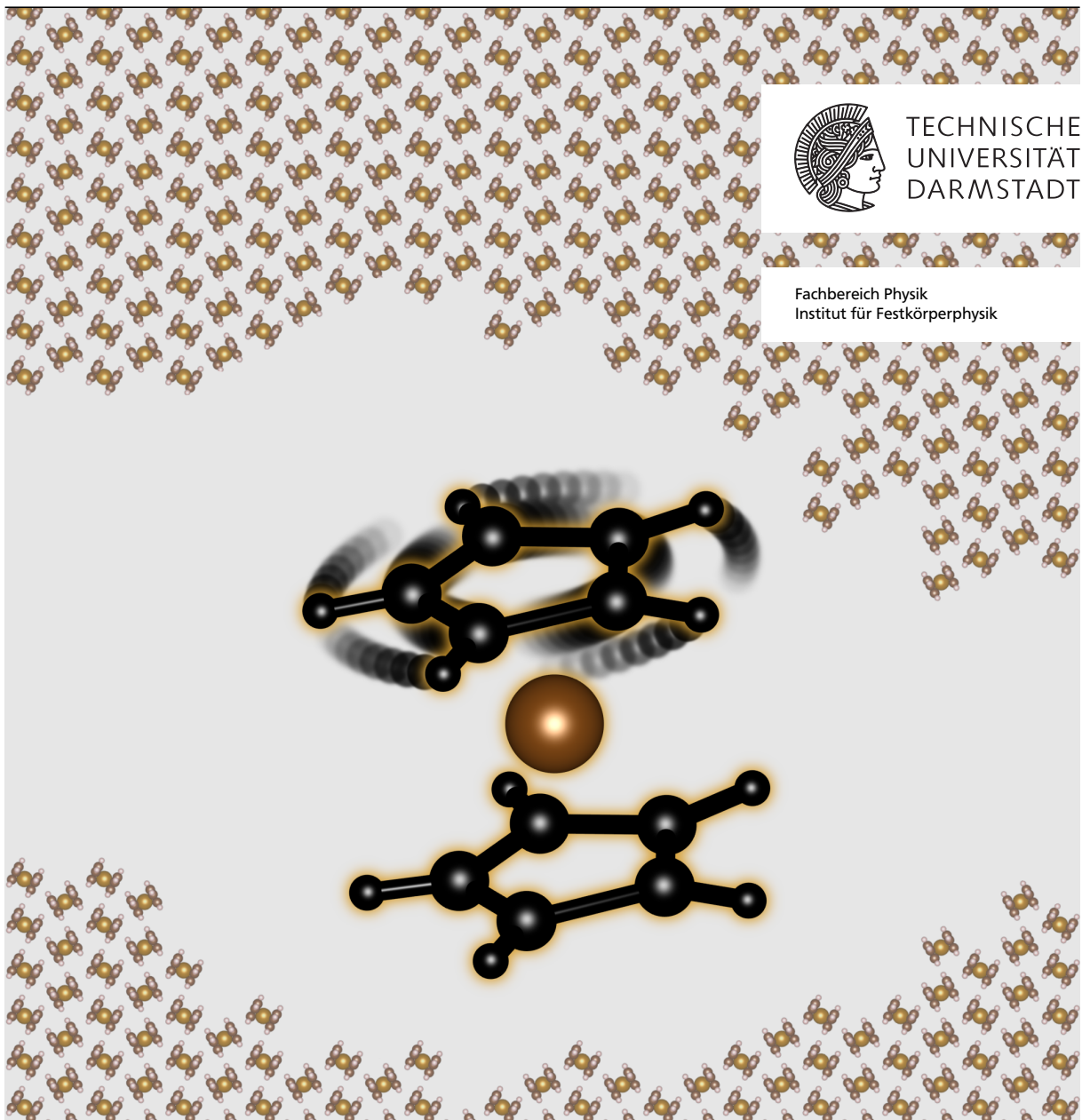
# Ring Rotation in Ferrocene and Ferrocene-containing Polymers

**Ringrotation in Ferrocen und ferrocen-haltigen Polymeren**

Zur Erlangung des Grades eines Doktors der Naturwissenschaften (Dr. rer. nat.)

genehmigte Dissertation von Markus Andreas Appel, M. Sc. aus Hanau

März 2015 – Darmstadt – D 17



Ring Rotation in Ferrocene and Ferrocene-containing Polymers  
Ringrotation in Ferrocen und ferrocen-haltigen Polymeren

Genehmigte Dissertation von Markus Andreas Appel, M. Sc. aus Hanau

1. Gutachten: Prof. Dr. Bernd Stühn
2. Gutachten: Prof. Dr. Michael Vogel

Tag der Einreichung: 25.07.2014

Tag der Prüfung: 03.11.2014

Darmstadt – D 17

Bitte zitieren Sie dieses Dokument als:

Please cite this document as:

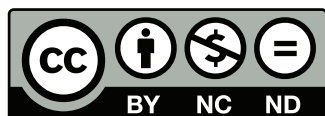
URN: urn:nbn:de:tuda-tuprints-42268

URL: <http://tuprints.ulb.tu-darmstadt.de/4226>

Dieses Dokument wird bereitgestellt von tuprints,  
E-Publishing-Service der TU Darmstadt

<http://tuprints.ulb.tu-darmstadt.de>

[tuprints@ulb.tu-darmstadt.de](mailto:tuprints@ulb.tu-darmstadt.de)



Diese Veröffentlichung steht unter folgender Creative Commons Lizenz:

Namensnennung – Keine kommerzielle Nutzung – Keine Bearbeitung 3.0 Deutschland

<http://creativecommons.org/licenses/by-nc-nd/3.0/de/deed.de>

This work is published under the following Creative Commons license:

Attribution – Non Commercial – No Derivatives 3.0 Germany

<http://creativecommons.org/licenses/by-nc-nd/3.0/de/deed.en>

---

The background of the title picture shows the (010) lattice plane of orthorhombic ferrocene,<sup>[23]</sup> with a single ferrocene molecule in the foreground. Initial graphics rendered with VESTA.<sup>[13]</sup>

---

## Abstract

Ferrocene is an organometallic molecular sandwich complex with an iron atom coordinated between two cyclopentadienyl rings. The reorientation of these rings in a process of rotational jump diffusion between multiple equilibrium sites on a circle is investigated using quasielastic neutron time of flight and backscattering spectroscopy experiments. Existing results on the ring rotation in bulk, crystalline ferrocene are extended, and the study is widened to oxidized ferrocenium cations in the triiodide complex  $\text{FcI}_3$ , and to ferrocene containing polymers like poly(vinylferrocene) PVFc. Emphasis is put on a robust data analysis of neutron scattering data, including corrections for multiple scattering and simultaneous analysis of many data sets taken on different spectrometers. It is shown that the 5-fold rotational jump diffusion model needs to be extended to a non-equivalent sites model to account for rotational disorder in the monoclinic room temperature phase of ferrocene which is metastable down to 164 K. In the triclinic phase below 164 K, the combination of time of flight and backscattering spectroscopy enables to separate two dynamical processes due to crystallographically different molecules in the unit cell. In the triiodide complex of ferrocenium cations,  $\text{FcI}_3$ , the barrier to rotation is found to be significantly lower than in bulk ferrocene. Moreover, a hitherto unknown phase transition is found at 85 K which causes a discontinuity in the temperature dependence of the correlation time of the ring rotation in  $\text{FcI}_3$ , very similar to the triclinic-monoclinic transition in ferrocene. The ring rotation above 85 K is closer to continuous rotation due to its low barrier, while 5-fold jumps are favored below 85 K. In the polymer PVFc, where ferrocene units are laterally attached to a polymer chain, it is shown that the ring rotation is still active, but the correlation times are broadly distributed. The neutron scattering data can be described very well by a rotation rate distribution model over the large temperature range from 80 K to 350 K. The average activation energy of the motion is  $9.61(2) \text{ kJ mol}^{-1}$ , with a distribution having circa one third of this value as second moment. Moreover, a vibrational study has been performed on ferrocene,  $\text{FcI}_3$ , and various ferrocene containing polymers. It turns out that the vibrational fingerprint modes of the molecule are mildly affected when the ferrocene unit is laterally attached to a polymer chain, but more severely if it is incorporated into the polymer backbone. Finally, measurements under external magnetic fields did not reveal any field dependence of the ring rotation dynamics in oxidized PVFc, where the oxidation leads to magnetic moments on the ferrocene units. Even though unrelated to the main topic of ring rotation, these experiments nicely demonstrated inelastic magnetic neutron scattering on Zeeman split levels of the electronic ground state, and high resolution measurements allowed to directly observe nuclear hyperfine splitting in external magnetic fields.



---

# Zusammenfassung

Ferrocen (Fc) ist ein organometallischer Sandwichkomplex und besteht aus einem Eisenatom, welches zwischen zwei Cyclopentadienyl-Ringen koordiniert ist. In dieser Arbeit wird der Sprungdiffusionsprozess der Ringrotation zwischen mehreren Gleichgewichtspositionen auf einem Kreis mittels quasielastischer Neutronenstreuung in Experimenten der Flugzeit- und Neutronenrückstreuungsspektroskopie untersucht. Die bekannten Resultate zur Ringrotation in kristallinem Fc werden vertieft und erweitert auf oxidierte Ferrocenium-Kationen in Ferroceniumtriiodid  $\text{FcI}_3$ , sowie auf ferrocen-haltige Polymere wie das Poly(vinylferrocen) PVFc. Eine wichtige Rolle spielt hierbei eine robuste Analyse der Neutronenstreudaten, die Korrekturen für Mehrfachstreuungsprozesse beinhaltet sowie die gleichzeitige Analyse vieler Datensätze von verschiedenen Spektrometern ermöglicht. Es wird gezeigt, dass das 5-fach Rotationsprungdiffusionsmodell auf ein Modell mit nicht äquivalenten Gleichgewichtspositionen erweitert werden muss, um die Orientierungsunordnung in der über 164 K existierenden monoklinen Kristallphase zu berücksichtigen. Unterhalb von 164 K, in der triklinen Phase, können zwei dynamische Prozesse mittels kombinierter Flugzeit- und Neutronenrückstreuungsspektroskopie separiert werden. Diese entstehen aufgrund kristallographisch unterschiedlicher Moleküle in der Einheitszelle. Es stellt sich weiterhin heraus, dass die Energiebarriere der Sprungbewegung in  $\text{FcI}_3$  deutlich kleiner ist als in reinem Fc. Ein bisher unbekannter und dem monoklin-triklinen Übergang in kristallinem Fc sehr ähnlicher Phasenübergang wurde in  $\text{FcI}_3$  bei 85 K entdeckt, bei dem die Temperaturabhängigkeit der Korrelationszeit der Rotationsprungdiffusion eine Diskontinuität aufweist. Aufgrund der niedrigen Energiebarriere ähnelt die Ringrotation über 85 K einer freien, kontinuierlichen Rotation, während bevorzugt 5-fach Sprünge in der Phase unterhalb von 85 K aufzutreten scheinen. Des Weiteren wird gezeigt, dass Ringrotationsprozesse auch in dem Polymer PVFc mit lateral an die Kette gebundenen Ferroceneinheiten noch aktiv sind, sich allerdings nur mit einer breiten Verteilung von Korrelationszeiten beschreiben lassen. Für die Analyse der Neutronenstreudaten wurde ein Rotationsratenverteilungsmodell angewandt ('rotation rate distribution model'), welches eine sehr gute Beschreibung der Dynamik über den großen Temperaturbereich von 80 K bis 350 K liefert. Die sich ergebende mittlere Aktivierungsenergie beträgt  $9.61(2) \text{ kJ mol}^{-1}$ , mit einem zweiten Moment der Verteilung welches circa ein Drittel dieses Wertes erreicht. Es wurde außerdem eine Studie der Vibrationsspektren an Ferrocen, an  $\text{FcI}_3$  und an verschiedenen ferrocen-haltigen Polymeren durchgeführt. Es zeigt sich, dass die charakteristischen Moden des Moleküls nur wenig beeinflusst werden, wenn dieses lateral an eine Polymerkette gebunden wird, wohingegen ein vollständiges Einbauen in die Hauptkette einen deutlichen Einfluss zeigt. Abschließend wurden Experimente unter äußeren Magnetfeldern an oxidiertem PVFc durchgeführt, bei welchem durch Oxidation ein magnetisches Moment in den Ferroceneinheiten entsteht. In diesen Messungen konnte kein Einfluss des äußeren magnetischen Feldes auf die Rotationsdynamik festgestellt werden. Andererseits wurde die Aufspaltung des elektronischen Grundzustands im äußeren Feld über magnetische Neutronenstreuungsprozesse im Spektrum sichtbar, wobei sich mit hochauflösender Neutronenrückstreuungsspektroskopie sogar die Hyperfeinaufspaltung der Kernspins im äußeren Feld direkt nachmessen ließ.



---

# Contents

<b>Nomenclature</b>	<b>vii</b>
<b>1 Introduction</b>	<b>1</b>
1.1 Ring rotation and polymorphism: bulk ferrocene . . . . .	2
1.2 Outline of this thesis . . . . .	4
<b>I Theory, models &amp; methods</b>	<b>5</b>
<b>2 Neutron scattering</b>	<b>7</b>
2.1 Basic definitions in neutron scattering experiments . . . . .	7
2.2 The scattering cross section for elastic scattering . . . . .	8
2.3 Coherent and incoherent scattering . . . . .	10
2.4 Inelastic neutron scattering and correlation functions . . . . .	11
2.4.1 Lattice vibrations and the Debye Waller factor . . . . .	13
2.5 Separation of coherent and incoherent scattering . . . . .	15
2.6 Magnetic neutron scattering . . . . .	16
<b>3 Model functions for molecular ring rotation</b>	<b>19</b>
3.1 Equivalent sites rotational jump diffusion model . . . . .	19
3.2 Multiple rings per unit cell: Two-ring rotational jump diffusion model . . . . .	23
3.3 Non-equivalent sites rotational jump diffusion model . . . . .	23
<b>4 Experimental methods</b>	<b>27</b>
4.1 Neutron sources . . . . .	27
4.2 Time of flight spectroscopy . . . . .	28
4.3 Backscattering spectroscopy . . . . .	29
4.4 Vibrational spectroscopy . . . . .	33
4.5 Polarized neutron diffraction . . . . .	33
<b>5 QENS data analysis and multiple scattering corrections</b>	<b>35</b>
5.1 Construction of model functions . . . . .	35
5.2 Determination of multiple scattering correction factors . . . . .	38
5.3 Model parameter refinement procedure . . . . .	40
<b>II Experiments &amp; results</b>	<b>43</b>
<b>6 Ring rotation dynamics in bulk ferrocene</b>	<b>45</b>
6.1 Experimental details . . . . .	45
6.2 Monoclinic high temperature phase . . . . .	46
6.3 Triclinic low temperature phase . . . . .	54
6.4 Results for the orthorhombic low temperature phase . . . . .	59
6.5 Conclusion: Ring rotation dynamics in all three phases of ferrocene . . . . .	60

<b>7</b>	<b>Ring rotation dynamics in ferrocenium triiodide – FcI<sub>3</sub></b>	<b>63</b>
7.1	Experimental details . . . . .	63
7.2	Structure and phase behavior of FcI <sub>3</sub> . . . . .	64
7.3	Results of inelastic scattering experiments . . . . .	67
7.3.1	Ring rotation dynamics above 85 K: ToF . . . . .	67
7.3.2	Ring rotation dynamics below 85 K: ToF & BS . . . . .	69
7.4	Discussion . . . . .	71
7.5	Conclusion . . . . .	73
<b>8</b>	<b>Ring rotation dynamics in poly(vinylferrocene) – PVFc</b>	<b>75</b>
8.1	Rotation rate distribution model for PVFc . . . . .	76
8.2	Experimental details . . . . .	78
8.3	Results . . . . .	79
8.3.1	Static structure factor of PVFc . . . . .	79
8.3.2	Ring rotation dynamics . . . . .	80
8.4	Discussion . . . . .	83
8.5	Conclusion . . . . .	85
<b>9</b>	<b>Vibrational spectroscopy</b>	<b>87</b>
9.1	Experimental section . . . . .	87
9.2	Results & Discussion . . . . .	88
9.3	Conclusion . . . . .	92
<b>10</b>	<b>Neutron spectroscopy under external magnetic fields</b>	<b>93</b>
10.1	Experimental details . . . . .	93
10.2	Zeeman splitting of electronic ground state . . . . .	93
10.3	Nuclear hyperfine splitting in the external field . . . . .	96
10.4	Conclusion . . . . .	97
<b>11</b>	<b>Summary</b>	<b>98</b>
	<b>Appendix</b>	<b>100</b>
<b>A</b>	<b>Multiple scattering correction</b>	<b>103</b>
A.1	Multiple scattering simulation algorithm . . . . .	103
A.2	Extrapolation of the jump rotation model function . . . . .	108
A.3	Example of the effect of multiple scattering corrections . . . . .	109
<b>B</b>	<b>Raw data correction</b>	<b>112</b>
<b>C</b>	<b>Debye Waller factor temperature dependence</b>	<b>114</b>
<b>D</b>	<b>Spin-1/2 system in external magnetic field</b>	<b>115</b>
	<b>Bibliography</b>	<b>117</b>



---

# Nomenclature

---

## Abbreviations

---

BS	backscattering
Cp	cyclopentadienyl, C <sub>5</sub> H <sub>5</sub>
D7	diffuse scattering spectrometer with polarization analysis at ILL, Grenoble <sup>[54]</sup>
DFT	density functional theory
DOS	density of states
EFWS	elastic fixed window scan
EISF	elastic incoherent structure factor
Fc	ferrocene, C <sub>10</sub> H <sub>10</sub> Fe
FcI <sub>3</sub>	ferrocenium triiodide, C <sub>10</sub> H <sub>10</sub> FeI <sub>3</sub>
FWHM	full width at half maximum
FWS	fixed window scan
GPC	gel permeation chromatography
HWHM	half width at half maximum
IFWS	inelastic fixed window scan
ILL	Institut Laue-Langevin
IN1-Lagrange	hot neutron vibrational spectrometer at ILL, Grenoble <sup>[53]</sup>
IN16	BS spectrometer at ILL, Grenoble (dismantled in fall 2013) <sup>[52]</sup>
IN16B	BS spectrometer at ILL, Grenoble <sup>[51]</sup>
IN5	multi disk chopper ToF spectrometer at ILL, Grenoble <sup>[46]</sup>
IN6	ToF spectrometer at ILL, Grenoble <sup>[47]</sup>
INS	inelastic neutron scattering
ISFs	incoherent structure factors
MS	multiple scattering
NMR	nuclear magnetic resonance
PST	phase space transformation
PVFc	poly(vinylferrocene), see <a href="#">Figure 1.2</a>
QENS	quasielastic neutron spectroscopy
RRDM	rotation rate distribution model, see <a href="#">section 8.1</a>
ToF	time of flight

---

## Important symbols and constants

---

$\alpha$	twist angle between configurations in the non-equivalent sites 2×5-fold model
$A_l(Q)$	incoherent structure factors. $A_0(Q)$ is also referred to as EISF
$B$	magnetic field
$b$	scattering length
$c$	speed of light in vacuum $c = 299\,792\,458\text{ m s}^{-1}$ <sup>[40]</sup>
$\Delta E$	energy resolution, given as FWHM unless indicated otherwise
$\delta_{kl}$	Kronecker delta: 1 if $k = l$ , zero otherwise
$\frac{d\sigma}{d\Omega}$	differential cross section, see <a href="#">eq. (2.17)</a>
$\frac{d^2\sigma}{d\Omega dE_f}$	double differential cross section, see <a href="#">eq. (2.21)</a>
$\Delta\omega_L$	peak width of librational mode, see <a href="#">eq. (5.2)</a>
$d\Omega$	differential solid angle element
$e$	elementary charge $e = 1.602\,176 \times 10^{-19}\text{ C}$ <sup>[40]</sup>
$\langle E_A \rangle$	average barrier height/activation energy in the RRDM, see <a href="#">eq. (8.4)</a>

$E_A$ .....	activation energy
$E_i, E_f$ .....	incident and final neutron energy
$f$ .....	population factor in rotational jump diffusion models
$F(\mathbf{Q})$ .....	magnetic form factor
$\gamma_n$ .....	gyromagnetic ratio of the neutron $\gamma_n = 1.832471 \times 10^8 \text{ s}^{-1} \text{ T}^{-1}$ <sup>[40]</sup>
$g$ .....	Landé $g$ -factor
$\gamma_0$ .....	preexponential factor of Arrhenius law
$\gamma_1, \gamma_2, \gamma_a, \gamma_b$ .....	jump rates in the non-equivalent sites 2×5-fold model
$\gamma/2$ .....	jump rate in the equivalent sites jump rotation model
$G(\mathbf{r}, t), G_s(\mathbf{r}, t)$ .....	pair and self correlation function, see eq. (2.23) and eq. (2.22)
$\mathcal{G}(\sigma_{\text{ex}}, \omega)$ .....	normalized Gaussian of standard deviation $\sigma_{\text{ex}}$
$G(\omega)$ .....	generalized density of states, see chapter 9
$H(\log \gamma)$ .....	relaxation rate distribution function in the RRDM, see eq. (8.4)
$\hbar$ .....	reduced Planck's constant, $\hbar = 1.054571 \times 10^{-34} \text{ J s} = 0.658212 \text{ meV ps}$ <sup>[40]</sup>
$h$ .....	$2\pi\hbar$
$I_{\text{coh}}(\mathbf{Q}, t), I_{\text{inc}}(\mathbf{Q}, t)$ ...	coherent and incoherent intermediate scattering function, see eq. (2.24) and eq. (2.25)
$j_0(x)$ .....	spherical Bessel function of zeroth order $j_0(x) = \sin(x)/x$
$J_{2\theta}^*(\omega)$ .....	hypothetical neutron flux in MS simulation with one scattering process and no absorption
$J_{2\theta}^{(n)}(\omega)$ .....	hypothetical neutron fluxes in MS simulation after exactly $n$ scattering processes
$k_B$ .....	Boltzmann constant $k_B = 1.380648 \times 10^{-23} \text{ J K}^{-1} = 0.861733 \text{ } \mu\text{eV K}^{-1}$ <sup>[40]</sup>
$\mathbf{k}_i, \mathbf{k}_f$ .....	initial and final neutron wave vector
$\Lambda, \lambda_l$ .....	diagonal matrix of negated eigenvalues in jump rotation models
$\mathcal{L}(\omega, \lambda_l)$ .....	normalized Lorentzian function, see eq. (3.16)
$\tilde{\gamma}$ .....	average relaxation rate in the RRDM, see eq. (8.5)
$L$ .....	scaling factor of librational mode, see eq. (5.2)
$\lambda_{\text{inc}}$ .....	incident neutron wavelength
$\mathbf{M}$ .....	transition matrix in jump rotation model
$\mu_B$ .....	Bohr magneton $\mu_B = 9.274009 \times 10^{-24} \text{ J T}^{-1} = 57.88381 \text{ } \mu\text{eV T}^{-1}$ <sup>[40]</sup>
$m_e$ .....	electron mass $m_e = 9.109382 \times 10^{-31} \text{ kg}$ <sup>[40]</sup>
$m_n$ .....	neutron mass $m_n = 1.674927 \times 10^{-27} \text{ kg}$ <sup>[40]</sup>
$\tilde{\nu}$ .....	wavenumber $\tilde{\nu} = E/(hc)$
$N$ .....	number of equilibrium sites in the rotational jump diffusion models
$n(\omega)$ .....	Bose-Einstein factor, see eq. (2.34)
$\omega_D$ .....	Debye frequency, see eq. (2.32)
$\mathbf{Q}$ .....	scattering vector $\mathbf{k}_i - \mathbf{k}_f$
$Q_{\text{el}}$ .....	scattering vector for elastic scattering $4\pi\lambda_{\text{inc}}^{-1} \sin \vartheta$
$r$ .....	radius of equilibrium sites in rotational jump diffusion models
$r_0^2$ .....	see eq. (2.36)
$R_{2\theta}^*(\omega)$ .....	correction factors from MS simulation
$\sigma$ .....	total scattering cross section
$\sigma_E$ .....	second moment of the barrier height distribution in the RRDM, see eq. (8.6)
$s_0$ .....	overall intensity scaling factor
$S_{\text{coh}}(\mathbf{Q}, \omega), S_{\text{inc}}(\mathbf{Q}, \omega)$ .....	coherent and incoherent dynamic structure factor, see eq. (2.26a)
$\sigma_E$ .....	width of the relaxation rate distribution in the RRDM, see eq. (8.4)
$\sigma_{\text{inc}}, \sigma_{\text{coh}}$ .....	incoherent and coherent scattering cross section, see eq. (2.18b)
$\tilde{S}(\mathbf{Q}, \omega)$ .....	dynamic structure factor without detailed balance, see eq. (2.28)
$S(\mathbf{Q})$ .....	static structure factor
$2\vartheta$ .....	scattering angle
$\langle u^2 \rangle$ .....	mean square displacement
$u_0^2$ .....	proportionality factor between mean square displacement and temperature, see eq. (2.31)
$W$ .....	exponent of the Debye Waller factor $\exp(-2W)$
$Y_{2\theta}(\omega), Y(\omega)$ .....	instrumental energy resolution function
$Z(\omega)$ .....	phonon density of states
$Z_D(\omega)$ .....	phonon density of states in the Debye model, see eq. (2.32)
$\omega_L$ .....	peak position of librational mode, see eq. (5.2)

# 1 Introduction

**Ferrocene** (Fc) is probably the most prominent organometallic complex molecule. It has the full name 'bis( $\eta^5$ -cyclopentadienyl)iron', and its chemical structure consists of an iron atom sandwiched between two cyclopentadienyl (Cp) rings as depicted in Figure 1.1. It was discovered in the early 1950s independently by Kealy and Pauson<sup>[1]</sup> and Miller et al.,<sup>[2]</sup> but neither group recognized the correct, unusual molecular structure of the obtained yellow crystalline compound. The sandwich structure was proposed shortly after, by Fischer and Pfab<sup>[3]</sup> and Wilkinson et al.,<sup>[4]</sup> and confirmed by Dunitz and Orgel<sup>[5]</sup> and Eiland and Pepinsky<sup>[6]</sup> using X-ray scattering in 1953. What followed was the opening of a new field of chemistry, described as 'renaissance of inorganic chemistry'.<sup>[7]</sup> The Nobel Prize in chemistry was awarded in 1973 to Fischer and Wilkinson 'for their pioneering work, performed independently, on the chemistry of the organometallic, so called sandwich compounds'.

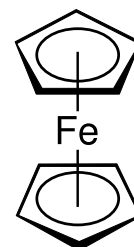


**Figure 1.1:**  
Ferrocene

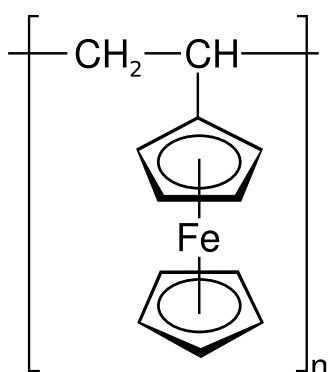


**Figure 1.2:**  
Poly(vinylferrocene)

One of the fields related to organometallic and macromolecular chemistry presently of strong interest is the synthesis and applications of ferrocene containing polymers. One such polymer, poly(vinylferrocene) (PVFc), is depicted in Figure 1.2. The ferrocene unit is laterally attached to a hydrocarbon backbone. The interest in applications using such polymers is thanks to the electron donor properties of Fc: it can be easily oxidized and reduced, with high stability over many cycles. This makes PVFc and other ferrocene containing polymers suitable candidates for stimuli-responsive materials, which, under the influence of external triggers, are in general able to change their properties like solubility or conformation, or can form and break covalent bonds.<sup>[8]</sup> In case of PVFc, use can be made of a redox-stimulus. The redox-responsiveness of various ferrocene containing polymers has been used, amongst other examples, in self-healing materials,<sup>[9]</sup> for switching surface wettability using grafted thin films,<sup>[10]</sup> or ion-selective membrane gating.<sup>[11]</sup>

The electronic structure of the ferrocene molecule shows a so-called  $\eta_5$  complex coordination bond involving 18 valence electrons. This bond allows for rotational reorientation of the Cp rings around the vertical 5-fold symmetry axis of the molecule. The main topic of this work is less related to immediate applications of the above mentioned systems, but pursues more fundamental questions to shed light on the **molecular ring rotation dynamics in the ferrocene molecule**. How is this dynamics changed through oxidation in the ferrocenium ion? Does ring rotation persist in ferrocene containing polymers like PVFc? Such questions are ideal for being studied by means of quasielastic neutron scattering (QENS), for example by using time of flight (ToF) and backscattering (BS) spectroscopy. These techniques access correlation times of the dynamics on a time scale from picoseconds to several nanoseconds. Moreover, they allow for a detailed study of the geometry of the motion, for example its spatial extent and the number of equilibrium sites.

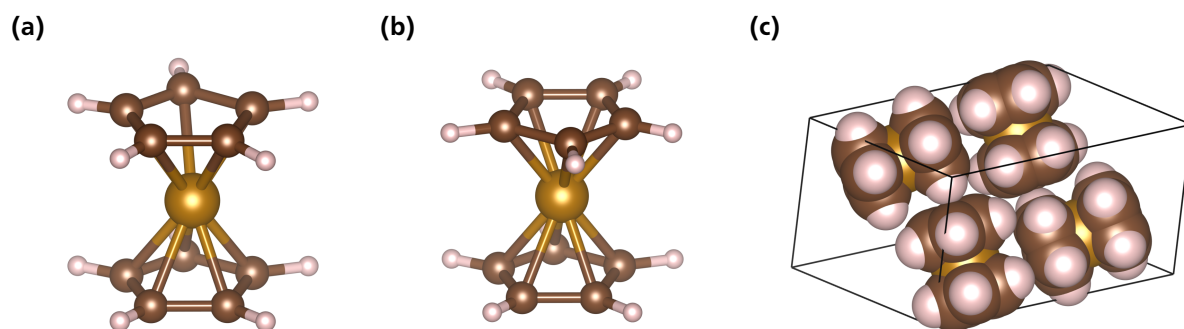


**Figure 1.3:** Ball-and-stick model of the ferrocene molecule in (a) eclipsed  $D_{5h}$  and (b) staggered  $D_{5d}$  conformation. (c) Unit cell of the metastable low temperature triclinic structure at 101 K.<sup>[12]</sup> (Images rendered with VESTA<sup>[13]</sup>)

### 1.1 Ring rotation and polymorphism: bulk ferrocene

The first obvious step in studying ring rotation dynamics of the ferrocene complex is to start with the supposedly simplest system: bulk ferrocene. But already the question of how the rings of the molecule are oriented with respect to each other does not have a simple answer. They could be in ‘eclipsed’ conformation, where the rings are congruent when projected along the vertical symmetry axis as shown in Figure 1.3a. This corresponds to  $D_{5h}$  point group symmetry. Or the rings could be ‘staggered’, with an inversion center on the central iron atom as in Figure 1.3b ( $D_{5d}$  symmetry). The latter is the form usually drawn in the chemical structure (see Figure 1.1).

This question has been dealt with in several studies of the crystal structure of ferrocene. It was found that ferrocene shows a unique polymorphism, which is different from similar organometallic complexes like ruthenocene or nickelocene.<sup>[14–16]</sup> At room temperature, ferrocene crystallizes in a monoclinic structure, where the Cp rings are rotationally disordered and the conformation is staggered ( $D_{5d}$ ) only on average.<sup>[17–20]</sup> As shown in the enthalpy diagram in Figure 1.4, the monoclinic phase becomes metastable upon cooling. Below 242 K, the stable phase is orthorhombic with Cp rings fully ordered in molecular eclipsed conformation ( $D_{5h}$ ). However, the stable phase can only be obtained under certain experimental conditions and was discovered only in the late 1970s.<sup>[21–23]</sup> Ferrocene usually stays in its monoclinic metastable phase when cooled and transforms to a triclinic phase below 164 K.<sup>[12,17,24]</sup> The rings are ordered in the triclinic phase, but a single molecule is neither in fully eclipsed nor staggered conformation: the rings are twisted by  $9^\circ$  from the eclipsed conformation ( $D_5$ ).<sup>[12]</sup> As an example, the packing of the triclinic structure is shown in Figure 1.3c, where the unit cell contains 2 independent molecules and 2 symmetry related molecules. Cooling single crystals below the monoclinic-triclinic phase transition leads to ‘crystal disintegration with explosive violence.’<sup>[25]</sup> If the fragments are subsequently annealed at 190 K, recrystallization to the orthorhombic phase can be obtained on a time scale of days. The orthorhombic phase is then easily overheated and starts to transform back to the monoclinic one above 242 K,<sup>[22,26]</sup> as indicated by the arrows in Figure 1.4.

Likewise the rotation dynamics of the Cp rings in ferrocene was attributed a considerable amount of attention and has been subject to numerous investigations using different techniques. In the gas phase, the equilibrium conformation was found to be eclipsed, and the intramolecular potential barrier to ring rotation was estimated by electron diffraction to  $(3.8 \pm 1.3) \text{ kJ mol}^{-1}$  by Haaland and Nilsson.<sup>[27]</sup> The different conformations in the different crystalline phases already indicate that the potential barrier to ring reorientation is significantly influenced by the local environment of the molecule, and by the packing of the crystal structure. Nuclear magnetic resonance (NMR) studies have indeed shown that the molecular reorientation rate is different

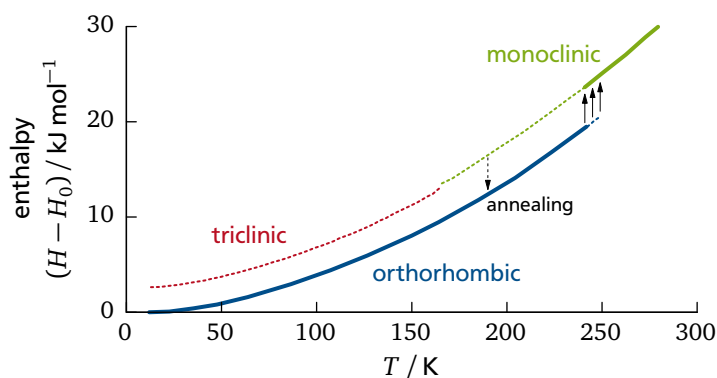


**Figure 1.4:** Enthalpy diagram, showing different phases of crystalline ferrocene. Data taken from Ogasahara et al.<sup>[26]</sup>

in all three crystalline phases, with different activation energies.<sup>[28–30]</sup> As expected, the dense, ordered orthorhombic phase shows the largest energy barrier while the disordered monoclinic high temperature phase has the smallest barrier. Later, energy barriers were also calculated from atomic displacement parameters extracted from diffraction measurements.<sup>[31]</sup> The lattice energy governed by non-bonding forces has been calculated, and conclusions have been drawn concerning the disorder of the rings in the monoclinic room temperature phase.<sup>[31,32]</sup> The rotational disorder has also been investigated by vibrational Raman and infrared spectroscopy.<sup>[33]</sup> Many aspects on Fc have been studied in the past and only a fraction of the work already done can be mentioned in this introduction. For a more comprehensive overview, numerous review articles can be consulted, e.g., by Braga<sup>[15]</sup> or Dunitz.<sup>[14]</sup> Most of the work and interest in crystalline Fc dates back to more than 30 years from today. But, as quoted from Dunitz in his review, ‘the ferrocene story is full of unexpected complications, and many aspects are still debatable.’<sup>[14]</sup>

QENS has been applied once before to determine correlation times, activation energies and the geometry of the rotational motion of Fc in the monoclinic phase by Gardner et al. in the early 1980s.<sup>[34]</sup> A rotational jump diffusion model with 5 equilibrium sites has been favored over 10 equilibrium sites, and Fc has become a prominent example for reorientational jump motion in molecular crystals.<sup>[35]</sup> Gardner et al. also studied the triclinic phase, but their neutron ToF experiments did not provide the energy resolution necessary to achieve a detailed analysis of the Cp ring rotation dynamics in the low temperature phase. The activation energies present in literature are based on NMR experiments,<sup>[28–30]</sup> potential energy calculations,<sup>[16,32]</sup> or extracted from atomic displacement parameters.<sup>[31]</sup>

In the course of this thesis, it turned out that the 5-fold jump rotation model for the ring rotation dynamics is a debatable aspect. The extension of data to a wider temperature and momentum transfer range necessitates to extend the present picture of rotational dynamics of the Cp rings in crystalline Fc. It will be shown that the rotational disorder in the monoclinic phase needs to be accounted for in modeling the dynamics in a consistent way, and the combination of neutron ToF and BS spectroscopy enables a study of the Cp ring rotation dynamics in the triclinic phase to an unprecedented extent. A key aspect here is a sophisticated approach to data analysis, including multiple scattering corrections and simultaneous model refinement using data from different instruments, temperatures, energy transfers and momentum transfers.

---

## 1.2 Outline of this thesis

---

The principle aim of this thesis is the study of ring rotation dynamics in the Fc molecule using QENS. The present picture and models of ring rotation dynamics in bulk Fc is extended, with the main focus on the triclinic and monoclinic crystalline phases. Subsequently, ring rotation in the salt  $\text{FcI}_3$  with ferrocenium ions, and ring rotation in the polymer PVFc will be investigated.

This thesis is structured in two parts. In [Part I](#), the basics of neutron scattering, the used models and the approach to data analysis will be discussed. The relevant parts of neutron scattering theory will be summarized in [chapter 2](#), with focus on the aspects relevant for the experiments. This comprises incoherent scattering, van Hove correlation functions, the influence of lattice vibrations on the measured spectra, and polarized neutron scattering. Magnetic neutron scattering will be briefly summarized as well. The model functions for rotational jump diffusion describing the molecular motion of the Cp rings as seen in incoherent neutron scattering are introduced in [chapter 3](#). The starting point is a model for equivalent sites on a circle, which will be extended to non-equivalent sites in order to account for the rotational disorder in the monoclinic phase of bulk Fc. Details on the neutron scattering experiments to study such dynamics and related aspects are given in [chapter 4](#). A key aspect of the QENS studies presented in this thesis is the approach to data analysis. In [chapter 5](#) the fitting routines will be discussed, which include iterative corrections for multiple scattering and allow for a global analysis of many data sets from different instruments.

Thereafter, the results of the experiments will be presented in [Part II](#). Starting with bulk Fc, [chapter 6](#) contains results and discussion of QENS experiments on all three crystalline phases. The study of ring rotation is then widened to oxidized ferrocene in the salt ferrocenium triiodide ( $\text{FcI}_3$ ) in [chapter 7](#). To the best of knowledge, there is no previous study of the ring rotation dynamics in  $\text{FcI}_3$ . Moreover, a hitherto unknown phase transition is found at 85 K, showing similarities to the monoclinic-triclinic transition in Fc regarding ring rotation dynamics.

Subsequently, the focus is shifted to ferrocene containing polymers. In [chapter 8](#) it will be seen that ring rotation is still active in PVFc, but shows a large dynamical heterogeneity. This demands the use of a relaxation rate distribution model (RRDM), taking into account the differences in local environment of the Fc units in the glassy polymer structure of PVFc.

Complementary to the study of comparably slow ring reorientation dynamics, the spectrum of vibrational modes of Fc,  $\text{FcI}_3$  and various ferrocene containing polymers will be determined in [chapter 9](#). The influence of oxidation and/or incorporation into a polymer structure on the vibrational spectrum of the Fc molecule will be discussed.

Finally, [chapter 10](#) will present measurements on oxidized PVFc under external magnetic fields. Oxidation of the ferrocene complex causes one unpaired electron leading to a magnetic moment on the ferrocene complex. While bulk ferrocene itself is diamagnetic, paramagnetic and even small ferromagnetic susceptibilities have been reported for ferrocene containing polymers.<sup>[36,37]</sup> In the experiments that will be presented, the quasielastic scattering originating from the ring rotation dynamics proved to be insensitive to the external magnetic field up to 2.5 T. On the other hand, an inelastic excitation was observed in oxidized PVFc which will be interpreted as Zeeman splitting of the electronic magnetic moment. Moreover, in high resolution BS spectroscopy the splitting of nuclear magnetic moments becomes visible in incoherent scattering on hydrogen. The results obtained in this chapter are for the most part not related to the main topic of molecular ring rotation dynamics. However, they do bear unique and novel results of fundamental physical effects, which can be obtained from a concise analysis of experimental data with little effort.

---

# Part I

## Theory, models & methods

---





---

## 2 Neutron scattering

Scattering experiments are versatile and often used in different disciplines of experimental physics. In general, they provide information about nano-, micro- and mesoscopic properties of a sample by analyzing the characteristics of scattered radiation. Scattering experiments can be performed with different kinds of radiation – and thanks to the particle-wave duality, the basic description in terms of wave properties holds for matter waves as well as for electromagnetic waves. In condensed matter physics, common experimental methods involve scattering of light, electrons, X-rays – or neutrons. Although the general theory of scattering is alike independent of the type of radiation used, the following sections focus on neutron scattering in view of the experiments presented in [Part II](#).

Moreover, neutron scattering has some peculiarities due to the spin of the neutron, the neutron-nuclei strong interaction, and the interaction with magnetic moments by electromagnetic forces. The rigorous treatment of neutron scattering in all details easily fills multiple textbooks, and a comprehensive introduction cannot be given here. The following brief recapitulation of neutron scattering theory is mostly along the lines of the textbook *Theory of Neutron Scattering from Condensed Matter*, Volumes 1 and 2, by [Lovesey](#),<sup>[38,39]</sup> which is one of several textbooks giving a more detailed and comprehensive treatment of the topic. After a very short general introduction to the basics of scattering experiments, the focus is quickly turned to aspects relevant to the analysis and the understanding of experiments in [Part II](#).

---

### 2.1 Basic definitions in neutron scattering experiments

---

The general description of a scattering experiment is usually given by considering each Fourier component of the incident radiation separately. The initial neutron state is thus a plane wave with wave vector  $\mathbf{k}_i$  and wavelength  $\lambda_{\text{inc}} = 2\pi k_i^{-1}$ , denoted by the quantum mechanical state vector  $|\mathbf{k}_i\rangle$  and the wave function

$$\psi_{\mathbf{k}_i}(\mathbf{r}) \propto \exp(i\mathbf{k}_i \cdot \mathbf{r}) \quad . \quad (2.1)$$

The energy of an incident neutron is accordingly

$$E_i = \frac{\hbar^2 k_i^2}{2m_n} \quad (2.2)$$

with the neutron mass  $m_n = 1.674927 \times 10^{-27}$  kg.<sup>[40]</sup>

In a scattering experiment, the intensity scattered from the sample in a given direction is measured by a detector, within a differential solid angle element  $d\Omega$ . Moreover, in certain experiments, the energy of scattered neutrons is analyzed, allowing detection of neutrons only in a differential energy interval  $[E_f, E_f + dE_f]$ . The unit of measured intensity is ‘neutron counts per unit time’.

The sketch in [Figure 2.1](#) shows the relationship between incident wave vector  $\mathbf{k}_i$ , the wave vector of the observed scattered radiation  $\mathbf{k}_f$ , and the scattering vector  $\mathbf{Q}$  which is defined as

$$\mathbf{Q} = \mathbf{k}_i - \mathbf{k}_f \quad . \quad (2.3)$$

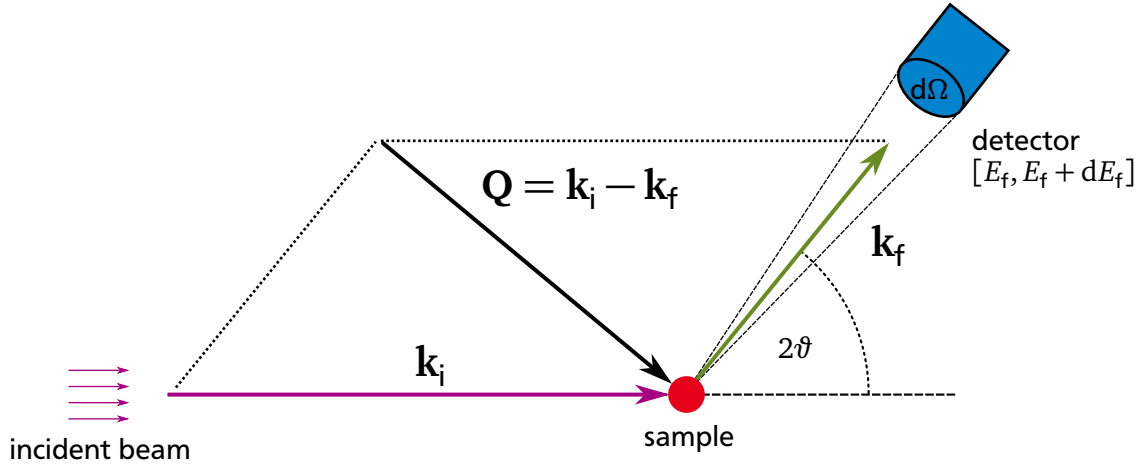


**Figure 2.1:** Wave vector relations in a general scattering experiment, showing wave vectors of incident and scattered waves  $\mathbf{k}_i$  and  $\mathbf{k}_f$ , scattering vector  $\mathbf{Q}$ , scattering angle  $2\vartheta$  and the solid angle element  $d\Omega$  observed with a detector.

Applying momentum and energy conservation laws, the momentum transfer from the neutron on the sample results to  $\hbar\mathbf{Q}$ , and the energy transfer to

$$E = E_i - E_f \quad . \quad (2.4)$$

In this definition, a positive value of  $E$  corresponds to neutron energy loss – it is thus always  $E \leq E_i$ , and  $E < 0$  for events where the neutron gained energy during the scattering process.

The magnitude of the scattering vector can be expressed by using the scattering angle  $2\vartheta$  between incident and scattered wave vector:

$$\begin{aligned} Q^2 &= k_f^2 + k_i^2 - 2k_i k_f \cos 2\vartheta \\ &= \frac{2m_n}{\hbar^2} (E_f + E_i - 2\sqrt{E_i E_f} \cos 2\vartheta) \\ &= \frac{2m_n}{\hbar^2} (2E_i - E - 2\sqrt{E_i(E_i - E)} \cos 2\vartheta) \end{aligned} \quad (2.5)$$

where eq. (2.2) was used to introduce the initial and final neutron energies. For elastic scattering with  $E = 0$  or scattering processes where energy transfer is sufficiently small ( $|E| \ll E_i$ ), eq. (2.5) can be simplified to the well known form

$$Q_{\text{el}} = \frac{4\pi}{\lambda_{\text{inc}}} \sin \vartheta \quad . \quad (2.6)$$

While eq. (2.6) can be sufficient in some cases to relate scattering angle to scattering vector, eq. (2.5) must generally be used in inelastic scattering experiments. This will be further discussed in the context of data analysis in chapter 5.

---

## 2.2 The scattering cross section for elastic scattering

---

In order to normalize the scattered intensity in an experiment, one usually quantifies the scattering power using the scattering cross section  $\sigma$ . We first consider only the directional dependency

of scattered neutrons, disregarding their energy for now. In this case, the differential cross section

$$\frac{d\sigma}{d\Omega} = \frac{I_s}{\Phi_0} \quad (2.7)$$

defines the scattering characteristics of a sample, where  $\Phi_0$  is the incident flux, i.e., neutrons per unit time and area, and  $I_s$  the number of neutrons per unit time detected in the solid angle element  $d\Omega$ . The total scattered intensity from the sample in any direction characterized by the total cross section  $\sigma$  can be obtained by integration of the differential cross section over the unit sphere:

$$\sigma = \oint d\Omega \frac{d\sigma}{d\Omega} \quad (2.8)$$

The scattering cross section can be understood as an equivalent surface perpendicular to the incident beam which receives an amount of intensity equal to the scattered intensity. Neutron scattering cross sections for elements are usually given in barn ( $1 \text{ barn} = 10^{-24} \text{ cm}^2$ ). If one considers for example a single  $^{12}\text{C}$  atom in an incoming homogeneous flux of thermal neutrons, the total scattered intensity is equivalent to the impinging integrated flux on a surface of  $5.559(3) \text{ barn}$ .<sup>[41]</sup>

In order to calculate the scattering from a given arrangement of atoms in the sample, assumptions must be made for the scattering potential. In contrast to X-rays, which are scattered on the comparably large electron cloud of atoms, neutrons are scattered from the small nuclei. They can also interact with magnetic moments, which is very useful for the study of magnetic structures or spin dynamics. But we will first focus here on the nuclear scattering only, while a short introduction to magnetic scattering will be given in [section 2.6](#). Thermal neutron wavelengths are by orders of magnitude larger than the dimensions of nuclei, and the scattering from a single nucleus is thus isotropic (so-called s-wave scattering). The scattering potential  $\hat{V}(\mathbf{r})$  can be modeled in very good approximation by the  $\delta$ -shaped Fermi pseudo-potential:<sup>[38]</sup>

$$\hat{V}(\mathbf{r}) = \frac{2\pi\hbar^2}{m_n} b \delta(\mathbf{r} - \mathbf{R}) \quad (2.9)$$

where  $\mathbf{R}$  is the position of the nucleus, and  $b$  the scattering length which is related to the single nucleus cross section  $\sigma$  by

$$\sigma = 4\pi|b|^2 \quad (2.10)$$

The scattering length  $b$  can be negative and/or complex, where the imaginary part models absorption of neutrons by radiative capture. In contrast to X-ray scattering, where the scattering length is proportional to the number of electrons and thus proportional to the atomic number, the neutron scattering length varies seemingly randomly from element to element. Moreover, it can show large differences for different isotopes of the same element, and ultimately depend on the relative spin orientation of neutron and nuclear spin.

The Hamilton operator for the neutron including the scattering potential is

$$\hat{\mathcal{H}} = \frac{\hbar^2 k^2}{2m_n} + \hat{V}(\mathbf{r}) \quad (2.11)$$

Given that the scattering potential is only a small perturbation of the free neutron state, the cross section for the transition between initial state  $|\mathbf{k}_i\rangle$  and final state  $|\mathbf{k}_f\rangle$  can be expressed in terms of the first Born approximation, that is, first order perturbation theory:

$$\frac{d\sigma}{d\Omega} = |\langle \mathbf{k}_i | \hat{V} | \mathbf{k}_f \rangle|^2 \quad (2.12)$$

In a rigorous treatment, the initial and final neutron states must be properly normalized as discussed by Lovesey.<sup>[38]</sup>

For further considerations, we will consider the cross section for a given monoatomic, static sample structure. One has to keep in mind that the scattering length of a given atom still depends on the specific isotope and nuclear spin state. The scattering potential of a monoatomic sample structure consists thus of scattering centers with different scattering lengths  $b_k$  at positions  $\mathbf{R}_k$ , and the potential from eq. (2.9) is extended to

$$\hat{V}(\mathbf{r}) = \frac{2\pi\hbar^2}{m_n} \sum_k b_k \delta(\mathbf{r} - \mathbf{R}_k) \quad . \quad (2.13)$$

The calculated cross section from eq. (2.12) is accordingly

$$\frac{d\sigma}{d\Omega} = \sum_{k,l} \overline{b_k^* b_l} \exp[i\mathbf{Q} \cdot (\mathbf{R}_l - \mathbf{R}_k)] \quad (2.14)$$

where the asterisk stands for complex conjugation, and the horizontal bar in  $\overline{b_k^* b_l}$  stands for averaging over random spin orientation and isotope distribution of the nuclei. The derivation using the appropriate formalism of calculation of the matrix element in eq. (2.12) is discussed in ref. [38]. This form of the scattering cross section can be further simplified by splitting eq. (2.14) into coherent and incoherent parts as discussed in the following.

---

### 2.3 Coherent and incoherent scattering

---

As already stated above, the neutron scattering length  $b$  for a given element is dependent on the isotope number and the spin orientation between nucleus and neutron. This gives rise to so-called coherent and incoherent scattering. If one considers, for the monoatomic sample from section 2.2, the distribution of isotopes and spin states to be fully random and uncorrelated to the atomic positions, the averaging of scattering lengths in eq. (2.14) can be expressed as

$$\overline{b_k^* b_l} = \begin{cases} \overline{|b_k|^2} = \overline{|b|^2} & \text{for } k = l \\ \overline{b_k^*} \overline{b_l} = \overline{|b|^2} & \text{for } k \neq l \end{cases} \quad (2.15)$$

or, using the Kronecker delta,

$$\overline{b_k^* b_l} = \overline{|b|^2} + \delta_{kl} \left( \overline{|b|^2} - \overline{|b|^2} \right) \quad . \quad (2.16)$$

Inserting this into eq. (2.14) allows to split the sum and rewrite the differential scattering cross section in the general form

$$\frac{d\sigma}{d\Omega} = N_t \frac{\sigma_{\text{coh}}}{4\pi} S(\mathbf{Q}) + N_t \frac{\sigma_{\text{inc}}}{4\pi} \quad (2.17)$$

with the total number of atoms  $N_t$ , the cross sections

$$\sigma_{\text{coh}} = 4\pi \overline{|b|^2} \quad , \quad (2.18a)$$

$$\sigma_{\text{inc}} = 4\pi \left( \overline{|b|^2} - \overline{|b|^2} \right) \quad (2.18b)$$


---

and

$$S(\mathbf{Q}) = \frac{1}{N_t} \sum_{k,l} \exp[i\mathbf{Q} \cdot (\mathbf{R}_l - \mathbf{R}_k)] \quad . \quad (2.19)$$

The quantity  $\sigma_{\text{coh}}$  is called coherent scattering cross section and calculated from the average scattering lengths of isotopes and spin states of a given element. It gives the part of scattering containing information about the structure of the sample characterized by the structure factor  $S(\mathbf{Q})$ , leading, e.g., to the well known Bragg peaks for crystalline samples. The variance of the scattering length densities relates to the incoherent scattering cross section  $\sigma_{\text{inc}}$ . It describes the part of the scattering from different scattering centers which cannot interfere due to the random arrangement of isotopes and spin states, thus leading to  $\mathbf{Q}$  independent, isotropic scattering. A list of cross sections for some elements and compounds relevant to this work is given in [Table 2.1](#) on [page 17](#) at the end of this chapter.

The incoherent part of the scattering is often considered spurious background in experiments focusing on structure determination, but it plays the central role in all inelastic neutron scattering experiments performed in this work, where the coherent part takes the role of spurious scattering. The significance of the incoherent scattering in inelastic neutron scattering experiments will be discussed in the following.

---

## 2.4 Inelastic neutron scattering and correlation functions

---

There are multiple techniques in neutron scattering that allow to determine the kinetic energy of scattered neutrons. These inelastic scattering experiments allow to investigate not only the structure of a sample, but also its microscopic dynamics on different time scales.

Corresponding to the differential cross section in [eq. \(2.7\)](#), the double differential scattering cross section

$$\frac{d^2\sigma}{d\Omega dE_f} = \frac{I_s}{\Phi_0} \quad (2.20)$$

is used in inelastic scattering experiments. While  $\Phi_0$  is still the incident neutron flux,  $I_s$  now stands for the scattered intensity in the differential solid angle element  $d\Omega$  and energy interval  $[E_f, E_f + dE_f]$ . To describe inelastic scattering, one can consider a scattering potential similar to [eq. \(2.13\)](#), but with time dependent positions of the scattering centers. However, a rigorous treatment necessitates to take the full quantum mechanical state of the sample into consideration together with the neutron state, as the scattering process can exchange energy between neutron and sample. The resulting differential scattering cross section is similar to [eq. \(2.17\)](#):

$$\frac{d^2\sigma}{d\Omega dE_f} = N_t \frac{k_f}{k_i} \left[ \frac{\sigma_{\text{coh}}}{4\pi} S_{\text{coh}}(\mathbf{Q}, \omega) + \frac{\sigma_{\text{inc}}}{4\pi} S_{\text{inc}}(\mathbf{Q}, \omega) \right] \quad . \quad (2.21)$$

When comparing [eq. \(2.17\)](#) and [eq. \(2.21\)](#), two things are noticed for inelastic scattering: Firstly, the term  $k_f/k_i$  appears which arises from the ratio of density of states for incident and scattered neutrons. Secondly, and more importantly, both the coherent and incoherent part now include  $\mathbf{Q}$  and  $\omega$  dependent terms  $S_{\text{coh}}(\mathbf{Q}, \omega)$  and  $S_{\text{inc}}(\mathbf{Q}, \omega)$ , which are called coherent and incoherent dynamic structure factor respectively. Both quantities are related to the structure and dynamical processes in the sample, and have a very useful relationship to the correlation functions of scattering centers, usually referred to as van Hove correlation functions. [Equation \(2.19\)](#) shows for the static case that the structure factor relates to the Fourier transform of pair correlations. This formalism involving Fourier transforms can be generalized for inelastic scattering (see ref. [38] for a detailed discussion). [Figure 2.2](#) gives a visualization of the resulting relationships, which will be discussed in the following.

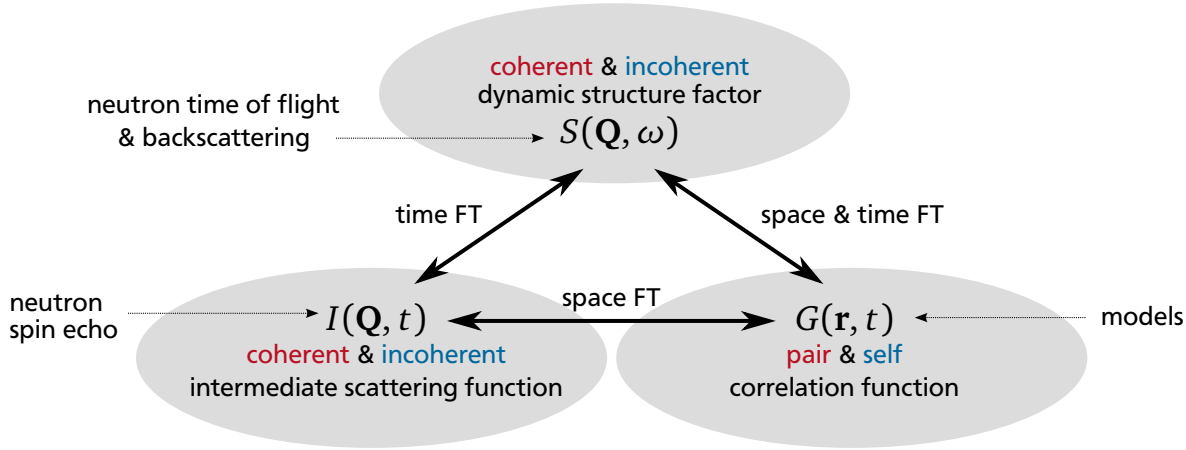


**Figure 2.2:** Relationship diagram for different quantities used in inelastic neutron scattering experiments and their accessibility by different methods. All quantities are related by Fourier Transformation (FT) with respect to space and/or time.

For a sound definition of the correlation functions, a quantum mechanical treatment is indispensable and it has to be taken into account that the time dependent position operators  $\hat{\mathbf{R}}_l(t)$  of the scattering centers in the sample do not commute in general. The pair correlation function of the particles in a monoatomic sample is defined as

$$G(\mathbf{r}, t) = \frac{1}{N_t} \sum_{k,l} \int d^3 r' \left\langle \delta \left\{ \mathbf{r} - [\mathbf{r}' - \hat{\mathbf{R}}_k(0)] \right\} \delta \left\{ \mathbf{r}' - \hat{\mathbf{R}}_l(t) \right\} \right\rangle \quad (2.22a)$$

$$\stackrel{\text{cl.}}{=} \sum_k \left\langle \delta \left\{ \mathbf{r} - [\mathbf{R}_k(t) - \mathbf{R}_0(0)] \right\} \right\rangle \quad (2.22b)$$

where the second equality only holds in a classical systems when all position operators commute and all particles are equivalent. The pair correlation function  $G(\mathbf{r}, t)$  essentially gives the probability of observing any particle at distance  $\mathbf{r}$  after time  $t$  relative to the position of a given particle at  $t = 0$ . In contrast to this, the self correlation function  $G_s(\mathbf{r}, t)$  gives the corresponding probability of finding exactly the same particle at distance  $\mathbf{r}$  after time  $t$ :

$$G_s(\mathbf{r}, t) = \frac{1}{N_t} \sum_k \int d^3 r' \left\langle \delta \left\{ \mathbf{r} - [\mathbf{r}' - \hat{\mathbf{R}}_k(0)] \right\} \delta \left\{ \mathbf{r}' - \hat{\mathbf{R}}_k(t) \right\} \right\rangle \quad (2.23a)$$

$$\stackrel{\text{cl.}}{=} \left\langle \delta \left\{ \mathbf{r} - [\mathbf{R}_0(t) - \mathbf{R}_0(0)] \right\} \right\rangle \quad (2.23b)$$

Note that the self correlation  $G_s(\mathbf{r}, t)$  is also contained in  $G(\mathbf{r}, t)$ . These correlation functions are usually what is calculable from models or simulations, e.g., from particle trajectories. The spatial Fourier transform of the correlation function is called intermediate scattering function. It turns out that the pair correlation function describing particle correlations causes coherent scattering:

$$I_{\text{coh}}(\mathbf{Q}, t) = \int d^3 r \exp(i\mathbf{Q} \cdot \mathbf{r}) G(\mathbf{r}, t) \quad , \quad (2.24)$$

and the self correlation function causes incoherent scattering accordingly:

$$I_{\text{inc}}(\mathbf{Q}, t) = \int d^3 r \exp(i\mathbf{Q} \cdot \mathbf{r}) G_s(\mathbf{r}, t) \quad . \quad (2.25)$$

The intermediate scattering functions are already directly accessible by experimental methods, for example neutron spin echo spectroscopy. A temporal Fourier transform relates both functions to the dynamic structure factors in eq. (2.21):

$$S_{\text{coh}}(\mathbf{Q}, \omega) = \frac{1}{2\pi\hbar} \int dt \exp(i\omega t) I_{\text{coh}}(\mathbf{Q}, t) \quad (2.26a)$$

$$S_{\text{inc}}(\mathbf{Q}, \omega) = \frac{1}{2\pi\hbar} \int dt \exp(i\omega t) I_{\text{inc}}(\mathbf{Q}, t) \quad (2.26b)$$

The dynamic structure factors are quantities that can directly be measured by inelastic neutron scattering techniques like time of flight or backscattering spectroscopy (see chapter 4). In the description of the jump rotation models in chapter 3, the self correlation function  $G_s(\mathbf{r}, t)$  will be calculated from a model, and subsequently transformed via the incoherent intermediate scattering function to the incoherent dynamic structure factor which can be used to analyze experimental data.

In this context, another important remark is to be made: From commutator relationships it can be shown in general that, in a quantum mechanical treatment, the dynamic structure factors fulfill the condition of detailed balance, i.e.

$$S(\mathbf{Q}, \omega) = \exp\left(\frac{\hbar\omega}{k_B T}\right) S(-\mathbf{Q}, -\omega) \quad (2.27)$$

where  $k_B$  is the Boltzmann constant. This condition reflects the thermal population asymmetry of energetically different states in the sample according to the Boltzmann factor. If a classical treatment is chosen in eq. (2.22), then the resulting dynamic structure factor is even in  $\omega$  and does not fulfill the condition of detailed balance. From eq. (2.27), an even function can be obtained by defining

$$\tilde{S}(\mathbf{Q}, \omega) = \exp\left(-\frac{\hbar\omega}{2k_B T}\right) S(\mathbf{Q}, \omega) \quad (2.28)$$

It is a common approach to introduce detailed balance in the end of a classical model calculation by replacing  $\tilde{S}(\mathbf{Q}, \omega)$  in eq. (2.28) with the dynamic structure factor obtained from a Fourier transformed classical correlation function.<sup>[35,38]</sup> Therefore, in this work, the tilde on  $\tilde{S}(\mathbf{Q}, \omega)$  generally signifies that detailed balance has not yet been included in the dynamic structure factor.

---

#### 2.4.1 Lattice vibrations and the Debye Waller factor

---

In principle, the van Hove formalism summarized above contains everything that is needed to obtain the dynamic structure factors, given the correlation functions of a sample. On the other hand, simple models like the rotational jump diffusion model do not aim to entirely describe the dynamics in a sample down to the last bit. It is therefore useful to be aware of the influence of other important dynamical processes not immediately included in the simplified models of that kind, with probably the most important one being lattice vibrations. Lattice vibrations displace the atoms around their equilibrium positions which leads to decreased scattered intensity due to the Debye Waller factor. Moreover, excitations can be seen in the inelastic spectrum by processes that create or annihilate phonons.

## The Debye Waller factor

In a solid sample that is not static and shows lattice vibrations, the average positions of the individual particles are smeared around their equilibrium positions. In a simplified approach, one can imagine that the particle density is convoluted with a narrow Gaussian smearing factor, such that the structure factor resulting from a Fourier transformation will be multiplied with a broad Gaussian according to the convolution theorem. If treated in more detail, it is found for elastic scattering that the cross section corresponding to eq. (2.17) is modified to

$$\left(\frac{d\sigma}{d\Omega}\right)_{\text{el}} = \left[ N_t \frac{\sigma_{\text{coh}}}{4\pi} S(\mathbf{Q}) + N_t \frac{\sigma_{\text{inc}}}{4\pi} \right] \exp(-2W) \quad (2.29)$$

The additional exponential factor is the Debye Waller factor, and  $W$  can be expressed as

$$2W = \frac{1}{3} Q^2 \langle u^2 \rangle \quad (2.30)$$

where  $\langle u^2 \rangle$  is the mean square displacement of the atoms from their equilibrium position. Technically, eq. (2.30) holds only for cubic crystals where displacements are isotropic, but is generally considered a good approximation.<sup>[35,38]</sup> Thus, lattice vibrations indeed lead to a Gaussian decrease of intensity with increasing  $Q$ , related to the inverse mean square displacement. Given the phonon density of states (DOS)  $Z(\omega)$ , the mean square displacement in eq. (2.30) can be replaced:

$$W = \frac{\hbar Q^2}{4M} \int_0^{\omega_m} d\omega \frac{Z(\omega)}{\omega} \coth\left(\frac{\hbar\omega}{2k_B T}\right) \stackrel{\text{Debye}}{\underset{T \gg \theta_D}{\approx}} \frac{1}{6} Q^2 u_0^2 T \quad (2.31)$$

where  $M$  is the mass of the nuclei and  $\omega_m$  is the maximum phonon frequency. In the second step, the integral in eq. (2.31) was approximated by assuming a Debye DOS for  $Z(\omega)$ :

$$Z(\omega) \mapsto Z_D(\omega) = \frac{3\omega^2}{\omega_D^3} \quad (2.32)$$

with the Debye frequency  $\omega_D = \omega_m$ . The Debye temperature  $\theta_D$  is related to the Debye frequency by  $\hbar\omega_D = k_B \theta_D$ . At temperatures above the Debye temperature, a linear temperature dependence of the mean square displacement with a proportionality factor  $u_0^2$  is a viable approximation as can be seen from eq. (2.31).

It can be shown that the Debye Waller factor also appears as additional term in inelastic phonon scattering (see next paragraph), or can be added in quasielastic models like the rotational jump diffusion model as side effect of lattice vibrations.<sup>[42]</sup> As such it will take the place of a general prefactor in the overall model for the dynamic structure factor used for data analysis. Usually, a linear temperature dependence of the mean square displacement will be used with  $u_0^2$  as free parameter, although a more elaborate approach has been tested in one case for low temperatures by numerical integration of a measured density of phonon states in [Appendix C](#).

## Phonon creation and annihilation

While the Debye Waller factor discussed above causes only a decrease of scattering intensity due to lattice vibrations, neutrons can also create and annihilate phonons by exchanging energy with the sample. As all samples in this work are strong incoherent scatterers, we will only consider the incoherent cross section of inelastic one-phonon scattering. It can be calculated using the correlation functions from [section 2.4](#) as discussed in ref. [38] and takes the form

$$S_{\text{inc}}^{\text{vib}}(Q, \omega) = \frac{1}{2M} Q^2 \exp(-2W) \frac{Z(\omega)}{\omega} [n(\omega) + 1] \quad (2.33)$$



where  $M$  is the mass of the nuclei,  $Z(\omega)$  the density of phonon states, and  $n(\omega)$  the Bose-Einstein factor

$$n(\omega) = \left[ \exp\left(\frac{\hbar\omega}{k_B T}\right) - 1 \right]^{-1}. \quad (2.34)$$

It can be seen that eq. (2.33) contains the Debye-Waller factor discussed above, and that it relates directly to the density of phonon states  $Z(\omega)$ . With the definition  $Z(-\omega) = Z(\omega)$ , the above scattering law holds for phonon creation and annihilation, and the condition of detailed balance postulated in eq. (2.27) is also fulfilled. In chapter 9, inelastic neutron spectroscopy experiments will be used to access the phonon density of states up to energies of molecular vibrational modes by transforming the measured scattering law into a density of states similar to eq. (2.33).

---

## 2.5 Separation of coherent and incoherent scattering

---

In most neutron scattering experiments, the sum of coherent and incoherent parts of the scattering cross section in eq. (2.21) are measured. In the interpretation of the results, it is then in general not possible to determine which part of the observed intensity is due to coherent or incoherent scattering. As the models for rotational jump diffusion presented in the next chapter will describe the incoherent scattering only, the coherent part of the scattering must be separated to allow for a detailed data analysis. This can be done easily for crystalline sample when the coherent scattering is localized in Bragg peaks, but for amorphous polymer samples another approach needs to be taken as they show diffuse coherent scattering.

Fortunately, the spin of the neutron can be used in polarized scattering experiments to separate overlaying coherent from incoherent scattering. The term ‘polarization’ signifies a preferred spin orientation of neutrons in the beam with respect to a given quantization axis. A coherent scattering process does not change the spin polarization of scattered neutrons, while the spin-incoherent process flips the spin of the neutron with a probability of  $2/3$ . The term ‘spin-incoherent’ means the part of incoherent scattering that is caused by random spin orientations of the target nuclei. The part that is caused by random distribution of different isotopes, the so-called ‘isotope-incoherent’ fraction, does not flip the spin during scattering and thus remains indistinguishable from coherent scattering in polarized neutron experiments. However, in practice, virtually all incoherent scattering in the samples considered in this work is caused by hydrogen in spin-incoherent scattering processes and can thus be nicely separated.

An overview and derivation of the equations describing the scattering cross sections for polarized neutrons can be found, e.g., in a paper by Schärpf and Capellmann.<sup>[43]</sup> The relevant part of the resulting formalism used here is the measurement of the two cross sections

$$\frac{d^2\sigma_{\uparrow\downarrow}}{d\Omega dE_f} = \frac{N_t k_f}{4\pi k_i} \left[ \frac{2}{3} \sigma_{\text{inc}} S_{\text{inc}}(\mathbf{Q}, \omega) \right] \quad (2.35a)$$

$$\frac{d^2\sigma_{\uparrow\uparrow}}{d\Omega dE_f} = \frac{N_t k_f}{4\pi k_i} \left[ \frac{1}{3} \sigma_{\text{inc}} S_{\text{inc}}(\mathbf{Q}, \omega) + \sigma_{\text{coh}} S_{\text{coh}}(\mathbf{Q}, \omega) \right] \quad (2.35b)$$

where contributions from magnetic and isotope-incoherent scattering have been omitted and the indices correspond to spinflip ( $\uparrow\downarrow$ ) and non-spinflip ( $\uparrow\uparrow$ ) processes respectively. Thus, by measuring spinflip and non-spinflip scattering separately, the coherent and incoherent contributions to the total cross section can be calculated by an appropriate linear combination of eq. (2.35). Although the above method can be used in principle for elastic and inelastic scattering, polarized neutron experiments presented in chapter 8 have only been performed as

---

diffraction experiments without energy analysis of the scattered neutrons. In these experiments, the goal was only to determine the static structure factor  $S(Q)$  of predominantly elastic coherent scattering.

---

## 2.6 Magnetic neutron scattering

---

Up to now, only the nuclear scattering of neutrons by the strong interaction has been considered. An entire subfield of neutron scattering is based on the magnetic moment of neutrons, which allows neutrons to interact with magnetic moments and scatter on magnetic structures like (anti-)ferromagnetic lattices, to create or annihilate spin waves, or to map the spin density in crystalline structures – to name a few examples.

A detailed introduction to magnetic scattering lies beyond the scope of this chapter, and can be found, e.g., in volume 2 of the monograph by Lovesey.<sup>[39]</sup> The most important practical differences between nuclear and magnetic scattering are summarized in the following:

- In magnetic scattering, neutrons interact with the electronic spin density around the atoms, a cloud that has a much larger extent in space than the small nucleus. The scattering potential is therefore not  $\delta$ -shaped like the Fermi pseudo-potential in eq. (2.9), and the scattering from a single particle is no longer isotropic. It shows a strong dependence on  $\mathbf{Q}$  known as magnetic form factor  $F(\mathbf{Q})$ .
- Due to the nature of the magnetic interaction, only the component of the magnetization perpendicular to the scattering vector  $\mathbf{Q}$  contributes to the scattering.
- The basic measure of the magnetic scattering cross section appearing as prefactor in most equations is

$$r_0^2 = \left( \frac{\gamma_n e^2}{m_e c^2} \right)^2 = 0.29 \text{ barn} \quad (2.36)$$

with gyromagnetic ratio of the neutron  $\gamma_n$ , charge  $e$  and mass  $m_e$  of an electron, and the speed of light  $c$ . The resulting value of 0.29 barn gives an idea about the magnitude of magnetic scattering. It is small, but nevertheless lies in the range of nuclear cross sections such that it is experimentally feasible to observe magnetic scattering and nuclear scattering at the same time.

Magnetic neutron scattering will only be relevant in [chapter 10](#), where transitions between Zeeman split levels of a spin-1/2 system in an external magnetic field are observed. The magnetic scattering cross section for this process is calculated in [Appendix D](#).

**Table 2.1:** Nuclear scattering cross sections for neutrons on some elements and all sample compounds used in this work.<sup>[41]</sup> For polymers, all values are given per monomer unit. The list contains atomic/molecular weight  $M$ , incoherent and coherent scattering cross sections  $\sigma_{\text{inc}}$  and  $\sigma_{\text{coh}}$  as well as absorption cross sections  $\sigma_{\text{abs}}$ .

element/compound	composition	$M / u$	$\sigma_{\text{inc}} / \text{barn}$	$\sigma_{\text{coh}} / \text{barn}$	$\sigma_{\text{abs}} / \text{barn}^a$
Hydrogen	H	1.008	80.26	1.76	1.15
Deuterium	D	2.01	2.04	5.6	0
Carbon	C	12.01	0.001	5.55	0.01
Oxygen	O	16	0.01	4.23	0
Aluminum	Al	26.98	0.01	1.49	0.8
Silicon	Si	28.09	0.02	2.16	0.59
Vanadium	V	50.94	5.19	0.02	17.73
Iron	Fe	55.85	0.39	11.44	8.92
Cadmium	Cd	112.4	0	3.3	8788
Iodine	I	126.9	0.31	3.5	21.42
Ferrocene	$\text{C}_{10}\text{H}_{10}\text{Fe}$	186.04	803	84.54	20.53
$\text{FeI}_3^b$	$[\text{C}_{10}\text{H}_{10}\text{Fe}]^+ \text{I}_3^-$	566.74	803.93	95.04	84.79
PVFc <sup>c</sup>	$[\text{C}_{12}\text{H}_{12}\text{Fe}]_n$	212.08	963.52	99.16	22.85
PFDMS <sup>d</sup>	$[\text{C}_{10}\text{H}_8\text{Fe Si}(\text{CH}_3)_2]_n$	242.18	1124.06	104.84	25.74
PFMS <sup>e</sup>	$[\text{C}_{10}\text{H}_8\text{Fe SiH CH}_3]_n$	228.15	963.54	95.77	23.43

<sup>a</sup> The absorption cross section is calculated for 6.27 Å neutrons, whereas values in literature are usually given for 1.8 Å. <sup>b</sup> Ferrocenium Triiodide <sup>c</sup> Poly(vinylferrocene) <sup>d</sup> Poly(ferrocenyldimethylsilane)  
<sup>e</sup> Poly(ferrocenylmethylsilane)



---

## 3 Model functions for molecular ring rotation

In this chapter, the basic models for describing rotational jump diffusion motions in inelastic neutron scattering will be presented. When looking at the ferrocene molecules shown in [Figure 1.3](#) on [page 2](#), it is clear that the rotation of a cyclopentadienyl ring by  $2\pi/5$  does not change the potential energy of the molecule – the rotational potential must be (at least) of 5-fold symmetry, and there must be (at least) five equivalent equilibrium positions. Moreover, the molecule would look exactly the same before and after the jump if atoms were indistinguishable. A reorientation has only the effect that all carbon and hydrogen atoms move to another equivalent position, which leads to loss of self correlation. As discussed in the previous chapter, incoherent scattering allows to access the self correlation function, which contains valuable information about the jump motion of the cyclopentadienyl rings. Fortunately the scattering cross section for neutrons in either sample in this work is largely dominated by incoherent scattering on hydrogen. To develop a model for analysis of scattering data, it is thus sufficient to calculate the self correlation function of the hydrogen atoms. Moreover, thanks to the nature of incoherent scattering, it is even sufficient to model the dynamics of a single hydrogen performing jumps between its possible equilibrium positions. The fact that all five hydrogen atoms in a ring are fully correlated has no influence in this case, and the cross section of  $N_t$  atoms will simply be  $N_t$  times the cross section of a single atom.

Therefore, models for rotational jump diffusion of a single particle will be discussed in the following sections. The aim is to determine their incoherent dynamic structure factor, hereafter simply referred to as  $S(Q, \omega)$ . The first model that will be discussed is the rotational jump diffusion model for  $N$  equivalent sites on a circle. It is the starting point for extensions to a two-ring model, and to a non-equivalent sites model. The latter includes the effects of dynamical disorder by introducing multiple equilibrium positions which will be needed for scattering experiments on monoclinic ferrocene in [chapter 6](#).

---

### 3.1 Equivalent sites rotational jump diffusion model

---

A general model for the description of molecular rotational jump diffusion between a given number of equivalent sites arranged on a circle was given by [Barnes](#).<sup>[42]</sup> In the following, his derivation of the resulting incoherent scattering law for this type of motion will be presented in more detail, as it will serve as the basis for the non-equivalent sites model later on.

The aim of the model is to calculate the incoherent inelastic scattering from a particle that jumps between  $N$  equilibrium sites equally distributed on a circle with radius  $r$ . [Figure 3.1](#) shows a sketch for  $N = 5$ , but the following calculation holds for arbitrary  $N > 2$ . Jumps are only possible between neighboring sites and occur on average at a rate of  $\gamma/2$ . The probability of finding the particle at a certain site  $i$  at time  $t$  is  $p_i(t)$  where  $i = 1 \dots N$ . The time evolution of  $p_i(t)$  is then given by the master equations

$$\dot{p}_i(t) = \frac{\gamma}{2} [p_{i-1}(t) + p_{i+1}(t) - 2p_i(t)] \quad (3.1)$$

with periodic boundary conditions  $p_i(t) = p_{i+N}(t)$ . [Equation \(3.1\)](#) can be written more compactly in vectorized form:

$$\dot{\mathbf{p}}(t) = \mathbf{M} \cdot \mathbf{p}(t) \quad (3.2)$$

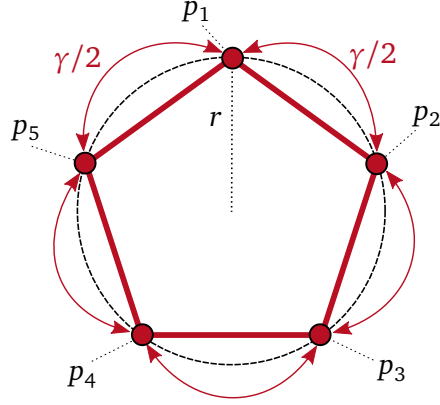


**Figure 3.1:** Sketch of the jump diffusion model for  $N = 5$  equivalent sites equally distributed on a circle with radius  $r$  and occupation probability  $p_i$ . Jumps can occur between nearest neighbors at rate  $\gamma/2$ .

with the transition matrix

$$\mathbf{M} = \begin{pmatrix} -\gamma & \gamma/2 & 0 & \dots & 0 & \gamma/2 \\ \gamma/2 & -\gamma & \gamma/2 & \dots & 0 & 0 \\ 0 & \gamma/2 & -\gamma & \dots & 0 & 0 \\ \vdots & \vdots & \vdots & \ddots & \vdots & \vdots \\ 0 & 0 & 0 & \dots & -\gamma & \gamma/2 \\ \gamma/2 & 0 & 0 & \dots & \gamma/2 & -\gamma \end{pmatrix}. \quad (3.3)$$

The solution of eq. (3.2), which is a system of linear differential equations of first order, is

$$\mathbf{p}(t) = \mathbf{P}(t) \cdot \mathbf{p}_0 \quad (3.4)$$

with  $\mathbf{p}_0$  being the initial state at  $t = 0$ . The time dependent matrix  $\mathbf{P}(t)$  can be calculated from the eigendecomposition of  $\mathbf{M} = -\mathbf{B}\mathbf{\Lambda}\mathbf{B}^{-1}$  with the diagonal matrix  $\mathbf{\Lambda}$  of negated eigenvalues  $\lambda_l$ . The negation of the eigenvalues is chosen for convenience such that  $\lambda_l$  will take non-negative values. The matrix  $\mathbf{B}$  contains the normalized eigenvectors of  $\mathbf{M}$  in its columns, and

$$\mathbf{P}(t) = \mathbf{B} \cdot \exp(-\mathbf{\Lambda}t) \cdot \mathbf{B}^{-1} \quad (3.5)$$

Because the matrix  $\mathbf{M}$  is real and symmetric, the matrix  $\mathbf{B}$  will be orthogonal and  $\mathbf{B}^{-1} = \mathbf{B}^T$ . The negated eigenvalues of  $\mathbf{M}$  are

$$\lambda_l = 2\gamma \sin^2\left(\frac{\pi l}{N}\right) \quad (3.6)$$

and the elements of  $\mathbf{B}$

$$B_{kl} = \sqrt{\frac{2}{N}} \cos\left[\frac{2\pi kl}{N} + \frac{\pi}{4}\right] \quad (3.7)$$

Now, the elements of  $\mathbf{P}(t)$  from eq. (3.5) can be calculated:

$$P_{kj}(t) = \sum_{l=1}^N B_{kl} \exp(-\lambda_l t) B_{jl} = \frac{1}{N} \sum_{l=1}^N \exp(-\lambda_l t) \cos\left[\frac{2\pi l(k-j)}{N}\right] \quad (3.8)$$

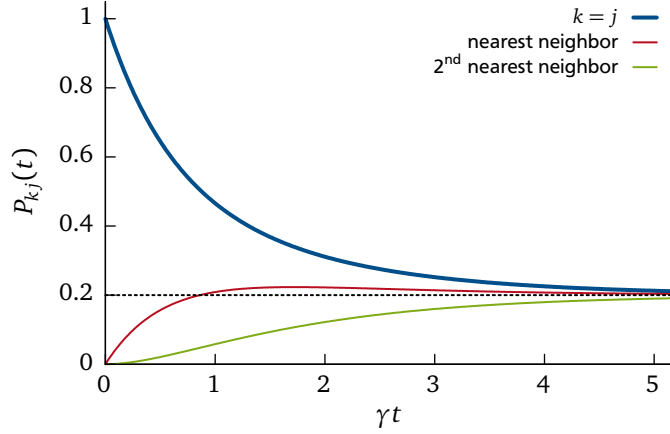


**Figure 3.2:** Correlation functions  $P_{kj}(t)$  for the equivalent sites jump rotation model with  $N = 5$ .

The values of  $P_{kj}(t)$  have a very illustrative meaning: Given that the particle is at site  $k$ , then  $P_{kj}(t)$  corresponds to the probability of finding the particle at site  $j$  after the time  $t$  has passed. Figure 3.2 shows  $P_{kj}(t)$  for  $N = 5$ , where every possible combination of  $k$  and  $j$  refers either to the same site ( $k = j$ ), nearest neighbors, or second nearest neighbors. In the long time limit, the probability of finding the particle on any site is equally distributed, hence  $P_{kj}(t \rightarrow \infty) = N^{-1}$  (dashed line).

As the powder average over all orientations will be calculated in a later step and all sites are equivalent, we can assume without the loss of generality that  $k = 1$ , that means, we will assume the particle to be on site 1 at  $t = 0$ . The self correlation function can then be easily constructed from  $P_{1j}(t)$ :

$$G_s(\mathbf{r}, t) = \sum_{j=1}^N P_{1j}(t) \delta[\mathbf{r} - (\mathbf{r}_1 - \mathbf{r}_j)] \quad , \quad (3.9)$$

where  $\mathbf{r}_j$  is the position vector of site  $j$ .

The incoherent dynamic structure factor  $S(Q, \omega)$  can now be calculated by applying the Fourier transformations discussed in section 2.4. First, the spatial Fourier transform is applied to obtain the intermediate scattering law<sup>1</sup>

$$I(\mathbf{Q}, t) = \int d^3r G_s(\mathbf{r}, t) \exp(i\mathbf{Q} \cdot \mathbf{r}) = \sum_{j=1}^N P_{1j}(t) \exp[i\mathbf{Q} \cdot (\mathbf{r}_1 - \mathbf{r}_j)] \quad . \quad (3.10)$$

Now, the powder average of the exponential term over all orientations of  $\mathbf{Q}$  can be calculated. The details of the averaging can be found in the paper by Barnes,<sup>[42]</sup> and the result is

$$I(Q, t) = 2\pi \sum_{j=1}^N P_{1j}(t) j_0\left[2Qr \sin\left(\frac{\alpha_{1j}}{2}\right)\right] \quad (3.11)$$

with the spherical Bessel function of zeroth order  $j_0(x) = \sin(x)/x$  and the angle  $\alpha_{1j}$  between site 1 and site  $j$  measured from the center of the circle:  $\alpha_{1j} = 2\pi(j-1)/N$ . The expression for  $P_{1j}(t)$  from eq. (3.8) is inserted and the obtained form of the intermediate scattering function can be rewritten as

$$I(Q, t) = 2\pi \sum_{l=0}^{N-1} A_l(Q) \exp(-\lambda_l t) \quad (3.12)$$

<sup>1</sup> The corresponding equation in ref. [42] seems to contain an additional  $N^{-1}$  by mistake.

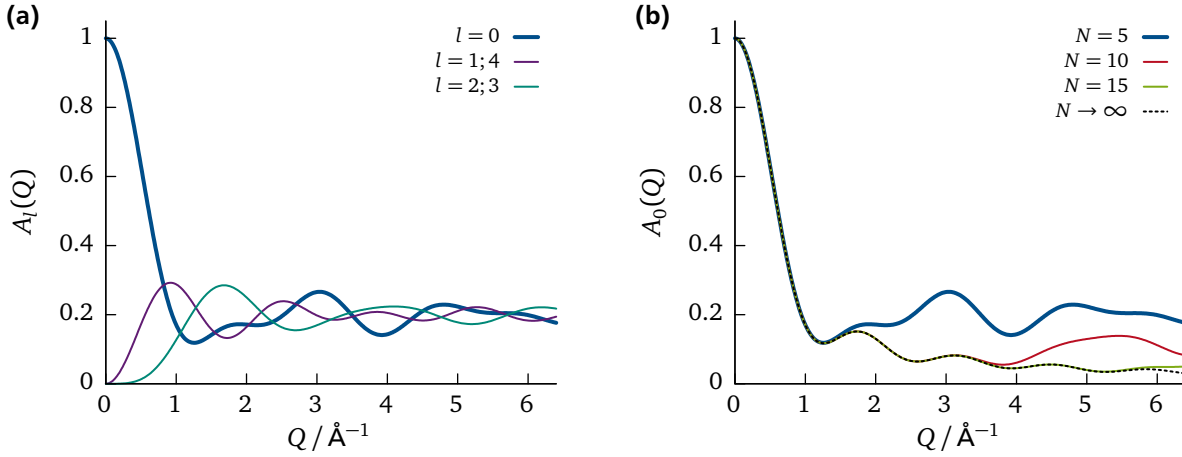


**Figure 3.3:** Incoherent structure factors for the equivalent sites rotational jump diffusion model with radius  $r = 2.33 \text{ \AA}$ . (a) Elastic and quasielastic structure factors  $A_l(Q)$  for  $N = 5$ . (b) Elastic structure factor  $A_0(Q)$  for different  $N$ .

where

$$A_l(Q) = \frac{1}{N} \sum_{j=0}^{N-1} j_0 \left[ 2Qr \sin\left(\frac{\pi j}{N}\right) \right] \cos\left(\frac{2\pi l j}{N}\right) \quad (3.13)$$

with

$$\sum_{l=0}^{N-1} A_l(Q) = 1 \quad . \quad (3.14)$$

The summation index in eq. (3.12) has been shifted to start from  $l = 0$ . Note that  $\lambda_0 \equiv \lambda_N = 0$  from eq. (3.6), meaning that the first term of the sum in eq. (3.12) is the time independent constant  $A_0(Q)$ . This has to be taken into account for the temporal Fourier transform, which is the last step of obtaining the incoherent dynamic structure factor:<sup>2</sup>

$$\tilde{S}(Q, \omega) = \frac{1}{2\pi} \int dt I(Q, t) \exp(i\omega t) = A_0(Q) \delta(\omega) + \sum_{l=1}^{N-1} A_l(Q) \mathcal{L}(\omega, \lambda_l) \quad (3.15)$$

where the constant term of the intermediate scattering function for  $l = 0$  is transformed into  $A_0(Q)\delta(\omega)$ , and the exponential decay terms become Lorentzians of the form

$$\mathcal{L}(\omega, \lambda_l) = \frac{1}{\pi} \frac{\lambda_l}{\lambda_l^2 + \omega^2} \quad . \quad (3.16)$$

The tilde in  $\tilde{S}(Q, \omega)$  is a reminder that this dynamic structure factor does not fulfill the condition of detailed balance (see section 2.4). From eq. (3.15) the significance of  $A_l(Q)$  as incoherent structure factors (ISFs) is evident:  $A_0(Q)$  is the  $Q$ -dependent strength of elastic scattering, and  $A_l(Q)$  for  $l \geq 1$  are  $Q$ -dependent intensities of Lorentzian quasielastic components of the spectra. Closer inspection of eq. (3.6) and eq. (3.13) reveal a degeneracy of eigenvalues, such that  $\lambda_l$  and  $A_l(Q)$  are identical when substituting  $l \mapsto (N - l)$ . Hence, the sum in eq. (3.15) can be grouped into only two Lorentzian terms for  $N = 5$ , five Lorentzian terms for  $N = 10$ , et cetera.

Figure 3.3a shows the shape of  $A_l(Q)$  for  $N = 5$  and radius  $r = 2.33 \text{ \AA}$  of the hydrogen atoms in cyclopentadienyl rings.<sup>[44,45]</sup> The incoherent structure factors  $A_l(Q)$  are characteristic for the

<sup>2</sup> For brevity and consistency with literature, the factor  $\hbar^{-1}$  in the Fourier transform is omitted from here on.



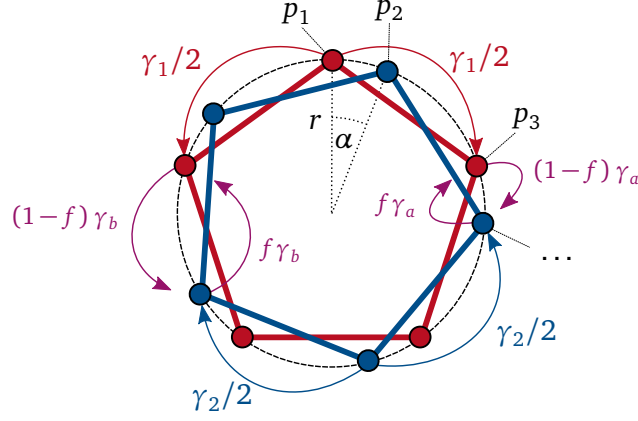


**Figure 3.4:** Schematics of the non-equivalent sites jump model showing two possible equilibrium positions of a single ring as configuration 1 (red) and configuration 2 (blue) as well as a subset of the allowed jumps between the 10 different sites.

geometry of the motion, i.e., the number of sites  $N$  and the spatial extent of the motion. The elastic incoherent structure factor (EISF)  $A_0(Q)$  for different values of  $N$  is shown in Figure 3.3b. With increasing  $N$ , differences in the curves are only seen at larger  $Q$ . For  $N \rightarrow \infty$ , the jump diffusion model converges to a continuous diffusion model.<sup>[35]</sup> In chapter 7, where the analysis of the ring rotation in  $\text{FeCl}_3$  is performed in terms of a 15-fold model, it must be taken into account that the 10-fold, 15-fold and continuous rotation model are not distinguishable in the experimentally observed  $Q$ -range below  $3 \text{ \AA}^{-1}$ .

### 3.2 Multiple rings per unit cell: Two-ring rotational jump diffusion model

The equivalent sites jump diffusion model presented in the previous section 3.1 assumes that all scattering particles in the sample move according to the model, with the same jump rate  $\gamma/2$ . In crystalline environments like the triclinic phase of Fc which will be discussed in chapter 6, the barrier to ring reorientation can easily differ between crystallographically different sites. This leads to different jump rates, and the scattering from the macroscopic sample will be a superposition of multiple contributions. Assuming two different kinds of rings in the sample, where a fraction  $f$  rotates with rate  $\gamma_1/2$  and the remaining fraction  $(1-f)$  with  $\gamma_2/2$ , the resulting incoherent dynamic structure factor  $\tilde{S}(Q, \omega)$  is simply a weighted superposition of two 1-ring models:

$$\tilde{S}(Q, \omega) = A_0(Q) \delta(\omega) + \frac{2}{\pi} \sum_{l=1}^2 A_l(Q) \left[ f \frac{\lambda_{1,l}}{\lambda_{1,l}^2 + \omega^2} + (1-f) \frac{\lambda_{2,l}}{\lambda_{2,l}^2 + \omega^2} \right] \quad (3.17)$$

where  $\lambda_{i,l}$  is defined similar to eq. (3.6) using  $\gamma_1/2$  and  $\gamma_2/2$  as jump rates between nearest neighbors in ring 1 and ring 2 respectively.

### 3.3 Non-equivalent sites rotational jump diffusion model

The analysis of scattering data in chapter 6 on monoclinic Fc will show that the equivalent sites model is not able to describe the data in an overall consistent way. As will be discussed in that chapter, the rings in monoclinic Fc are dynamically disordered. The dynamical disorder is projected here onto a non-equivalent sites rotational jump diffusion model, referred to as  $2 \times 5$ -fold

model in the following. The reasoning behind this is that the disorder introduces a changing local environment, which leads to two nonequivalent rotational orientations for a single ring, hereafter called ‘configurations’. Within each configuration, the ring can undergo 5-fold jumps according to its  $D_5$  symmetry. The transition from configuration 1 to configuration 2 will be modeled with a simple transition rate.

A detailed schematics of the extended model is shown in Figure 3.4. It consists of  $N = 2 \times 5$  sites distributed on a circle, where the sites are arranged on the corners of two pentagons which are twisted by an angle  $\alpha$ . Those represent the two possible configurations for each ring, shown in red and blue. The 5-fold symmetry jumps occur with a rate of  $\gamma_1/2$  between odd (ring configuration 1, red) and  $\gamma_2/2$  between even (ring configuration 2, blue) numbered sites. The transitions between the two configurations (magenta colored in Figure 3.4) follow a slightly more complicated pattern, as they have to be self-consistent with a possible population asymmetry of both configurations. If we define  $f$  as the probability of the ring being in configuration 1, then the clockwise transition from configuration 1 to 2 occurs at rate  $(1-f)\gamma_a$  while the reverse, counterclockwise transition from configuration 2 to 1 occurs at rate  $f\gamma_a$ . Accordingly, the rate for counterclockwise transition from configuration 1 to 2 is  $(1-f)\gamma_b$  and  $f\gamma_b$  for the reverse direction.

In order to obtain the incoherent scattering law for this model, the same calculation as for the equivalent sites model presented in section 3.1 can be used. The transition matrix can be constructed with the help of Figure 3.4, and the result is

$$\mathbf{M} = \begin{pmatrix} M_{11} & (1-f)\gamma_a & \gamma_1/2 & 0 & 0 & 0 & 0 & 0 & \gamma_1/2 & (1-f)\gamma_b \\ f\gamma_a & M_{22} & f\gamma_b & \gamma_2/2 & 0 & 0 & 0 & 0 & 0 & \gamma_2/2 \\ \gamma_1/2 & (1-f)\gamma_b & M_{11} & (1-f)\gamma_a & \gamma_1/2 & 0 & 0 & 0 & 0 & 0 \\ 0 & \gamma_2/2 & f\gamma_a & M_{22} & f\gamma_b & \gamma_2/2 & 0 & 0 & 0 & 0 \\ 0 & 0 & \gamma_1/2 & (1-f)\gamma_b & M_{11} & (1-f)\gamma_a & \gamma_1/2 & 0 & 0 & 0 \\ 0 & 0 & 0 & \gamma_2/2 & f\gamma_a & M_{22} & f\gamma_b & \gamma_2/2 & 0 & 0 \\ 0 & 0 & 0 & 0 & \gamma_1/2 & (1-f)\gamma_b & M_{11} & (1-f)\gamma_a & \gamma_1/2 & 0 \\ 0 & 0 & 0 & 0 & 0 & \gamma_2/2 & f\gamma_a & M_{22} & f\gamma_b & \gamma_2/2 \\ \gamma_1/2 & 0 & 0 & 0 & 0 & 0 & \gamma_1/2 & (1-f)\gamma_b & M_{11} & (1-f)\gamma_a \\ f\gamma_b & \gamma_2/2 & 0 & 0 & 0 & 0 & 0 & \gamma_2/2 & f\gamma_a & M_{22} \end{pmatrix} \quad (3.18)$$

where  $M_{11} = -\gamma_1 - (1-f)(\gamma_a + \gamma_b)$  and  $M_{22} = -\gamma_2 - f(\gamma_a + \gamma_b)$ .

Unfortunately, an analytical expression for the eigendecomposition of the matrix  $\mathbf{M} = -\mathbf{B}\mathbf{A}\mathbf{B}^{-1}$  could not be obtained in contrast to the case of the equivalent sites N-fold jump diffusion model. Therefore the eigenvectors and eigenvalues will be computed numerically for specific values of the transition rates. Moreover,  $\mathbf{M}$  is not symmetric any more, such that  $\mathbf{B}$  is not necessarily orthogonal and is numerically inverted to obtain  $\mathbf{B}^{-1}$ . The values of the correlation function  $P_{kj}(t)$  are then calculated from

$$P_{kj}(t) = \sum_{l=1}^N B_{kl} \exp(-\lambda_l t) (\mathbf{B}^{-1})_{lj} \quad . \quad (3.19)$$

Figure 3.5 shows the correlation function  $P_{kj}(t)$  for a typical set of parameters assuming the particle is at site  $k = 1$  in configuration 1 at time  $t = 0$ . As expected, the long time limit reflects the population asymmetry of  $f = 0.3$  in this example. The dashed lines in the figure indicate that, in the long time limit, the fraction  $f$  is distributed equally over all 5 sites of configuration 1, and the remaining fraction  $(1-f)$  over the 5 sites of configuration 2, such that

$$P_{1j}(t \rightarrow \infty) = \begin{cases} f/5 & \text{if } j \in \text{configuration 1 (red),} \\ (1-f)/5 & \text{if } j \in \text{configuration 2 (blue).} \end{cases} \quad (3.20)$$

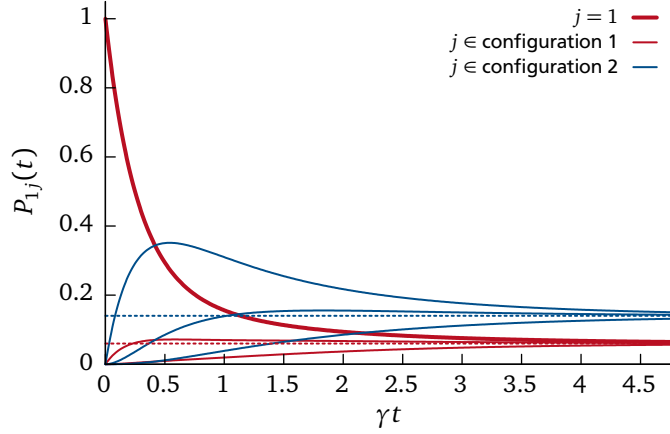


**Figure 3.5:** Correlation functions  $P_{kj}(t)$  for the non-equivalent sites  $2 \times 5$ -fold jump rotation model assuming the particle starts at site  $k = 1$  at  $t = 0$ . The jump rates shown here are  $\gamma_1 = \gamma_2 = \gamma$  and  $\gamma_a = 3\gamma$  and  $\gamma_b = 0$ , and the population of configuration 1 is  $f = 0.3$ .

The non-equivalence of the sites means that it is not sufficient to consider the particle being at site 1 at  $t = 0$  in the following, as it was the case in the equivalent sites model in [section 3.1](#). Instead, the form of the intermediate scattering function in powder average corresponding to [eq. \(3.11\)](#) is

$$I(Q, t) = 2\pi \left\langle \sum_{j=1}^N j_0 \left[ 2Qr \sin\left(\frac{\alpha_{kj}}{2}\right) \right] P_{kj}(t) \right\rangle_k \quad (3.21)$$

where  $\alpha_{kj}$  is the angle between the vectors from the ring center to site  $k$  and  $j$  respectively, and the outer average is carried out over all sites  $k$ . In the next step the expression for the matrix elements  $P_{ij}(t)$  is inserted into [eq. \(3.21\)](#) and the result is rewritten as

$$I(Q, t) = 2\pi \sum_{l=1}^N \exp(-\lambda_l t) \left\langle \tilde{A}_{kl}(Q) \right\rangle_k \quad (3.22)$$

where

$$\left\langle \tilde{A}_{kl}(Q) \right\rangle_k = f \tilde{A}_{1l}(Q) + (1-f) \tilde{A}_{2l}(Q) \quad (3.23a)$$

and

$$\tilde{A}_{kl}(Q) = B_{kl} \sum_{j=1}^N j_0 \left[ 2Qr \sin\left(\frac{\alpha_{kj}}{2}\right) \right] (\mathbf{B}^{-1})_{lj} \quad (3.23b)$$

The averaging over non-equivalent sites leads to the sum in [eq. \(3.23a\)](#) with  $f$  and  $(1-f)$  being the fractional population of the configuration 1 and 2 respectively. Due to the 5-fold symmetry,  $\tilde{A}_{1l}(Q)$  is representative for the structure factor originating from sites belonging to configuration 1 and  $\tilde{A}_{2l}(Q)$  to that from configuration 2.

As in case of the equivalent sites model, the symmetries of the model lead to some degeneracy in the eigenvalues of the matrix  $\mathbf{M}$ . In the numerical implementation of the model, the computed eigenvalues and eigenvectors are therefore sorted and paired appropriately. The

eigenvalue corresponding to the elastic part is defined as  $\lambda_0 = 0$ , and the remaining 9 eigenvalues are further grouped into 4 pairs and one non-degenerate value. The order of eigenvalues is then chosen such that  $\lambda_0 \dots \lambda_5$  are all different,<sup>3</sup> and the definition

$$A_l(Q) = m_l \langle \tilde{A}_{kl}(Q) \rangle_k \quad (3.24)$$

where  $m_l$  is the multiplicity of the  $l$ -th eigenvalue allows to restrict the summation over  $l$  to the first five different nonzero eigenvalues. The resulting incoherent dynamic structure factor is then

$$\tilde{S}(Q, \omega) = A_0(Q) \delta(\omega) + \sum_{l=1}^5 A_l(Q) \mathcal{L}(\omega, \lambda_l) \quad (3.25)$$

and takes a form very similar to the equivalent sites model in eq. (3.15) with an elastic contribution of strength  $A_0(Q)$  and several Lorentzian quasielastic components. The details of motion over nonequivalent sites described by the model are now fully contained in the structure factors  $A_l(Q)$  and the linewidths  $\lambda_l$ .

In summary, the incoherent dynamic structure factor  $\tilde{S}(Q, \omega)$  for the non-equivalent  $2 \times 5$ -fold model as shown in Figure 3.4 is calculated numerically from its parameter set  $\{\gamma_1, \gamma_2, \gamma_a, \gamma_b, \alpha, f\}$  as follows: Firstly, the matrix  $\mathbf{M}$  is constructed and its decomposition in negated eigenvalues  $\lambda_l$  and eigenvectors in the matrix  $\mathbf{B}$  is calculated. The eigenvalues are then rearranged as described above. Subsequently, the structure factors  $A_0(Q)$  to  $A_5(Q)$  are calculated from  $\mathbf{B}$  and  $\alpha$  according to eq. (3.23) and eq. (3.24). Finally, the incoherent dynamic structure factor  $\tilde{S}(Q, \omega)$  is obtained from eq. (3.25). This calculation was implemented and used as model function in the analysis of inelastic neutron scattering data on monoclinic ferrocene.

---

<sup>3</sup> Depending on the exact numerical values of the jump rates, a higher multiplicity and degeneracy of eigenvalues can occur, but the implementation of the model is able to handle them in a well defined manner.

---

## 4 Experimental methods

This chapter aims to give an overview and introduction of the experimental methods used in this work. All are variants of neutron scattering, including polarized diffraction, inelastic high resolution spectroscopy, and vibrational spectroscopy. In contrast to electron, X-ray or light scattering, which are frequently used in many laboratories, neutrons stand out already due to practical reasons: A beam of free neutrons suitable for scattering experiments can be obtained nowadays only in large scale research centers running a nuclear reactor or a particle accelerator with a spallation target. The corresponding instrumentation is thus mostly unique, complex and highly specialized, providing limited access for experiments to a large user community.

In the following, a short section is dedicated to neutron sources which provide a suitable beam of neutrons for the instruments that will be presented thereafter. The techniques that will be discussed comprise neutron time of flight spectroscopy, high resolution backscattering spectroscopy, vibrational spectroscopy, and polarized diffraction. All experiments presented in this work have been carried out on different instruments at the high flux research reactor of the Institut Laue-Langevin (ILL) in Grenoble, France.

---

### 4.1 Neutron sources

---

Neutrons are spin- $\frac{1}{2}$  elementary particles without charge and are usually tightly bound in the nuclei of atoms by the strong force. Free neutrons are unstable and decay with a half-life of approximately 10 min into a proton, electron and an electron antineutrino. In order to obtain free neutrons which are suitable for scattering experiments, nuclear reactions of heavier nuclei are used in either nuclear fission or spallation. There are only several research facilities worldwide providing neutron beams for scientific experiments. They either run a particle accelerator, bombarding a target (e.g., mercury or tungsten) with high energy protons to ‘spall’ neutrons from nuclei, or a nuclear reactor, where neutrons are produced as a by-product of nuclear fission (e.g., of  $^{235}\text{U}$ ).

Some examples for spallation sources are ISIS at the Rutherford Appleton Laboratory (Oxford, UK), SNS at the Oak Ridge National Laboratory (Oak Ridge, USA), or MLF at J-PARC (Tokai, Japan). Nuclear research reactors providing neutron beams for condensed matter experiments are for example the ILL (Grenoble, France), at NIST (Gaithersburg, USA), OPAL at ANSTO (Lucas Heights, Australia), or the FRM2 (Garching, Germany).

Whatever method is chosen to free neutrons from nuclei, they usually have kinetic energies of several MeV and need to be moderated before being of use for the condensed matter physics scattering experiments described here. The moderation proceeds by multiple collisions and thermalization of neutrons with the nuclei of an appropriate moderator material. The moderator is kept at a given temperature, such that the energy distribution of the moderated neutrons results in an approximately Maxwellian spectrum corresponding to the moderator temperature. The average kinetic energy of neutron beams is classified according to the moderator temperatures into cold neutrons (liquid deuterium,  $T \approx 25\text{ K}$ , 0.5 meV to 10 meV), thermal neutrons (liquid  $\text{D}_2\text{O}$ ,  $T \approx 300\text{ K}$ , 10 meV to 150 meV) and hot neutrons (graphite,  $T \approx 2000\text{ K}$ , 10 meV to 1000 meV).<sup>[35]</sup>

Neutrons in these energy ranges have wavelengths of roughly 0.3 Å to 12 Å and thus match inter-atomic length scales in condensed matter. Moreover, the energies of cold, thermal and hot neutrons also match the energy range of excitations and dynamics, e.g., phonons, magnons,

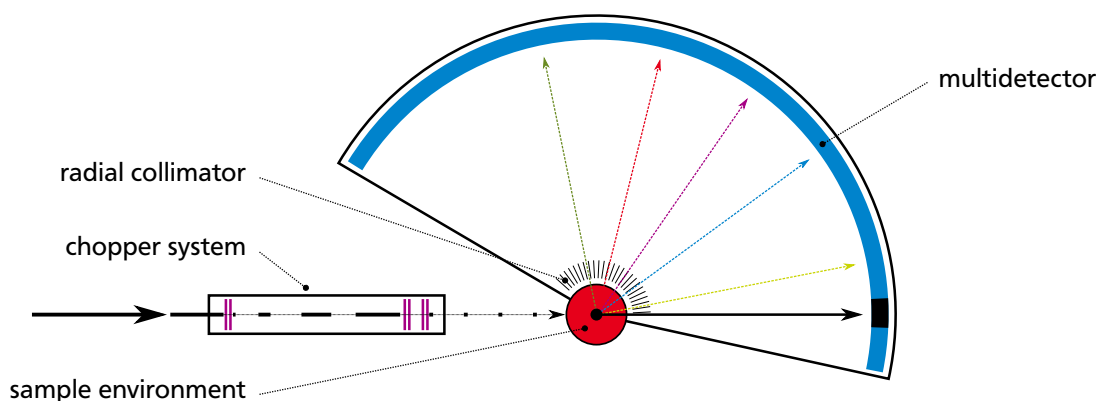


**Figure 4.1:** Schematics of a direct geometry multi disk chopper neutron time of flight spectrometer (e.g., IN5 at ILL, Grenoble).

molecular reorientations and vibrations, making them an excellent probe for these processes on the femto- to nanoseconds time scale.

After free neutrons are produced in the source and thermalized in the moderator, they are guided in beam tubes usually consisting of multilayer coated glass substrates (supermirrors) over distances of about 5 m to 150 m to different instruments. Each neutron source supplies multiple instruments which are specialized for certain purposes, but covering a variety of applications and disciplines altogether. In the following sections, the experimental techniques used in this work will be introduced.

## 4.2 Time of flight spectroscopy

The relatively slow thermal neutron velocity of typically several hundreds to a few thousands of meters per second offers a simple way of determining neutron energies by measuring the time of flight (ToF) over the distance of a few meters. The schematics of a multi disk chopper ToF spectrometer exploiting this method is shown in Figure 4.1. The neutrons first pass a chopper system which monochromatizes the beam to define the incident energy  $E_i$  and chops it into very short pulses of low repetition rate for the ToF measurement. These short pulses scatter on the sample, and the scattered neutrons are counted in a multidetector covering a large solid angle. From the measured time of flight between chopper and detector, the final energy  $E_f$  of each scattered neutron event can be calculated. A radial collimator helps to avoid neutrons scattered from the sample environment to reach the multidetector.

Time of flight spectrometers offer great flexibility of choosing energy resolution, energy and momentum transfer range in order to adapt to many different experimental needs. In this work, two different ToF spectrometers at the ILL were used:

### IN5

The IN5 ToF spectrometer<sup>[46]</sup> is a multi disk chopper spectrometer as shown in Figure 4.1. The incident beam comes from a cold neutron source. Experiments have been carried out using three different instrumental configurations: Depending on the speed and relative phase of the choppers, different incident neutron wavelengths  $\lambda_{inc}$  and energy resolutions  $\Delta E$  can be selected. The incident wavelength also defines the accessible range of scattering vector  $Q$ . An overview of the respective values is given in Table 4.1. Typical for ToF instruments is the fact that longer incident wavelengths  $\lambda_{inc}$  lead to better energy resolution, but restrict the available

**Table 4.1:** Characteristics of the different configurations on time of flight (ToF) and backscattering (BS) spectrometers used in this work: Incident neutron wavelength  $\lambda_{\text{inc}}$ , energy resolution FWHM  $\Delta E$ , and covered ranges of scattering vector  $Q$  and energy transfer  $E$ .

method	instrument	$\lambda_{\text{inc}} / \text{\AA}$	$\Delta E / \mu\text{eV}$	$Q / \text{\AA}^{-1}$		$E / \text{meV}$	
				from	to	from	to
ToF	IN5	12.0	8	0.07	0.95	$-\infty$	0.2
	IN5	6.3	40	0.14	1.76	$-\infty$	1
	IN6	5.12	80	0.3	2.0	$-\infty$	1.5
	IN5	3.6	170	0.24	3.0	$-\infty$	3
BS	IN16	6.271	0.8	0.2	1.9	-0.015	0.015
	IN16B	6.271	0.8	0.2	1.9	-0.031	0.031

$Q$ -range. The maximum neutron energy loss in the sample is limited by the incident neutron energy, while the neutron energy gain is a priori unlimited.

### IN6

The IN6 ToF spectrometer<sup>[47]</sup> uses a Bragg reflex on pyrolytic graphite crystal monochromators instead of disk choppers to select an incident wavelength  $\lambda_{\text{inc}}$ . For the time of flight measurement, the monochromatized beam is then also chopped into very short pulses by a so-called Fermi chopper, consisting of a rotating collimator. The characteristics of the configuration used on the IN6 spectrometer is given in Table 4.1.

### 4.3 Backscattering spectroscopy

Complementary to time of flight spectroscopy, the method of neutron backscattering (BS) spectroscopy allows to improve energy resolution by one to two orders of magnitude and study slower processes on a different time scale, typically from several tens of picoseconds up to some nanoseconds. In the following, the instrumental technique will be briefly summarized. It has been proposed by Maier-Leibnitz, and a first spectrometer was build at the FRMI in Garching in the 1960s by Alefeld, Heidemann and Birr.<sup>[48,49]</sup> A more detailed introduction is given, e.g., in *Neutron Backscattering Spectroscopy* by Frick.<sup>[50]</sup>

In a BS spectrometer, monochromatization of the incoming beam and energy analysis of scattered neutrons are performed by single crystals. The term ‘backscattering’ is not related to the scattering of neutrons on the sample, but refers to the fact that the crystal monochromator and analyzers are used in backscattering geometry. The reflection of the neutron beam from a single crystal in backscattering, i.e., with scattering angle  $2\vartheta = 180^\circ$ , is key to achieve the high energy resolution. This can be deduced from the well known Bragg law for diffraction on crystals, where a wave with wavelength  $\lambda$  is diffracted according to

$$\lambda = 2d \sin \vartheta \quad (4.1)$$

where  $2\vartheta$  is the angle between incoming and reflected beam and  $d$  the distance between the diffracting crystal lattice planes, usually characterized by Miller indices (hkl). To estimate the sensitivity of the reflected neutron wavelength on crystal and beam parameters, eq. (4.1) can be differentiated to

$$\frac{\Delta\lambda}{\lambda} = \frac{\Delta d}{d} + \Delta\vartheta \cot \vartheta \quad . \quad (4.2)$$

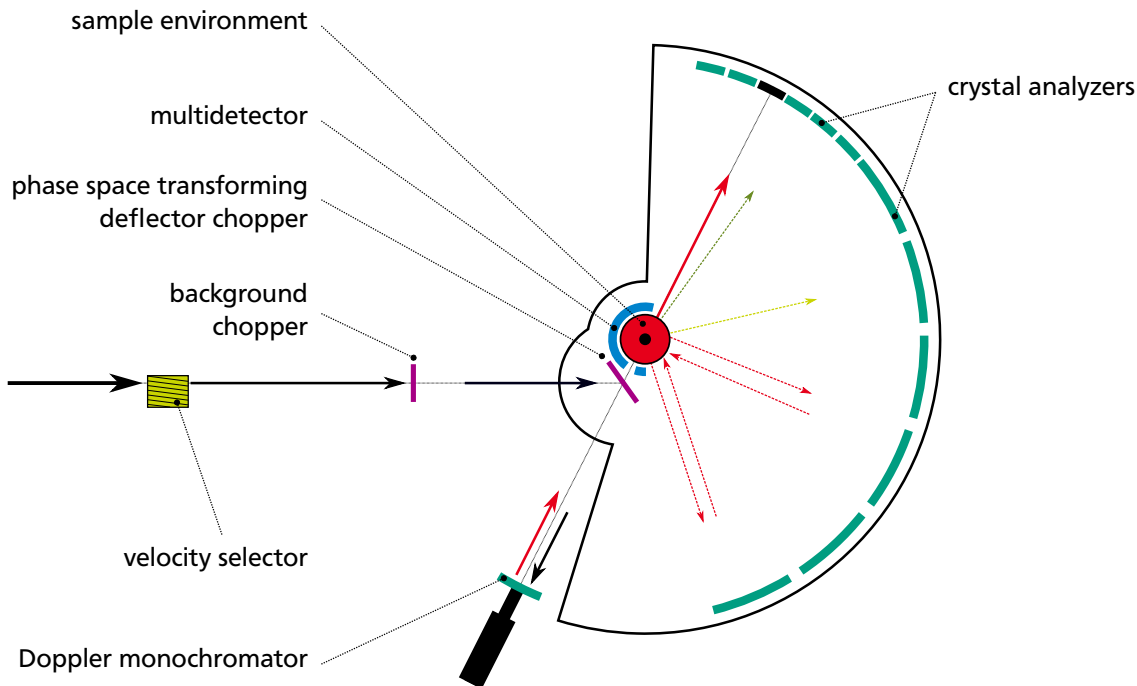


**Figure 4.2:** Schematics of a neutron backscattering spectrometer (e.g., IN16B at ILL, Grenoble)

Here,  $\Delta\vartheta$  is a measure for the beam divergence. In backscattering geometry with  $\vartheta = 90^\circ$  and thus  $\cot\vartheta = 0$ , the second term is zero and the width of the reflected wavelength band is independent of the beam divergence in this first order approximation. The achievable energy resolution is now dominated by the term  $\Delta d/d$ , which accounts for factors like crystal quality, lattice strains, and includes extinction in the crystal. The latter effects of extinction can and have to be estimated in the context of dynamical diffraction theory, which does not rely on the first Born approximation, as the concept of first Born approximation holds only for weak perturbations of the initial state which is certainly not the case for a Bragg reflection. Typical values of  $\Delta d/d$  that can be achieved with high quality single crystals are in the order of  $10^{-5}$ . A common monochromator material is silicon, using the Si (111) reflex in backscattering. The fact that incident and reflected beam follow the same path in backscattering geometry complicates the construction of such a spectrometer. Figure 4.2 shows the schematics of a third generation neutron backscattering spectrometer like IN16B (ILL).<sup>[51]</sup> The experimental setup is described in the following:

The beam from a cold neutron source coming from the left is pre-monochromatized by a velocity selector which consists of a rotating drum with twisted blades, selecting a wavelength band of 10 % to 15 % (FWHM) in  $\Delta\lambda/\lambda$ . The continuous beam is then chopped into pulses of about 50 % duty cycle by a background chopper and continues to the phase space transforming (PST) deflector chopper.

From the deflector chopper the beam is sent directly towards the monochromator, where the neutron energy is selected with high precision in exact backscattering as explained above. During reflection on the moving graphite crystals mounted on the PST deflector chopper, the phase space of the neutron beam is deformed and optimized to the acceptance region of the monochromator, leading to a significant increase in intensity. The pulsed beam structure allows the neutrons reflected from the monochromator to pass through an open window in the deflector chopper and reach the sample, where they are scattered in all directions. The scattered neutrons reach the crystal analyzers which cover a large solid angle, are analyzed with



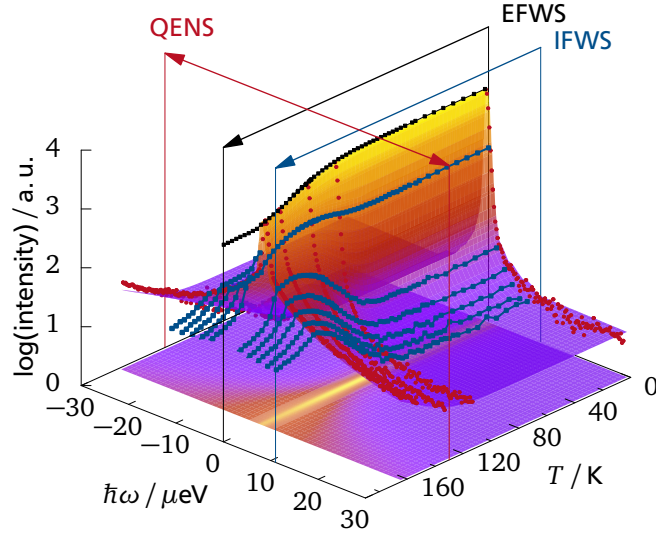


**Figure 4.3:** Illustration of different modes of measurement on the IN16B backscattering spectrometer using the example of triclinic ferrocene: Elastic fixed window scan (EFWS), inelastic fixed window scans (IFWS) and full energy spectra (QENS).

the same precision as on the monochromator in perfect backscattering and focused back on the sample. They may pass through the sample a second time before reaching the detectors located closely behind the sample environment. The second passage does not pose a problem, as sample transmission is usually high and the energy analysis has already been performed.

The monochromator is mounted on a Doppler drive which allows to move it forwards and backwards with different velocities. Assuming that  $E_i$  is the neutron energy that would be reflected from the resting monochromator in backscattering, then the energy of neutrons after reflection from a moving monochromator is  $E_i + \Delta E$  where

$$\Delta E = 2 \frac{v_D}{v_n} E_i \quad (4.3)$$

with  $v_n$  being the neutron velocity and  $v_D$  the Doppler monochromator velocity. Equation (4.3) is a first order approximation for  $v_D \ll v_n$ . Depending on if and how the monochromator is moved, different types of measurements can be performed. Figure 4.3 gives an overview and illustration of the different measurements using the example of the triclinic low temperature phase of ferrocene which will be discussed in detail in chapter 6. The figure shows the scattered intensity as function of temperature and energy transfer. With increasing temperature, the jumps between equilibrium sites of the cyclopentadienyl rings become more and more frequent, leading to broadening of the elastic line in energy spectra. The different types of measurements shown in Figure 4.3 are:

**Elastic fixed window scans (EFWS):** When the monochromator is resting, all events reaching the detector must have been scattered elastically on the sample, or at least with an energy transfer within the instrumental resolution. The elastically scattered intensity at  $E = 0$  can be recorded as a function of sample temperature and gives a quick overview of the dynamics in the sample. When dynamical processes accelerate with increasing temperature and become faster than the time defined by the instrumental energy resolution, the observed intensity decreases. The black line in Figure 4.3 shows this decrease between 120 and 160 K.

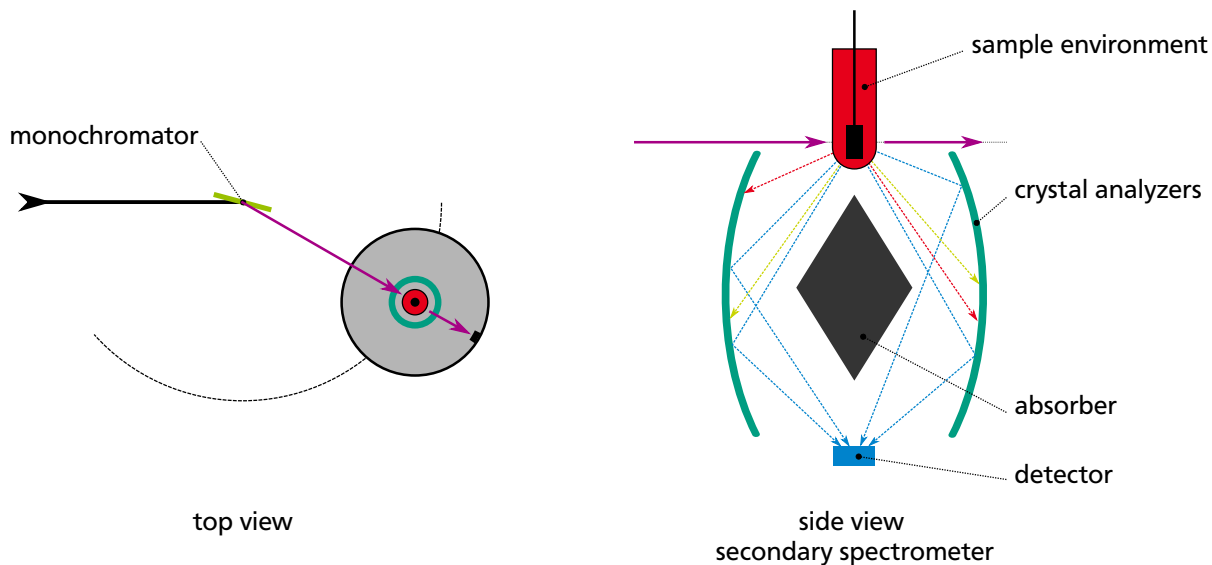


**Figure 4.4:** Schematics of the IN1-Lagrange vibrational spectrometer at ILL, Grenoble.

**Inelastic fixed window scans (IFWS):** This mode is an extension of the elastic fixed window scan presently only available on the IN16B spectrometer in the form described here. The monochromator is moved following a quasi-rectangular velocity profile with plateau velocities  $\pm v_0$ , probing the scattering in a given inelastic fixed energy transfer window. While the sample temperature follows a continuously increasing ramp, different inelastic energy transfer windows can be repeatedly cycled in order to measure all the blue lines in Figure 4.3 at once. When the dynamical ring rotation process accelerates with increasing temperature, a peak as function of temperature is observed in the IFWS between 120 and 160 K. The sudden decrease of intensity in the high temperature flank of the peak at 164 K is due to the phase transition of ferrocene to the monoclinic crystal phase (see section 1.1). The advantage of the EFWS/IFWS technique is that the temperature dependence can quickly be measured with good statistics. The counting time for each point along the EFWS/IFWS curves in Figure 4.3 was between 30 seconds and 1 minute, such that the entire set of elastic and inelastic fixed window temperature scans could be obtained in under 5 hours.

**Energy transfer spectra (QENS):** Full energy transfer spectra can be recorded at fixed sample temperature by using a sinusoidal velocity profile for the Doppler monochromator movement. The incident energy is thus periodically modulated, and neutron counts from the detectors are sorted by a multichannel analyzer into a spectrum as function of energy transfer. This ‘classical’ mode of measurement is shown in red in Figure 4.3 and allows to analyze the line shape of the scattering at fixed temperatures. The measurement time on IN16B was between one and two hours per temperature.

The measurements presented in Part II were carried out on two backscattering spectrometers at the ILL, namely IN16B and its predecessor IN16. Their characteristics are given in Table 4.1. Typical for backscattering spectrometers is the extremely good energy resolution in a comparably large  $Q$ -range, the downside being the relatively small maximum energy transfer. As predecessor of the IN16B spectrometer, the older IN16 spectrometer<sup>[52]</sup> offered a smaller maximum energy transfer of  $\pm 15 \mu\text{eV}$  and less flux than its successor. It possessed a deflector chopper without phase space optimization, and the flight paths in the secondary spectrometer were in air. The IN16 spectrometer was decommissioned and dismantled in fall 2013.

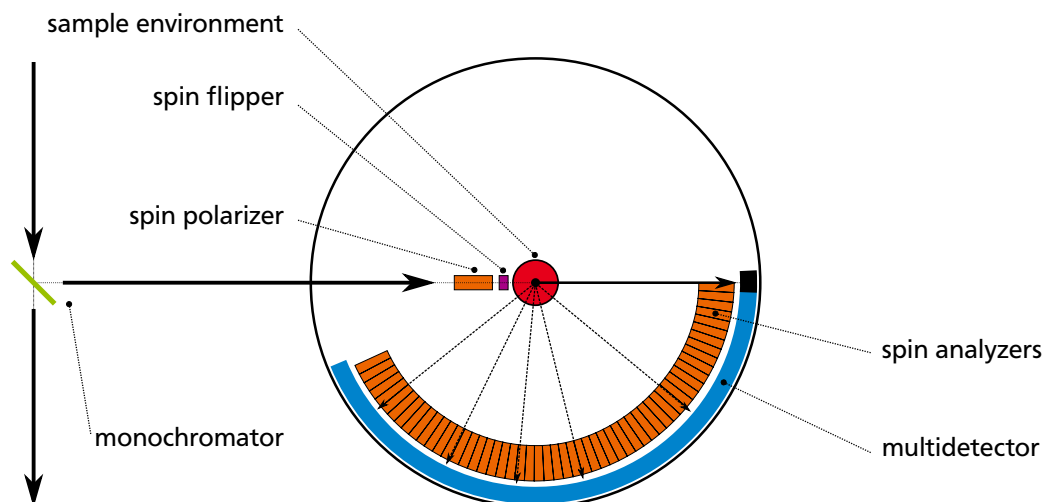


**Figure 4.5:** Schematics of a polarized neutron diffractometer (e.g., D7 at ILL, Grenoble).

#### 4.4 Vibrational spectroscopy

Additionally to the time of flight and backscattering experiments focusing on slow reorientational dynamics of the ferrocene molecule, vibrational spectroscopy has been performed. The vibrational modes are naturally much faster than the ring rotation, and necessitate much higher energy transfers in their investigation using inelastic scattering experiments.

Vibrational spectroscopy was performed on the recently commissioned IN1-Lagrange hot neutron spectrometer at ILL.<sup>[53]</sup> The spectrometer layout is shown in a sketch in Figure 4.4. The top view on the left side of the image illustrates the selection of incident neutron energy  $E_i$  by Bragg reflection on a crystal monochromator. The energy  $E_i$  can be varied by varying the take-off angle and moving the secondary spectrometer along the dashed line. By additionally using three different monochromator Bragg reflections, a large range of incident energies  $E_i$  can be covered: Si (111): 5 meV to 22 meV; Si (311): 17 meV to 70 meV; and Cu (220): 40 meV to 500 meV.

The secondary spectrometer shown in side view on the right side of Figure 4.4 contains many small pyrolytic graphite analyzer crystals arranged on a rotational ellipsoid. The downward scattered neutrons from the sample are selected at fixed energy  $E_f = 4.5$  meV and focused on a single detector, while the direct view between detector and sample is blocked by an absorber. The scattering angles  $2\vartheta$  that are covered by the analyzer are in the range of  $\approx 21^\circ$  to  $159^\circ$ . A typical energy resolution is 2% to 4% in energy transfer  $E = E_i - E_f$  depending on the selected monochromator reflection and  $E_i$ .

#### 4.5 Polarized neutron diffraction

Polarized neutron diffraction experiments help to separate coherent from incoherent scattering as discussed in section 2.5. They allow to measure the static structure factor  $S(Q)$  of semi-crystalline and amorphous polymer samples, which is a key element in the analysis in inelastic data studying the ring rotation in ferrocene containing polymers in chapter 8. In contrast to all other scattering methods discussed in this chapter, no energy analysis of scattered neutrons is performed in this experiment.

---

Polarized neutron diffraction was performed on the D7 diffuse scattering spectrometer at ILL.<sup>[54]</sup> Although the instrument is in principle capable of full xyz-polarization and time of flight analysis, it was only used as diffractometer to separate coherent from incoherent scattering in this work. The layout of the instrument is sketched in Figure 4.5. The incident neutron wavelength of  $\lambda_{\text{inc}} = 3.12 \text{ \AA}$  is selected by a pyrolytic graphite PG (002) monochromator from a cold neutron guide. Subsequently, only neutrons of a certain spin orientation are selected by a polarizer. This polarizer consists of a supermirror, which uses magnetically polarized ferromagnetic materials in a multilayer coating such that neutrons are reflected under grazing incidence for one spin orientation, but transmitted and absorbed for the opposite spin direction. The polarization of the incident beam can be inverted by a spin flipper, which uses a localized magnetic field transverse to the quantization axis in which the spins precess by  $180^\circ$ . The neutrons which are scattered from the sample pass through polarization analyzers functioning similarly to the polarizer, and are counted in multiple detectors located behind the analyzers. Two subsequent measurements with activated and deactivated spin flipper respectively allow to measure the intensities of spinflip and non-spinflip scattered neutrons. These quantities are then used to determine the coherent and incoherent cross sections of the sample separately as described in section 2.5 and Appendix B.

---

## 5 QENS data analysis and multiple scattering corrections

In this chapter, the general approach to data analysis in order to validate jump diffusion models and extract parameters of the ring rotation dynamics will be presented. The quasielastic neutron scattering data obtained using ToF and BS spectroscopy experiments presented in the previous chapter is therefore to be analyzed in terms of the models introduced in [chapter 3](#). Prior to the analysis process, the raw data from the instruments is treated by standard methods to apply several corrections, subtract empty cell scattering, and normalize the spectra. The details of raw data reduction are discussed in [Appendix B](#). We will focus here on the further analysis process using physical models of the ring rotation dynamics in the sample. However, instrumental corrections and model fitting cannot be fully disentangled due to multiple scattering corrections that have been incorporated into the analysis process.

---

### 5.1 Construction of model functions

---

The central part of the model function used for the analysis of QENS data consists of the rotational jump diffusion models presented in [chapter 3](#). But for the accurate description of experimental scattering data, additional factors need to be included in the full model. [Figure 5.1](#) shows a sketch of the typical shape of observed QENS spectra, where the elastic and quasielastic contributions are part of the rotational jump diffusion models. Additional contributions are due to vibrational modes, the effect of finite instrumental resolution and possible multiple scattering processes in the sample, and will be discussed in the following.

#### Inelastic phonon contributions

Inelastic neutron scattering processes can create or annihilate phonons in the sample, such that a measured spectrum contains the density of phonon states – the details have been discussed in [section 2.4.1](#). Most of the phonon modes however lie at energies outside the region

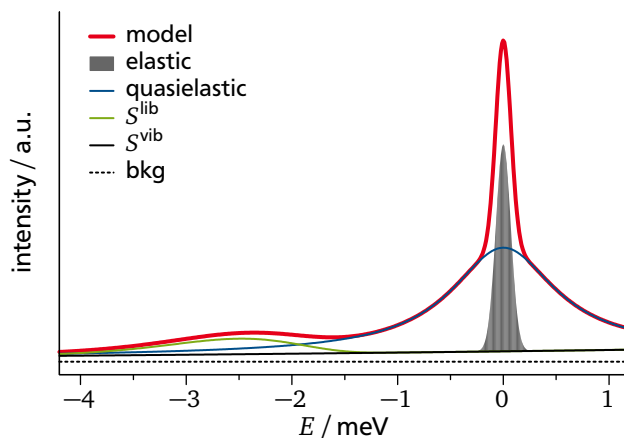


**Figure 5.1:** Sketch of the model function used for analysis of QENS data. The individual contributions are discussed in the text.

relevant for this QENS study, with exception of the librational mode discussed in the next paragraph. The measured spectrum of the phonon density of states for crystalline Fc is shown in [Appendix C](#). Here, the contribution from the low energy part of the lattice vibration spectrum can be very well approximated using the Debye density of phonon states  $Z_D$  from [eq. \(2.32\)](#) on [page 14](#) with the Debye frequency  $\omega_D$ . The incoherent dynamic structure factor contribution due to vibrational modes is then, according to [section 2.4.1](#):

$$S^{\text{vib}}(Q, \omega) = Z_D(\omega) \frac{Q^2}{\omega} [1 + n(\omega, T)] = \frac{3\omega Q^2}{\omega_D^3} [1 + n(\omega, T)] \quad . \quad (5.1)$$

The effect on the measured energy spectra is a smooth, nearly flat background (as function of  $\omega$ ) which increases with  $Q^2$  and is characterized by a single free scaling parameter  $\omega_D^{-3}$ . The resulting value of the Debye frequency  $\omega_D$  has not been further interpreted or evaluated. The Debye Waller factor is not included in [eq. \(5.1\)](#) as it will be a general prefactor of the model function.

### Librational mode

Another minor contribution in the full model accounts for a possible librational motion of the Cp rings. A ‘librational mode’ corresponds to the lowest quantum mechanical oscillator excitation of rotational motion in a potential minimum. In bulk Fc at low temperatures, a broad inelastic peak is clearly distinguishable around  $E = -2.5$  meV similar to the sketch in [Figure 5.1](#) (see [chapter 6](#) for experimental data). This peak has been interpreted as librational motion of the Cp rings.<sup>[34]</sup> A lognormal distribution analogous to the boson peak phenomenon<sup>[55]</sup> gives an adequate description of the observed data, which is however only an empirical modeling. The libration peak is thus described with

$$\tilde{S}^{\text{lib}}(Q, \omega) = \frac{LQ^2}{\Delta\omega_L \sqrt{2\pi}} \exp\left[-\frac{(\ln|\omega| - \ln\omega_L)^2}{2(\Delta\omega_L)^2}\right] \quad (5.2)$$

and characterized by peak width  $\Delta\omega_L$ , peak position  $\omega_L$  and a scaling factor  $L$ . The librational mode is in principle a part of the vibrational density of states, thus its intensity scales with  $Q^2$  similar to the phonon contributions. Modeling of the librational mode is however not always included in the full model function – the reasons and implications of this will be discussed at the relevant points throughout this work.

### Instrumental energy resolution

Every experimental method of spectroscopy naturally has a certain resolution limit. In neutron ToF and backscattering spectroscopy, the experimental uncertainty of determining incident and final neutron energy defines the resolution capabilities of the instrument. This leads to a convolution of the dynamic structure factor of the sample with the resolution function.<sup>1</sup> In all experiments presented in this work, it is possible to determine the instrumental resolution function experimentally for each sample measurement. This is achieved by cooling the sample to 2 K which freezes all dynamics on the sensitivity scale of any of the instruments, and the scattering can be assumed to be purely elastic with  $E = 0$ . The measured elastic peak then corresponds to the instrumental energy resolution, taking into account the exact orientation and geometry of the sample. In the data evaluation of measurements at higher temperatures, the model function is then numerically convoluted with this resolution function.

<sup>1</sup> Strictly speaking, the resolution of ToF instruments generally depends on energy transfer, thus the resolution smearing is not a simple convolution operation. In the case of QENS with low energy transfer and smooth Lorentzian line broadening as discussed here, the assumption of constant energy resolution is considered to be a good approximation.

## Multiple scattering (MS)

The description of scattering theory given in [chapter 2](#) is based on the assumption that the measurement of a scattered neutron under the scattering angle  $2\vartheta$  with energy transfer  $E = \hbar\omega$  can be ascribed to a single scattering process in the sample, and that accumulated statistics allows to determine the dynamic structure factor  $S(Q, \omega)$ . Typical samples for neutron scattering are usually prepared to have a total transmission of 85 % to 90 % of the incident beam. If a scattering process takes place in the sample, there is thus a small but not necessarily negligible probability that another scattering process takes place along the path of the neutron on its way to the sample boundary. In that case, the final neutron direction and energy is falsified, and it will potentially be counted in a detector and energy channel with parameters  $2\vartheta$  and  $E$  that may be totally unrelated to any of the actual scattering processes.

While there are analytical approaches to account for multiple scattering, e.g., formulated in a paper by [Sears](#)<sup>[56]</sup> or as used by [Zorn et al.](#),<sup>[57]</sup> a Monte-Carlo simulation technique was chosen here following the approach by [Johnson](#)<sup>[58]</sup> to correct for multiple scattering. This correction has been applied in all QENS data analyses unless indicated otherwise. Essentially, the correction algorithm assumes a known scattering law  $S(Q, \omega)$  and calculates multiplicative correction factors for every scattering angle  $2\vartheta$  and energy transfer  $E$  that allow to scale the measured data to remove the effects of multiple scattering. It is found that the multiple scattering corrections are important especially for the detailed evaluation of the incoherent structure factors  $A_0(Q)$  and  $A_1(Q)$ . The implementation of the multiple scattering algorithm was a major effort, and a more detailed presentation of the used technique and effect of the correction is discussed below in [section 5.2](#) and [Appendix A](#). For now, we note the existence of correction factors  $R_{2\vartheta}^*(\omega)$  that will be part of the model function.<sup>2</sup>

### Full model function

The model function that is used to analyze the QENS spectra of scattered intensity is the combination of all above mentioned contributions. It is given as function of energy transfer  $E = \hbar\omega$  and scattering angle  $2\vartheta$ , and takes the following form:

$$S^{\text{fit}}(2\vartheta, \omega) = s_0 \left( \left\{ \left[ \tilde{S}^{\text{jump}}(Q_{\text{el}}, \omega) + \tilde{S}^{\text{lib}}(Q_{\text{el}}, \omega) \right] \times \exp\left(\frac{\hbar\omega}{2k_{\text{B}}T}\right) + S^{\text{vib}}(Q_{\text{el}}, \omega) \right\} \times \frac{\exp(-2W)}{R_{2\vartheta}^*(\omega)} \right) \otimes Y_{2\vartheta}(\omega) + \text{bkg} \quad (5.3)$$

It is prepended with an overall scaling factor  $s_0$  that accounts for the absence of a strict absolute normalization of the data. The sum of the jump diffusion model  $\tilde{S}^{\text{jump}}(Q_{\text{el}}, \omega)$  and the libration peak  $\tilde{S}^{\text{lib}}(Q_{\text{el}}, \omega)$  is multiplied with the detailed balance factor and added to the phonon background  $S^{\text{vib}}(Q_{\text{el}}, \omega)$ . This sum is then multiplied with a Debye Waller factor using (see [section 2.4.1](#))

$$2W = \frac{1}{3} Q_{\text{el}}^2 u_0^2 T \quad , \quad (5.4)$$

followed by division with the correction factors  $R_{2\vartheta}^*(\omega)$  originating from the multiple scattering simulation. Subsequently, the model is convoluted with the experimentally obtained instrumental resolution function  $Y_{2\vartheta}(\omega)$  and a constant background is added. This constant background accounts for any bias from systematic errors, as could be introduced, e.g., by the empty cell subtraction.

The nonstandard transformation from scattering angle  $2\vartheta$  to scattering vector  $Q$  deserves some detailed explanation at this point. In general, the magnitude of the scattering vector  $Q$

<sup>2</sup> The asterisk notation is chosen for compatibility with literature and does not imply complex values of  $R_{2\vartheta}^*(\omega)$ .

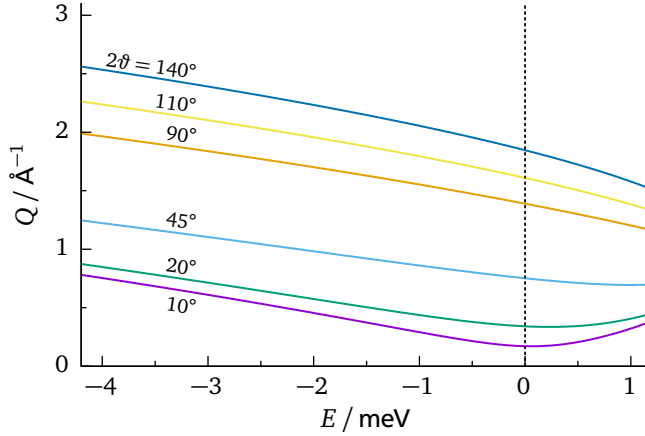


**Figure 5.2:** Scattering vector  $Q$  for inelastic scattering of neutrons with constant incident energy  $E_i = 2$  meV (corresponding to  $\lambda_{\text{inc}} = 6.3 \text{ \AA}$ ) as function of energy transfer  $E$  for some fixed values of scattering angle  $2\vartheta$ .

depends on scattering angle  $2\vartheta$  and energy transfer  $E$  according to eq. (2.5). Figure 5.2 shows this relationship for a typical incident wavelength of  $\lambda_{\text{inc}} = 6.3 \text{ \AA}$ . A physical detector located at fixed scattering angle  $2\vartheta$  will measure energy spectra that are cuts through the  $(Q, E)$ -plane along the colored lines. The well known relationship  $Q_{\text{el}} = 4\pi\lambda_{\text{inc}}^{-1} \sin \vartheta$  holds only for elastic scattering (dashed line). As all models are usually defined as function of  $Q$  and not  $2\vartheta$ , a transformation needs to be performed before or during the data analysis process. This could be achieved by rebinning the experimental data along constant- $Q$  cuts through the  $(2\vartheta, E)$ -plane prior to model fitting. However, this would be unpractical regarding multiple scattering simulations as correction factors are calculated depending on sample geometry for every scattering angle  $2\vartheta$ . It seemed more straightforward to include the transformation from constant  $2\vartheta$  to constant  $Q$  in these correction factors. The scattering law calculated for  $Q_{\text{el}}$  is then transformed to constant scattering angle  $2\vartheta$  by the correction factors  $R_{2\vartheta}^*(\omega)$ . The details on how these factors are calculated will be presented in the next section.

## 5.2 Determination of multiple scattering correction factors

The above mentioned correction factors  $R_{2\vartheta}^*(\omega)$  account for multiple scattering, sample self absorption and the transformation of scattering angle  $2\vartheta$  to scattering vector  $Q$ . They are obtained from a Monte-Carlo simulation based on the multiple scattering correction program DISCUS written in Fortran by Johnson in the 1970s.<sup>[58]</sup> In the course of this work, the algorithm was re-implemented using the free software package GNU/Octave,<sup>[59]</sup> and a number of details of the original algorithm have been changed or extended. The entire approach to obtaining the correction factors will be discussed in the following, where the basics are adapted from the technical report on the original program by Johnson.<sup>[58]</sup>

In principle, hypothetical neutron fluxes are calculated for each energy channel of each detector by a Monte-Carlo simulation technique. The path of a virtual neutron through the actual sample cell geometry is sampled as shown in Figure 5.3 for a hollow cylinder geometry. Although an arbitrary number of scattering processes can be considered, the number of randomized scattering events within the sample was usually limited to four. After each scattering process, the probabilities of scattering into every energy channel of a specific detector located under the angle  $2\vartheta$  from the incident beam are calculated. This calculation is repeated for many randomized trajectories through the sample and averaged. The resulting hypothetical neutron fluxes  $J_{2\vartheta}^{(n)}(\omega)$  then separately give the intensity corresponding to exactly  $n$  scattering processes



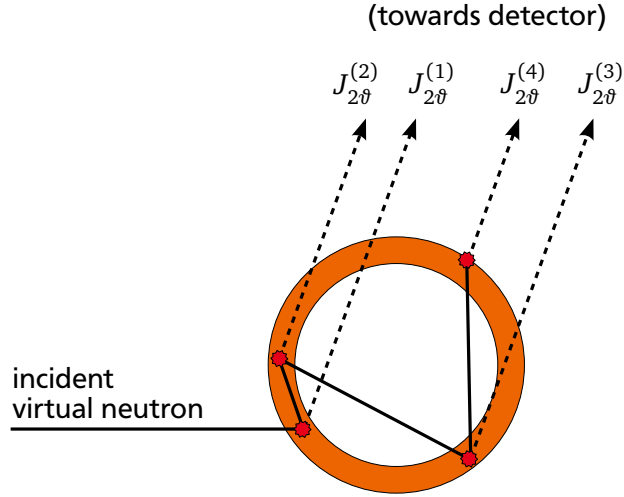


**Figure 5.3:** Sketch of multiple scattering processes in a hollow cylinder sample (orange). In the Monte-Carlo simulation, the hypothetical neutron fluxes  $J_{2\vartheta}^{(n)}(\omega)$  after  $n = 1, 2, 3, \dots$  scattering processes are calculated.

within the sample. The quantity that would be useful for comparison with model functions for the dynamic structure factor would be the neutron flux that would have been measured if

- there was only a single scattering process in the sample, and
- neutrons would be able to pass through the sample without absorption.

This quantity can easily be calculated in the simulation as well, and will be called  $J_{2\vartheta}^*(\omega)$ . In contrast to Johnson's original algorithm, the corresponding scattering event for this flux is weighted with the scattering law  $S(Q_{\text{el}}, \omega)$  using the elastic value of the scattering vector  $Q_{\text{el}} = 4\pi\lambda_{\text{inc}}^{-1} \sin \vartheta$ , even for inelastic events. The correction factors  $R_{2\vartheta}^*(\omega)$  used in section 5.1 are now calculated from the ratio of the wanted flux  $J_{2\vartheta}^*(\omega)$  and the experimentally observable flux which is the sum over all  $J_{2\vartheta}^{(n)}(\omega)$ :

$$R_{2\vartheta}^*(\omega) = \frac{J_{2\vartheta}^*(\omega)}{\sum_{n=1}^4 J_{2\vartheta}^{(n)}(\omega)} \quad . \quad (5.5)$$

This construction of the correction factors allows to simply multiply the data with (or divide the model function by)  $R_{2\vartheta}^*(\omega)$  in order to remove the effects of multiple scattering, correct for sample self absorption and transform the measured spectra to constant  $Q$ . On the downside, these correction factors can only be calculated accurately if the scattering law  $S(Q, \omega)$  of the sample is known beforehand – and not only within the  $(Q, \omega)$ -region observed in the experiment, but also beyond these limits. Therefore, the data analysis process becomes more complex, and requires repeated model refinements and multiple scattering simulations until a self-consistent solution has been found. This procedure will be discussed in the next section.

An important detail distinguishing the present algorithm from the DISCUS program is the special attention to elastic scattering. As the simulation is performed with the unsmearred scattering law  $S(Q, \omega)$ , the delta-shaped elastic peak poses a significant problem that needs special attention. A description of the implementation of the entire algorithm including technical details and exemplary comparisons of data analysis with and without multiple scattering corrections is given in Appendix A. It turns out that these corrections have a significant effect on the linewidths of quasielastic scattering, and are especially important for the accurate extraction of the elastic incoherent structure factor, notably at low  $Q$ .

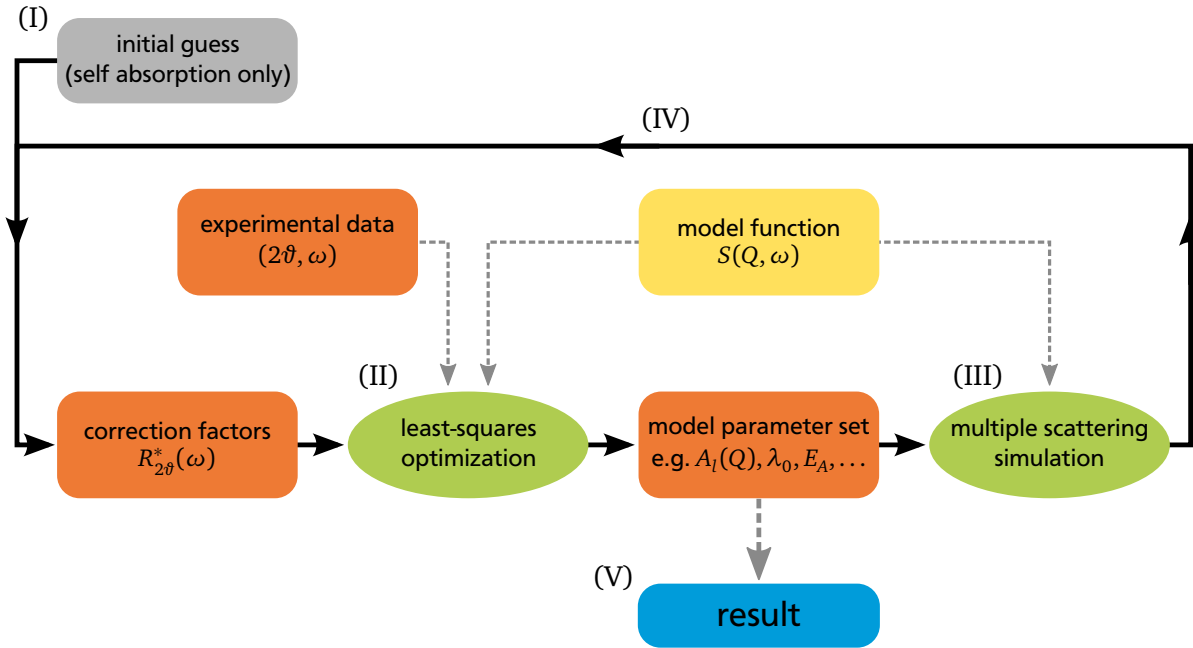


**Figure 5.4:** Flow chart of the iterative refinement process in the analysis of inelastic neutron scattering data in order to account for multiple scattering. The result is obtained after 5 iterations of the loop (thick lines).

### 5.3 Model parameter refinement procedure

The inclusion of the multiple scattering simulation complicates the model refinement procedure as indicated above. This is due to the fact that the correction factors from the simulation are needed to perform the least-square model refinement, but the resulting model parameters need to be known in order to calculate the correction factors. Therefore, the analysis proceeds iteratively as illustrated in the flow chart in Figure 5.4, implemented using GNU/Octave:<sup>[59]</sup>

- (I) Firstly, an initial guess for the correction factors  $R_{2\theta}^*(\omega)$  is made by considering only sample self absorption, that is, attenuation of the incident and scattered beam by the sample itself. The factors are obtained either from an analytical formula for flat samples using the infinite slab approximation as given by Sears,<sup>[56]</sup> or the multiple scattering algorithm for hollow cylindrical samples assuming only isotropic elastic scattering.
- (II) A set of refined model parameters is obtained by Levenberg-Marquardt nonlinear regression of the model function to the experimental data. The correction factors and instrumental resolution are taken into account as indicated in eq. (5.3).
- (III) The multiple scattering simulation is launched with the scattering law  $S(Q, \omega)$  defined by the model function and the obtained parameter set.
- (IV) The refined set of correction factors  $R_{2\theta}^*(\omega)$  is used to repeat the model parameter fitting by going back to item (II).
- (V) The loop (II)–(IV) is repeated for a fixed number of five iterations, after which a stable and self consistent state is usually reached. The last parameter set obtained is then taken as final result.

Some details of the analysis procedure deserve some further commenting and explanation. Firstly, the nonlinear regression of the model function to the experimental data was implemented as highly flexible ‘global fit’-procedure. It allows for a pool of experimental data to be analyzed simultaneously. In the simplest case, this can be a set of energy spectra measured for different  $Q$ . In more advanced cases, the data pool comprises sets of energy spectra for different  $Q$  and different temperatures  $T$ . Therefore, the temperature dependent jump rates  $\gamma(T)$  of the jump diffusion models introduced in [chapter 3](#) are replaced by Arrhenius laws of the form

$$\gamma(T) = \gamma_0 \exp\left(\frac{E_A}{k_B T}\right) \quad (5.6)$$

with activation energy  $E_A$  and preexponential factor  $\gamma_0$ , which are used as free parameters directly. The fitting algorithm also allows to pool data from different instruments or instrument configurations, e.g., different incident wavelengths on ToF spectrometers, or the combination of ToF and BS. As the model function can be rendered an analytical function of  $T$  with the above mentioned substitution of the jump rates with Arrhenius laws, the analysis of elastic and inelastic fixed window temperature scans (EFWS/IFWS) presented in [section 4.3](#) is straightforward and even allows for proper resolution smearing in these cases. Ultimately, everything can be combined:  $Q$ -dependent energy spectra taken on different instruments at different temperatures together with elastic and inelastic fixed window temperature scans. This can go as far as the simultaneous analysis of data for 16 different  $Q$ -values in a total of 96 fixed window scans and 79 energy spectra combining ToF and BS spectroscopy on triclinic Fc in [chapter 6](#), or more than 30 different  $Q$ -values in 306 energy spectra for PVFc in [chapter 8](#), where some of these analyses involve more than  $10^5$  individual data points. The algorithm was not extensively optimized for speed, and usually run on a standard quad-core desktop computer (2.9 GHz) with fully parallelized multiple scattering simulation and partially parallelized least-square refinement. For small data sets, one iteration of the loop in [Figure 5.4](#) typically takes in the order of 30 seconds to a few minutes, where most of the time is used for the multiple scattering simulation. For very large data sets, the execution time can increase up to one hour per iteration, as numerous individual multiple scattering simulations have to be performed for data subsets.

A second comment concerns the approach towards model validation of the rotational jump diffusion models. In general, a comparison of the experimentally determined EISF curve  $A_0(Q)$  with the model prediction gives a very good and reliable way of confirming or dismissing a model. For this to be possible, the EISF needs to be a free fit parameter. Therefore, the values of  $A_0(Q)$  and  $A_1(Q)$  have been used as free parameters, while all remaining structure factors  $A_l(Q)$  for  $l \geq 2$  were fixed to  $A_1(Q)$  using the ratios given by the assumed model function. However, doing this, these parameters will be fully correlated to the overall scaling factor  $s_0$  and  $u_0^2$  in the exponent of the Debye-Waller factor. To resolve this,  $s_0$  and  $u_0^2$  are not fitted directly. Instead, after the least-square refinement in step (II) of the analysis loop above, the values of  $u_0^2$  and  $s_0$  are obtained from a fit of the sum over  $A_l(Q)$ . This step assures normalization of the structure factors, meaning that

$$\sum_{l=0}^{N-1} A_l(Q) \stackrel{!}{=} 1 \quad .$$

During the refinement loop,  $s_0$  and  $u_0^2$  then approach their stationary value similar to all other parameters. An exception to this is the analysis of data that contains elastic fixed window temperature scans, as their temperature dependence is characterized by the value of  $u_0^2$ . In these cases,  $u_0^2$  can be fitted directly. For Fc, where the phonon density of states  $Z(\omega)$  was experimentally determined, the temperature dependence of the Debye Waller factor was improved at low temperatures by numerical integration of  $Z(\omega)$ . The details are discussed in [Appendix C](#).

---

The third and last important comment concerns the handling of coherent Bragg peak scattering. This is observed for crystalline powder samples of Fc and FcI<sub>3</sub>. The ToF instruments contain a large number of detectors which are grouped to typically 20 to 30 different  $Q_{el}$ -values for data analysis. This grouping was adapted for each measured temperature to isolate Bragg peaks into designated groups. Detector groups contaminated by Bragg peaks are not removed from the data sets such that their elastic scattering within the experimentally accessed  $Q$ -range can then be taken into account in the multiple scattering simulations. The values of the resulting final elastic structure factors  $A_0(Q)$  however will be presented without data points containing Bragg peak scattering in order to avoid confusion. The inelastic contribution  $A_1(Q)$  is not influenced by the elastic Bragg scattering and will be shown for all detector groups. For the amorphous sample PVFc, the coherent scattering is diffuse and will be handled by a different approach as discussed in [chapter 8](#).

---

# **Part II**

## **Experiments & results**

---



---

## 6 Ring rotation dynamics in bulk ferrocene

In this chapter, the first and supposedly simplest step in the study of ring rotation dynamics in the ferrocene molecule is documented: bulk ferrocene. But as it turns out, the dynamics in the molecular crystal of ferrocene is anything but simple. The polymorphism of ferrocene discussed in [section 1.1](#) is a first indication of the entanglement of structure and dynamics. In the following, the experiments and analyses will be separated according to the three crystalline phases. After a short explanation of the experimental details, the monoclinic high temperature phase with dynamically disordered rings will be discussed. Subsequently, the study of the metastable triclinic low temperature phase is presented, and a short paragraph will deal with a measurement on the stable orthorhombic low temperature phase as well. In the end, the different dynamics in all three phases of crystalline ferrocene will be discussed and summarized.

---

### 6.1 Experimental details

---

Ferrocene was purchased from Alfa Aesar (purity 99%) and used without further purification. For neutron time of flight experiments, approximately 0.7 g of sample was filled in standard flat  $3 \times 4 \text{ cm}^2$  aluminum samples holders of  $\approx 0.5 \text{ mm}$  sample thickness. The calculated transmission for  $6.3 \text{ \AA}$  neutrons is around 85%. For neutron backscattering experiments in the triclinic phase, a hollow cylinder aluminum sample holder of 22 mm outer diameter and 0.5 mm sample thickness filled with 1.45 g of ferrocene powder has been used. The calculated transmission is 80% to 85%.

In order to obtain the orthorhombic phase of ferrocene, attempts were made to anneal the sample at  $T = 190 \text{ K}$  for  $> 24 \text{ h}$  after quenching in liquid nitrogen similar to the procedure described by [B  rar et al.](#)<sup>[22]</sup> Transformation to the orthorhombic phase was verified by a low resolution neutron diffractogram, but could only be achieved for a freshly sublimed sample. As was pointed out by [B  rar et al.](#), transformation to the orthorhombic phase does not occur for a sample containing too small crystallites (below circa  $40 \mu\text{m}$ ). The original sample was probably broken down into small crystallites after repeated cooling and heating cycles through the monoclinic-triclinic transition during previous experiments. The sublimation leading to larger crystallites then re-enables the transformation to the orthorhombic phase. However, crystallites may not be too large either (above circa  $300 \mu\text{m}$ ) as they tend to disintegrate explosively into small fragments after cooling through the monoclinic-triclinic transition.<sup>[22,25,26]</sup> The above described procedure was performed for 231 mg freshly sublimed ferrocene in a flat  $3 \times 4 \text{ cm}^2$  aluminum sample holder of 0.6 mm thickness which was stored at liquid nitrogen temperature after successful transformation.

Temperature on all experiments was controlled by a standard ILL orange cryofurnace in the range of 2 K to 320 K. Inelastic neutron measurements on Fc were carried out on the time of flight spectrometers IN5 and IN6, and high resolution neutron spectroscopy was performed on the backscattering spectrometer IN16B. The mode of operation, schematics and characteristics of these spectrometers were presented in [chapter 4](#). For measurements on the triclinic sample, the analyzers of IN16B were partly covered with neutron absorbing Cadmium plates in the angular ranges under which coherent Bragg peak scattering occurs. Moreover, on IN16B, the different modes of measurement described in [section 4.3](#) have been used. Firstly, fixed window scans (FWS) were used to measure the temperature dependent scattering intensity for fixed energy transfers of 0, 1, 3, 5, 7, 9 and  $11 \mu\text{eV}$ . Subsequently, complete spectra as a function

**Table 6.1:** Listing of sample temperatures for neutron scattering experiments on triclinic/monoclinic Fc using backscattering spectroscopy (IN16B) and ToF spectroscopy (IN5/IN6).

instrument	$T / \text{K}$							
IN16B (FWS <sup>a</sup> )	→							
IN16B	110	130	150	160				
IN5 ( $\lambda_{\text{inc}} = 12 \text{ \AA}$ )		130	150	155 <sup>b</sup>	160			
IN5 ( $\lambda_{\text{inc}} = 6.3 \text{ \AA}$ )				160	170	190	230	290
IN6 ( $\lambda_{\text{inc}} = 5.12 \text{ \AA}$ )						200	260	320
IN5 ( $\lambda_{\text{inc}} = 3.6 \text{ \AA}$ )					190		230	

<sup>a</sup> Elastic and inelastic fixed window scans with continuous heating ramp

<sup>b</sup> Measured during heating, the given temperature value is averaged

of energy transfer in the range of  $\pm 30 \mu\text{eV}$  were recorded at fixed temperatures. A list of all sample temperatures for experiments on the triclinic/monoclinic phase is given in Table 6.1. The orthorhombic sample could only be measured once in a fixed window scan with multiple offset energies on IN16B due to limited experimental time.

## 6.2 Monoclinic high temperature phase

The general shape of the obtained energy spectra on IN5 is shown in Figure 6.1. As expected, the spectrum shows significant quasielastic scattering which broadens with increasing temperature. In the metastable triclinic low temperature phase at  $T = 160 \text{ K}$  an inelastic feature is clearly distinguishable around  $E = -2.5 \text{ meV}$  which has been attributed to the librational motion of the Cp rings.<sup>[34]</sup> While this inelastic contribution is clearly separated from the line broadening at  $T = 160 \text{ K}$ , they merge in the monoclinic phase at higher temperatures and libration cannot be distinguished from quasielastic broadening. In the following, a detailed data analysis in terms of the equivalent sites 5- and 10-fold model as well as the non-equivalent  $2 \times 5$ -fold sites model will be presented.

### Equivalent sites 5- and 10-fold jump models

The equivalent sites 5- and 10-fold jump models do not include a contribution broad enough in energy to adequately describe the spectra, thus the modeling of librational motion is included for these models as discussed in chapter 5. If the librational peak is not included in the model function, excess intensity in the spectra around  $-2 \text{ meV}$  is immediately obvious. However, the position of the libration peak had to be restricted to  $|\hbar\omega_L| > 1.5 \text{ meV}$  in order to achieve a stable model refinement. This limit value was usually attained in the process, questioning the reliability of the modeling of the librational motion. In retrospect, even though the description of experimental data seems much better by using the libration peak, its impact on the relevant parameters of the equivalent sites 5- and 10-fold model turned out to be insignificant.

Apart from the restrictions concerning the libration peak, the analysis of the equivalent sites 5- and 10-fold jump models proceeds straightforward. The results from the analysis are composed in Figure 6.2 and 6.3 for the 5- and 10-fold model respectively. Exemplary spectra recorded on IN5 with  $\lambda_{\text{inc}} = 3.6 \text{ \AA}$  at  $T = 190 \text{ K}$  are shown in Figure 6.2b and 6.3b together with the best fit of the respective model function and the contributions from elastic scattering (dark gray area), the quasielastic Lorentzian broadenings (green lines), the libration peak (violet line) and the



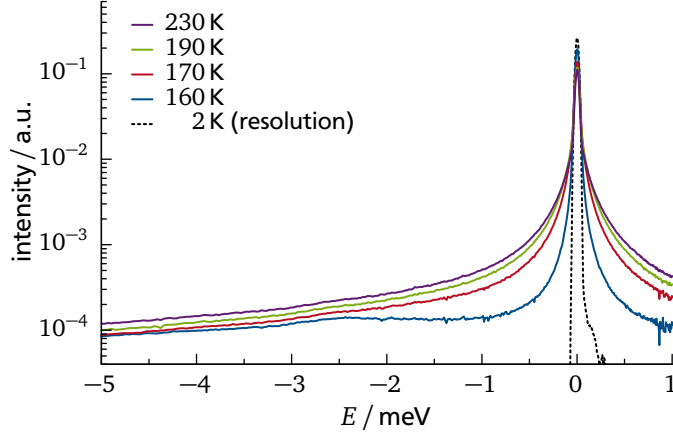


**Figure 6.1:** Energy spectra obtained by neutron time of flight spectroscopy on triclinic and monoclinic ferrocene at different temperatures on IN5 with  $\lambda_{\text{inc}} = 6.3 \text{ \AA}$ , summed over all scattering angles. At  $T = 160 \text{ K}$  below the triclinic-monoclinic phase transition, a broad peak can be seen around  $E = -2.5 \text{ meV}$  caused by the librational mode of the Cp rings.

phonon background (black line). The flat background lies far below the plotted region and is not shown. It should be stressed again at this point that the data is presented for constant scattering angle and the given values of the momentum transfer  $Q_{\text{el}}$  only apply to the point of elastic scattering. The individual contributions shown in the plot include the correction factors  $R_{2\theta}^*(\omega)$  obtained from the multiple scattering simulation and are thus not cuts along constant  $Q$ , but correspond to an increasing value of  $Q$  with increasing magnitude of energy transfer  $E$ . This dependency is especially strong at low scattering angles  $2\theta$ , explaining the two-wing shape of the supposedly monotonically increasing phonon background in the foremost spectra.

Figure 6.2c and 6.3c show the resulting amplitudes  $A_0(Q)$  of the elastic part and  $A_1(Q)$  of the quasielastic part for all investigated temperatures in the range of 170 K to 320 K. The theoretical curve for these parameters from the equivalent sites 5- and 10-fold jump model according to eq. (3.13) is shown as thick red line. It can be seen in Figure 6.2c that the analysis in terms of the equivalent sites 5-fold model results in excess elastic intensity  $A_0$  in the intermediate  $Q$ -range below  $2 \text{ \AA}^{-1}$  which is especially pronounced at lower temperatures. At larger  $Q$  above  $2 \text{ \AA}^{-1}$ , the shape of the model curve shows strong disagreement with the obtained values of  $A_0(Q)$ . The equivalent sites 10-fold model in Figure 6.3c is in very good agreement with the data up to circa  $1 \text{ \AA}^{-1}$  to  $1.5 \text{ \AA}^{-1}$ , but shows excess elastic intensity at larger  $Q$ .

Figure 6.2d and 6.3d show the resulting correlation times  $\tau = \gamma^{-1}$  in an Arrhenius plot. For easier comparison, Figure 6.3d contains the results obtained using the 5-fold model in light gray. The correlation times extracted with the equivalent sites 5-fold jump model (Figure 6.2d, open symbols) show serious discrepancies between different instruments and incident wavelengths and do not fall on a single line. While a deviation from Arrhenius type behavior might be arguable, the resulting parameters have to be consistent for measurements at the same temperature with different wavelengths. This is not the case for the points representing results from IN5 at  $\lambda_{\text{inc}} = 3.6 \text{ \AA}$  and  $6.3 \text{ \AA}$  at  $T = 190 \text{ K}$  and  $230 \text{ K}$ . The two respective measurements for both temperatures have been carried out directly after each other without any change of sample environment. In order to achieve a more consistent analysis in terms of the equivalent sites 5-fold jump model, each pair of the above mentioned data sets at  $T = 190 \text{ K}$  and  $230 \text{ K}$  are analyzed simultaneously yielding the correlation times shown as full diamonds. Subsequently, all data sets are pooled in a single refinement procedure and analyzed simultaneously using

$$\tau(T) = \tau_0 \exp\left(\frac{E_A}{k_B T}\right) \quad (6.1)$$

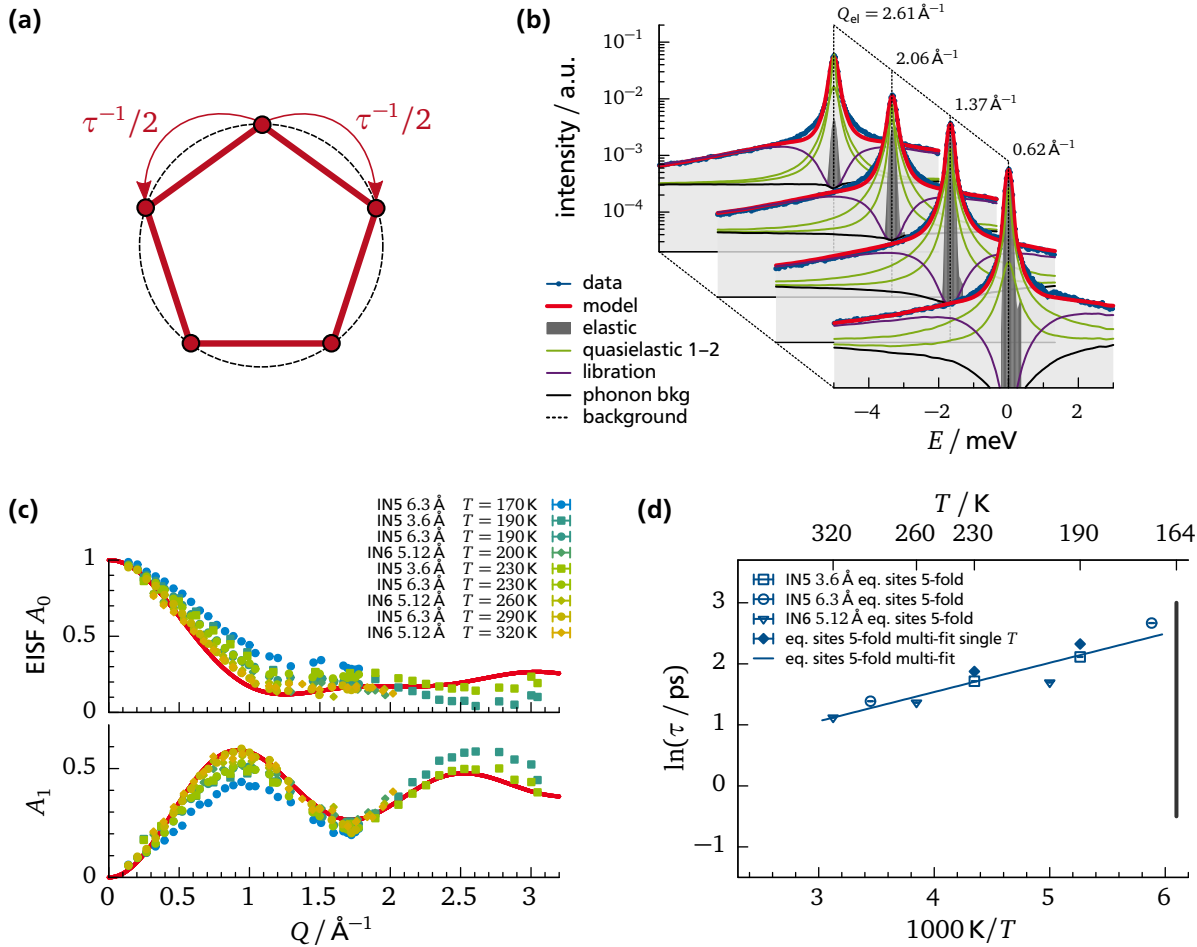


**Figure 6.2:** Overview of the results from data analysis using the equivalent sites 5-fold jump model. (a) Visualization of the equivalent sites 5-fold jump model with a single correlation time  $\tau$ . (b) Energy spectra (IN5,  $\lambda_{inc} = 3.6 \text{ \AA}$ ,  $T = 190 \text{ K}$ ) with fits of the model function. Spectra are shown for constant scattering angle (see text). (c) Resulting incoherent structure factors of the elastic part  $A_0$  and the quasielastic part  $A_1$  compared to the 5-fold jump model (red line). (d) Temperature dependent correlation times  $\tau$  of the jump motion. It is seen that the  $Q$ -dependence of the structure factors in (c) is different from the model function (red line), and measurements with different incident wavelengths lead to different correlation times in (d). Errors are typically smaller than symbols.

to account for temperature dependence of the correlation time. Instead of directly refining the correlation time  $\tau$  (or the corresponding rate  $\gamma = \tau^{-1}$ ), the prefactor  $\tau_0$  and activation energy  $E_A$  of its Arrhenius law are now used as free parameters. All other parameters remain independent for different temperatures. The resulting Arrhenius law is shown as solid line in Figure 6.2d, the values of activation energy  $E_A$  and  $\tau_0$  are given in Table 6.3. Care must be taken in the interpretation of the estimated standard deviations given for both of these parameters as they are highly correlated (correlation coefficient  $-0.98$ ). The amplitudes  $A_0(Q)$  and  $A_1(Q)$  shown in Figure 6.2c for the 5-fold model also correspond to the analysis of all temperatures simultaneously.

In case of the equivalent sites 10-fold jump model, the correlation times shown in Figure 6.3d are roughly halved with respect to the equivalent sites 5-fold model due to the doubled number of sites. More importantly, the independent analysis of data from different instruments and wavelengths is now consistent and the resulting correlation times can be approximated with a single Arrhenius law. Thus, a simultaneous analysis of multiple temperatures is not per-

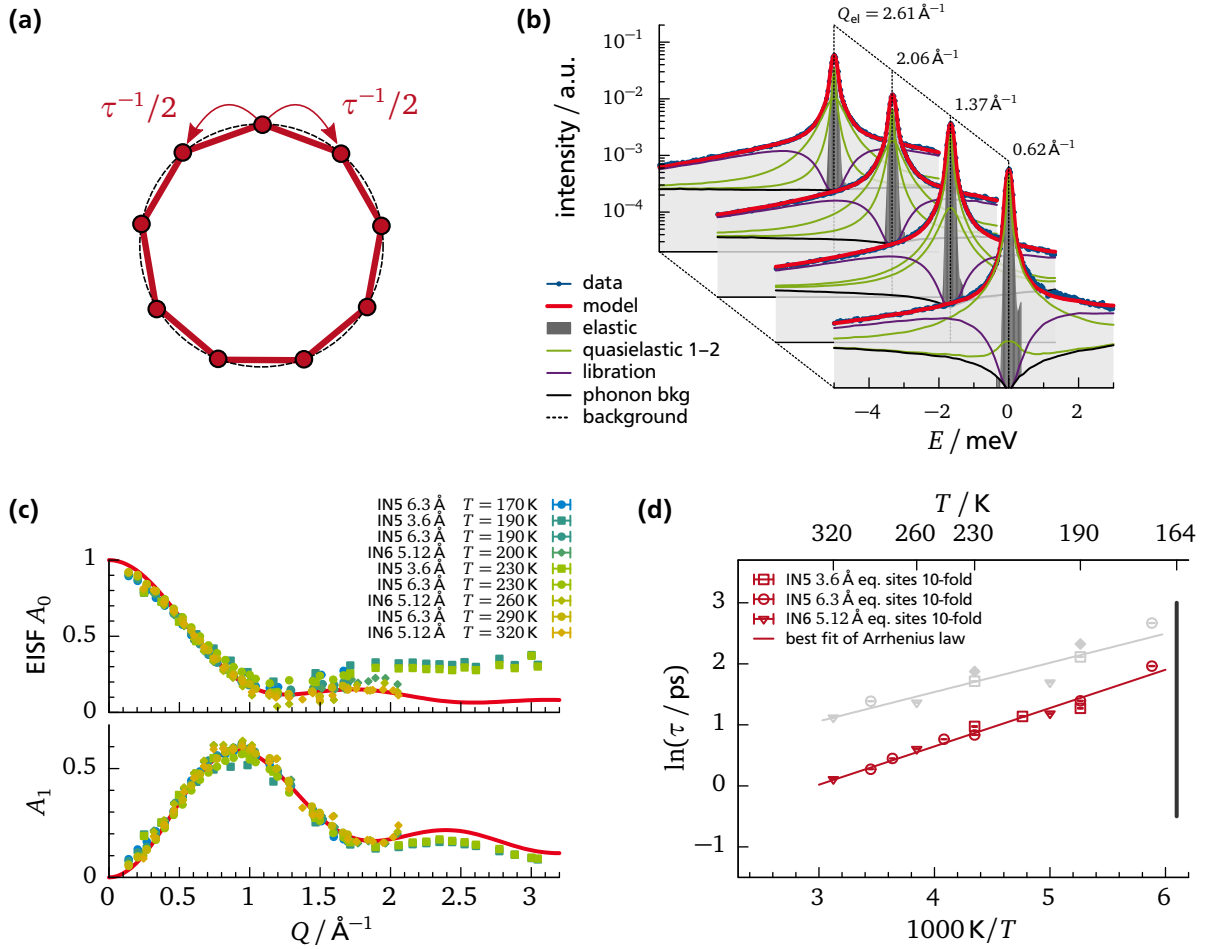


**Figure 6.3:** Similar to Figure 6.2, but showing results from data analysis using the equivalent sites 10-fold jump model. The gray results in (d) correspond to the analysis using the 5-fold model for easier comparison (cf. Figure 6.2d). The  $Q$ -dependence of the structure factors in (c) differs significantly from the model function (red line), especially above  $2 \text{ \AA}^{-1}$ . For the 10-fold model, the correlation times in (d) are consistent for different incident wavelengths in contrast to results using the 5-fold model shown in Figure 6.2d. Errors are typically smaller than symbols.

formed for the equivalent sites 10-fold jump model. Activation energy and prefactor are directly obtained from a best fit of eq. (6.1) to the obtained values of  $\tau(T)$  and given in Table 6.3.

However, concerning the incoherent structure factors  $A_0(Q)$  and  $A_1(Q)$ , neither the equivalent sites 5-fold nor the equivalent sites 10-fold model led to a consistent description of the experimental data over the entire range of temperatures investigated.

### Non-equivalent sites $2 \times 5$ -fold jump model

Due to higher complexity of the non-equivalent sites model and the increased number of free parameters, data analysis using this model must be carried out carefully. Especially the task of refining twist angle  $\alpha$  and population factor  $f$  requires data at large  $Q$ , as these parameters define the local dynamics between neighboring sites. For this reason, this model should preferably be fitted simultaneously to data sets containing multiple temperatures and/or incident wavelengths. In a first step, for each of the fixed temperatures  $T = 190 \text{ K}$  and  $230 \text{ K}$  the measurements using wavelengths  $\lambda_{\text{inc}} = 6.3 \text{ \AA}$  and  $3.6 \text{ \AA}$  on IN5 were analyzed simultaneously. Also, all four jump rates  $\gamma_{1,2,a,b}$  are initially unconstrained. The results always show comparable values for the 5-fold symmetry jump rates  $\gamma_1$  and  $\gamma_2$  of each ring configuration, while one of the jump rates  $\gamma_a$  or  $\gamma_b$  always converged to zero. Moreover, the part of the energy spectrum which

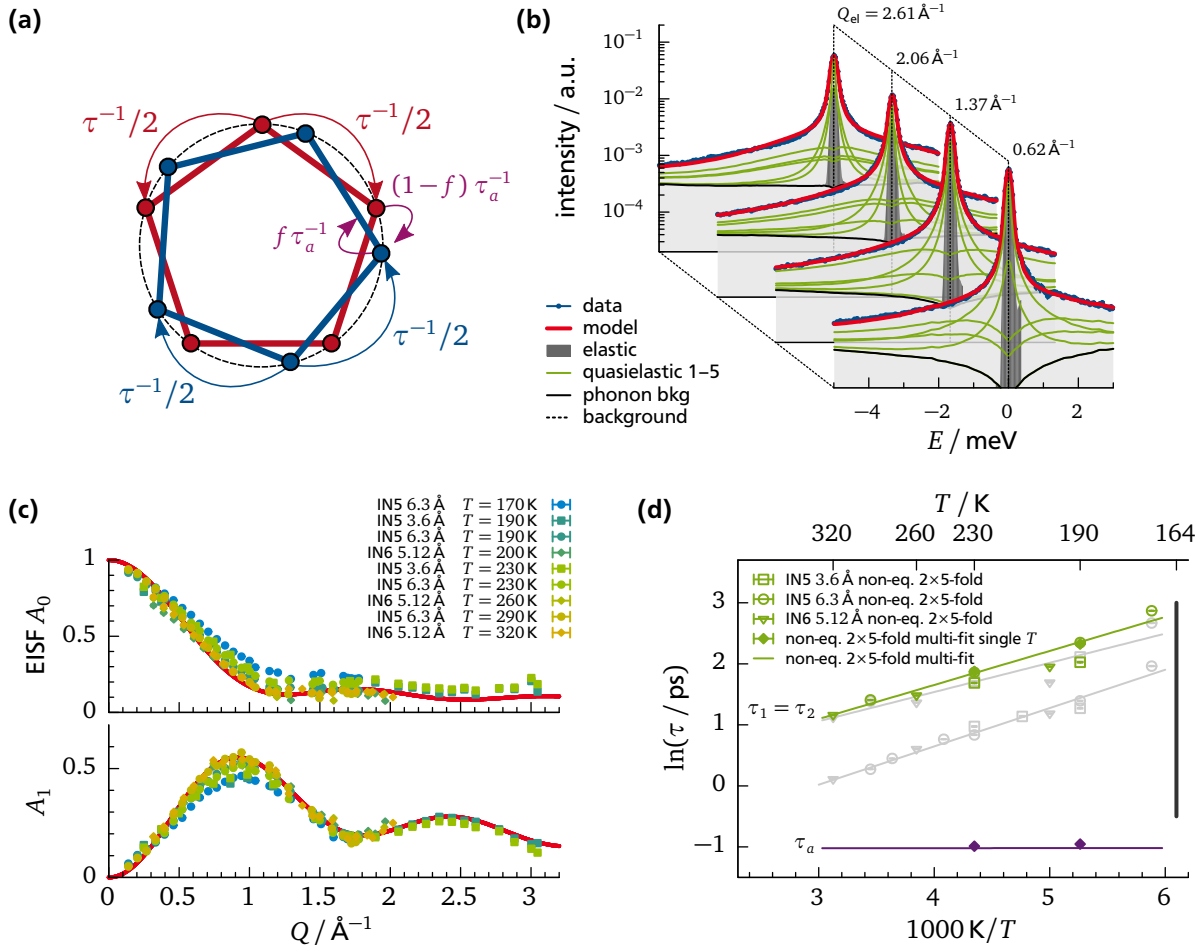


**Figure 6.4:** Similar to Figure 6.2 and Figure 6.3, but showing results for the non-equivalent sites 2x5-fold model. In (d) the results of the analysis using the 5- and 10-fold model are shown in gray for easier comparison (cf. Figure 6.2d and 6.3d). Among the studied jump models, this model shows the best agreement between data and model, especially for the incoherent structure factors in (c). Errors are typically smaller than symbols.

required the libration peak in case of the equivalent sites 5- and 10-fold models is described by a broad quasielastic contribution generated by a comparatively large value of  $\gamma_a$  or  $\gamma_b$ . From these observations, constraints are introduced for the non-equivalent sites model to reduce the number of free parameters: The libration peak was removed and not used for the extended model, the jump rates  $\gamma_1$  and  $\gamma_2$  were forced to be equal and  $\gamma_b$  was set to zero.

After the data sets taken at  $T = 190$  K and  $230$  K were analyzed, all data sets for multiple temperatures are analyzed simultaneously. As in the case of the equivalent sites 5-fold model, the jump rates  $\gamma_1$  and  $\gamma_a$  were replaced by Arrhenius laws and characterized by an activation energy and a prefactor each.

Figure 6.4 shows the results of the analysis in terms of the non-equivalent sites 2x5-fold model. The exemplary data set in Figure 6.4b can be well described with the model separating in a narrow contribution of 2 Lorentzians governed by the 5-fold symmetry rotations with rate  $\gamma_1$  and a broad contribution consisting of 3 Lorentzians mostly governed by transitions between the two configurations at rate  $\gamma_a$ .

The amplitudes of elastic and quasielastic contributions  $A_0(Q)$  and  $A_1(Q)$  are shown in Figure 6.4c. In general, the corresponding model curve for the non-equivalent sites model depends on the jump rates and could thus be different for each temperature, however, the above mentioned restrictions which are applied to the model result in a temperature indepen-

**Table 6.2:** Values of twist angle  $\alpha$  and occupation probability  $f$  using the non-equivalent sites model.

data set	$f$	$\alpha / ^\circ$
$T = 190\text{ K}$	0.280(5)	30.2(2)
$T = 230\text{ K}$	0.49(1) <sup>a</sup>	29.6(2)
all $T$	0.49(1) <sup>a</sup>	27.3(2)

<sup>a</sup> Limit value reached during refinement (see text)

dent form of the model curve shown as thick red line. It is in good agreement with the results, although lower temperatures have the tendency to show slightly increased elastic intensity virtually over the entire  $Q$ -range.

The results for the correlation times  $\tau_1 = \tau_2$  and  $\tau_a$  are shown in Figure 6.4d. Similar to the case of the equivalent sites 5-fold model, the results from simultaneous analysis of data sets at  $T = 190\text{ K}$  and  $230\text{ K}$  are shown as full diamonds and the lines correspond to the analysis of all temperatures using a  $T$  dependency similar to eq. (6.1) for  $\tau_1 = \tau_2$  and  $\tau_a$ . The agreement between both these results is excellent. While the values of  $\tau_1 = \tau_2$  are very similar to the ones obtained for the equivalent sites 5-fold model, the value of  $\tau_a$  is by one order of magnitude smaller and independent of temperature within experimental accuracy. The resulting parameters of the corresponding Arrhenius laws are given in Table 6.3, where activation energy and prefactor are again highly correlated as stated for the equivalent sites 5-fold model above.

The resulting values of  $f$  and  $\alpha$  are given in Table 6.2. Some values for  $f$  reached their arbitrarily chosen limit value of 0.49 during the refinement procedure. This limit value was introduced as the model shows a symmetry in the value of  $f$  with a vanishing derivative of the squared residuals  $\partial\chi^2/\partial f$  at  $f = 0.5$  which could ‘trap’ the refinement process at this value. Within the experimental accuracy, a value of  $f = 0.5$  meaning equal population of both configurations can be assumed as result for the analysis of the data sets at  $T = 230\text{ K}$  and the simultaneous analysis of all temperatures.

As further check of model reliability, the data sets for each temperature and incident wavelength are analyzed individually in a last step. However, the values of  $\tau_a$ ,  $\alpha$  and  $f$  are fixed to the ones obtained in the simultaneous analysis of all data sets. The resulting values of  $\tau_1 = \tau_2$  are then reported as open symbols in Figure 6.4d. The agreement with the prior analysis of multiple data sets is moderate, but improved with respect to the corresponding graph obtained using the equivalent sites 5-fold model.

### Comparison of results for different models

The first point in discussing the results for the monoclinic high temperature phase is concerned with technical aspects of comparison of the three different models. From the overviews in Figure 6.2, 6.3 and 6.4 it is evident that the non-equivalent sites model gives the best description of the experimental data in terms of the incoherent structure factors  $A_0(Q)$  and  $A_1(Q)$ . The preference for the non-equivalent sites over the equivalent sites 10-fold model relies mostly on the mismatch in the EISF  $A_0$  obtained for  $\lambda_{\text{inc}} = 3.6\text{ \AA}$  for the latter model. Regarding the equivalent sites 5-fold model, it is the measurements with short wavelength as well which show the most prominent discrepancies. Together with the inconsistency of the obtained correlation times  $\tau$  for the equivalent sites 5-fold model this raises the justified question whether the observed mismatch is an artifact of insufficient instrumental energy resolution for the  $3.6\text{ \AA}$  measurements. The higher resolution measurements result in an average, unconvoluted FWHM

**Table 6.3:** Obtained values for activation energy  $E_A$  and prefactor  $\tau_0$  of the jump motion using different models.

model	$E_A/\text{kJ mol}^{-1}$	$\tau_0/10^{-12}\text{ s}$	method
eq. sites 5-fold	3.94(1)	0.935(5)	iQENS
	4.4(5)	0.8	iQENS <sup>a</sup>
	5.4(5)		NMR <sup>b</sup>
eq. sites 10-fold	5.2(2)	0.15(2)	iQENS
non-eq. sites ( $\tau_1, \tau_2$ )	4.635(8)	0.562(2)	iQENS
non-eq. sites ( $\tau_a$ )	0.00(3)	0.359(6)	iQENS

<sup>a</sup> from ref. [34]    <sup>b</sup> from ref. [30]

of the quasielastic contribution of  $110\ \mu\text{eV}$  to  $160\ \mu\text{eV}$  at  $T = 190\ \text{K}$  and  $160\ \mu\text{eV}$  to  $250\ \mu\text{eV}$  at  $T = 230\ \text{K}$  respectively. This value corresponds to the energy resolution of roughly  $170\ \mu\text{eV}$  (FWHM) at  $3.6\ \text{\AA}$  and shows that resolution effects must be taken into account carefully, but should not hinder the extraction of proper correlation times given an adequate model function. For the above mentioned reasons, the large inconsistency in correlation times and ISFs obtained using the equivalent sites 5-fold jump model is attributed to shortcomings of the model in describing the actual motion of Cp rings in monoclinic Fc.

Comparing the equivalent sites models, the 10-fold model shows an improved consistency in describing the experimental data concerning the ISFs and more importantly the correlation times  $\tau$  with respect to the 5-fold model. The obtained values of  $\tau$  are compatible for measurements with different incident wavelengths and thus different energy resolutions and  $Q$ -ranges. Although the agreement of the EISF for  $Q > 2\ \text{\AA}^{-1}$  is largely unsatisfactory, it seems that the increased number of sites is, loosely speaking, a step in the right direction.

The non-equivalent sites  $2\times 5$ -fold model, which has been introduced due to the insufficiency of the equivalent sites  $N$ -fold jump models, results in the best agreement in the ISFs. A small drawback is that the individual analysis of different data sets especially at  $\lambda_{\text{inc}} = 3.6\ \text{\AA}$  results in significantly lower correlation times  $\tau_1$  than the simultaneous analysis of multiple data sets. This apparent dependency on instrumental resolution is similar to the case of the 5-fold model, although discrepancies for the non-equivalent sites model are much smaller. However, amongst the three investigated models, the non-equivalent sites model gives by far the best overall description of Cp ring rotation for data collected on the monoclinic phase of Fc. This statement fully relies on data collected for  $T \leq 230\ \text{K}$ . In fact, all data sets for  $T \geq 260\ \text{K}$  can be described with either of the models giving a striking agreement of the ISFs with the model functions in each case, but no data at  $\lambda_{\text{inc}} = 3.6\ \text{\AA}$  giving access to  $Q > 2\ \text{\AA}^{-1}$  was collected at these temperatures.

### Rotational dynamics of Cp rings and context of previously obtained results

The obtained value of circa  $4.6\ \text{kJ mol}^{-1}$  for the rotational barrier of 5-fold symmetry jumps in case of the non-equivalent sites model is in good agreement with previously obtained results cited in Table 6.3. As expected, it is larger than the rotational barrier measured for the free molecule of  $(3.8 \pm 1.3)\ \text{kJ mol}^{-1}$  using electron diffraction by Haaland and Nilsson,<sup>[27]</sup> although care must be taken due to their large experimental error. A more detailed overview of the potential barriers to rotation obtained by various methods is given, e.g., by Braga.<sup>[15]</sup>

---

It has already become evident in early studies of the crystal structure of monoclinic Fc that the molecules are rotationally disordered, occupying different rotational conformations.<sup>[18–20,33]</sup> The dynamical situation is thus dramatically complicated compared to a fully ordered phase. 5-fold jumps of the rings due to the Cp symmetry are certainly possible, but the disorder may introduce different potential barriers due to intermolecular interactions. Moreover, the dynamical character of the disorder leads to transitions between different conformations depending on the surroundings of a single ring. In an even more complicated picture, these transitions propagate as small domains in a correlated motion through the crystal and are overlaid with librational motion of the Cp rings.<sup>[60]</sup> All of these aspects have been attributed a great deal of attention in numerous earlier publications on Fc, some of which will be referred to in the following.

Regarding the analysis of Cp rotational dynamics in monoclinic Fc presented here, all effects of disorder are neglected in the picture of the equivalent sites 5-fold jump model. The additional contribution which is added to the model accounting for ‘librational motion’ can thus cover the effects of actual librational motion as well as transitions between conformations. When the angle of rotation between different conformations is sufficiently small, a large amplitude librational motion might not even be separable from such transitions.

Results obtained from the modeling of the librational motion in the equivalent sites 5- and 10-fold model are not discussed due to the empirical description and the imposed constraints for their parameters. It should be emphasized again that even without the part describing librational motion the parameters obtained for the equivalent sites 5- and 10-fold model are essentially the same and show the discussed large inconsistencies.

The equivalent sites 10-fold model itself on the other hand requires some justification, as the intramolecular part of the potential energy of the Cp ring shows only 5-fold symmetry due to the symmetry of the single molecule. However, it has been shown by [Levendis and Boeyens](#)<sup>[32]</sup> in lattice energy calculations involving a simplified ‘concerted rotation’ of Cp rings that, for some types of rotation, additional minima due to intermolecular interactions can occur in the potential energy surface of a Cp ring. These are taken into account by the equivalent sites 10-fold model, but only in a very rudimentary way. The transition rate between neighboring sites is constant and any effects of disorder are ignored. Results from the analysis using the equivalent sites 10-fold model show that it fails at large  $Q$  – the detailed localized dynamics can thus not be accurately described with this model.

The simplest model which takes disorder into account is the non-equivalent sites  $2 \times 5$ -fold model. It allows the ring to be in 2 distinct configurations, undertaking 5-fold rotations within these configurations over independent potential barriers as well as transitions between both configurations by clockwise or counterclockwise rotation. The results show that both barriers are equally high and the transitions between the two states proceed at much higher rate, but only over one possible route (i.e.,  $\gamma_b = 0$ ). The latter observation is plausible, as a high transition rate over both routes (clockwise and counterclockwise transitions from ring state 1 to 2) would completely shadow the slower 5-fold intra-ring jumps. In the experimental data, the fast transitions between configurations take into account the part of scattering which was modeled as ‘libration’ in the simple  $N$ -fold models. Whether there is additional, ‘actual libration’ when using the non-equivalent sites model cannot be deduced from the data at this point. As stated above, libration and transitions between states might not even be clearly separable.

A certainly questionable result at this point is the apparent temperature independence of the transition rate between configurations  $\gamma_a$ . The transitions between configurations are most probably complicated correlated motions depending on the individual environment of the ring, and could have a much lower activation energy than the 5-fold symmetry jumps of a single ring. Moreover, they contribute to the incoherent scattering mostly at larger  $Q$  which were only investigated at the two temperatures of 190 K and 230 K which does not allow for a detailed analysis of the temperature dependence of that process.

---

The way of data analysis presented here allowed for refinement of the twist angle  $\alpha$  between the two states of the non-equivalent sites model. The resulting value of  $\alpha$  close to  $30^\circ$  proved surprisingly robust for different, extreme starting parameters as well as for different data sets (see Table 6.2). Moreover, it is in striking agreement with the study by Levendis and Boeyens<sup>[32]</sup> who, in their lattice energy calculations of a ‘concerted rotation model’, found  $30^\circ$  rotations as possible separators between correlated microdomains. Calvarin et al.<sup>[60]</sup> identified from their calculations possible transitions of  $29^\circ$  over a small potential barrier for one ring in the molecule to change from one configuration to another. Moreover, Brock and Fu<sup>[20]</sup> found from analysis of X-ray diffraction data that a two ring disorder model would be separated by  $22(2)^\circ$  at 173 K and  $28(2)^\circ$  at 298 K, Takusagawa and Koetzle<sup>[19]</sup> found circa  $24^\circ$  from neutron diffraction. Given that the value obtained in this work is obtained from spectroscopic measurements using a dynamical model, the agreement is most satisfactory and confirms the dynamical character of ring disorder.

The versatility and the extent of information extractable from quasielastic neutron scattering makes it a unique tool for the investigation of molecular reorientation on this timescale. To the best of knowledge, there is only one prior study of the ring dynamics in monoclinic Fc using neutron spectroscopy, carried out by Gardner et al.<sup>[34]</sup> on an earlier version of the same spectrometer IN5 used in this work more than 30 years ago. Their “evidence suggests strongly that the rings reorient in a 5-fold potential”, while they compared the equivalent sites 5- and 10-fold jump model. However, this conclusion is based on the presented analysis of the EISF at a single temperature of 303 K in a momentum transfer range up to  $Q < 2.2 \text{ \AA}^{-1}$ , and the necessity of further measurements at higher momentum transfers was pointed out. The data presented here shows that, in the limited range around 290 K to 320 K and within the  $Q$ -range in question, all three studied models are in very good agreement with the observations. The success of the non-equivalent sites model should be seen as an extension and refinement of the established 5-fold model based mostly on measurements at large  $Q$  and  $T$  below 230 K.

---

### 6.3 Triclinic low temperature phase

---

Data for triclinic ferrocene obtained on IN16B summed over all detectors was shown in Figure 4.3 on page 31, to demonstrate the relationship between quasielastic neutron scattering energy spectra (QENS) and elastic/inelastic fixed window scans (EFWS/IFWS). The Cp ring rotation leads to broadening of the energy spectra which becomes detectable above circa 100 K. In the elastic fixed window scan, the broadening appears as decrease in intensity with increasing temperature when the reorientation process becomes faster than the time scale associated with the instrumental energy resolution. In the inelastic fixed window scans, the broadening leads to a peak which is disrupted at 164 K by the phase transition into the monoclinic phase.

In contrast to the monoclinic high temperature phase, the rings are ordered in the triclinic phase,<sup>[12]</sup> such that the equivalent sites jump models can be expected to give a good description of the dynamics. However, due to the fact that there are two crystallographically different ferrocene molecules in the triclinic unit cell, the existence of different potential barriers for different rings is imaginable, as indicated by NMR experiments by Kubo et al.<sup>[30]</sup> In the following, we will start with the analysis in terms of a simple equivalent sites model, and extend the analysis to a two-ring model thereafter.

#### One-ring model

This model assumes equivalent dynamics for all Cp rings in the triclinic phase of ferrocene. For the analysis, data from ToF and BS experiments are treated separately. The refinement is carried out for each set of energy spectra obtained for different  $Q$  at fixed temperature. The resulting values for the mean residence time  $\tau = \gamma^{-1}$  are shown in an Arrhenius plot in Figure 6.5 a.



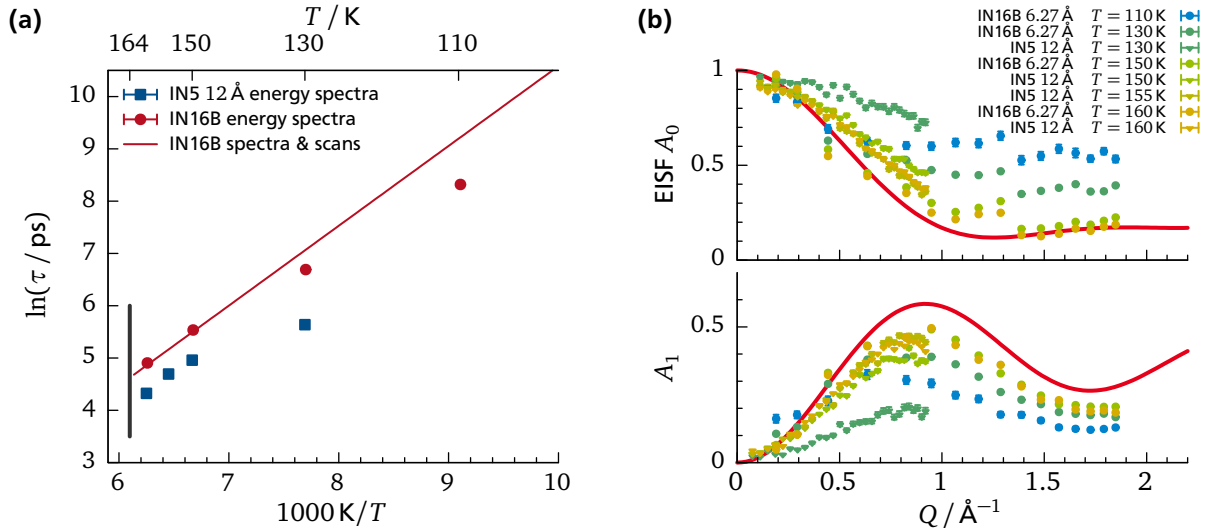


**Figure 6.5:** Results of the data analysis for triclinic ferrocene using a one-ring model. (a) Mean residence time  $\tau$  of the jump motion obtained from IN5 ToF data (blue squares), IN16B BS energy spectra (red circles) and IN16B BS energy spectra and temperature scans (line). (b) Resulting values of incoherent structure factors  $A_0(Q)$  and  $A_1(Q)$  for different temperatures compared to the model function for 5-fold circular jump diffusion (line).

Subsequently, all FWS and energy spectra measured on IN16B are analyzed simultaneously, yielding the Arrhenius law drawn as solid line with activation energy  $E_B = 12.70(3) \text{ kJ mol}^{-1}$  and prefactor  $\tau_0 = 9.2(2) \times 10^{-15} \text{ s}$ . The Arrhenius law is in very good agreement with the model refinement of IN16B data at individual temperatures of 150 K and 160 K, but shows discrepancies at lower temperatures (red circles). The mean residence times obtained from IN5 ToF data (blue squares) are obviously inconsistent with the BS results, and seem to be systematically shifted to smaller correlation times  $\tau$ .

The resulting amplitudes of elastic and quasielastic contributions, i.e., the EISF  $A_0(Q)$  and its counterpart  $A_1(Q)$ , are shown in Figure 6.5b for the one-ring model. The model function according to eq. (3.13) is shown as solid red line. While the results at 150 K and 160 K are in moderate agreement with the model function, the results obtained for lower temperatures are largely inconsistent with the model.

The one-ring model thus proves insufficient for a consistent description of the experimental data, motivating the analysis using a two-ring model. In order to substantiate, strengthen and understand the discrepancy between ToF and BS data seen in the obtained residence times, a Fourier transformation is performed on an exemplary pair of spectra measured at  $T = 160 \text{ K}$  for  $Q = 0.85 \text{ Å}^{-1}$  on IN5 and IN16B. The Fourier transformed spectra are divided by the respective instrumental resolution function to yield the intermediate scattering function  $I(Q, t)$  shown in Figure 6.6. It can be seen that the broad decay is neither entirely covered by ToF (blue squares) nor BS data (green circles). To further demonstrate the effect of the emerging discrepancy when analyzing each data set separately, the best fit of a Fourier transformed one-ring model to ToF and BS data (dashed lines) is shown in Figure 6.6, ignoring any multiple scattering corrections. Both lead to different residence times, and it can be seen that the observed overall decay is too stretched to be modeled by a single process. However, the superposition of two processes as described by the two-ring model gives a very good description of both data sets (solid red line in Figure 6.6), and we will further pursue the analysis in terms of the two-ring model in the following.

Even though the technique of Fourier transformation to the time domain provides a very useful possibility of merging ToF and BS energy spectra, further analysis is done in the energy

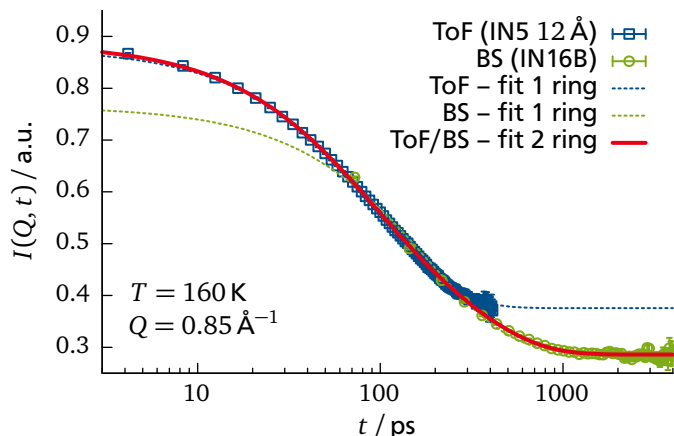


**Figure 6.6:** Exemplary compound Fourier transformed data from neutron time of flight (ToF) measurement on IN5  $\lambda_{\text{inc}} = 12 \text{ \AA}$  and neutron backscattering (BS) on IN16B for ferrocene at  $T = 160 \text{ K}$  and  $Q = 0.85 \text{ \AA}^{-1}$ . The best fit of a one-ring model to each data set is shown as broken lines, but only a two-ring model (solid line) can describe both data sets over the entire dynamic range.

domain using  $S(Q, \omega)$  rather than  $I(Q, t)$ . This facilitates the application of multiple scattering corrections obtained from Monte Carlo methods, and is notably advantageous for the treatment of fixed energy window temperature scans. We circumvent the necessity of transforming, deconvoluting and merging the data with the evaluation strategy of fitting the model simultaneously to data obtained on different instruments, while still being able to use the entire dynamic range provided by the combination of different methods.

### Two-ring model

The two-ring model accounts for crystallographically different sites in the triclinic phase of ferrocene, and the resulting possibly different energy barriers of Cp ring rotation on each of these sites. As discussed in the end of the previous paragraph, the analysis in terms of the two-ring model requires a dynamic range provided only by the combination of BS and ToF techniques. Consequently, the model refinement is performed simultaneously on data from both instruments. To enable this analysis, the IN5 ToF spectra were regrouped to match the mean  $Q$  values of the IN16B spectra in the range  $Q < 0.95 \text{ \AA}^{-1}$  in order to describe all data with the same set of amplitudes  $A_l(Q)$ .

A small excerpt of the analyzed data is shown in Figure 6.7. Fixed window scans of different energy transfers for  $Q = 0.83 \text{ \AA}^{-1}$  are shown in Figure 6.7a together with the best fit of the model (red solid line) and individual contributions of elastic, quasielastic and background scattering. In Figure 6.7a, the background part is too small to be distinguishable. Data points above 160 K shown as open circles were excluded from the refinement due to the triclinic-monoclinic phase transition. Exemplary energy spectra from IN16B BS and IN5 ToF ( $\lambda_{\text{inc}} = 12 \text{ \AA}$ ) taken at  $T = 150 \text{ K}$  are shown in Figure 6.7c and 6.7d for different magnitudes of the scattering vector  $Q$  together with the best fit of the model function.

The resulting Arrhenius laws for the mean residence time of ring 1 and 2 are plotted in Figure 6.8a with the parameters given in Table 6.4. As a further check of consistency, the refinement was also performed only for sets of energy spectra at fixed temperatures, but still using the combination of BS and ToF at different  $Q$ . These results are shown as full diamonds in Figure 6.8a, where each pair of data points at 130 K, 150 K and 160 K corresponds to separate analyses. The open symbol at 130 K stands for the fact that this parameter needed to be fixed during the refinement procedure as this process is too slow to be reliably refined using only

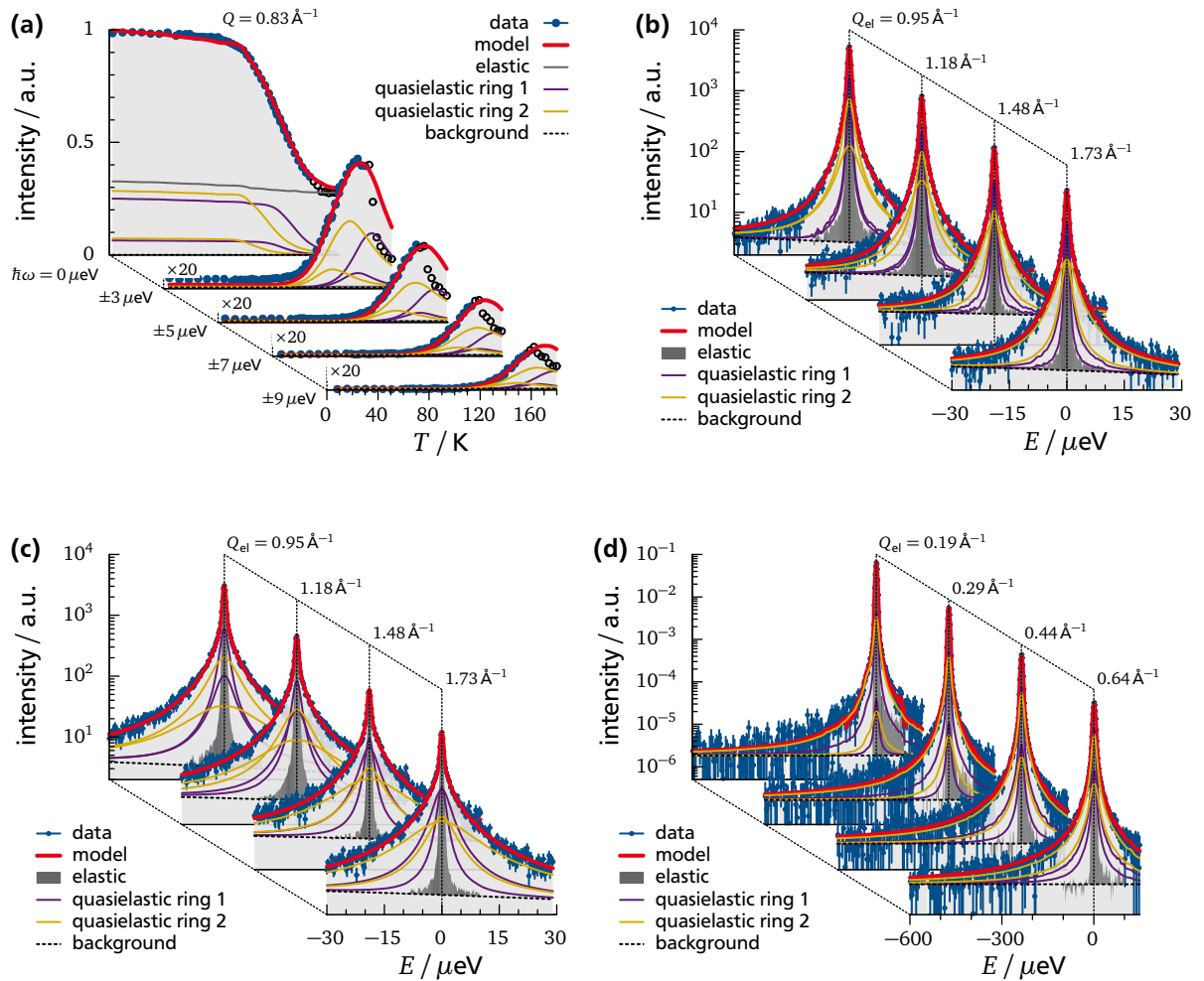


**Figure 6.7:** Small excerpt of the data for triclinic ferrocene used in simultaneous analysis in terms of the two-ring model. The best fit of the model function is shown as solid red line together with its separate elastic, quasielastic and background contributions. (a) Fixed window temperature scans with different energy offsets  $E$  at  $Q = 0.83 \text{ \AA}^{-1}$ . The background contribution is too low to be distinguishable. The shown energy spectra were obtained on IN16B BS (b) at 130 K and (c) at 150 K, and (d) IN5 ToF ( $\lambda_{\text{inc}} = 12 \text{ \AA}$ ) at  $T = 150 \text{ K}$ .

data at 130 K. Nevertheless, the resulting values are in very good agreement with the Arrhenius laws.

Figure 6.8a also shows the result obtained for the one-ring model in light gray for easier comparison. Moreover, the times corresponding to the respective energy resolutions of the instrumental configuration used on IN16B BS and IN5 ToF are shown as horizontal lines. Although the residence times  $\tau$  do not directly correspond to the width of the broadening observed in energy spectra, the horizontal lines give a good estimate whether a particular process can be resolved by the corresponding method or not. The slower a process is with respect to the resolution limit, i.e., the further it lies above the horizontal line, the less reliable the residence time obtained by the respective method is. This allows to observe a very interesting relationship between the results obtained by the analysis of the one- and two-ring model: At temperatures above 150 K, the one-ring model analysis of IN5 ToF data (gray squares) ‘sees’ only the corresponding faster process of the two-ring model, while the one-ring model analysis of IN16B BS data (gray circles) yields some average of both processes in that temperature range. At 110 K the one-ring model analysis of IN16B BS data yields a result corresponding to the faster process of the two-ring model, as the slower process is by far not resolvable any more considering the

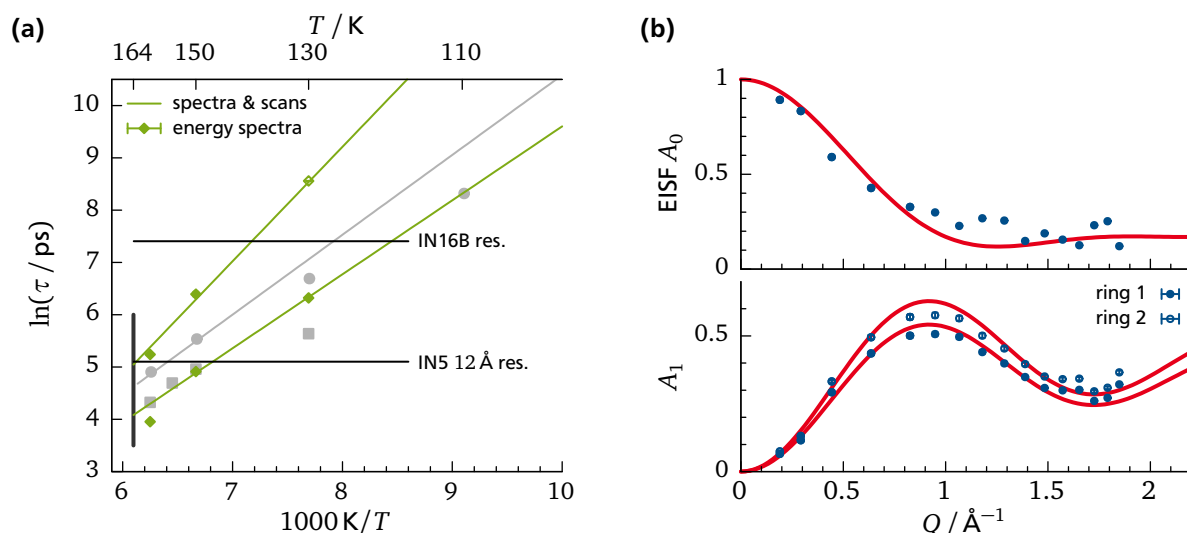


**Figure 6.8:** Results of data analysis for triclinic ferrocene using a two-ring model. (a) Mean residence time of jump rotation  $\tau$  for ring 1 and 2, obtained by analysis of energy spectra only (full diamonds) and spectra and fixed window scans (lines). Results of the analysis of the one-ring model from Figure 6.5a are shown in gray for comparison. (b) Resulting values of incoherent structure factors  $A_0(Q)$  and  $A_1(Q)$  compared to the model curve for rotational 5-fold jump diffusion.

extrapolation of its Arrhenius law. The slower process at 110 K is then wrongfully considered as elastic scattering in terms of the one-ring model and leads to the increase of the EISF in Figure 6.5b with decreasing temperature. These observations further explain the discrepancies in the analysis using the one-ring model and underline the necessity of using a two-ring model considering different energy barriers of ring rotation at different Cp sites in the triclinic ferrocene crystal.

The structure factors  $A_l(Q)$  obtained by using the two-ring model are shown in Figure 6.8b. The determined population factor of ring 1 with the larger energy barrier is  $f = 0.468(8)$ . The structure factors are in very good agreement with the model function, especially considering that in the range between  $0.8 \text{ Å}^{-1}$  to  $1.5 \text{ Å}^{-1}$ , a large fraction of analyzer surface (ranging from 20% to 80%) of IN16B BS was covered to avoid detection of coherent Bragg scattering. While the shown data set is obtained from the simultaneous analysis of all data and thus independent of temperature, the analyses of data at 130 K, 150 K and 160 K lead to similar results with slightly different values of the ring 1 population factor  $f$  (130 K: 0.50(1); 150 K: 0.46(2); 160 K: 0.63(2)).

The slightly different population factors obtained for different temperatures are consistent with the reasonable assumption that there are actually more than only two different energy barriers for the 4 crystallographically different sites. However, as the analysis demonstrates, the two-ring model already gives a very good approximation of the actual dynamics. It has already been pointed out by Kubo et al. in NMR experiments that the spin-lattice relaxation time  $T_1$  in the triclinic phase can only be described by the sum of two processes instead of one.<sup>[30]</sup> However, both activation energies of  $10.3(5) \text{ kJ mol}^{-1}$  and  $11(2) \text{ kJ mol}^{-1}$  obtained by their very basic analysis are close to the faster process of  $11.74(4) \text{ kJ mol}^{-1}$  observed in this work using the two-ring model (c.f. Table 6.4). A very good agreement of the experimental results is found in the potential energy barriers obtained from an atom-atom pairwise potential energy calculation by Braga and Grepioni.<sup>[16]</sup> As can be seen in Table 6.4, the largest and the smallest of their energy barriers obtained for 4 independent rings correspond very well to the result in terms of the two-ring model from the present work.

**Table 6.4:** Arrhenius law prefactor  $\tau_0$  and energy barrier  $E_B$  obtained for ferrocene in different crystalline phases.

phase	$\tau_0 / 10^{-15} \text{ s}$	$E_B / \text{kJ mol}^{-1}$		
	QENS	QENS	NMR <sup>b</sup>	ppe <sup>c</sup>
triclinic <sup>a</sup>	0.23(3)	18.3(2)	11(2)	18.4
	10.9(3)	11.74(4)	10.3(5)	14.2
				10.9
				10
orthorhombic	26(3)	— <sup>d</sup>	24.8(1)	42

<sup>a</sup> two-ring model for QENS; 4 independent Cp rings in ppe

<sup>b</sup> from ref. [30]

<sup>c</sup> atom-atom pairwise potential energy calculation, from ref. [16]

<sup>d</sup>  $E_B$  fixed to value obtained from NMR

The results thus present indisputable, direct experimental evidence of the fact that the Cp rings in the triclinic low temperature phase of ferrocene located on crystallographically different sites have different potential barriers of rotation. The quality of the results from analysis of the EISF provides the unique possibility of confirming that the geometry of the observed processes are indeed consistent with 5-fold rotational jump diffusion. Finally, the combination of multiple data sets from ToF and BS spectroscopy, energy spectra and fixed window temperature scans in a simultaneous analysis provides a novel, highly robust and accurate way of extracting multiple dynamic processes at the same time.

#### 6.4 Results for the orthorhombic low temperature phase

To complete the study of dynamics in crystalline ferrocene using neutron spectroscopy, the more exotic, stable low temperature orthorhombic phase was also investigated. Due to limited experimental time available, the orthorhombic phase could only be measured once in a FWS on IN16B BS with multiple energy offsets during which the sample was heated above the nonreversible orthorhombic-monoclinic phase transition. For comparison, a second, short FWS was performed on the same sample after storing 48 h at room temperature.

The result is shown in Figure 6.9a. During the first scan with the sample being in the orthorhombic phase, a broad and weak peak can be seen in the inelastic part (offset  $E = 3 \mu\text{eV}$ ) around 160 K corresponding to a remaining small fraction of triclinic ferrocene in the sample. The elastically scattered intensity however shows no indication of the monoclinic-triclinic transition and decreases only slightly, consistent with an increasing Debye Waller factor up to a temperature of 250 K. Here, the sample transforms into the monoclinic phase seen as steep decrease in elastically scattered intensity. At the same time, a peak can be seen in the inelastic fixed window scan at 250 K, indicating a quasielastic process entering the dynamic range of the spectrometer. In the second scan, the orthorhombic phase is not restored and the sample shows as expected the triclinic-monoclinic phase transition both in elastic and inelastic part.

Further analysis of this data is complicated by two facts: The large activation energy of the dynamics in the orthorhombic phase of  $(24.8 \pm 1.0) \text{ kJ mol}^{-1}$  as obtained from NMR<sup>[30]</sup> leads to very slow rotation dynamics which becomes resolvable in the present experiment only close to the phase transition. Secondly, the orthorhombic phase is easily overheated<sup>[21,22]</sup> and the decreasing side of the peak in the inelastic scan above 250 K is most probably governed by a

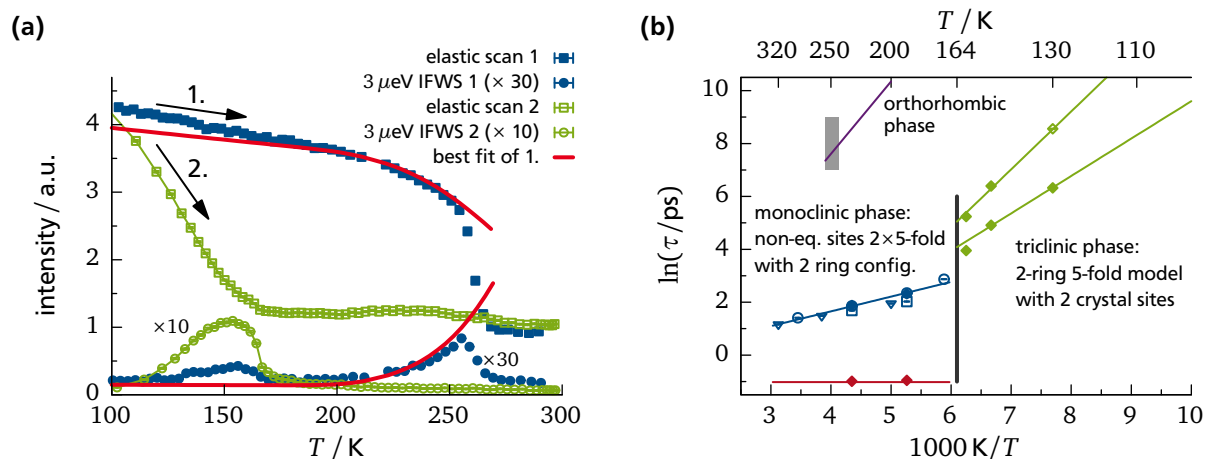


**Figure 6.9:** Overview of ring rotation dynamics in all three crystal phases of ferrocene: monoclinic, triclinic and orthorhombic. (a) Two subsequent fixed window temperature scans with energy offsets of  $0\ \mu\text{eV}$  and  $3\ \mu\text{eV}$  on a ferrocene sample initially in the orthorhombic phase. The inelastic fixed window scans (IFWS) are scaled in intensity as indicated. (b) Obtained mean residence times  $\tau$  of ferrocene ring rotation in all three crystalline phases, combining the results of this chapter.

decreasing fraction of orthorhombic phase rather than due to accelerating dynamics following an Arrhenius behavior.

Due to the high symmetry of the orthorhombic phase (space group  $Pnma$ ) with exactly eclipsed  $D_{5h}$  molecules,<sup>[23]</sup> the one-ring model can be expected to give an accurate description of the ring rotation dynamics as there are no crystallographically different sites. Assuming the activation energy obtained from NMR,<sup>[30]</sup> the one-ring model is fitted to the fixed window scan (no multiple scattering corrections) with the result shown in Figure 6.9a as solid line. Unfortunately, the data does not allow for an analysis to the same extent as for the triclinic phase at this point – only the scattered intensity summed over all detectors is analyzed in the temperature range of 180 K to 250 K and only the prefactor of the Arrhenius law is refined. The resulting parameter value is given in Table 6.4, and the resulting Arrhenius law is shown in Figure 6.9b. This figure contains an overview of the ring rotation dynamics in all three crystalline phases of ferrocene summarizing results from this chapter, and will be further discussed in the following section 6.5.

## 6.5 Conclusion: Ring rotation dynamics in all three phases of ferrocene

To summarize the study of the ring rotation dynamics of ferrocene in all three crystalline phases using neutron spectroscopy, the results for the mean residence time  $\tau$  of the rotational jump diffusion are combined in Figure 6.9b.

An elaborate analysis was performed for the metastable, triclinic phase forming below 164 K covering the right part of the diagram in Figure 6.9b. Therefore, multiple energy spectra, elastic and inelastic fixed window temperature scans from BS were combined with ToF energy spectra and refined in a simultaneous refinement process including multiple scattering corrections. The result clearly shows that the Cp ring rotation dynamics cannot be described by a single process in terms of a one-ring model, but crystallographically different sites with individual energy barriers must be considered. Here, the two-ring model with two independent rings proves sufficiently consistent, although there are four independent rings in the triclinic structure.<sup>[12]</sup> By combining neutron ToF and BS spectroscopy in a simultaneous analysis, it becomes possible to reliably separate the overlapping dynamical processes of the two-ring model. The resulting energy

---

barriers are in very good agreement with previous potential energy calculations.<sup>[16]</sup> Moreover the evaluation of the incoherent structure factors allows to confirm the 5-fold geometry of the jump motion.

The monoclinic high temperature phase above 164 K covers the lower left part of Figure 6.9b. While the established conclusion about the equivalent sites 5-fold jump motion of the cyclopentadienyl rings could only be verified for  $T \geq 260$  K, a non-equivalent sites  $2 \times 5$ -fold model was proposed. It takes the dynamical disorder into account by allowing two distinct configurations for a single Cp ring. Although it seems related to the two-ring model used for the triclinic phase, it describes a conceptually different situation. While the two rings in the two-ring model describe physically different Cp rings, the non-equivalent sites  $2 \times 5$ -fold model describes two configurations of the same Cp ring. Compared to the equivalent sites 5- and 10-fold jump rotation model, the non-equivalent sites model gives the most consistent description of the experimental data especially at  $T \leq 230$  K and large momentum transfer. Within this extended model, the activation energy of the 5-fold reorientational jumps is found to be lower than that in the triclinic phase, which is in accordance with the well established literature results.<sup>[15,16,30,34]</sup> The transition rate between states is found to be mostly independent of temperature. This latter observation, however, would need to be substantiated by additional measurements at large momentum transfer and different temperatures. In conclusion, the non-equivalent sites model shows that the dynamics of the Cp rings can be more adequately described by introducing 2 ring configurations twisted by approximately  $30^\circ$  which is in very good agreement with previous diffraction studies and lattice energy calculations, thus underlining and evidencing the dynamical character of disorder in monoclinic ferrocene.

The investigation of the orthorhombic phase, which is the stable one below 242 K to 250 K<sup>[21,22,26]</sup> confirms the significantly increased energy barrier of ring rotation. The result is shown as violet line in Figure 6.9b with the gray box around 250 K indicating the transition range from the stable orthorhombic phase to the monoclinic phase. Unfortunately, the dynamics is too slow to be studied to the same extent as the triclinic phase on present neutron backscattering spectrometers. It becomes detectable just below the phase transition which complicates the reliability of the results. In order to study the dynamics of ring rotation in the orthorhombic phase and verify the 5-fold geometry using the elastic incoherent structure factor, a significantly higher energy resolution would be needed. This could be feasible using incoherent neutron spin-echo spectroscopy, or by future backscattering techniques regarding the planned upgrade on IN16B using prototype GaAs monochromator and analyzers.<sup>[51]</sup> Such experiments could be complementary to deuterium-NMR spin alignment, which is capable of studying dynamics on much slower timescales than neutron spectroscopy.<sup>[61]</sup> Nevertheless, regarding the results obtained for the monoclinic and triclinic phase, the experiments presented in this chapter substantiate, refine and significantly extend the understanding of ring rotation in the crystalline phases of ferrocene.





# 7 Ring rotation dynamics in ferrocenium triiodide – $\text{FcI}_3$

In this chapter, the effect of oxidation on the ring rotation dynamics in the ferrocene molecule will be explored. For this purpose, the ionic compound ferrocenium triiodide ( $\text{FcI}_3$ ), consisting of ferrocenium cations ( $\text{Fc}^+$ ) and triiodide anions ( $\text{I}_3^-$ ) is investigated with neutron spectroscopy. Open questions motivating the experiments are whether the  $\text{FcI}_3$  structure shows phase transitions comparable to Fc, and how the geometry and activation energy of the ring rotation compares to bulk, unoxidized Fc. Aspects to consider in the interpretation will involve differences of the intramolecular rotational potential in neutral Fc and ionized ferrocenium on the one hand, and intermolecular potential barriers in the crystal structure of  $\text{FcI}_3$  on the other hand.

## 7.1 Experimental details

$\text{FcI}_3$  was obtained by stoichiometric mixing of ferrocene (Alfa Aesar, purity 99%) and iodine in dichloromethane and subsequent evaporation of the solvent yielding a black powder. The sample was investigated in multiple experiments using polarized neutron diffraction on D7, time of flight spectroscopy on IN5, and high resolution backscattering spectroscopy on IN16 and IN16B. For a description of the experimental techniques, see [chapter 4](#). On IN16 and IN16B, neutron absorbing cadmium plates were mounted on the crystal analyzers in the regions where coherent Bragg peak scattering was expected in order to restrict the observed intensity to incoherent scattering.

The  $\text{FcI}_3$  powder sample was contained in different aluminum sample cells: Flat  $3 \times 4 \text{ cm}^2$  of circa 0.4 mm thickness holding 757 mg of sample (D7, IN16), and of circa 0.3 mm holding 509 mg of sample (IN5); and hollow cylinders of 22 mm in diameter and 0.6 mm wall thickness holding 875 mg of sample powder (IN16B). A list of all sample temperatures that were investigated is given in [Table 7.1](#).

**Table 7.1:** List of sample temperatures for neutron scattering experiments on  $\text{FcI}_3$  using backscattering spectroscopy (IN16/IN16B), ToF spectroscopy (IN5), and polarized diffraction (D7).

instrument	$T / \text{K}$								
IN16B (FWS <sup>a</sup> )	→								
IN16B	55	65	75						
IN16		60	70		80				
IN5 ( $\lambda_{\text{inc}} = 12 \text{ \AA}$ )				78	92				
IN5 ( $\lambda_{\text{inc}} = 6.3 \text{ \AA}$ )				78	92	120	170	230	290
IN5 ( $\lambda_{\text{inc}} = 3.6 \text{ \AA}$ )						120	170		290
D7	5					100			320

<sup>a</sup> Elastic and inelastic fixed window scans with continuous heating ramp

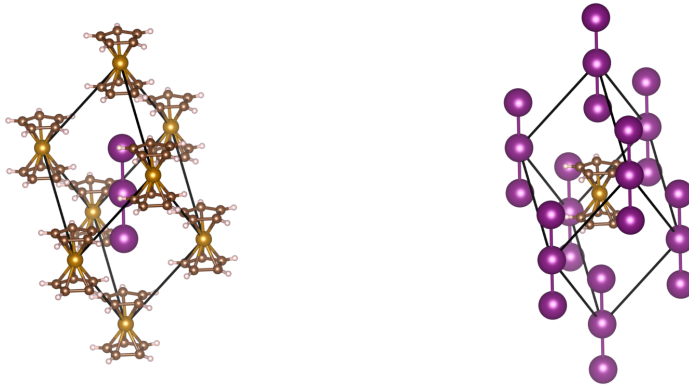


**Figure 7.1:** Sketch of the rhombohedral unit cell of  $\text{FcI}_3$  at 300 K,<sup>[62]</sup> centered on  $\text{I}_3^-$  and  $\text{Fc}^+$  respectively. The rotational orientation around the vertical axis of the rings in the ferrocenium cation was presumed disordered and is drawn here in an arbitrary position. (Image rendered with VESTA<sup>[13]</sup>)

## 7.2 Structure and phase behavior of $\text{FcI}_3$

The first step in the analysis of experimental results obtained for  $\text{FcI}_3$  is concerned with structure and phase behavior of the sample. The structure of  $\text{FcI}_3$  was previously investigated by Bernstein and Herbstein<sup>[62]</sup> and found to be trigonal between 300 K and 130 K from X-ray diffraction experiments, with probable space group  $R\bar{3}m$ . No phase transition was observed within that temperature range, and measurements at lower temperatures have not been performed. The dimensions of the rhombohedral unit cell have been determined at 300 K:  $a_R = 7.517(5)\text{\AA}$  and  $\alpha_R = 69.1(2)^\circ$ . A sketch of the unit cell is shown in Figure 7.1, centered on  $\text{I}_3^-$  and  $\text{Fc}^+$  ions respectively. The rotational orientation of the rings in the ferrocenium cation around the vertical axis could not be determined by the authors and was presumed to be rotationally disordered.

Although the triiodide complex has been reported to be the most stable ferrocenium polyiodide, different crystalline forms of  $\text{FcI}_x$  with  $x$  from 4 to 7.5<sup>[63]</sup> and an even more iodine rich phase of  $\text{Fc}_3\text{I}_{29}$ <sup>[64]</sup> were observed. Under the conditions of sample preparation described in the previous section with a mixing ratio of 1.5 of  $\text{I}_2$  to Fc, the formed compound is expected to be ferrocenium triiodide  $\text{FcI}_3$ . During the diffraction experiment aiming to determine the static structure factor of ferrocene containing polymers (see chapter 8) using polarized neutrons, the coherent structure factors of bulk, crystalline ferrocene and of the sample presumed to be  $\text{FcI}_3$  were determined as well to confirm this assumption. Subsequently, elastic and inelastic fixed window scans using backscattering spectroscopy were performed on  $\text{FcI}_3$  in order to get a first overview of the dynamics and to explore the question whether  $\text{FcI}_3$  shows a phase transition, possibly related to ring rotation, similar to the monoclinic-triclinic transition in Fc. Both these experiments will be presented and discussed in the following.

### Structure verification of the $\text{FcI}_3$ sample

Figure 7.2 shows the resulting static structure factors  $S(Q)$  for  $\text{FcI}_3$  at different temperatures obtained from polarized neutron diffraction as described in section 2.5. For comparison, a measurement on monoclinic Fc is shown in gray. Several Bragg peaks are clearly distinguishable in  $\text{FcI}_3$  and do not seem to show any substantial temperature dependence between 5 K and 320 K. The effect of thermal expansion is visible as a slight shift to lower  $Q$  with increasing temperature. To confirm that the sample compound is  $\text{FcI}_3$  (and not another stable compound of the  $\text{FcI}_x$  family), the unit cell parameters obtained at 300 K by Bernstein and Herbstein<sup>[62]</sup>

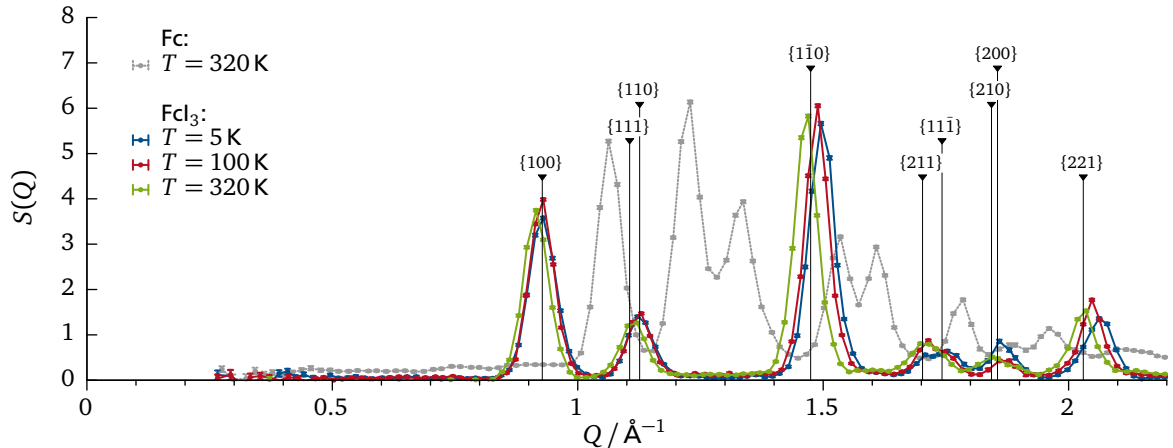


**Figure 7.2:** Static structure factor  $S(Q)$  obtained from polarized neutron diffraction (D7) on  $\text{FCl}_3$  at different temperatures in order to verify the sample structure. For comparison, the indexed positions of reflections of trigonal  $\text{FCl}_3$ <sup>[62]</sup> are indicated by vertical lines, and the structure factor obtained for monoclinic Fc is shown as dashed gray line.

have been used to calculate the position of the first 9 Bragg reflections  $\{hkl\}$ . These positions are indicated by the vertical lines in Figure 7.2 and coincide exactly with the measured peaks at 320 K, confirming that the composition of the investigated compound is indeed  $\text{FCl}_3$ . Moreover, it can be seen that no significant amount of crystalline, unoxidized monoclinic Fc is left in the sample, as this would lead to contribution of Bragg peaks shown as dashed gray line in Figure 7.2 which is not the case.

### Phase behavior of $\text{FCl}_3$

In order to get a fast overview of the dynamics in  $\text{FCl}_3$ , elastic and inelastic fixed window scans were performed on IN16 and IN16B. The result is shown in the middle plot of Figure 7.3 and compared to similar scans for initially triclinic Fc. The thermal activation of ring rotation in Fc leads to continuous decrease of elastically scattered intensity from 100 K to 164 K. In the same temperature range, intensity moving through the inelastic window at  $E = 3 \mu\text{eV}$  can be observed. At 164 K, Fc transforms to the monoclinic phase which is visible as a significant discontinuity in the inelastic scan and a very small step in elastically scattered intensity. This phase transition can also be seen in the low resolution diffractogram which could be recorded simultaneously with an elastic fixed window scan on IN16. The position of the  $\{210\}$  reflex of Fc is shown in top of Figure 7.3, where the step at 164 K marks the phase transition to the monoclinic structure.

The scans on  $\text{FCl}_3$  show a similar behavior with significant decrease of elastic intensity with a simultaneous peak in inelastic intensity, both followed by a small step, but at much lower temperatures than for Fc. The observed onset of the dynamical process is between 40 K and 50 K, and a phase transition takes place at 85 K. The thermodiffractogram recorded simultaneously on IN16 does not offer the possibility to analyze many different Bragg peaks, as it is measured only for  $Q < 1.8 \text{ \AA}$  on high incoherent background for the protonated sample, and two of the peaks unfortunately coincide with small gaps between the detector banks. Nevertheless a clear discontinuity was found in the width  $\Delta Q$  of the  $\{1\bar{1}0\}$  reflex shown in the lower part of Figure 7.3. The discontinuity shows that at 85 K a structural phase transition takes place in  $\text{FCl}_3$ , where the reason for a larger width of the reflex below 85 K could indicate an unresolved splitting of the Bragg peak. To the best of knowledge, this transition has not been documented in existing literature yet.

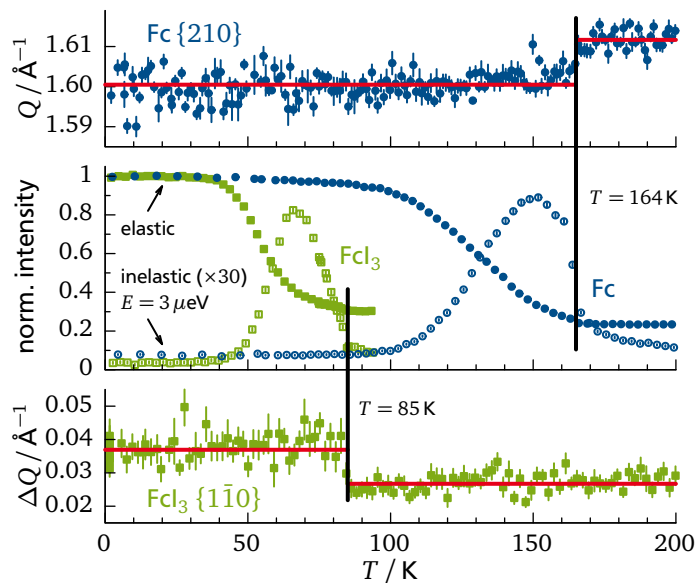


**Figure 7.3:** Comparison of elastic and inelastic fixed window scans on Fc and  $\text{FcI}_3$ . The top and bottom plots show the temperature dependence of the position of the  $\{210\}$  reflex in Fc and the width  $\Delta Q$  of the  $\{1\bar{1}0\}$  reflex of  $\text{FcI}_3$  respectively. Discontinuities corresponding to phase transitions are marked by vertical black lines, the red horizontal lines indicate the average of the data.

As the characteristic correlation time of the rotational motion in  $\text{FcI}_3$  moves through the same observation window at much lower temperatures than in Fc, it can safely be assumed already at this point that the potential energy barrier to ring rotation in  $\text{FcI}_3$  is much lower than in Fc. Another very interesting observation in the comparison of the fixed window scans on Fc and  $\text{FcI}_3$  is that the phase transition takes place after the decrease of elastic intensity, and cuts the peak in inelastic intensity on its decreasing flank in both cases. This means that, although the phase transition takes place at very different temperatures, the respective correlation times of the dynamical processes are roughly comparable near the transition point. This strongly indicates that the transition in  $\text{FcI}_3$  is, as it is the case for Fc,<sup>[20,26,65]</sup> closely related to the ring rotation itself, where the structure adapts for ordered rings at low temperatures and rotational disorder above the phase transition. The presence of rotational disorder at room temperature was already concluded from X-ray diffraction experiments,<sup>[62]</sup> and will be further studied in section 7.3.

The change in crystal structure at the phase transition in  $\text{FcI}_3$  is only subtle, as the static structure factors shown in Figure 7.2 have very similar form as discussed above. It should be noted that the diffraction data from experiments presented here does not enable a full structure refinement. For that purpose, more suitable X-ray or neutron diffraction experiments offering much larger  $Q$ -range and better resolution should be carried out on powder or even single crystal samples. While this aspect is left for future experiments, we will instead focus on the ring rotation dynamics which will be investigated in more detail by inelastic neutron scattering experiments. With the ring rotation being intimately involved in the phase transition, the analysis in the following section is given separately for the high temperature phase above 85 K and the low temperature phase below 85 K.

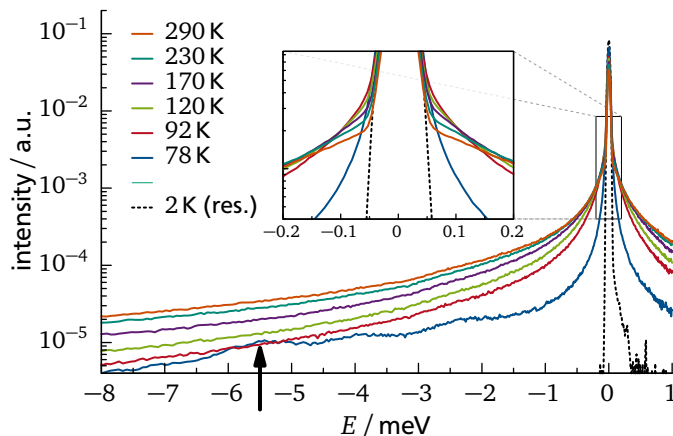


**Figure 7.4:** Inelastic spectra for  $\text{FCl}_3$  at different temperatures measured on IN5 with  $\lambda_{\text{inc}} = 6.3 \text{ \AA}$ . A strong quasielastic broadening can be seen with increasing temperature, as well as three low energy excitations in the spectrum at 78 K.

### 7.3 Results of inelastic scattering experiments

In this section, the results of inelastic neutron spectroscopy experiments on  $\text{FCl}_3$  will be presented. As indicated by the elastic fixed window scan discussed in the previous section, the methods of choice are high resolution backscattering spectroscopy focusing on the phase below 85 K, and time of flight spectroscopy at higher temperatures.

Exemplary energy spectra summed over all detectors from neutron time of flight spectroscopy are shown in Figure 7.4 for different temperatures. Similar to the experiments on Fc in chapter 6, a quasielastic broadening is observed with increasing temperature. The temperatures of 78 K and 92 K are closely above and below the phase transition at 85 K. The dynamics slightly below the phase transition at 78 K can still be resolved with time of flight spectroscopy. It can be seen that the quasielastic contribution broadens significantly when heating above the transition, indicating strong acceleration of the rotation dynamics.

Moreover, in the spectrum recorded at 78 K, three additional inelastic excitations can be distinguished at circa  $-2.4 \text{ meV}$ ,  $-3.9 \text{ meV}$  and  $-5.4 \text{ meV}$ . In Fc, an inelastic excitation around  $-2.5 \text{ meV}$  was interpreted as librational mode<sup>[34]</sup> (see chapter 6). The excitations in  $\text{FCl}_3$  show increasing intensity with  $Q$  and are assumed to be vibrational modes (e.g., librational motion of the rings). The temperature dependence of their intensity should then be monotonically increasing proportional to the Bose-Einstein factor (see section 2.4.1). But these peaks are not distinguishable any more at 92 K, and, more importantly, the peak at  $-5.4 \text{ meV}$  lies at 78 K already above the corresponding spectrum at 92 K (arrow in Figure 7.4). This concludes that the mode corresponding to that peak does either not exist above the phase transition, or it is extremely broadened. This aspect will be further discussed in section 7.4 in context of the results from a more detailed analysis of the quasielastic scattering.

#### 7.3.1 Ring rotation dynamics above 85 K: ToF

As discussed in section 7.2, the rings in  $\text{FCl}_3$  are found to be disordered at room temperature from X-ray diffraction.<sup>[62]</sup> If this is due to a low barrier of rotation such that the dynamics cannot be described by single, well isolated jumps between potential minima, the 5-fold jump model cannot be expected to adequately describe the dynamics. Moreover, the environment of nearest neighbors of the ferrocenium ion in the unit cell, consisting of triiodide ions, has threefold rota-

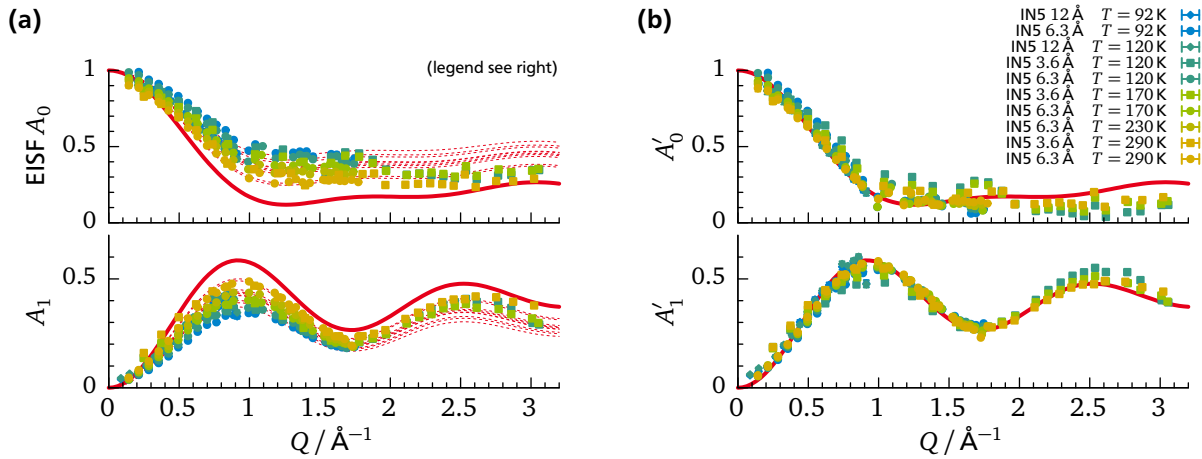


**Figure 7.5:** Structure factor analysis for ring rotation in  $\text{FCl}_3$  in the phase above 85 K assuming a 5-fold jump model. (a) Elastic and quasielastic structure factors  $A_0(Q)$  and  $A_1(Q)$ . Red dashed lines show the rescaled model with an additional constant elastic contribution. (b) Structure factors corrected for constant elastic contribution (see text). Even after rescaling, data and model are not consistent at  $Q > 2 \text{ \AA}^{-1}$ .

tional symmetry around the vertical axis which is at the same time the axis of the ferrocenium ion's fivefold symmetry (see Figure 7.1 right). Consequently, the intramolecular part of the rotational potential for the rings has to be of 15-fold symmetry. Unfortunately, a distinction between 15-fold jumps and continuous uniaxial rotation (i.e., ' $\infty$ -fold') of cyclopentadienyl cannot be made in the  $Q$ -range that was probed in the presented experiments as discussed in section 3.1.

In the following, the dynamics will be analyzed in terms of a 5-fold and 15-fold jump model, keeping in mind that, within this analysis, the 15-fold model is indistinguishable from continuous uniaxial rotation. The analysis is similar to the scheme described in chapter 5, including iterative model refinement with repeated multiple scattering simulations.

### 5-fold jump model above 85 K

Despite the argumentation in the previous paragraph, the first attempt to describe the rotation dynamics in  $\text{FCl}_3$  is made using the equivalent sites 5-fold rotational jump model (see chapter 3). The values of the elastic and quasielastic incoherent structure factors  $A_0$  and  $A_1$  resulting from this analysis of time of flight data taken above 85 K are shown in Figure 7.5a. The obtained values of the EISF lie systematically above the model function (thick red line) for all temperatures. Assuming that only a fraction  $f$  of the incoherent scattering is from rings that reorient according to the model while the remaining fraction  $1 - f$  is fixed (or slowed) and scatters only elastically, the structure factors can be rescaled according to:

$$A_l(Q) = fA'_l(Q) + \begin{cases} 1 - f & \text{if } l = 0 \text{ (elastic),} \\ 0 & \text{otherwise (quasielastic),} \end{cases} \quad (7.1)$$

where  $A'_l(Q)$  are the structure factors of the rotational jump model. Of course, a physical justification for this assumption and the rescaling needs to be given. But at this point, we are only interested in whether values of  $f < 1$  could render the model consistent with the data. Further discussion of this aspect in context of the obtained results will be postponed to section 7.4. The rescaling was done for each data set and temperature, and values of  $f$  were determined to minimize the residuals between data and model. Figure 7.5a shows the rescaled model as dashed red lines. In Figure 7.5b the values of  $A'_l(Q)$  are given, meaning that the data sets are corrected for their respective values of  $f$ . In the latter representation, the data should coincide with the

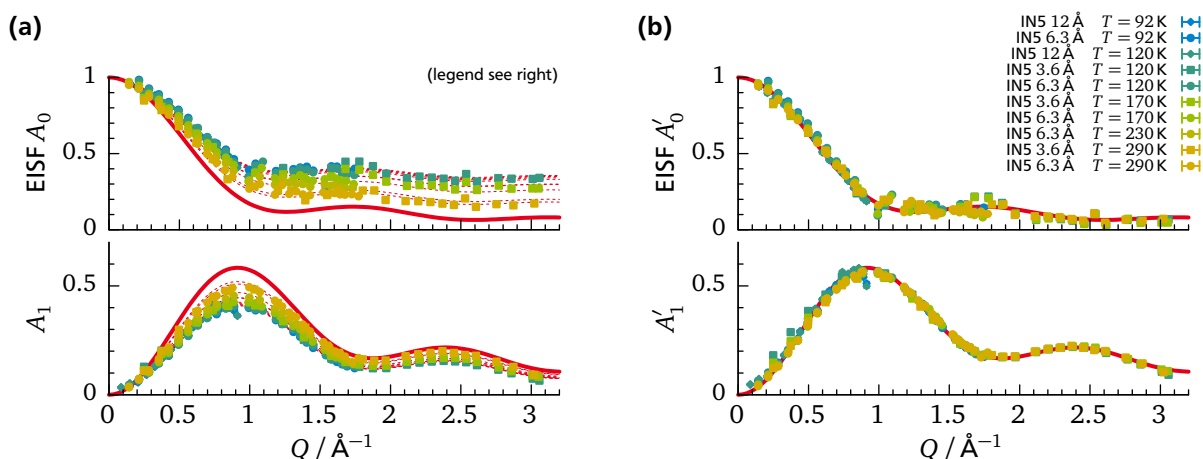


**Figure 7.6:** Similar to Figure 7.5, but assuming a 15-fold jump model (indistinguishable from continuous rotation). After rescaling in (b), data and model are consistent over the entire  $Q$ -range.

uncorrected model function, which is not the case especially at  $Q > 2 \text{ \AA}^{-1}$ . The obtained values of  $f$  are between 0.6 and 0.85 and shown in blue in Figure 7.9a. They are increasing approximately linearly with temperature, but values obtained at the same temperature depend on the used incident wavelength and consequently on the used energy resolution on the IN5 spectrometer. This dependence is also seen in the resulting correlation times  $\tau$  above 85 K which are shown in blue in Figure 7.9b. The 5-fold jump model thus does not give a consistent modeling of the dynamics, even by adding a constant elastic fraction in the structure factors via rescaling of the model with the factor  $f$ .

### 15-fold jump model above 85 K

As discussed above, the intermolecular potential for the cyclopentadienyl rings in  $\text{FeCl}_3$  according to the structure obtained from X-ray diffraction at 300 K is of 15-fold symmetry. The structure factors resulting from the analysis of quasielastic scattering in terms of a 15-fold jump model are shown in Figure 7.6a. Again, the EISF shows more intensity than expected for the jump model only. However, in case of the 15-fold jump model, a rescaling with  $f < 1$  as described in the previous paragraph is able to superimpose model function and data. The rescaled data points in Figure 7.6b show excellent agreement with the model function. Moreover, the values obtained for  $f$  shown in red in Figure 7.9a are more consistent for measurements performed at the same temperature, and so are the correlation times  $\tau$  in Figure 7.9b. An Arrhenius fit of the obtained correlation times results in the parameters given in Table 7.2. The value of the activation energy is as low as  $E_A = 1.65(9) \text{ kJ mol}^{-1}$ , comparable to thermal energy at a temperature of  $E_A/k_B = (198 \pm 10) \text{ K}$ . In light of this low barrier to rotation, it is reasonable that the 15-fold model, which is indistinguishable from continuous rotation in this case, gives a better description of the ring rotation dynamics than the 5-fold jump model in the high temperature phase.

### 7.3.2 Ring rotation dynamics below 85 K: ToF & BS

A reasoning about the symmetry of the rotational potential barrier for the phase below 85 K is complicated by missing information about the crystal structure. In the following, a comparable analysis as for the phase above 85 K will be carried out, using the 5-fold and the 15-fold jump model respectively. Due to the much slower dynamics, neutron backscattering and time of flight spectroscopy will be combined.

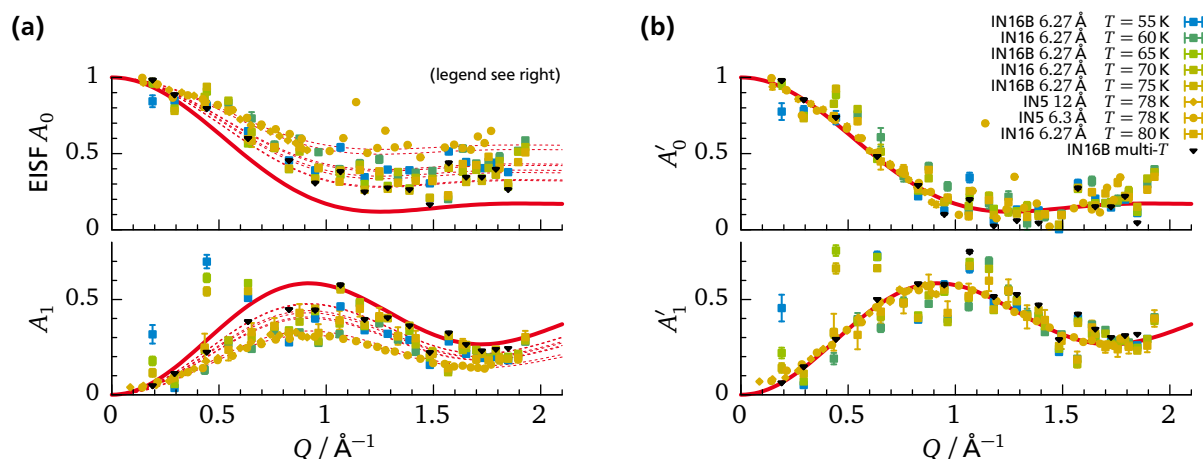


**Figure 7.7:** Similar to Figure 7.5 and Figure 7.6, but for the phase below 85 K assuming a 5-fold jump model. After rescaling in (b), data and model are consistent.

### 5-fold jump model below 85 K

The resulting structure factors from the analysis using the 5-fold model are shown in Figure 7.7a. Measurements have been carried out on the IN16 and IN16B backscattering spectrometer, and on the IN5 time of flight spectrometer at 78 K with two incident wavelengths. On IN16B, elastic and inelastic fixed window scans comparable to those on Fc presented in chapter 6 were evaluated as well. The structure factors resulting from the analysis are shown in Figure 7.7a, where the analysis including all IN16B energy spectra and fixed window scans is shown in black (“multi- $T$ ”). Again, all resulting EISFs lie systematically above the model function, but the rescaling introduced in section 7.3.1 using  $f < 1$  superimposes data and model. The rescaled values  $A'_l(Q)$  are shown in Figure 7.7b. The rescaling amplifies the scatter of data points, which seems to be underestimated by the uncertainty extracted from the refinement process. Single outlying points could have been introduced during normalization of the raw data, when the cadmium screens on the analyzers were not in exactly the same position during normalization and sample measurement. The scatter of results from ToF (IN5) is as expected much lower, and the data points show excellent agreement with the model function.

The values of the scaling factor  $f$  below 85 K are shown in blue in Figure 7.9a. Backscattering experiments result in values of 0.7 to 0.8, while the time of flight experiments give 0.5 to 0.6. The correlation times of the assumed 5-fold jump motion are shown in Figure 7.9b. All values show consistent Arrhenius behavior, except the IN5 6.3 Å measurement leading to a slightly lower value. This could be the effect of insufficient energy resolution, although the linewidth obtained from backscattering experiments is circa  $20 \mu\text{eV}$  which corresponds to half the resolution of  $40 \mu\text{eV}$  and should in principle not hinder its proper extraction. The parameters of a fitted Arrhenius law are given in Table 7.2, where the activation energy of  $E_A = 4.90(1) \text{ kJ mol}^{-1}$  corresponding to  $E_A/k_B = 589(1) \text{ K}$  is circa by a factor of three larger than in the phase above 85 K, and moreover is much larger than the average thermal energy in the low temperature phase.

### 15-fold jump model below 85 K

The analysis of inelastic spectroscopy measurements on  $\text{FCl}_3$  in terms of the 15-fold model below 85 K is short and unambiguous: At 78 K, the EISF resulting from time of flight spectroscopy shown in Figure 7.8 is not in accordance with the model. Due to its increase between  $Q$  values of  $1 \text{ \AA}^{-1}$  and  $1.8 \text{ \AA}^{-1}$ , it can furthermore not be described in terms of the rescaling introduced in section 7.3.1 using  $f < 1$ , as shown by the dashed red lines in the figure. Therefore, the 15-fold or continuous jump rotation model is discarded for the low temperature phase.



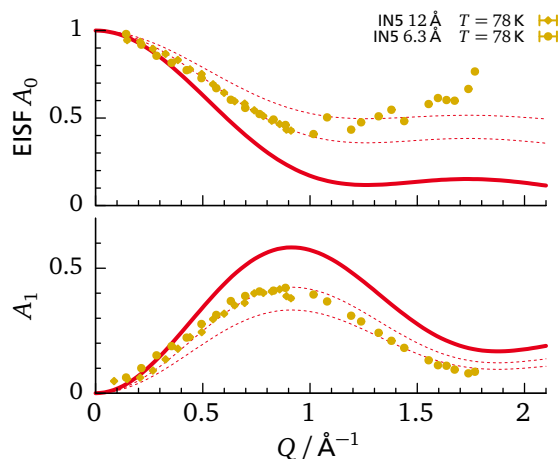


**Figure 7.8:** Structure factor analysis for ring rotation in  $\text{FCl}_3$  in the phase below 85 K assuming a 15-fold jump model. As is obvious, even a rescaling of the model (dashed red lines) cannot superimpose model and data.

## 7.4 Discussion

The results of the inelastic scattering experiments obtained in the previous [section 7.3](#) can be summarized as follows: The ring rotation dynamics above the phase transition at 85 K has a very low activation energy and is closer to continuous rotation than to discrete 5-fold jumps. At the phase transition, the temperature dependence of the correlation time of jump motion is discontinuous. The activation energy below 85 K is circa three times larger than above the transition, and the character of the motion resembles rather 5-fold jumps than continuous rotation or 15-fold jumps. Despite the fact that all models needed to be rescaled by adding a constant elastic fraction, this already shows that the potential energy landscape of ring rotation in  $\text{FCl}_3$  changes dramatically at the phase transition, affecting activation energy and type of the motion.

Another indication of the change in potential was seen in the inelastic spectrum of  $\text{FCl}_3$  shown in [Figure 7.4](#), where three low energy excitations were distinguishable below the phase transition. It is imaginable that, presumed that these excitations are librational motions and the unit cell of  $\text{FCl}_3$  contains independent ferrocenium cations below the phase transition or breaks its inversion symmetry, there could be independent rings with different potentials and thus different librational frequencies. With the lower barrier above the transition and the much higher average thermal energy compared to barrier height, the librational motion is then not distinguishable any more. On the other hand, the observed excitations could also be higher oscillator levels of the same potential, where a strong anharmonicity leads to the overtones at circa 1.6 and 2.2 times the base frequency. However, the detailed interpretation of these inelastic excitations is purely speculative at this point. Their disappearance above the phase transition simply underlines the fundamental changes in the local environment of the rings. The comprehensive evaluation of these excitations would certainly contribute to the understanding of the local ring environment, but for this the exact structure of the low temperature phase should be solved first.

Knowledge of the low temperature structure would also help to interpret the presumed finding of continuous rotation above and 5-fold jump motion below the phase transition. A weakness of the analysis in [section 7.3](#) using the jump rotation models is the necessity to rescale the structure factors by adding a constant, significant fraction  $1 - f$  of elastic scattering. As can be seen from [Figure 7.9a](#), the obtained values are not always consistent. The 15-fold model above 85 K leads to an approximate linear dependence of  $f$  on  $T$ . This behavior does not extrapolate to the phase below 85 K, the values found there are larger for backscattering spectroscopy and

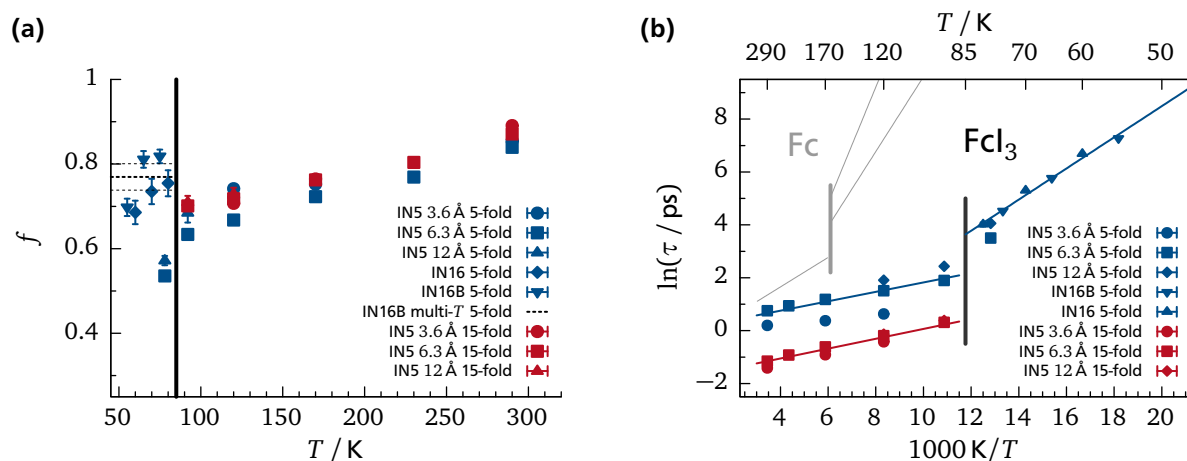


**Figure 7.9:** (a) Scaling factors  $f$  that were applied to jump rotation models to superimpose model and data, corresponding to the addition of a constant elastic fraction  $1 - f$  (see text). (b) Arrhenius plot of the correlation times of jump motion obtained for  $\text{FcI}_3$  using different models. The vertical black line indicates the phase transition at 85 K. For comparison, the Arrhenius laws obtained for monoclinic and triclinic Fc are shown in light gray (see Figure 6.9b on page 60).

smaller for time of flight spectroscopy. There are many conceivable explanations for obtaining values of  $f < 1$ , and some will be discussed in the following: A possible explanation holding below 85 K could be the existence of multiple dynamical processes, in case the low temperature structure contains independent rings. If they have different activation energy, and a part of the dynamics is slower than the corresponding experimental resolution, additional elastic intensity would appear. In this case, the values of  $f$  would be smaller than one and depend on the instrumental energy resolution, which is in agreement with the observations below 85 K.

Above 85 K, the values of  $f$  are consistent for different incident wavelengths and thus energy resolutions, but depend on temperature and are significantly lower than 1. It could very well be that the actual dynamics is more complicated than suggested by the 15-fold or continuous uniaxial rotation model. In fact, the obtained low value of activation energy is close to the intramolecular potential barrier obtained from density functional theory (DFT) calculations on a single ferrocenium ion.<sup>[66]</sup> If we assume that the intramolecular potential is the governing part of the observed ring motion, then both rings of the molecule have to be considered simultaneously in a more complex model. However, this approach and the question whether it could lead to the observed rescaling of the 15-fold/continuous jump rotation model has not been further considered at this point yet.

In general, a comparison of the results obtained here for the ring rotation in  $\text{FcI}_3$  to those obtained for monoclinic/triclinic Fc in chapter 6 and literature cited therein shows many parallels. Similar to Fc, the high temperature phase of  $\text{FcI}_3$  shows rotational disorder of the rings which transforms upon cooling to an ordered state showing presumed 5-fold jump rotation. The barriers of rotation are significantly larger in the respective low temperature phases in both cases. In Figure 7.9b, the Arrhenius laws for the jump rotation obtained for Fc are shown in gray. Upon heating, the phase transition takes place at comparable values of the correlation time  $\tau$ . Due to the lower barrier of rotation in  $\text{FcI}_3$ , this point is reached already at 85 K instead of 164 K as in Fc. The DFT calculations mentioned above<sup>[66]</sup> indicate that, due to one missing, bonding electron in the highest occupied molecular orbital, the ferrocenium ion has an internal barrier to rotation which is by a factor of circa 2 to 4 lower than for the neutral Fc molecule. This factor alone is in principle fully compatible with the ratio of the 5-fold jump barrier in the high temperature phases of Fc and  $\text{FcI}_3$ , which could mean that the disorder ‘averages out’ the intermolecular contribution to the rotational potential. But in order to unravel the type of

**Table 7.2:** Obtained values for activation energy  $E_A$  and prefactor  $\tau_0$  of the Arrhenius law describing the jump motion in different phases of Fc and  $\text{FcI}_3$ .

compound	$T / \text{K}$	crystal system	model	$E_A / \text{kJ mol}^{-1}$	$\tau_0 / 10^{-12} \text{ s}$
$\text{FcI}_3$	> 85	trigonal	15-fold/continuous rot. <sup>a</sup>	1.65(9)	1.0(3)
	< 85	( <i>unknown</i> )	5-fold <sup>a</sup>	4.90(1)	0.0037(1)
ferrocene <sup>b</sup>	>164	monoclinic	non-eq. sites 2×5-fold	4.635(8)	0.562(2)
	<164	triclinic	2-ring 5-fold	18.3(2)	0.23(3)
	<250	orthorhombic	5-fold	11.74(4)	10.9(3)
				24.8(1) <sup>c</sup>	26(3)

<sup>a</sup> rescaled model (see text)    <sup>b</sup> results from chapter 6    <sup>c</sup> obtained from NMR<sup>[30]</sup>

ring motion in the low temperature phases, the intermolecular potential in the different crystal environments would have to be taken into account as is obvious from the significantly increased energy of activation below the transition.

## 7.5 Conclusion

In this chapter, the investigation of ring rotation dynamics in the ionic compound  $\text{FcI}_3$  was presented. An up to now undiscovered phase transition has been found at 85 K which involves crystal structure and ring rotation dynamics of the sample. It appears that the transition shows parallels to the triclinic-monoclinic transition in Fc, with ordered rings below and rotationally disordered rings above the phase transition. The ring rotation dynamics in  $\text{FcI}_3$  has been studied for the first time. It turned out that the favored rotational jump model to describe the ring rotation above 85 K is the 15-fold jump model, which matches the presumed intramolecular potential symmetry, but is effectively indistinguishable from continuous uniaxial rotation in the presented experiments. The assumption of continuous rotation above 85 K is supported by the low activation energy of 1.65(9)  $\text{kJ mol}^{-1}$ . Below 85 K, the observed motion is more consistent with jumps between 5 equilibrium sites and shows a threefold increase in activation energy. In all cases, a small but significant fraction of elastic scattering needed to be added to the model, such that a more complicated type of motion and/or multiple processes cannot be excluded at this point.



## 8 Ring rotation dynamics in poly(vinylferrocene) – PVFc

The study of the ring rotation dynamics in different crystalline phases of bulk ferrocene presented in [chapter 6](#) has shown that the local environment of the molecules plays an important role in the nature of the reorientation process. The influence of oxidation studied on  $\text{FcI}_3$  in [chapter 7](#) supports this fact, as the accelerated jump motion was interpreted as a result of modified intramolecular forces on the one hand and the different crystal structure on the other hand. In this chapter, the ring reorientation in ferrocene will be studied in a non-crystalline local environment, namely the macromolecular structure of poly(vinylferrocene) (PVFc).

The chemical structure of PVFc is shown in [Figure 8.1 a](#), consisting of a linear hydrocarbon backbone with laterally attached ferrocene units on every second carbon atom. The polymer was found to be in a glassy state at room temperature, with relatively high glass transition temperatures in the range of 450 K to 500 K depending on chain length.<sup>[67,68]</sup> Due to the bonding to the immobile chain, it can be expected that at most one ring of the ferrocene molecule is able to perform reorientational jumps. As virtually all incoherent scattering of neutrons on PVFc is due to the large cross section of hydrogen, the fraction  $f = 5/12$  of hydrogen atoms situated in the rotating ring as illustrated in [Figure 8.1 b](#) will need to be accounted for in the analysis of scattering data. The experimental data will show that a quasielastic signal is found for PVFc in a broad dynamic range on backscattering and ToF spectrometers (e.g., data for 140 K in [Figure 8.4](#) on [page 81](#)). This can be explained by dynamic heterogeneities in the amorphous structure of the polymer, and it necessitates to extend the jump rotation model in terms of a distribution of potential energy barriers. This rotation rate distribution model will be presented first, followed by the analysis of neutron scattering data. In contrast to the crystalline samples Fc and  $\text{FcI}_3$  studied in the previous chapters, the static structure factor of PVFc needs to be known beforehand to enable a meaningful data analysis due to coherent scattering. After the static structure factor is determined using polarized neutron diffraction, inelastic neutron spectroscopy data obtained by time of flight and backscattering methods will be presented and analyzed in terms of the rotation rate distribution model, followed by a discussion of the results.

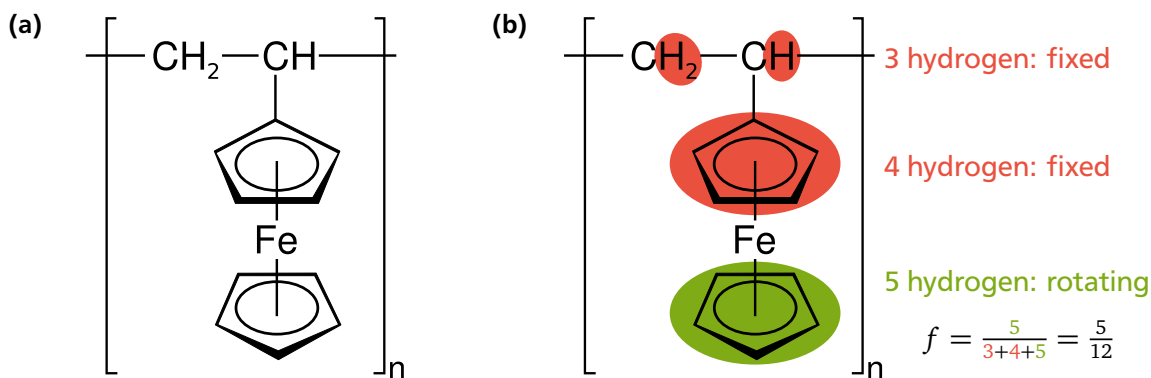


**Figure 8.1:** (a) Chemical structure of poly(vinylferrocene) (PVFc). (b) Derivation of the fraction  $f$  of hydrogen atoms which are part of the lower, free ring while the remaining ones are considered immobilized.

## 8.1 Rotation rate distribution model for PVFc

Quasielastic neutron scattering data on PVFc shows line broadening on different time scales, indicating a broad distribution of relaxation rates. In the amorphous structure of PVFc, the local environment of the rotating ring of each Fc unit can be different, and thus lead to a distribution of energy barriers where the dynamics can then not be described by a single activation energy as in a crystalline environment. This situation is very similar to the rotational reorientation of methyl groups in glassy polymers. Methyl group dynamics have been extensively studied in many polymers with inelastic neutron scattering, as summarized for example in a review article by Colmenero et al.<sup>[69]</sup> A ‘rotation rate distribution model’ (RRDM) was proposed by Cahid et al.,<sup>[70]</sup> assuming a Gaussian distribution of rotational barriers which transforms into a distribution of jump rotation rates, which in turn allows to calculate the dynamic structure factor  $S(Q, \omega)$ . In the analysis in terms of the RRDM, the temperature dependent jump rate is characterized by the Arrhenius law preexponential factor, the average activation energy, and additionally the width of the distribution of activation energies. The model is adapted here to describe the reorientation of the free ring in the Fc units in PVFc. In the following, the RRDM will be presented along the lines of Colmenero et al.<sup>[69]</sup> The full model as discussed by these authors includes the description of quantum mechanical rotational tunneling at very low temperatures, and its transition to ‘classical hopping’ with increasing temperature. We will only adapt the classical part of the description, as quantum tunneling is not observed.

The starting point of the RRDM is the averaging of the incoherent dynamic structure factor of the jump motion with a probability density distribution  $g(E_A)$  of activation energies  $E_A$ :

$$\tilde{S}^{\text{jump}}(Q, \omega) = \int_0^{\infty} dE_A g(E_A) \tilde{S}^{\text{jump}}(Q, \omega, E_A) \quad . \quad (8.1)$$

Here,  $\tilde{S}^{\text{jump}}(Q, \omega)$  on the left hand side is the averaged structure factor that will be used in modeling of the scattering data, whereas  $\tilde{S}^{\text{jump}}(Q, \omega, E_A)$  in the integral on the right hand side is the rotation model as discussed in chapter 3 calculated for a single activation energy  $E_A$ . In first approximation, the distribution  $g(E_A)$  of rotational barriers is assumed to be a Gaussian

$$g(E_A) = \frac{1}{\sqrt{2\pi}\sigma_E} \exp\left[-\frac{(E_A - \langle E_A \rangle)^2}{2\sigma_E^2}\right] \quad (8.2)$$

with mean value  $\langle E_A \rangle$  and width  $\sigma_E$ . From the activation energy  $E_A$  for a specific ring, its jump rate  $\gamma$  is calculated from the well known Arrhenius law

$$\gamma = \gamma_0 \exp\left(-\frac{E_A}{k_B T}\right) \quad . \quad (8.3)$$

The preexponential factor  $\gamma_0$  is assumed to be barrier independent for ‘classical hopping’,<sup>[69]</sup> such that the Gaussian distribution  $g(E_A)$  of activation energies transforms into a lognormal distribution  $H(\log \gamma)$  of jump rates:<sup>1</sup>

$$H(\log \gamma) = \frac{1}{\sqrt{2\pi}\sigma} \exp\left[-\frac{(\log \gamma - \log \tilde{\gamma})^2}{2\sigma^2}\right] \quad (8.4)$$

where

$$\tilde{\gamma} = \gamma_0 \exp\left(-\frac{\langle E_A \rangle}{k_B T}\right) \quad (8.5)$$

<sup>1</sup> The base-10 logarithm is used in  $H(\log \gamma)$  for easier understanding of the following figures.

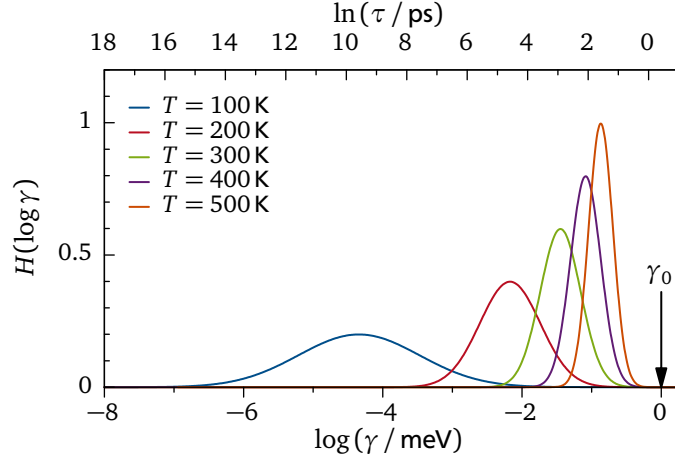


**Figure 8.2:** Exemplary relaxation rate distributions  $H(\log \gamma)$  of the rotation rate distribution model for  $\langle E_A \rangle / k_B = 1000 \text{ K}$ ,  $\sigma_E / k_B = 200 \text{ K}$  and  $\gamma_0 = 1 \text{ meV}$  at different temperatures.

and

$$\sigma = \frac{\sigma_E}{k_B T} \log(e) \quad . \quad (8.6)$$

Note the difference between  $\sigma$  and  $\sigma_E$ : While  $\sigma_E$  is a measure of the temperature independent width of the barrier distribution given in units of energy, the value of  $\sigma$  is temperature dependent and describes the width of the resulting distribution of relaxation rates on logarithmic scale in orders of magnitude. The typical temperature dependence of the distribution  $H(\log \gamma)$  is shown in Figure 8.2 for an arbitrary set of parameters. With increasing temperature, the distribution becomes narrower as a consequence of eq. (8.6) and its maximum  $\tilde{\gamma}$  approaches  $\gamma_0$  according to eq. (8.5).

Now, using the 5-fold jump model introduced in chapter 3, the right hand side of eq. (8.1) can be written explicitly as

$$\tilde{S}^{\text{jump}}(Q, \omega) = A_0(Q) \delta(\omega) + 2 \sum_{l=1}^2 A_l(Q) \int_{-\infty}^{+\infty} d(\log \gamma) H(\log \gamma) \mathcal{L}(\omega, \lambda_l) \quad (8.7)$$

with the  $\gamma$ -dependent halfwidths  $\lambda_l = 2\gamma \sin^2(\pi l/5)$  according to their definition in chapter 3, and the  $\gamma$ -independent structure factors  $A_l(Q)$ . Effectively, the RRDM replaces the Lorentzian functions  $\mathcal{L}(\omega, \lambda_l)$  describing the quasielastic scattering of the 5-fold jump model by averages over Lorentzians of different width, weighted with the lognormal distribution function  $H(\log \gamma)$ . The integral in eq. (8.7) can be evaluated numerically and depends on 3 free parameters only: The average activation energy  $\langle E_A \rangle$ , the width  $\sigma_E$  of the barrier distribution, and the preexponential factor  $\gamma_0$ .

For analysis of scattering data, the RRDM is embedded in a model for the scattering cross section of the PVFc sample as measured in an experiment. In addition to the incoherent scattering from the rotating ring, the incoherent scattering of the remaining hydrogen atoms is considered elastic and isotropic, given that the experiments are carried out far below the supposed glass transition of the polymer where the chain can be expected to be immobilized. The coherent part of the scattering is considered elastic as well, and its  $Q$ -dependence is described by the static

**Table 8.1:** Listing of sample temperatures for neutron spectroscopy experiments on PVFc.

instrument	$T / \text{K}$							
	80	110	140	200	250	300	350	
IN16	80	110	140	200	250	300	350	
IN5 ( $\lambda_{\text{inc}} = 12 \text{ \AA}$ )	80		140					
IN5 ( $\lambda_{\text{inc}} = 6.3 \text{ \AA}$ )	80		140	200	275 <sup>a</sup>	320 <sup>a</sup>	345 <sup>a</sup>	350
IN5 ( $\lambda_{\text{inc}} = 3.6 \text{ \AA}$ )				200				

<sup>a</sup> Measured during heating, the given temperature value is averaged.

structure factor  $S(Q)$ . Moreover, a librational mode and vibrational contributions are taken into account similar to the model functions in [chapter 5](#), such that the full model reads as follows:

$$S^{\text{fit}}(Q, \omega) = s_0 \exp(-2W) \left\{ \sigma_{\text{coh}} S(Q) \delta(\omega) + \sigma_{\text{inc}} \left[ (1-f) \delta(\omega) + f \tilde{S}^{\text{jump}}(Q, \omega) + \tilde{S}^{\text{lib}}(Q, \omega) \times e^{\frac{\hbar\omega}{2k_B T}} + S^{\text{vib}}(Q, \omega) \right] \right\} + \text{bkg} \quad (8.8)$$

where  $s_0$  is a scaling factor, the following exponential term is the Debye Waller factor with  $W = Q^2 u_0^2 T / 6$  according to [eq. \(2.31\)](#),  $\tilde{S}^{\text{lib}}(Q, \omega)$  and  $S^{\text{vib}}(Q, \omega)$  are librational and vibrational contributions as discussed in [chapter 5](#), and the second exponential term is the detailed balance factor. As shown in [Figure 8.1b](#), only a fraction  $f = 5/12$  of all hydrogen atoms is part of the potentially rotating ring. Hence the jump model is scaled down by  $f$  and the remaining fraction  $(1-f)$  is added as additional elastic incoherent scattering. For the sake of simplicity, the convolution with the instrumental resolution function and application of multiple scattering correction factors is not explicitly included in [eq. \(8.8\)](#), but has naturally been performed as described in [chapter 5](#).

For the analysis of the jump rotation in Fc and  $\text{FcI}_3$  in previous chapters, the chosen approach was to use the elastic and quasielastic structure factors  $A_0(Q)$  and  $A_1(Q)$  as free parameters and compare the result to the curves predicted by the model function. In case of PVFc and the RRDM, the broad distribution of relaxation times virtually always leads to narrow, unresolvable quasielastic components in the spectrum that strongly correlate with the elastic part  $A_0(Q)$  due to finite instrumental resolution. Therefore, the approach taken here is to fix all incoherent structure factors  $A_i(Q)$  to the 5-fold jump model, and use experimentally determined values of the static structure factor  $S(Q)$  from polarized neutron diffraction. Under these circumstances, the parameters of the distribution of activation energies can reliably be determined which will be presented in [section 8.3](#).

## 8.2 Experimental details

PVFc was synthesized<sup>2</sup> by anionic polymerization according to procedures described in literature.<sup>[71]</sup> The weight averaged molecular weight of the sample is  $M_w = 20 \text{ kg mol}^{-1}$  corresponding to an average number of 94 repeat units per molecule, with a polydispersity index (PDI) of 1.08. For neutron scattering experiments, 396 mg of the powder sample were filled in

<sup>2</sup> Synthesis of PVFc and its characterization with gel permeation chromatography (GPC) was performed by Johannes Elbert and Markus Gallei (Department of Chemistry, TU Darmstadt), whose collaboration is gratefully acknowledged.



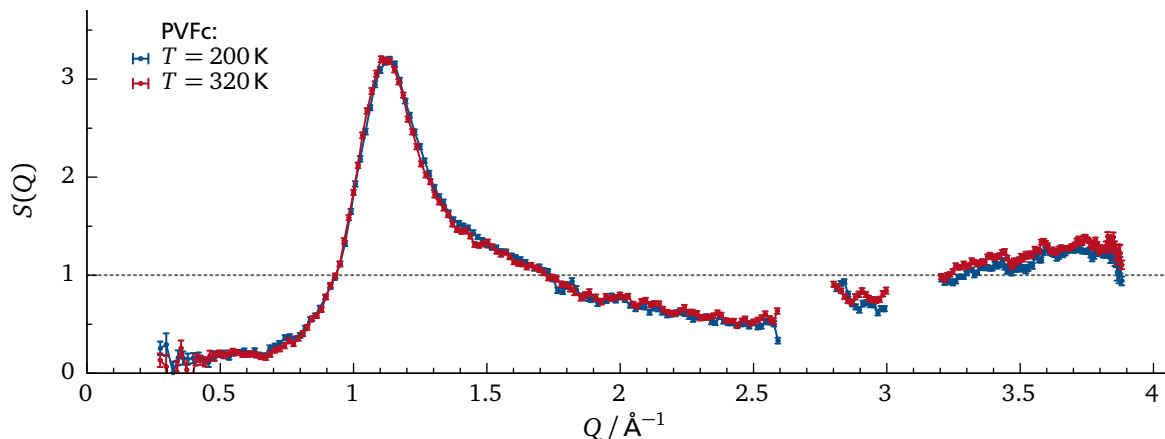


**Figure 8.3:** Static structure factor  $S(Q)$  obtained from polarized neutron diffraction (D7) on PVFc (in absolute units).

$3 \times 4 \text{ cm}^2$  flat standard Al sample holders of 0.5 mm thickness, and the calculated transmission of the sample was circa 90 %. To determine the static structure factor, polarized neutron diffraction was performed on D7 at 200 K and 320 K, while the ring rotation dynamics was studied in the temperature range of 80 K to 350 K with inelastic neutron spectroscopy using time of flight measurements on IN5 and neutron backscattering on IN16. Details about the instruments and techniques can be found in [chapter 4](#). An overview of the temperatures at which inelastic scattering data has been collected is given in [Table 8.1](#).

### 8.3 Results

In inelastic neutron spectroscopy experiments, the line broadening presumed to be caused by jump rotation of the Cp ring was distinguishable in a large dynamic range. Exemplary data sets are shown in an overview in [Figure 8.4](#) for four different temperatures from 80 K to 350 K measured with different instrumental energy resolutions of  $0.8 \mu\text{eV}$ ,  $8 \mu\text{eV}$  and  $40 \mu\text{eV}$ . The fact that a quasielastic signal can be clearly seen on all time scales, e.g., at 140 K, indicates that the barriers to rotation are broadly distributed. In the following, these data will be analyzed in terms of the RRDM introduced in [section 8.1](#). As a prerequisite for this analysis, the static structure factor for PVFc needs to be determined which will be briefly presented first.

#### 8.3.1 Static structure factor of PVFc

For the intended analysis of the ring rotation dynamics in PVFc, the elastic coherent scattering emerging from the polymer structure must be known. In case of the crystalline samples of Fc and  $\text{FcI}_3$  investigated in previous chapters, the elastic coherent scattering was localized in well defined Bragg peaks. This allowed to simply remove certain data points contaminated by Bragg peaks from the obtained elastic structure factor, such that the remaining points represented fully incoherent scattering. Because the structure of PVFc is not crystalline, but nevertheless shows a certain degree of short range order, the coherent scattering is neither fully localized in Bragg peaks, nor isotropic. Using polarized neutron diffraction on D7, the coherent and spin-incoherent parts of the scattering can be separated as discussed in [section 2.5](#), allowing to determine the static structure factor  $S(Q)$  of the polymer.

The resulting shape of  $S(Q)$  at 200 K and 320 K is shown in [Figure 8.3](#). A dominant peak can be seen at  $1.12 \text{ \AA}^{-1}$  followed by broad oscillations towards larger  $Q$ . The two gaps in the curve

around  $3 \text{ \AA}^{-1}$  are due to strong aluminum Bragg peaks caused by the sample holder. In principle, the observed shape of  $S(Q)$  is the result of the superposition of the partial correlation of different atomic species in the sample. Further analysis and interpretation in order to unravel the local, short range order in the polymer is generally feasible, but in itself a complex task. This is shown, for example, in studies of the static structure factor of poly(isoprene) (PI)<sup>[72]</sup> and poly(styrene) (PS)<sup>[73]</sup> using neutron scattering in combination with molecular dynamics simulations.

The strong correlation peak at  $1.12 \text{ \AA}^{-1}$  in PVFc lies between the first two Bragg peaks in monoclinic Fc (see Figure 7.2 on page 65), and corresponds to a length scale of  $2\pi Q^{-1} = 5.6 \text{ \AA}$ . This could be a reasonable average value for the distance between two neighboring Fc units, given that the ring diameter measured on the H-atoms is  $4.66 \text{ \AA}$  and the ring-ring distance is  $3.4 \text{ \AA}$ .<sup>[19]</sup> On the other hand, the structure factors for PS and PI show a comparable shape with a strong peak between  $1.1 \text{ \AA}^{-1}$  to  $1.3 \text{ \AA}^{-1}$  that was attributed to either main chain carbon-carbon correlations in PI<sup>[72]</sup> or carbon-carbon correlations predominantly in phenyl rings of PS.<sup>[73]</sup> This shows that the interpretation of features of the structure factor is not straightforward and can be ambiguous without additional data or simulations. In the following, the experimentally determined shape of  $S(Q)$  will only be used as essential input for the analysis of quasielastic scattering data.

---

### 8.3.2 Ring rotation dynamics

---

The inelastic neutron spectroscopy data from time of flight and backscattering experiments was analyzed in terms of the RRDM described in section 8.1. With the static structure factor  $S(Q)$  as input, eq. (8.8) has only 9 free parameters. The intensity scaling factor  $s_0$  and the constant background are instrument dependent parameters, while the remaining 7 parameters have global, temperature independent character: The temperature proportionality factor  $u_0^2$  in the Debye Waller factor, the average  $\langle E_A \rangle$  and width  $\sigma_E$  of the energy barrier distribution, the Arrhenius preexponential factor  $\gamma_0$ , a scaling factor of the phonon background in  $S^{\text{vib}}(Q, \omega)$ , and position and intensity scaling of the libration peak  $S^{\text{lib}}(Q, \omega)$ . The width of the libration peak was fixed to its low temperature value of  $\Delta\omega_L = 0.45$  at 80 K, as it gets swamped by quasielastic scattering at higher temperatures and cannot be easily separated any more.

In a first step, each data set from Table 8.1 comprising multiple spectra for different  $Q$  measured for one temperature on one instrument was analyzed individually. This does not allow the simultaneous refinement of the Arrhenius law parameters  $\langle E_A \rangle$  and  $\gamma_0$ , and instead the position  $\tilde{\gamma}$  of the maximum of the relaxation rate distribution on the left hand side of eq. (8.5) is used directly. The results are shown in an Arrhenius plot in Figure 8.5 as colored boxes. The circles indicate the position  $\tilde{\tau} = \tilde{\gamma}^{-1}$  of the maximum of the distribution, while the box extends vertically to  $\pm\sigma$  from the former value. In order to sense the reliability of the results, the dynamic ranges of the different instrumental setups are shown as semi-transparent horizontal boxes which lie in the lower part of the figure. They extend from the corresponding value of the instrumental energy resolution half width at half maximum (top end) to the maximum energy transfer (bottom end, only relevant for IN16). The top end of the boxes is drawn smeared out for two reasons: First, the question how far below the resolution a possible line broadening can still be resolved is subject to interpretation and depends moreover on the strength of the elastic contribution. Second, the value of  $\gamma = \tau^{-1}$  in the 5-fold jump model corresponds only approximately to the effective HWHM of the quasielastic part in the spectrum, the latter varies depending on  $Q$  between 0.8 to 1.05 times  $\gamma$ . However, it seems clear that at 80 K the majority of relaxation processes are too slow for either of the instruments. With increasing temperature, the distribution shifts to lower  $\tau$ , crossing the respective dynamic range of each instrument successively. As expected from eq. (8.6), the width of the distribution becomes narrower with increasing temperature. At temperatures above 200 K, the IN5 measurements at  $6.3 \text{ \AA}$  shown

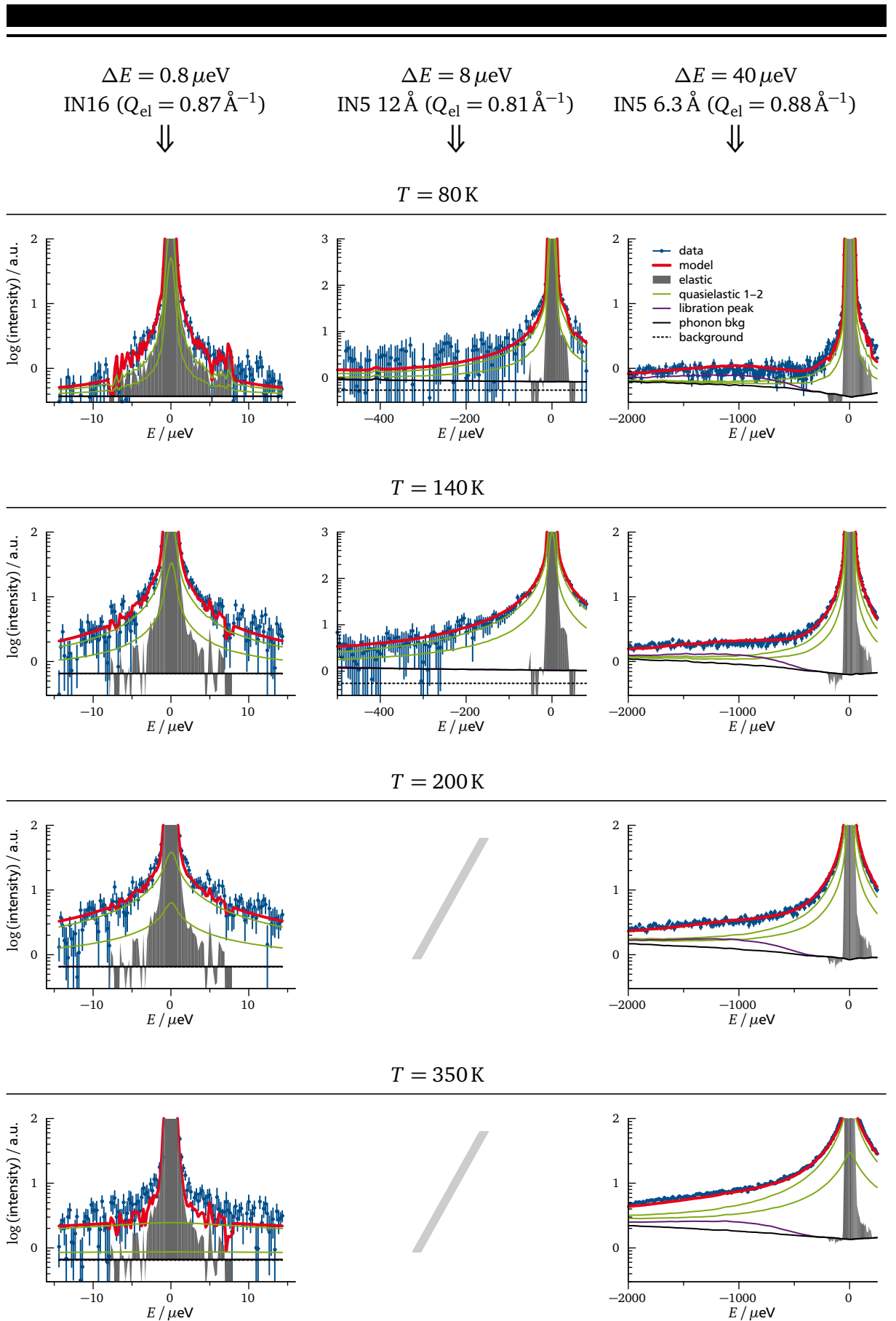


**Figure 8.4:** Inelastic neutron spectroscopy data measured on PVFc at different temperatures with multiple instrumental energy resolutions, together with the ‘multi- $T$ ’ fit of the model function. The shown data is only a small fraction of the 306 spectra analyzed in this procedure.

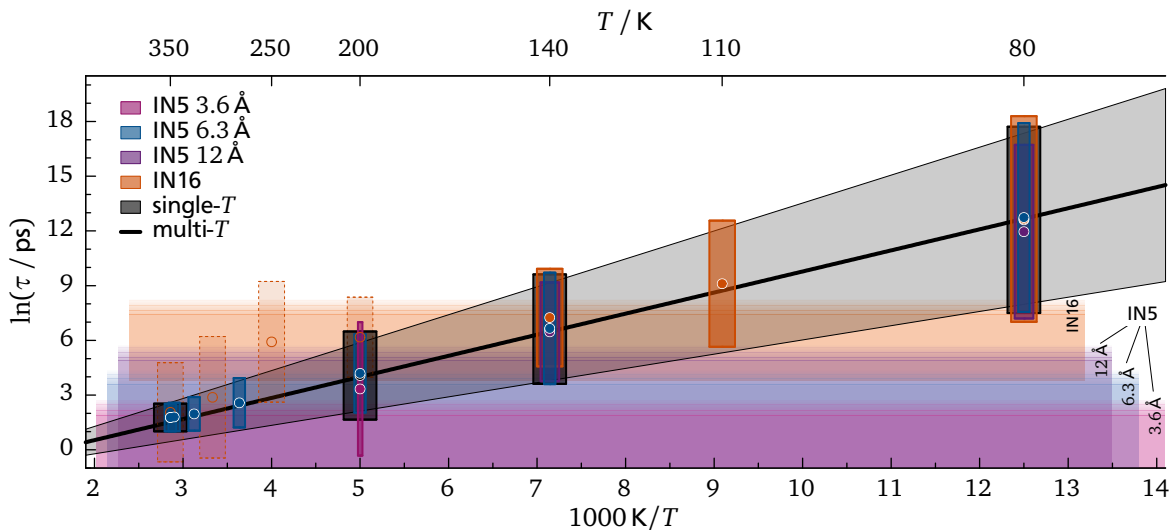


**Figure 8.5:** Arrhenius plot of the rotation rate distributions obtained from inelastic neutron spectroscopy on PVFc. The boxes extend to  $\pm\sigma$  from the mean value of the obtained distributions shown as circles. The horizontal semi-transparent rectangles indicate the dynamic range of the respective spectrometer configurations. The ‘multi- $T$ ’ analysis (thick black line with its surrounding  $\pm\sigma$ -area) assumes temperature independent Arrhenius parameters, while the ‘single- $T$ ’ results are obtained separately for each temperature, but still combining different instruments. The dashed boxes for IN16 above 200 K represent unreliable results due to the accelerated dynamics.

in blue indicate that the relaxation has become faster than the corresponding maximum energy transfer of IN16. The analysis of the respective IN16 measurements thus leads to extremely broadened distributions which reach an arbitrarily set upper bound of  $\sigma_E/k_B = 10^3$  K for this parameter – these results are clearly unreliable and only shown with dashed boxes.

Apart from the IN16 results above 200 K, the results of analyses of individual temperatures are in reasonable agreement with each other and the positions of the distribution maxima consistently follow an Arrhenius behavior. In the next step, multiple measurements taken at the same temperature but on different instruments are analyzed simultaneously to increase the dynamic range and thus the accuracy of the results. This has been done at 80 K, 140 K, 200 K and 350 K and is shown as dark gray boxes in Figure 8.5 (‘single- $T$ ’). Finally, all data sets (except those measured during heating, see Table 8.1) have been analyzed simultaneously by directly using the average energy barrier  $\langle E_A \rangle$  and the preexponential factor  $\gamma_0$  as free parameters. The resulting Arrhenius law is shown in Figure 8.5 as thick black line (‘multi- $T$ ’) with its surrounding  $\pm\sigma$  environment shadowed in light gray. Figure 8.6 shows the relaxation rate distributions for the ‘single- $T$ ’ evaluations (colored lines) and compares them to the idealized Arrhenius result from the ‘multi- $T$ ’ evaluation (black dashed lines). While both methods of evaluation result in virtually identical distributions at lower temperatures, differences are observed at 200 K and especially at 350 K.

The obtained parameter values of the relaxation rate distributions are given in Table 8.2. For some of the model fits like the ‘single- $T$ ’ fit at 80 K parameter uncertainties could not be determined, most probably due to strong correlations caused by the fact that the major part of the relaxation rate lies outside of the dynamic range of the instruments at certain temperatures. It is clear that certain data sets are not suited for being analyzed independently, especially those at 80 K as well as the IN16 data sets taken above 200 K. However, they contribute to the coherence of the results in the global ‘multi- $T$ ’ analysis. The latter results in a rotational

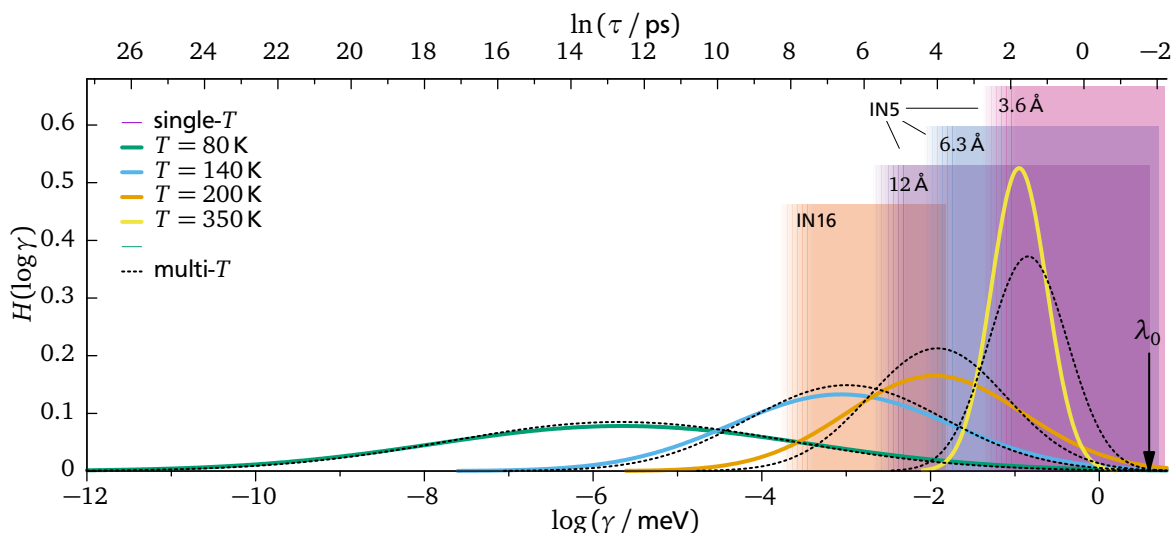


**Figure 8.6:** Temperature dependence of the obtained relaxation rate distribution functions  $H(\log \gamma)$ . Semi-transparent boxes are similar to Figure 8.5. The ‘multi- $T$ ’ analysis (dashed line) assumes temperature independent Arrhenius parameters with preexponential factor  $\gamma_0$  (arrow), while the ‘single- $T$ ’ results are obtained separately for each temperature. The temperatures at which the ‘multi- $T$ ’ distributions are drawn correspond to the ‘single- $T$ ’ analyses.

jump barrier distribution with the average height of  $\langle E_A \rangle = 9.61(2) \text{ kJ mol}^{-1}$ . The width of  $\sigma_E = 3.12(1) \text{ kJ mol}^{-1}$  roughly corresponds to one third of the average.

Within the ‘multi- $T$ ’ evaluation, a large number of 306 spectra has been analyzed simultaneously. Figure 8.4 shows a selection of spectra for different temperatures and instrument configurations, with the best ‘multi- $T$ ’ fit of the model function and its individual contributions. The noise in the model function visible especially at low temperatures on IN16 originates from the convolution with the experimental resolution function. Keeping in mind the large range of analyzed temperatures and time scales, the agreement between model and data is very good. Slight differences are seen, e.g., in IN16 data at 350 K where the quasielastic contribution from the RRDM model is essentially flat, but a narrow component of the line broadening is still distinguishable in the data.

Further differences which are not shown occur in the IN5  $3.6 \text{ \AA}$  measurement at  $Q$  above  $2 \text{ \AA}^{-1}$ , where the phenomenological description of the libration peak fails to describe the shape of the spectra in the low energy inelastic region. The mixing between quasielastic scattering and the librational mode especially at larger  $Q$  most probably also explains the much broader relaxation time distribution obtained for IN5  $3.6 \text{ \AA}$  data at 200 K (see Figure 8.5).

## 8.4 Discussion

First of all, the good coherence of the results as shown in Figure 8.5 and the agreement between model and data in Figure 8.4 over the large temperature and extended dynamic range proves the initial assumption that one ring of each ferrocene unit in PVFc is performing rotational reorientations. Comparing the results obtained for the ring rotation dynamics in PVFc to the results on Fc and  $\text{FcI}_3$  obtained in the previous chapters, the first observation is that the dynamics follows a single uninterrupted Arrhenius behavior in contrast to the phase transitions observed in Fc and  $\text{FcI}_3$ . The continuous behavior is what one would expect in a polymeric system far below the glass transition temperature, where the structure is essentially frozen. The average activation energy in PVFc of  $\langle E_A \rangle = 9.61(2) \text{ kJ mol}^{-1}$  is more than twice as large as the one in monoclinic Fc of  $4.635(8) \text{ kJ mol}^{-1}$ , and below the smaller barrier of  $11.74(4) \text{ kJ mol}^{-1}$  found

**Table 8.2:** Obtained values for the width  $\sigma_E$  and average value  $\langle E_A \rangle$  of the jump barrier distribution in PVFc, and preexponential factor  $\gamma_0$ . The latter two values are only obtained in the ‘multi- $T$ ’ analysis, where the ‘single- $T$ ’ analyses give the average relaxation rate  $\tilde{\gamma}$  instead.

	$T / \text{K}$	$\sigma_E$		$\tilde{\gamma} / \text{meV}$	$\langle E_A \rangle$		$\gamma_0 / \text{meV}$
		$/ k_B \text{K}$	$/ \text{kJ mol}^{-1}$		$/ k_B \text{K}$	$/ \text{kJ mol}^{-1}$	
<b>single-<math>T</math></b>	80	<sup>a</sup> 408	<sup>a</sup> 3.40	<sup>a</sup> 2.2 $\times 10^{-6}$			
	140	420(2)	3.49(2)	$8.78(9) \times 10^{-4}$			
	200	483(3)	4.01(2)	$1.12(1) \times 10^{-2}$			
	350	266(2)	2.21(1)	$1.12(1) \times 10^{-1}$			
<b>multi-<math>T</math></b>	—	375(1)	3.12(1)		1156(2)	9.61(2)	3.91(3)

<sup>a</sup> Parameter uncertainties could not be determined (see text).

in triclinic Fc (see chapter 6). However, considering the width  $\sigma_E = 3.12(1) \text{ kJ mol}^{-1}$ , both the values of monoclinic and triclinic Fc lie well within the distribution of potential energy barriers in PVFc. The amorphous structure of PVFc thus causes local environments leading to different reorientational barriers which extend beyond the differences seen between the monoclinic and triclinic phase of bulk Fc. On the other hand, the barrier height distribution in PVFc does not come even close to the  $26(3) \text{ kJ mol}^{-1}$  in the densely packed structure of orthorhombic Fc.

The obtained average barrier height is moreover within the range of those found for methyl groups in various polymers from circa  $4 \text{ kJ mol}^{-1}$  to above  $16 \text{ kJ mol}^{-1}$ .<sup>[69]</sup> Similarly, the width of the distribution  $\sigma_E$  which amounts to circa one third of the average barrier height in PVFc is comparable to results obtained for methyl group rotation. However, an important difference between methyl group rotation and rotation of the ring in PVFc is the existence of an important intramolecular contribution in the Fc unit. The superposition of inter- and intramolecular potentials is not straightforward, as will be shown in more detail in the following.

### Superposition of phase shifted inter- and intramolecular rotational potentials

The intramolecular potential in ferrocene was found to be of 5-fold sinusoidal shape from DFT calculations.<sup>[66]</sup> In first approximation, we now consider the intermolecular potential to be sine shaped and of 5-fold symmetry as well, corresponding to a first order Fourier series expansion. The total potential energy  $E(\varphi)$  as function of the rotation angle  $\varphi$  of the free ring can then be written as

$$E(\varphi) = \frac{E_{\text{intra}}}{2} \sin(5\varphi) + \frac{E_{\text{inter}}}{2} \sin(5\varphi - \Delta\varphi) \quad (8.9)$$

where  $E_{\text{intra}}$  and  $E_{\text{inter}}$  are the potential barriers due to intra- and intermolecular interactions respectively, and  $\Delta\varphi$  is the relative phase between these two contributions. It is clear that depending on the phase  $\Delta\varphi$  the resulting total barrier can be a ‘constructive’ or ‘destructive’ sum of both contributions. Using basic trigonometric identities, the right side of eq. (8.9) can be rewritten to

$$E(\varphi) = \frac{E_{\text{total}}}{2} \sin(5\varphi - \varphi_0) \quad (8.10)$$

where the value of  $\varphi_0$  is of no further relevance, and the total energy barrier is

$$E_{\text{total}} = \sqrt{E_{\text{intra}}^2 + E_{\text{inter}}^2 + 2 E_{\text{intra}} E_{\text{inter}} \cos \Delta\varphi} \quad (8.11)$$

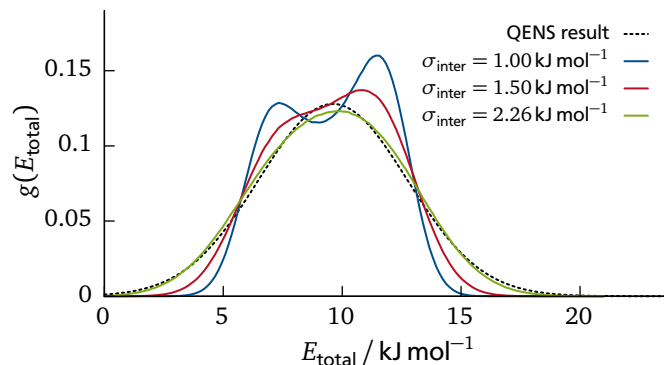


**Figure 8.7:** Hypothetical 5-fold jump barrier distribution functions obtained for a fixed intramolecular contribution of  $E_{\text{intra}} = 3 \text{ kJ mol}^{-1}$  added at random phase to a distributed intermolecular contribution around  $\langle E_{\text{inter}} \rangle = 9.3 \text{ kJ mol}^{-1}$  with different widths  $\sigma_{\text{inter}}$ . The obtained QENS result can be reproduced, but non-Gaussian distributions are readily generated as well.

In order to evaluate the shape of the resulting distribution, the intramolecular part is roughly estimated to  $E_{\text{intra}} = 3 \text{ kJ mol}^{-1}$ ,<sup>[66]</sup> and a uniform distribution of the relative phase  $\Delta\varphi$  has been assumed. Figure 8.7 shows numerically calculated distributions of  $E_{\text{total}}$  resulting from a Gaussian distribution of  $E_{\text{inter}}$  and a constant intramolecular part  $E_{\text{intra}}$ . The best agreement with the experimental result is found for  $\langle E_{\text{inter}} \rangle = 9.3 \text{ kJ mol}^{-1}$  and  $\sigma_{\text{inter}} = 2.26 \text{ kJ mol}^{-1}$ . Thus, it seems like the measured average barrier of  $\langle E_A \rangle = 9.61(2) \text{ kJ mol}^{-1}$  could correspond nearly entirely to the average height of the intermolecular part. Superposition with the constant intramolecular part at random phase could then increase the width of the distribution of intermolecular barriers to the measured value of  $\sigma_E = 3.12(1) \text{ kJ mol}^{-1}$ . On the other hand, Figure 8.7 also shows that the distribution can significantly change its shape for different values of  $\sigma_{\text{inter}}$ , and it can be seen that smaller widths could readily lead to a bimodal distribution of the total energy barrier.

Although this short calculation shows on the one hand that the observed energy barrier distribution can be reproduced under reasonable assumptions, it also demonstrates that the first ansatz of a Gaussian barrier distribution in the RRDM for PVFc may need to be reevaluated. For further conclusions on that matter, the local environment of the rings would need to be investigated in more detail, e.g., by molecular dynamics simulations. The sinusoidal shape of the intermolecular potential and the assumption of uniformly distributed relative phases could then be adjusted, which would allow verification of the assumed 5-fold motion on the one hand and potentially introduce a non-Gaussian distribution of the total energy barrier. While this is not a trivial endeavor, these details could be a possible explanation for the small differences that remain in the otherwise coherent agreement between model and data within the analysis presented above.

---

## 8.5 Conclusion

---

This chapter focused on the ferrocene ring rotation dynamics in the glassy polymer PVFc, where the ferrocene units are laterally attached to a polymer chain. There are two main consequences for the ring rotation dynamics: First, only one ring per ferrocene unit is undergoing rotational reorientation, as the other one is covalently bound to the polymer backbone. Second, it was shown that the amorphous structure leads to a broad distribution of potential energy barriers of the reorientational jumps. Accounting for both these points, incoherent neutron scattering data could successfully be described in terms of the rotation rate distribution model with only few parameters across the large temperature range from 80 K to 350 K, combining neutron

---

backscattering and time of flight methods to access the dynamic range from sub- $\mu\text{eV}$  to a few meV. The obtained distribution of energy barriers to reorientational jumps lead to an average of  $\langle E_A \rangle = 9.61(2) \text{ kJ mol}^{-1}$  with a width of circa one third of this value. The distribution extends beyond the different barriers that were found for monoclinic and triclinic Fc. Further discussion of the jump barrier distribution resulting from the superposition of intra- and intermolecular contributions showed that the initial assumption of a Gaussian distribution may need to be refined. This could be achieved, e.g., by molecular dynamics simulations in order to explore the local environment of the rotating ring in the glassy polymer structure. Nevertheless, the analysis presented here has already shown a consistent and reliable description of the ring rotation, underlining its dynamic heterogeneity in PVFc.



## 9 Vibrational spectroscopy

In the previous chapters, the focus was on the comparatively slow dynamics of ring reorientation in the ferrocene molecule, and the effect of oxidation and incorporation into a polymer structure on that process. Another possibility of studying the consequences of the changes in local environment of the molecule is probing dynamics on a faster time scale, resolving vibrational modes of the molecule. The oxidation which leads to a change in the electronic structure of the molecule as well as bonding of the molecule to a polymer chain can be expected to significantly influence its vibrational spectrum. Vibrational spectroscopy can be performed with light (Raman), infrared radiation (IR), or neutrons. Both former techniques provide a comparably good energy resolution, but are sensitive only to vibrational modes which fulfill certain selection rules accounting for the interaction with electric dipoles. Neutrons on the other hand interact directly with the nuclei and are not subject to any selection rules, probing the entire vibrational spectrum of the sample. In this chapter, neutron vibrational spectroscopy will be presented for all samples in the previous chapters, namely bulk ferrocene,  $\text{FcI}_3$ , and PVFc. Moreover, an oxidized version of the redox-active PVFc, referred to as  $\text{PVFcI}_x$ , will be studied, as well as ferrocene containing polymers which contain ferrocene as part of the polymer backbone. These polymers are shown in Figure 9.1. In order to be able to separate scattering from methyl groups in poly(ferrocenyldimethylsilane) shown in Figure 9.1 b, a modified version of the polymer with one methyl group substituted with a hydrogen (Figure 9.1 c) has been included into the study. After a short description of the experimental details, the vibrational spectra on all samples will be discussed.

### 9.1 Experimental section

The samples of ferrocene,  $\text{FcI}_3$  and PVFc were identical to those used in previous chapters. PFDMS<sup>[74]</sup> ( $16 \text{ kg mol}^{-1}$  and  $88 \text{ kg mol}^{-1}$ ) and PFMS<sup>[75]</sup> ( $28 \text{ kg mol}^{-1}$ ) were synthesized by anionic polymerization according to procedures described in literature.<sup>1</sup> In order to obtain

<sup>1</sup> Synthesis of PFDMS and PFMS and their characterization using GPC was performed by Johannes Elbert and Markus Gallei (Department of Chemistry, TU Darmstadt), whose collaboration is gratefully acknowledged.

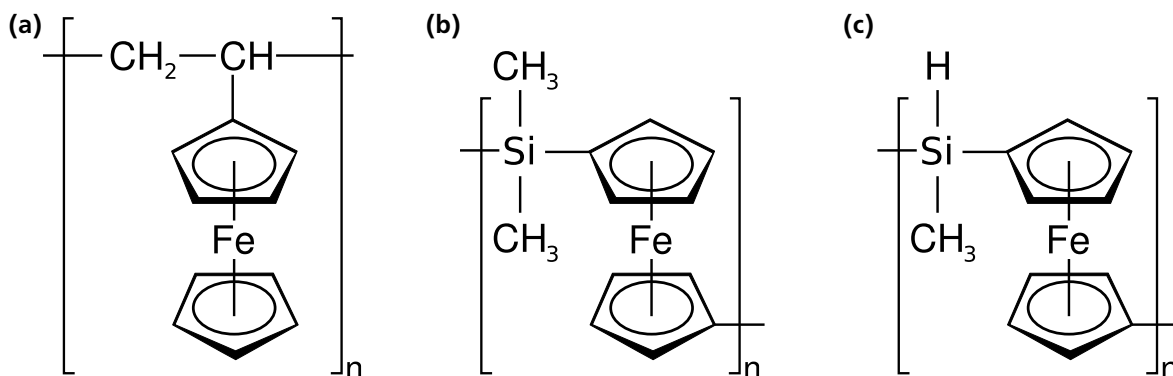


**Figure 9.1:** Chemical structure of ferrocene-containing polymers investigated in this chapter: (a) poly(vinylferrocene) (PVFc), (b) poly(ferrocenyldimethylsilane) (PFDMS), and (c) poly(ferrocenylmethylsilane) (PFMS).

oxidized PVFc, iodine was added to a solution of PVFc in THF. After 1 h, diethyl ether was added to precipitate the oxidized polymer. 250 mg oxidized PVFc is obtained after washing with diethyl ether and drying in vacuo. As the distribution and character of the iodine counterions (e.g.,  $I^-$  or  $I_3^-$ ) was not investigated further, the oxidized compound is referred to as  $PVFcI_x$ .

Vibrational spectra were recorded on the hot neutron spectrometer IN1-Lagrange described in chapter 4. For the neutron scattering experiments the powder samples of  $FcI_3$  and  $PVFcI_x$  were packed in aluminum foil and rolled into a hollow cylinder of circa 15 mm diameter. The remaining samples (Fc, PVFc, PFDMS16, PFDMS88, PFMS) were loaded in  $3 \times 4 \text{ cm}^2$  flat aluminum containers of 0.3 mm to 0.5 mm thickness. All experiments were performed at a sample temperature of  $T = 10 \text{ K}$  controlled by a standard closed-cycle He cryostat.

For primary data reduction, scattering from the empty cell is subtracted, and the recorded intensity is normalized and corrected for energy dependent monitor efficiency. Subsequently, correction factors from a water sample measurement are applied to compensate for a minor dependency of the monitor flux on the monochromator take-off angle. The resulting intensity is proportional to the dynamic structure factor  $S(Q, \omega)$  of the sample, where the magnitude of the scattering vector  $Q$  depends on  $\omega$  and the scattering angle  $2\vartheta$  which is sampled over the whole  $2\vartheta$ -range covered by the analyzer. Finally, from the relationship in eq. (2.33) the density of states is calculated and will be discussed further in this chapter. It should be noted that the density of states discussed here is the so-called generalized density of states, which contains the sum of vibrational modes for all atomic species in the sample weighted by the ratio of scattering cross section to atomic mass. Therefore, the symbol  $G(\omega)$  is used in contrast to  $Z(\omega)$  in section 2.4.1. According to common practice in vibrational spectroscopy, the spectra will be presented as a function of wavenumber  $\tilde{\nu}$  given in  $\text{cm}^{-1}$ , where

$$E = \hbar\omega = hc\tilde{\nu}$$

with Planck's constant  $h = 2\pi\hbar$  and speed of light  $c$ . An energy of 1 meV thus corresponds to  $8.1 \text{ cm}^{-1}$ .

---

## 9.2 Results & Discussion

---

In the following, the vibrational spectra collected in this study will be presented. We start with a comparison of bulk Fc in its triclinic crystalline phase and various ferrocene-containing polymers. Subsequently, we will turn to the effect of oxidation and discuss the oxidized compounds  $FcI_3$  and  $PVFcI_x$ .

### Ferrocene and ferrocene-containing polymers

The vibrational spectra of triclinic Fc and different ferrocene-containing polymers is shown in Figure 9.2. Vertical lines correspond to maxima in the Fc spectrum for easier comparison. The spectrum for Fc (shown in the bottom part of figure 9.2) exhibits collective lattice modes in the low energy range up to  $100 \text{ cm}^{-1}$  as well as local molecular excitations at higher frequencies. It compares well to previous INS measurements published by Kemner et al.,<sup>[76]</sup> where a detailed discussion, assignment and visualization of the individual modes is given. The sketch below the graph in Figure 9.2 indicates the displacements associated with the modes between  $180 \text{ cm}^{-1}$  and  $595 \text{ cm}^{-1}$ . The broadened, intense peak structure at higher frequencies between  $800 \text{ cm}^{-1}$  and  $1100 \text{ cm}^{-1}$  is caused by several modes involving internal distortions of the Cp rings and has been analyzed in more detail by Kemner et al.

Compared to crystalline ferrocene, the spectrum of amorphous PVFc in the middle part of Figure 9.2 shows less detail as expected. However, for this polymer, one would expect the

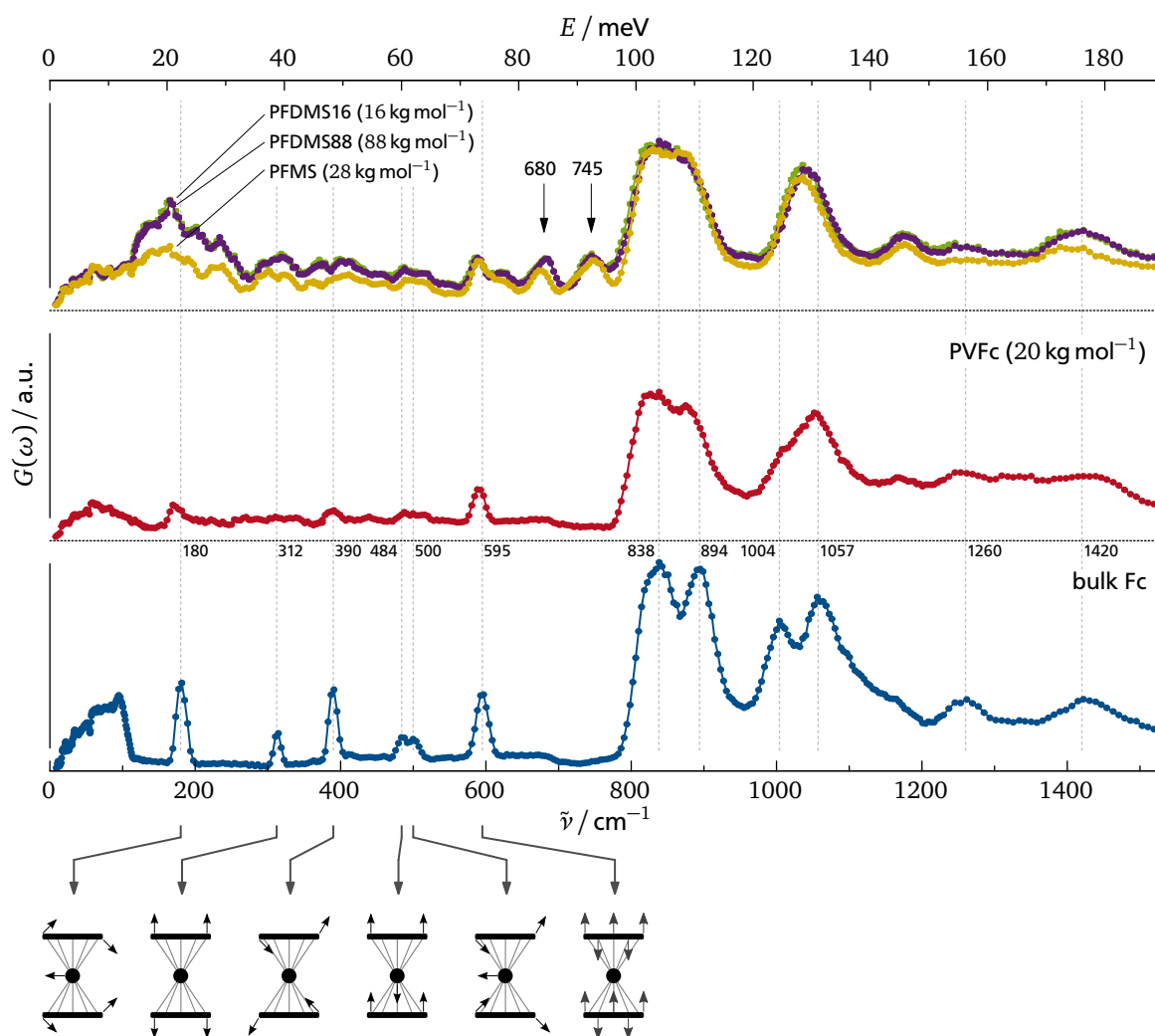


**Figure 9.2:** Experimental generalized density of states  $G(\omega)$  for triclinic ferrocene (Fc), poly(vinylferrocene) (PVFc), poly(ferrocenyldimethylsilane) (PFDMS) with two molecular weights, and poly(ferrocenylmethylsilane) (PFMS). All spectra were recorded at  $T = 10$  K. Vertical lines show characteristic maxima of the Fc spectrum for easier comparison ( $\tilde{\nu}$  given in cm<sup>-1</sup>). The sketch below the graph indicates the type of distortion associated with some fingerprint modes of the ferrocene molecule.

vibrational spectrum to bear the most resemblance to bulk Fc as the ferrocene moieties are attached only laterally as side chain by a single C—C bond. Indeed the modes at 390 cm<sup>-1</sup>, 484 cm<sup>-1</sup>, 500 cm<sup>-1</sup> and 595 cm<sup>-1</sup> are clearly distinguishable in the spectrum of PVFc, and only the mode at 500 cm<sup>-1</sup> shows a slight shift to higher frequencies and the mode 595 cm<sup>-1</sup> a slight shift to lower frequencies with respect to bulk Fc. The mode at 180 cm<sup>-1</sup> corresponding to ring-metal-ring bending with antisymmetric ring tilt is also slightly shifted to lower frequencies and broadened in PVFc. The superposition of multiple modes mostly involving ring distortion and C—H bending leading to the 4 broad peaks between 800 cm<sup>-1</sup> and 1100 cm<sup>-1</sup> appear even more smeared in PVFc, but not shifted.

Interestingly, the mode at 312 cm<sup>-1</sup> is not easily visible in the spectrum of PVFc. This mode corresponds to ring-metal-ring stretching involving the collective oscillation of both Cp rings towards the metal, which is here found to be significantly influenced when the Fc moiety is attached to the polymer chain in PVFc. One could speculate that this mode is, due to its large

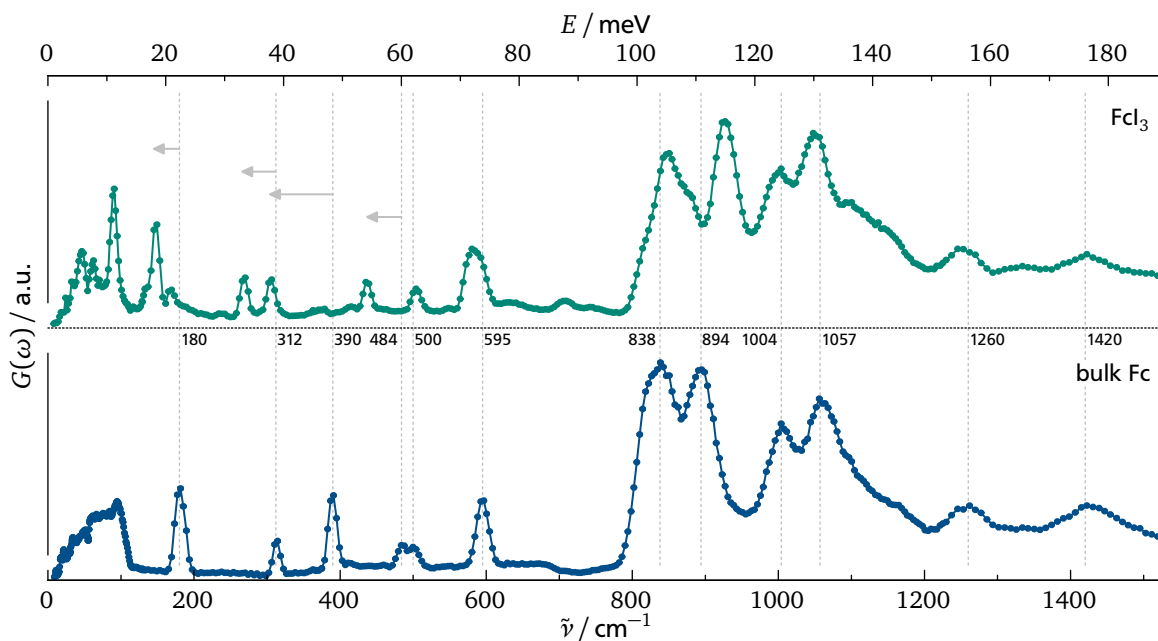


**Figure 9.3:** Experimental generalized density of states  $G(\omega)$  for triclinic ferrocene (Fc), and ferrocenium triiodide ( $\text{FcI}_3$ ). All spectra were recorded at  $T = 10$  K. Vertical lines show characteristic maxima of the Fc spectrum for easier comparison ( $\tilde{\nu}$  given in  $\text{cm}^{-1}$ ).

collective displacement, particularly sensitive to the local environment and extremely broadened in the amorphous polymer.

We now come to the polymers PFDMS and PFMS where the ferrocene complex is part of the polymer backbone itself (see Figure 9.1). Their vibrational spectra are shown in top part of Figure 9.2 and are scaled in intensity to overlap in the low frequency range  $\tilde{\nu} < 100 \text{ cm}^{-1}$  and around the broad peak at  $800 \text{ cm}^{-1}$  to  $900 \text{ cm}^{-1}$ . For PFDMS, two molecular weights of  $16 \text{ kg mol}^{-1}$  and  $88 \text{ kg mol}^{-1}$  were investigated. Assuming that the latter broad peak is governed by internal modes of the ferrocene complex, this corresponds to a normalization to the number of monomer units. In this representation, it is obvious that the spectra of PFDMS16 and PFDMS88 are identical and independent of the molecular weight. The spectrum of PFMS differs mostly in the range from  $100 \text{ cm}^{-1}$  to  $300 \text{ cm}^{-1}$  where the broad peak structure is less intense, but of similar shape.

As the only difference in the chemical structure of PFMS and PFDMS is the number of methyl groups per monomer, this supports the conclusion that the torsional mode of the methyl groups contributes in this frequency region. A comparison<sup>[77,78]</sup> with poly(dimethylsiloxane) (PDMS)<sup>[77,78]</sup> shows that the mode around  $140 \text{ cm}^{-1}$  might be ascribed to the methyl group torsional mode, followed by the  $180 \text{ cm}^{-1}$  ring-metal-ring bending mode of ferrocene which is shifted to lower frequency.

Moreover, the spectrum of PDMS as discussed by Jayes et al.<sup>[77]</sup> helps to assign the newly appearing peaks at  $680$  and  $745 \text{ cm}^{-1}$  (arrows in the top part of Figure 9.2) in PFDMS and PFMS to  $\text{CH}_3$  rocking modes. However, one may expect a decreased intensity of these modes in PFMS due to the reduced number of methyl groups which is not the case for the right peak at  $745 \text{ cm}^{-1}$ .

Concerning the characteristic modes of the ferrocene complex, one finds for PFDMS and PFMS instead of a single ring-metal-ring stretching mode at  $312 \text{ cm}^{-1}$  a symmetrically split double peak – the same holds for symmetric ring tilt at  $390 \text{ cm}^{-1}$ . We can imagine that the breaking of the rotational symmetry of the Fc complex caused by inclusion in the polymer backbone leads to a splitting of the vibrational modes.

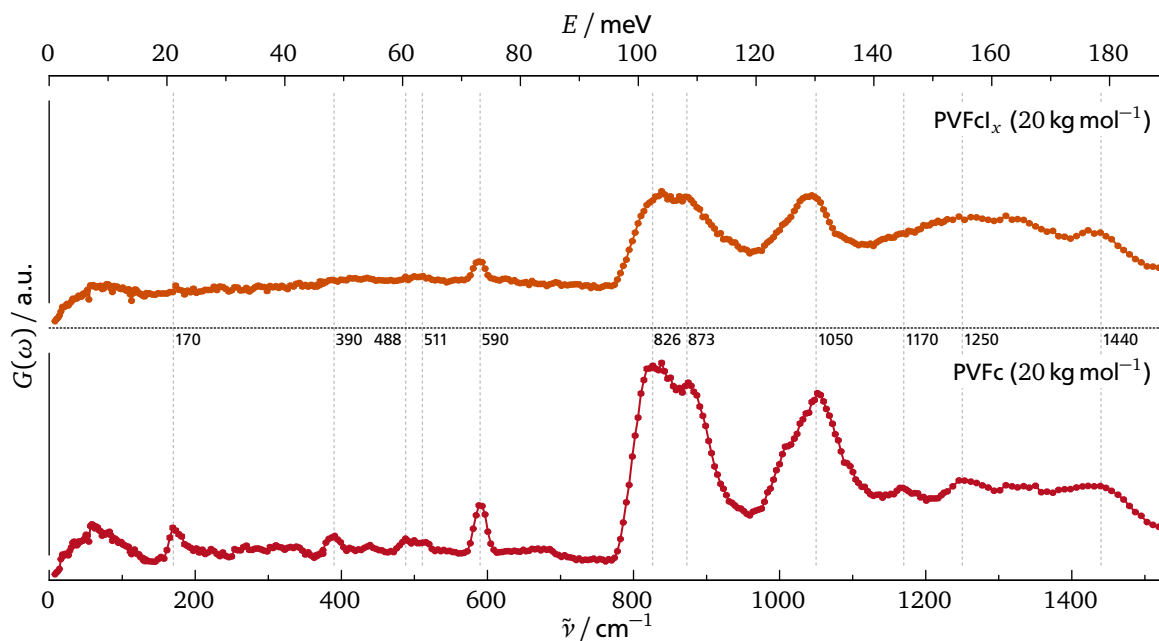


**Figure 9.4:** Experimental generalized density of states  $G(\omega)$  for poly(vinylferrocene) (PVFc), and poly(vinylferrocene) oxidized with iodine (PVFCl<sub>x</sub>). All spectra were recorded at  $T = 10$  K. Vertical lines show characteristic maxima of the PVFc spectrum for easier comparison ( $\tilde{\nu}$  given in  $\text{cm}^{-1}$ ).

At higher frequencies, the two peaks at  $1004\text{ cm}^{-1}$  and  $1057\text{ cm}^{-1}$  in bulk Fc merge to a single peak in PFDMS and PFMS. They correspond to C—H bending modes in the Cp ring plane which are expected to be strongly modified when the ferrocene molecule is bound as part of a polymer chain.

### Oxidized compounds

In addition to ferrocene and ferrocene-containing polymers, the oxidized compounds FcI<sub>3</sub> and PVFCl<sub>x</sub> were studied in order to investigate the influence of oxidation on the ferrocene complex. Figure 9.3 shows the comparison of bulk Fc with FcI<sub>3</sub>. Both substances are in a crystalline phase. The low energy part of the spectrum below  $100\text{ cm}^{-1}$  shows several sharp peaks for FcI<sub>3</sub>. One can speculate that this peak structure is caused by optical phonon branches corresponding to low energy out-of-phase vibrations of the Fc<sup>+</sup> and I<sub>3</sub><sup>-</sup> molecules. The first distinguishable peak around  $45\text{ cm}^{-1}$  was already observed in ToF spectroscopy in chapter 7, and subject to speculation whether it could be interpreted as librational mode. The remaining modes between  $180\text{ cm}^{-1}$  and  $484\text{ cm}^{-1}$  differ significantly in FcI<sub>3</sub> with respect to Fc. It is consistent with the expectation that the weakening of the ferrocenium ion by a missing electron leads to a shift to lower frequencies for internal modes involving the  $\eta^5$ -complex bond. The grey arrows in the figure give a possible assignment of the modes undergoing a shift. Modes at higher frequencies involving deformation of the Cp rings show less differences, with the exception of the peak at  $894\text{ cm}^{-1}$ . A more detailed study and phonon calculations of FcI<sub>3</sub> could certainly help in giving the correct assignment and interpretation of the influence of oxidation on the vibrational spectrum of ferrocene, but has not been performed in the context of this work.

In contrast to Fc and FcI<sub>3</sub>, the comparison of the ferrocene-containing polymer PVFc and its iodine oxidized compound PVFCl<sub>x</sub> shown in Figure 9.4 exhibits significantly less detail. For the oxidized polymer, the background is much higher and aside from the broad ring deformation modes above  $800\text{ cm}^{-1}$  which are left mostly uninfluenced by the oxidation, only the out of plane ring deformation mode at  $590\text{ cm}^{-1}$  is distinguishable in the spectrum of PVFCl<sub>x</sub>. This

---

mode is, as in the case of  $\text{FcI}_3$ , not shifted with respect to the unoxidized compound. The peak at  $170\text{ cm}^{-1}$  corresponding to ring-metal-ring bending with antisymmetric ring tilt is not distinguishable in the spectrum of  $\text{PVFcI}_x$  anymore. The comparison of Fc and  $\text{FcI}_3$  has already shown that this mode is significantly shifted to lower frequencies and is thus probably not separable from the low energy excitations.

---

### 9.3 Conclusion

---

Inelastic neutron spectroscopy was used to investigate the vibrational spectrum of the ferrocene complex in different redox-responsive ferrocene-containing polymers. When the ferrocene moiety is attached as a side group as in PVFc, significant broadening of the ring-metal-ring bending with antisymmetric ring tilt is found, and no sign of the ring-metal-ring stretching mode. With these exceptions, no shift of the vibrational fingerprint modes in the range from  $100\text{ cm}^{-1}$  to  $800\text{ cm}^{-1}$  was detected. In contrast to this, a more dramatic influence on the vibrational modes was observed when the ferrocene is part of the polymer backbone as in PFDMS. The interpretation of these data is complicated by significant contributions from methyl groups in the polymer. However, the study of PFMS and comparison to previous results for PDMS helped in identifying methyl group torsion contributions. In case of oxidation of the ferrocene complex, the weakening of the coordination bond in  $\text{FcI}_3$  leads to a significant shift of multiple fingerprint modes to lower frequencies. These observations could be substantiated by future DFT studies, which would also allow an unambiguous assignment of the vibrational modes.

---

# 10 Neutron spectroscopy under external magnetic fields

In this chapter, the results of inelastic neutron scattering experiments on oxidized poly(vinylferrocene) (PVFCl<sub>x</sub>) under external magnetic fields will be presented. In these experiments, the quasielastic scattering originating from the ring rotation dynamics proved to be insensitive to the external magnetic field up to 2.5 T, but an inelastic excitation was observed in PVFCl<sub>x</sub> which is interpreted as Zeeman splitting of the electronic magnetic moment. The field dependence and strength of the excitation will be analyzed in more detail.

Likewise, high resolution neutron backscattering experiments under external magnetic fields did not reveal a magnetic field dependence of the quasielastic scattering either. But with the high energy resolution the hyperfine splitting of hydrogen in the external magnetic field is resolvable and leads to significant broadening of the effective instrumental resolution function. Hyperfine splitting of nuclear moments is commonly used in neutron backscattering spectroscopy to probe the strong internal field in ferromagnetic materials,<sup>[79,80]</sup> but to the best of knowledge, it has not been observed in comparable measurements with external magnetic fields.

---

## 10.1 Experimental details

---

The same samples of FCl<sub>3</sub> and PVFCl<sub>x</sub> as in [chapter 7](#) and [chapter 9](#) were used for the experiments described here. Powder samples were filled in hollow cylinder aluminum sample holders of 14 mm diameter and circa 0.5 mm wall thickness.

Neutron spectroscopy was carried out on the IN5 ToF spectrometer and the IN16 backscattering spectrometer. The sample was placed in an ILL standard superconducting cryomagnet on both instruments, allowing for vertical magnetic fields of up to 2.5 T to be applied at the sample position at temperatures from 2 K to 300 K. The available vertical opening of  $\pm 5^\circ$  restricted the scattering plane of observed scattered neutrons to be approximately perpendicular to the magnetic field. On IN16 therefore only about a quarter of the analyzer height was usable. In addition the large diameter of the sample environment made the use of the standard IN16 multidetector impossible. Instead, three single detectors were positioned to measure the scattered and energy analyzed neutron intensity for magnitudes of the scattering vector  $Q$  of  $0.85 \text{ \AA}^{-1}$ ,  $1.26 \text{ \AA}^{-1}$  and  $1.6 \text{ \AA}^{-1}$ . This experiment was the first and only cryomagnet experiment on IN16 ever. Raw data was treated as described in [Appendix B](#), but no multiple scattering simulations have been performed for the analysis in this chapter. The spectra were therefore corrected for angular dependent sample self absorption.

---

## 10.2 Zeeman splitting of electronic ground state

---

The neutron time of flight spectra on PVFCl<sub>x</sub> under magnetic fields revealed a very weak inelastic peak, four orders of magnitude less intense than the elastic peak. A shift of its position with changing field strength was observed as shown in [Figure 10.1](#) for  $T = 80 \text{ K}$ . The peak position appears to be independent of temperature between 2 K to 140 K and even up to 300 K, but increasing quasielastic scattering from the ferrocene ring rotation is superimposed at 300 K complicating a reliable interpretation.

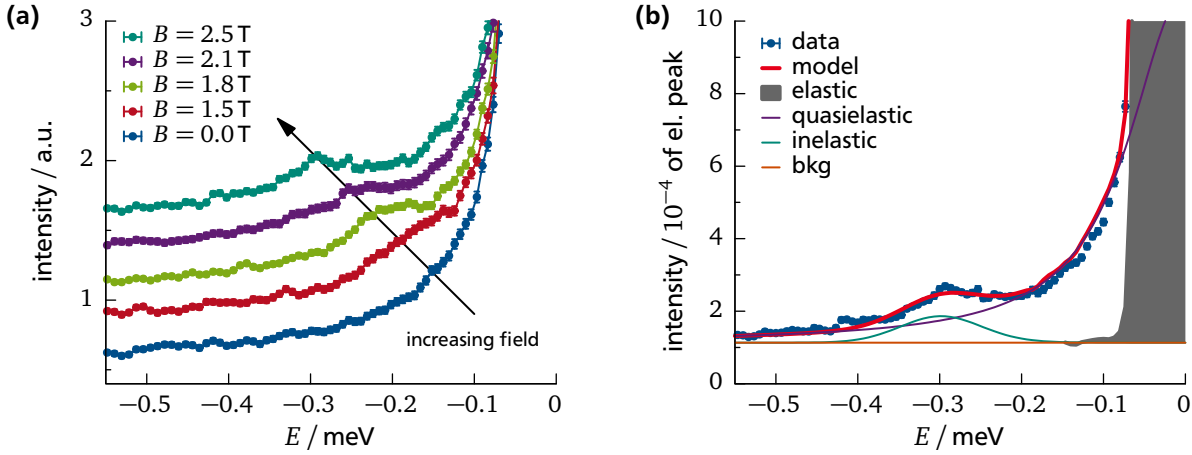


**Figure 10.1:** Inelastic time of flight data (IN5) on  $\text{PVFCl}_x$  under an external magnetic field summed over all scattering angles. (a) Shift of the inelastic excitation with increasing magnetic field. Curves are vertically shifted for clarity. (b) Fit of a spectrum at  $T = 80$  K and  $B = 2.5$  T with a quasielastic Lorentzian and an inelastic Gaussian contribution.

In contrast to the more complicated model functions used in previous chapters, a simpler approach is used here. The neutron energy gain side of the spectra summed over all detectors is analyzed with a simple model function accounting for a delta-shaped elastic, Lorentzian quasielastic and Gaussian inelastic contribution. The sum is convoluted with the experimentally determined resolution function and a constant background is added, such that the model function for the analysis of the inelastic excitation is

$$S(\omega) = s_0 \left[ A_0 \delta(\omega) + A_1 \exp\left(\frac{\hbar\omega}{2k_B T}\right) \mathcal{L}(\gamma, \omega) + C \mathcal{G}(\sigma_{\text{ex}}, \omega + \omega_0) \right] \otimes Y(\omega) + \text{bkg} \quad (10.1)$$

where  $s_0$  is an overall scaling factor,  $A_0$  and  $A_1$  are the incoherent structure factors of nuclear scattering,  $C$  is the intensity of the inelastic excitation, the exponential factor is the detailed balance,  $\mathcal{L}(\gamma, \omega)$  a normalized Lorentzian of HWHM  $\gamma$ ,  $\mathcal{G}(\sigma_{\text{ex}}, \omega)$  a normalized Gaussian of standard deviation  $\sigma_{\text{ex}}$ , and  $Y(\omega)$  the experimentally determined instrumental resolution function. An exemplary fit is shown in Figure 10.1b at  $T = 80$  K and  $B = 2.5$  T.

In contrast to the inelastic scattering, the quasielastic contribution was, within its uncertainty, independent of the applied field. Thus the Lorentzian width was fixed to the value obtained without external field in order to extract parameters of the inelastic contribution more reliably. The field dependency of the inelastic peak position  $E_0 = \hbar\omega_0$  is found to be linear as shown in Figure 10.2a. It is assumed here that this peak arises from transitions between Zeeman split electronic ground state levels in the external field  $B$  caused by an unpaired electron in the oxidized ferrocene complex. The Zeeman splitting is known to depend on  $B$  according to

$$E_0 = \hbar\omega_0 = g\mu_B B \quad (10.2)$$

with the Bohr magneton  $\mu_B$  and the Landé factor  $g$ . The slope of the linear fit in Figure 10.2a is  $0.1185(8) \text{ meV T}^{-1}$ , corresponding to  $g = 2.05(1)$ . This value is only slightly larger than the spin-only value. Moreover, it differs significantly from the anisotropic  $g$ -factors of  $g_{\parallel} = 4.35(5)$  and  $g_{\perp} = 1.26(6)$  obtained from electron spin resonance for ferrocenium ions in solution, but these experiments also found decrease of the  $g$ -factor anisotropy for substituted ferrocenes.<sup>[81,82]</sup> In fact, the excitation observed here is broader than the instrumental resolution, and the deconvoluted width  $\sigma_{\text{ex}}$  shows the tendency to increase with increasing field as



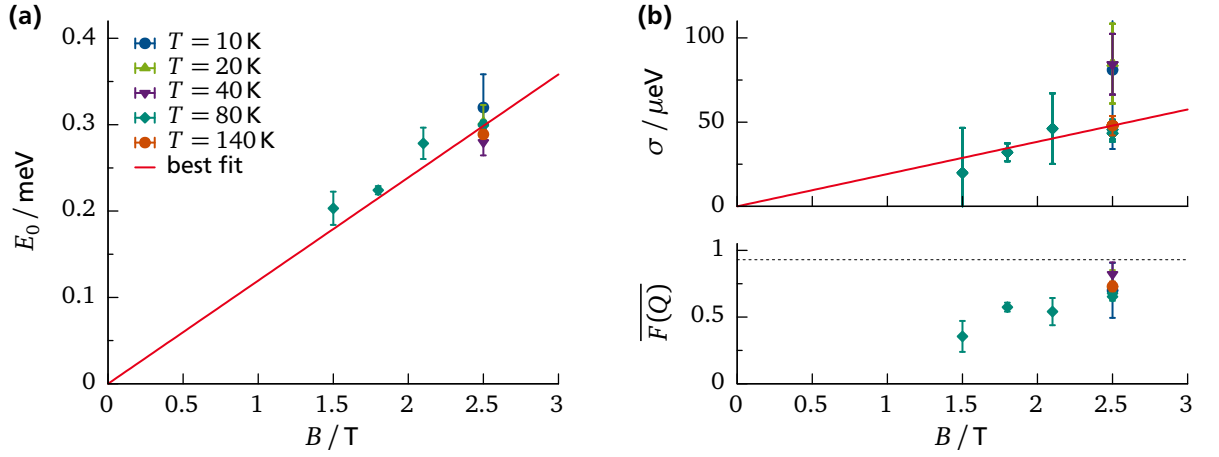


**Figure 10.2:** Results of analysis of the inelastic excitation observed for  $\text{PVFCl}_x$  in neutron time of flight spectroscopy. Obtained parameter values for (a) energy  $E_0$ , (b) unconvoluted width  $\sigma_{\text{ex}}$  and averaged magnetic form factor  $\overline{F(Q)}$  of the inelastic excitation in  $\text{PVFCl}_x$  as function of applied magnetic field  $B$ .

shown in Figure 10.2b. This could mean that the obtained value of  $g = 2.05(1)$  is the mean value of a remaining, unresolved  $g$ -factor anisotropy. This anisotropy would be, however, less pronounced than in the ferrocenium ion, which could be explained by further delocalization of the electron through the attached polymer chain.

In order to estimate the intensity of the magnetic scattering, the double differential cross section for an uncorrelated spin- $\frac{1}{2}$  system in an external magnetic field is calculated. The details of the calculation are discussed in Appendix D. The result helps in identifying the contributions in eq. (10.1), where coherent and incoherent nuclear scattering were added:

$$A_0 = \frac{\sigma_{\text{coh}}}{4\pi} \overline{S(Q)} + \frac{\sigma_{\text{inc}}}{4\pi} \overline{A_0^{\text{inc}}(Q)} + \frac{\sigma_{\text{mag}}}{4\pi} \quad (10.3a)$$

$$A_1 = \frac{\sigma_{\text{inc}}}{4\pi} \left[ 1 - \overline{A_0^{\text{inc}}(Q)} \right] \quad (10.3b)$$

$$C = \frac{\sigma_{\text{mag}}}{4\pi} \left[ 1 + \exp\left(-\frac{\Delta E}{k_B T}\right) \right]^{-1} \quad (10.3c)$$

with

$$\frac{\sigma_{\text{mag}}}{4\pi} = \frac{1}{4} r_0^2 \left[ \frac{g}{2} \overline{F(Q)} \right]^2 \quad (10.4)$$

where  $\overline{S(Q)}$  and  $\overline{A_0^{\text{inc}}(Q)}$  are the static and elastic incoherent structure factor averaged over the probed  $Q$ -range respectively. The intensity of the inelastic excitation originating from scattering of neutrons on magnetic moments is described by the magnetic scattering cross section in eq. (10.4) and the thermal population factor in eq. (10.3c).

A value of  $\overline{S(Q)} = 1.45$  was obtained from averaging the static structure factor of  $\text{PVFCl}_x$  which looks similar to the one shown for  $\text{PVFc}$  in Figure 8.3 on page 79. Now, the magnetic form factor  $\overline{F(Q)}$  of the oxidized ferrocene units averaged over the probed  $Q$ -range from  $0.6 \text{ \AA}^{-1}$  to  $1.7 \text{ \AA}^{-1}$  is the only unknown and can be calculated from the intensity of the excitation. The resulting values are shown in Figure 10.2b. Unfortunately they are plagued by large uncertainties, but the values between circa 0.6 to 0.8 could indicate that the electron is more delocalized than expected for a Fe 3d shell. The expected form factor of a Fe 3d electron in this  $Q$ -range is

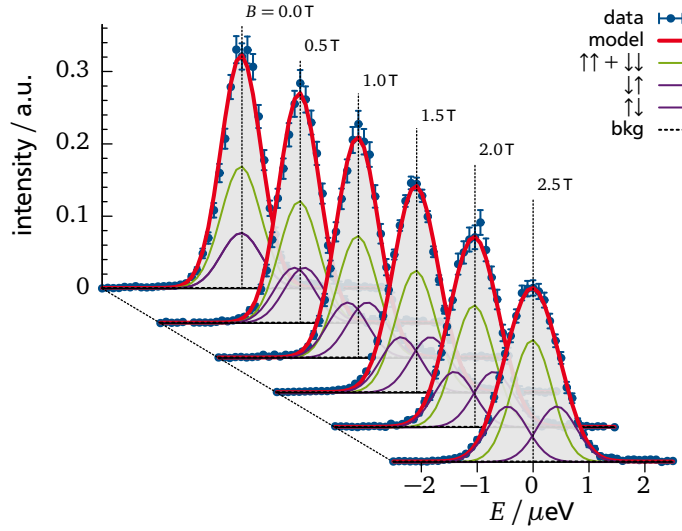


**Figure 10.3:** Broadening of the elastic peak in neutron backscattering spectroscopy (IN16) observed on  $\text{PVFCl}_x$  at  $T = 2\text{ K}$  under external magnetic fields  $B$ . The data was analyzed with a model accounting for hydrogen nuclear Zeeman splitting of non spinflip ( $\uparrow\uparrow+\downarrow\downarrow$ ) and spinflip scattering ( $\downarrow\uparrow$  and  $\uparrow\downarrow$ ).

circa  $0.92^{[83]}$  and shown as dashed line in the bottom part of Figure 10.2b. This is in qualitative agreement with studies of the electronic structure of ferrocene concluding that the highest occupied  $e'_2$  orbital consists of the Fe  $d_{x^2-y^2}$  or  $d_{xy}$  shell mixed with a small contribution of the  $\pi$  orbitals of the cyclopentadienyl ligands.<sup>[84]</sup> Moreover, it would agree with the possible explanation of further electron delocalization caused by the polymer chain leading to the reduced  $g$ -factor anisotropy. However, these results should be interpreted with great care as the evaluation of the magnetic scattering intensity is sensitive to the fraction of oxidized ferrocene units. They are expected to lie close to unity, but remain effectively unknown for the present sample.

### 10.3 Nuclear hyperfine splitting in the external field

In high resolution neutron backscattering spectroscopy, a significant broadening of the elastic line was observed under external magnetic fields. Figure 10.3 shows data obtained for  $\text{PVFCl}_x$  at  $T = 2\text{ K}$  at different external field strengths. The observed broadening of the elastic line is consistent with an unresolved splitting due to hyperfine splitting of the nuclear ground state of hydrogen in the external magnetic field. An incoherent scattering process with spinflip of the neutron changes the orientation of the hydrogen spin relative to the quantization axis by  $\Delta m_I = \pm 1$ , thus changing its energy by a magnitude of

$$E_0 = \hbar\omega_0 = g_I\mu_N B \quad . \quad (10.5)$$

All three processes ( $\Delta m_I = 0; \pm 1$ ) are equally probable, and the incoherent scattering is thus split equally between an elastic and two symmetric inelastic peaks. The scattering cross section can be written in the form as derived by Heidemann:<sup>[79]</sup>

$$\frac{d^2\sigma}{d\Omega d\omega} = s_0 \left\{ \left[ \frac{\sigma_{\text{coh}}}{\sigma_{\text{inc}}} \overline{S(Q)} + \frac{1}{3} \right] \delta(\omega) + \frac{1}{3} \delta(\omega - \omega_0) + \frac{1}{3} \delta(\omega + \omega_0) \right\} \otimes Y(\omega) + \text{bkg} \quad (10.6)$$

to which an elastic coherent contribution using the  $Q$ -averaged static structure factor  $\overline{S(Q)}$  was added. For  $Y(\omega)$ , a Gaussian with fixed width of the experimental resolution function obtained

**Table 10.1:** Resulting Landé factors of nuclear magnetic moment  $g_I$  and values used as average structure factor  $\overline{S(Q)}$  for hydrogen containing samples and vanadium.

sample	$T / K$	$\overline{S(Q)}$	$g_I$
PVFcI <sub>x</sub>	2	1.52	5.81(4)
PVFcI <sub>x</sub>	20	1.52	5.74(5)
PVFcI <sub>x</sub>	40	1.52	5.60(5)
FcI <sub>3</sub>	10	1.6	5.05(8)
Fc	2	1.81	5.96(8)
Reference value for <sup>1</sup> H:			5.58 <sup>a</sup>
Vanadium	2	0	1.1(5)
Reference value for <sup>51</sup> V:			1.47 <sup>a</sup>

<sup>a</sup> From ref. [85]

without magnetic field has been used. The incoherent part of the scattering splits up in 3 peaks of equal intensity located at  $E = 0$  and  $\pm E_0$ . With values of  $\overline{S(Q)}$  obtained from a polarized neutron diffraction experiment on D7, eq. (10.6) was fitted to the data as shown in Figure 10.3. The refinement was performed simultaneously for spectra obtained at different fields using  $g_I$  as free parameter. The values used for  $\overline{S(Q)}$  and the resulting values of  $g_I$  are given in Table 10.1. For the samples PVFcI<sub>x</sub>, FcI<sub>3</sub> and Fc virtually all incoherent scattering originates from hydrogen. The proximity of the results to the reference value of  $g_I = 5.58$ <sup>[85]</sup> confirms that the observed line broadening is caused by the interaction of hydrogen nuclear spins with the external magnetic field. However, the agreement within the given uncertainties is moderate indicating a larger uncertainty of systematic origin, for example field inhomogeneities. But given that the splitting lies within the resolution function, the result is satisfactory and demonstrates the sensitivity of the experimental high resolution technique to external magnetic fields.

Table 10.1 also shows the result obtained for a vanadium sheet. Due to the small Landé factor of the vanadium nuclear spin the broadening is barely distinguishable in the present setup, but the result corresponds within its large uncertainty to the reference value of  $g_I = 1.47$ .<sup>[85]</sup>

---

## 10.4 Conclusion

---

In this chapter, the ground state splitting in external magnetic fields on electronic and nuclear magnetic moments was observed using neutron spectroscopy experiments. The spectrum of the oxidized redox-responsive polymer poly(vinylferrocene) showed an inelastic excitation which is assumed to be caused by splitting of the paramagnetic electronic ground state of the oxidized ferrocene units, with a Landé factor of  $g = 2.05(1)$ . The results indicate that this could be the averaged value of an unresolved  $g$ -factor anisotropy, which would however be less pronounced than in the ferrocenium ion. In a second experiment, the nuclear hyperfine splitting under external magnetic fields caused significant broadening of the elastic line in incoherent neutron backscattering spectroscopy, where the analysis showed consistency with the nuclear  $g_I$ -factors for hydrogen and vanadium.

---

# 11 Summary

The main topic of this thesis was the study of cyclopentadienyl (Cp) ring rotation dynamics in the ferrocene (Fc) molecule. The molecular reorientation was studied in the different crystalline phases of bulk ferrocene, in the salt ferrocenium triiodide ( $\text{FcI}_3$ ) with oxidized ferrocene cations, and in the polymer poly(vinylferrocene) (PVFc) where the ferrocene units are laterally attached to a polymer chain. Quasielastic neutron scattering (QENS) using time of flight (ToF) and backscattering (BS) techniques was applied as experimental technique allowing to study the molecular reorientation on a time scale from picoseconds to nanoseconds. Emphasis was put on a robust approach to data analysis. The used fitting algorithm allowed for multiple scattering corrections with a Monte Carlo simulation, and the simultaneous analysis of data for different instruments, temperatures or  $Q$ -values, with the possibility to include fixed window temperature scans on the backscattering spectrometer IN16B.

In bulk ferrocene, the extension of previous data to a larger temperature and  $Q$ -range refined the picture of ring rotation dynamics in the monoclinic phase which is stable at room temperature and metastable down to 164 K. It turned out that the previously favored equivalent sites rotational jump diffusion model needs to be extended to a non-equivalent sites model, accounting for dynamical disorder of the rings. The analysis resulted in 5-fold rotational jump diffusion overlaid with fast transitions between two ring configurations twisted by circa  $30^\circ$ . This finding using a dynamical model corresponds surprisingly well to earlier diffraction studies and calculations of the potential lattice energy. In the ordered, metastable triclinic phase below 164 K, the combination of ToF and BS spectroscopy enabled the separation of two dynamic components, ascribed to crystallographically different molecules in the unit cell. The geometry of the motion can be described with a 5-fold rotational jump diffusion model. The barrier to ring reorientation is higher than in the monoclinic phase, and changes significantly at the phase transition. In the orthorhombic phase of crystalline Fc which is the stable one below 242 K, dynamical processes on the time scale observable on backscattering spectrometers only occurred very close to the phase transition. The stable, dense orthorhombic phase shows the largest barrier to ring rotation.

In the next step of the study of ring rotation dynamics, the effect of oxidation was investigated in the ionic compound  $\text{FcI}_3$ . While bulk Fc has received a lot of attention by previous authors, little is known about the dynamics in  $\text{FcI}_3$ . A hitherto unknown phase transition was found at 85 K, with a discontinuity in the temperature dependence of the correlation time of the motion similar to the triclinic-monoclinic transition in bulk Fc. The ring rotation in both phases above and below 85 K showed a significantly lower rotational barrier than monoclinic and triclinic Fc. This can be explained by different intra- and intermolecular potentials barriers. Due to the low barrier, the motion above 85 K is indistinguishable from continuous rotation, while it is more consistent with 5 equilibrium sites below 85 K. However, a rescaling of the model by adding additional elastic scattering was necessary in all cases, indicating that the dynamics might not be entirely described by the simple models.

Furthermore, a QENS study on ring rotation in the macromolecular structure of PVFc revealed that the ring rotation dynamics is also active in the polymer far below its assumed glass transition between 450 K to 500 K. As can be expected, only one ring of the molecule is rotating as the other one is covalently bound to the main chain. It was shown that the correlation times are broadly distributed over some orders of magnitude, meaning that the barrier of rotation is significantly influenced by the amorphous, glassy structure of the polymer. In terms of a

---

rotation rate distribution model, the local ring rotation dynamics can be very well described over the large temperature range from 80 K to 350 K. The average barrier was determined to  $9.61(2) \text{ kJ mol}^{-1}$ , with a distribution having circa one third of this value as second moment.

Complementary to QENS experiments focusing of the comparatively slow dynamics, a vibrational study was performed on ferrocene,  $\text{FcI}_3$ , and various ferrocene containing polymers. In PVFc, where ferrocene is attached laterally to the chain, a broadening but no significant shift of the vibrational fingerprint modes was observed. A more dramatic influence was found in poly(ferrocenylsilanes), where the ferrocene unit is incorporated into the polymer backbone. In the oxidized ferrocene complex, it seemed like the coordination bond weakened by one missing electron lead to a shift of fingerprint modes to lower frequencies.

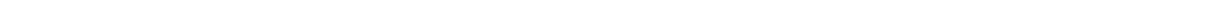
Finally, QENS experiments on oxidized PVFc were performed under external magnetic fields to explore possible effects due to the magnetic moment of the oxidized ferrocene moiety. No effect on the ring rotation dynamics was observable up to fields of 2.5 T, but an excitation due to Zeeman splitting of the electronic ground state helped to determine the average Landé factor to  $g = 2.05(1)$ , with a possible residual anisotropy. In high resolution experiments, the Zeeman splitting of the nuclear spin of hydrogen was observable in incoherent scattering. These measurements reveal fundamental physical effects which are not commonly observed in the way presented here, even though they are unrelated to the main topic of Cp ring rotation in ferrocene.



---

# Appendix

---





---

# A Multiple scattering correction

The correction for multiple scattering has been performed by a Monte Carlo simulation implemented using the free software package GNU/Octave,<sup>[59]</sup> and the algorithm is a modified version of the one used in the program DISCUS by Johnson.<sup>[58]</sup> The general approach to the correction method was presented in section 5.2. Here, more technical details about the implementation and some examples of the results will be given.

---

## A.1 Multiple scattering simulation algorithm

---

The simulation takes the scattering law  $S(Q, \omega)$  as input, without any resolution smearing. The elastic peak which is analytically described by  $\delta(\omega)$  is implemented as narrow box function of fixed area and finite width. However, the width is much smaller than the spacing of the energy channels for which we aim to determine the correction factors. The simulation input also comprises the definition of sample geometry as well as some instrument parameters like nominal incident neutron energy, beam divergence and location and size of the detectors. The cross sections for coherent and incoherent scattering  $\sigma_{\text{coh}}$  and  $\sigma_{\text{inc}}$  and for absorption  $\sigma_{\text{abs}}$  as well as the number density of scatterers  $\rho$  in the sample must be given. From these values, the following relevant macroscopic cross sections denoted by  $\Sigma$  are calculated:<sup>1</sup>

$$\Sigma_{\text{S}} = \rho(\sigma_{\text{coh}} + \sigma_{\text{inc}}) \quad (\text{A.1a})$$

$$\Sigma_{\text{abs}} = \rho \sigma_{\text{abs}} \sqrt{E_{\text{abs}}/E} \quad (\text{A.1b})$$

$$\Sigma_{\text{T}} = \Sigma_{\text{S}} + \Sigma_{\text{abs}} \quad (\text{A.1c})$$

where  $\Sigma_{\text{S}}$  describes the macroscopic cross section for scattering,  $\Sigma_{\text{abs}}$  the one for absorption, and  $\Sigma_{\text{T}}$  the total cross section. The absorption part depends on kinetic neutron energy  $E$ , where the tabulated values of  $\sigma_{\text{abs}}$  are usually given for  $E_{\text{abs}} = 25.3$  meV. The given scattering law  $S(Q, \omega)$  should contain incoherent and coherent scattering, which is the case as Bragg peak scattering is still contained in the data during the iterative refinement analysis as described in section 5.3. The goal of the simulation is the generation of correction factors  $R_{2\theta}^*(\omega)$  according to

$$R_{2\theta}^*(\omega) = \frac{J_{2\theta}^*(\omega)}{\sum_{n=1}^4 J_{2\theta}^{(n)}(\omega)} \quad (\text{A.2})$$

For this, the hypothetical neutron fluxes  $J_{2\theta}^{(n)}(\omega)$  after exactly  $n$  scattering processes in the sample are calculated, as well as the ‘wanted’ flux  $J_{2\theta}^*(\omega)$  with only one scattering process and no absorption by the sample. These quantities are calculated by means of a Monte-Carlo Ray-Tracing simulation, where typically up to  $n = 4$  scattering processes are considered. Randomized trajectories of virtual neutrons from the incident beam through the sample towards the detector are sampled. Along each trajectory, the probability for scattering of a real neutron is calculated and averaged in the detector. A sketch of such a trajectory is shown in Figure 5.3 on page 39.

---

<sup>1</sup> Actually, the quantities  $\Sigma$  are attenuation coefficients of dimension  $\text{m}^{-1}$ , but usually referred to as cross sections.

Each neutron, indexed by  $j$ , is defined by the following properties:

- $\mathbf{r}_j$  position vector in real space
- $\tilde{\mathbf{v}}_j$  unit vector of velocity direction
- $E_j$  kinetic energy
- $p_j$  statistical weight

The simulation is run separately for every detector and proceeds as follows:

**(I) Initialize a certain number of virtual neutrons.**

The positions  $\mathbf{r}_j$  of typically 5000 virtual neutrons are sampled randomly across the sample surface facing the incoming beam. The velocity directions  $\tilde{\mathbf{v}}_j$  are sampled taking into account an approximate, small beam divergence of the real instrument. The energies  $E_j$  are set to the nominal incident energy  $E_0$ , the initial statistical weight is  $p_j = 1$ , and the neutrons have undergone  $n = 0$  scattering events up to now.

The following steps will be repeated in a loop, up to the maximum number of scattering events:

**(II) Determine the position of the next scattering event.**

For each neutron, the path length  $d$  that is still lying in the sample along its flight path is calculated. The probability for interaction with the sample somewhere along this path is

$$1 - \exp(-\Sigma_T d) \quad .$$

It would be very inefficient to have only the above small fraction of virtual neutrons actually interact with the sample – therefore, a scattering event is forced to occur within the sample for all virtual neutrons. The path length  $l \in [0, d]$  to this event is sampled according to the probability distribution

$$p(l) = \exp(-\Sigma_T l) \times \frac{\Sigma_T}{1 - \exp(-\Sigma_T d)}$$

where the second term on the right hand side assures normalization of the distribution. Random numbers with this distribution are generated from a uniformly distributed random variable  $\xi \in [0, 1]$  using<sup>[58]</sup>

$$l = \ln \left\{ 1 - \xi [1 - \exp(-\Sigma_T d)] \right\} \quad .$$

The virtual neutron is then propagated to the position of the scattering event by

$$\mathbf{r}_j \mapsto \mathbf{r}_j + l \tilde{\mathbf{v}}_j$$

and its statistical weight is adjusted to compensate for the forced interaction with

$$p_j \mapsto p_j \times [1 - \exp(-\Sigma_T d)] \quad . \tag{A.3}$$

At this position, the neutrons will undergo their next scattering event:

$$n \mapsto n + 1 \quad .$$

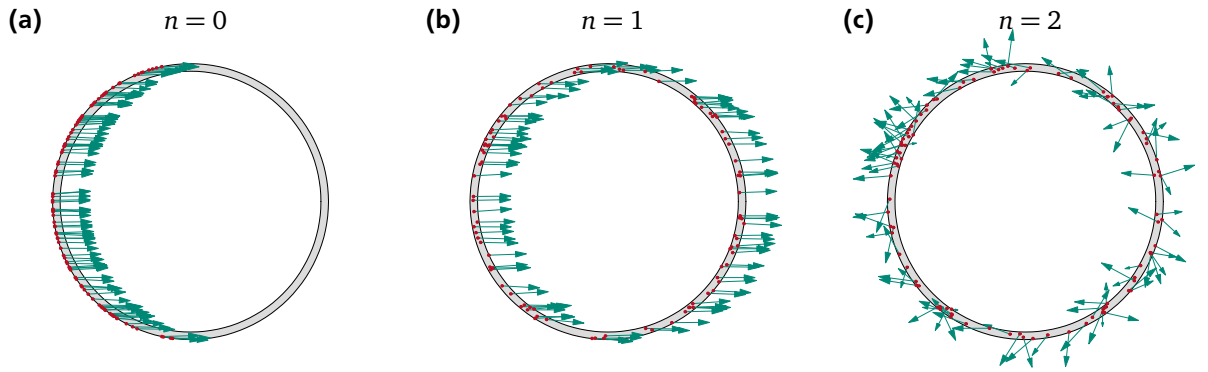


**Figure A.1:** Exemplary position and direction of velocity for 150 virtual neutrons for a hollow cylinder sample in vertical projection (a) when entering the sample, (b) right before the first scattering event, and (c) right before the second scattering event. Incident beam direction is from the left.

For hollow cylinder sample geometry,<sup>2</sup> the path length  $d$  inside the sample might be fragmented as the neutron path can exit and re-enter the sample. In that case, all fragments of the path through the sample are calculated and collapsed into one length  $d$ , and the randomized value of  $l$  is re-expanded accordingly such that virtual neutrons can traverse the hollow inner part of the sample between two scattering events. An example is shown in Figure A.1 with the initial positions of neutrons entering the simulation, and their position and velocity direction right before the first and second scattering process.

(IIIa) **Calculate the probability of scattering into the detector.**

This step of the simulation does not change the state of the virtual neutrons, it only extracts the probability of neutrons reaching the detector from their current state. The detector center position is defined as angle  $2\vartheta$  in the horizontal plane with respect to the incident beam axis, and the covered solid angle element is given in spherical coordinates with polar extent  $\Delta(2\vartheta)$  and azimuthal extent  $\Delta\varphi$ . The term ‘detector’ used here does not necessarily refer to the actual detectors in the real instrument, but it describes the solid angle of detection for which the present spectrum was measured. The ‘detector’ in the simulation can thus correspond to a group of detectors (for IN6 ToF), to an integration area across a multidetector (for IN5 ToF), or to a crystal analyzer surface area in a backscattering spectrometer (for IN16/IN16B).

Within the given solid angle element, a certain direction is randomized, and the probability for scattering along this direction into each energy channel of the detector is determined. The energy change in this scattering process is

$$\hbar\omega = E_j - (E_0 - \hbar\omega_D)$$

where  $\hbar\omega_D$  corresponds to the nominal energy transfer associated with the detector channel. For the first scattering process with  $n = 1$  it follows that  $\hbar\omega = \hbar\omega_D$ , but for  $n > 1$  the neutron energy can have changed in previous scattering processes such that  $E_j \neq E_0$  and consequently  $\hbar\omega \neq \hbar\omega_D$ . The value of  $Q$  is calculated for inelastic scattering according to eq. (2.5) on page 8, where the scattering angle is the angle between

<sup>2</sup> Hollow cylinder sample geometry is not supported by the original DISCUS program.

$\tilde{\nu}_j$  and the randomized direction towards the detector. The probability  $p'_j$  of a neutron reaching the detector along this trajectory is

$$p'_j(\omega_D) = \underbrace{p_j}_{(1)} \times \underbrace{\frac{\Sigma_S}{\Sigma_T}}_{(2)} \times \underbrace{\frac{S(Q, \omega)}{4\pi} \sqrt{\frac{E_j - \hbar\omega}{E_j}}}_{(3)} \times \underbrace{\exp(-\Sigma_T d_D)}_{(4)} \quad (\text{A.4})$$

where the individual factors are:

- (1) statistical weight of previous trajectory,
- (2) probability of this interaction being a scattering event, and no absorption,
- (3) normalized scattering cross section for this scattering event corresponding to eq. (2.21) on page 11, where the square root expression is equal to  $k_f/k_i$  and the dynamic structure factor is averaged over the energy bin width of the detector channel,
- (4) probability of the neutron leaving the sample without further interaction towards the detector along the remaining path length  $d_D$  inside the sample.

The hypothetical flux into the detector can now be calculated from

$$J_{2\vartheta}^{(n)}(\omega_D) = \langle p'(\omega_D) \rangle$$

by averaging over all virtual neutrons. In the first iteration when  $n = 1$ , the flux  $J_{2\vartheta}^*(\omega)$  is additionally calculated in a similar way, with the difference that sample absorption is set to zero in eq. (A.3) and eq. (A.4). Moreover the value of  $Q$  in eq. (A.4) is set to

$$Q \mapsto Q_{\text{el}} = 4\pi\lambda_{\text{inc}}^{-1} \sin \vartheta$$

where  $2\vartheta$  is the nominal angle between detector and incident beam axis. With this substitution, the resulting correction factors can be used to transform constant- $2\vartheta$  spectra into constant- $Q$  spectra.<sup>3</sup>

### (IIIb) Randomize parameters of this scattering event.

In this step, the random scattering event which determines the next step of the neutron trajectory through the sample is calculated. Although it seems natural to use  $S(Q, \omega)$  directly as probability distribution for the randomization of scattering events, this would be an unfavorable approach. As explained by Johnson,<sup>[58]</sup> this leads to good statistics of the simulation where  $S(Q, \omega)$  gives high probability of scattering, and bad statistics for processes of lower probability. In fact, the simulation would then very much resemble a real scattering experiment that quickly achieves good counting statistics in high intensity regions, and needs to run much longer to reduce the noise in low intensity regions.

Fortunately, probability of scattering and counting statistics can be easily decoupled in numerical simulations. Therefore, in DISCUS, the scattering events are sampled with a uniform distribution in  $(Q, \omega)$ -space, and the statistical weight of the virtual neutrons is adjusted to the probability of the event. But in the present case, where strong elastic scattering occurs, a fully uniform distribution would give a very bad sampling of the narrow elastic box function in  $S(Q, \omega)$ . This is resolved by adjusting the sampling distribution by forcing a certain number of neutrons (typically 20 % to 30 %) to scatter in the near elastic region with twice the width of the elastic box function to give an accurate

<sup>3</sup> This substitution is not made in the original DISCUS program.

sampling of the elastic peak. The physically allowed section in  $(Q, \omega)$ -space is moreover limited by  $Q < 3Q_{\max}$  and  $|\omega| < 2\omega_{\max}$  where  $Q_{\max}$  and  $\omega_{\max}$  are the maximum values used in the refinement procedure of the actual data.

Figure A.2 shows a typical density of scattering events in the  $(Q, \omega)$ -plane for the second scattering event in the sample. In the first scattering event, only the region marked with the black lines is accessible because all virtual neutrons have  $E_j = E_0$ . In subsequent events,  $E_j$  can be larger and the accessible region in  $(Q, \omega)$  grows accordingly. The high density around  $\hbar\omega = 0$  is due to the above mentioned forced near-elastic scattering. After the parameters  $Q$  and  $\omega$  have been determined, the neutron direction is updated:

$$\tilde{\mathbf{v}}_j \mapsto \tilde{\mathbf{v}}'_j$$

where the scattering angle  $2\vartheta = \cos^{-1}(\tilde{\mathbf{v}}_j \cdot \tilde{\mathbf{v}}'_j)$  for this event fulfills eq. (2.5) on page 8, and the orientation of the scattering plane is randomized. The statistical weight is then updated as follows:

$$p_j \mapsto p_j \times \underbrace{A_{(Q,\omega)}}_{(1)} \times \underbrace{\frac{\Sigma_S}{\Sigma_T}}_{(2)} \times \underbrace{\frac{S(Q, \omega)Q}{\langle S(Q, \omega)Q \rangle}}_{(3)}$$

where the individual factors are:

- (1) weight correction accounting for the focusing of scattering events in the near-elastic region, calculated from the ratio of accessible areas in the  $(Q, \omega)$  plane,
- (2) probability of this interaction being a scattering event, and no absorption,
- (3) normalized scattering cross section for this scattering event. This expression differs from the one in eq. (A.4) due to the uniform density sampling in  $(Q, \omega)$ . The probability of scattering is proportional to the cross section<sup>[58]</sup>

$$\begin{aligned} \frac{d^2\sigma}{dQ d\omega} &= \frac{d^2\sigma}{d\Omega d\omega} \times \frac{d\Omega}{d\theta} \times \frac{d\theta}{dQ} \\ &\propto \frac{k_f}{k_i} S(Q, \omega) \times 2\pi \sin \theta \times \frac{Q}{2 k_i k_f \sin \theta} \\ &\propto S(Q, \omega) Q \quad (\text{for constant } k_i). \end{aligned}$$

Therefore, the statistical weight is adjusted by  $S(Q, \omega)Q$  and normalized by  $\langle S(Q, \omega)Q \rangle$ , where the latter is calculated as average over all sampled virtual neutrons.

Now, the virtual neutrons can be propagated to the location of the next scattering event by closing the loop and going back to step (II).

After the above calculation has been iterated multiple times, the hypothetical neutron fluxes  $J_{2\vartheta}^{(n)}(\omega)$  and  $J_{2\vartheta}^*(\omega)$  are obtained and the correction factors can be calculated from eq. (A.2). The fact that every virtual neutron is scattered into every detector channel helps to increase the statistics of the result, but it also introduces systematic correlations between the correction factors of adjacent energy channels. To estimate this correlation, the calculation for a single detector is repeated 25 times with different initial states for the pseudorandom number generator, using 5000 neutrons in each run. These values were chosen such that the noise on the resulting correction factors is reasonably small.

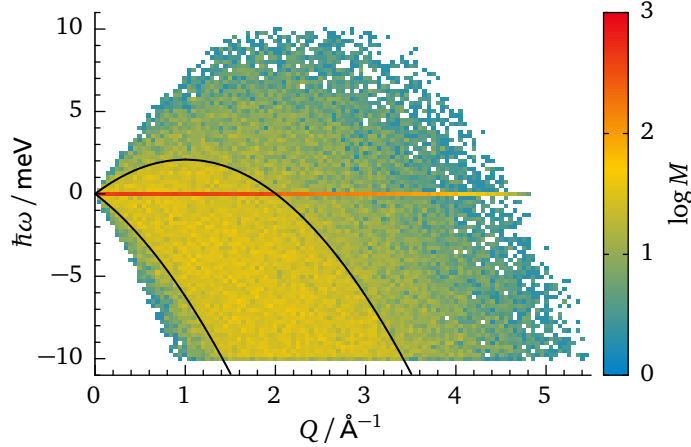


**Figure A.2:** Typical density of randomized scattering events in the  $(Q, \omega)$ -plane for the second scattering event in the sample. The black line marks the region accessible during the first scattering event for  $E_0 = 2.08$  meV, and  $M$  corresponds to the number of events per  $10^5$ . Note the increased density around the elastic line  $\hbar\omega = 0$ .

The energy channels of the detectors in the simulation are not the same as for the experimental data. The correction factors in the simulation are calculated on a coarser grid and interpolated on the actual energy channels, where the simulation grid is adapted with a higher channel density in the low energy transfer region. The special treatment of the elastic peak introduces a discontinuity in the correction factors at  $\omega = 0$ . When the resulting correction factors are applied in the model function in eq. (5.3) on page 37, the correction factor for the elastic simulation channel is applied to the elastic  $\delta(\omega)$ -scattering only, while inelastic simulation channels are interpolated. The subsequent convolution with the experimental resolution function then leads to proper correction of elastic and inelastic intensity in the resulting model function.

Technically, the above described method is only suited for direct geometry spectrometers, meaning that the incident neutron energy  $E_i$  is constant. Backscattering spectroscopy on the other hand is an indirect technique, where the final neutron energy  $E_f$  is constant and the incident energy  $E_i$  is modulated. However, the energy transfers relevant in BS are so small that the energy dependence of the absorption cross section can be neglected, such that the correction algorithm can be used for either experimental technique.

## A.2 Extrapolation of the jump rotation model function

For the multiple scattering simulation, the scattering law should ideally be known in the entire  $(Q, \omega)$ -plane extending beyond the region observed in the experiment. To give the best possible extrapolation for the jump rotation models discussed in this work, the variable ratio  $f$  of apparently rotating to apparently fixed hydrogen atoms discussed in section 7.3 is always used in the intermediate step of the iterative data analysis. This ratio shifts the balance between elastic and quasielastic contributions and was necessary to achieve a continuous extrapolation for all models.

This approach is fully justified, as the multiple scattering simulation should use a structure factor  $S(Q, \omega)$  which describes best the actual sample, even if it is not consistent with the imposed model function in the analysis routine. Of course this only works up to a certain degree. Figure 7.5 on page 68 for example shows that the rescaling using  $f < 1$  cannot superimpose the EISF of the 5-fold jump model with the results from the data analysis in  $\text{FeCl}_3$  above 85 K, and

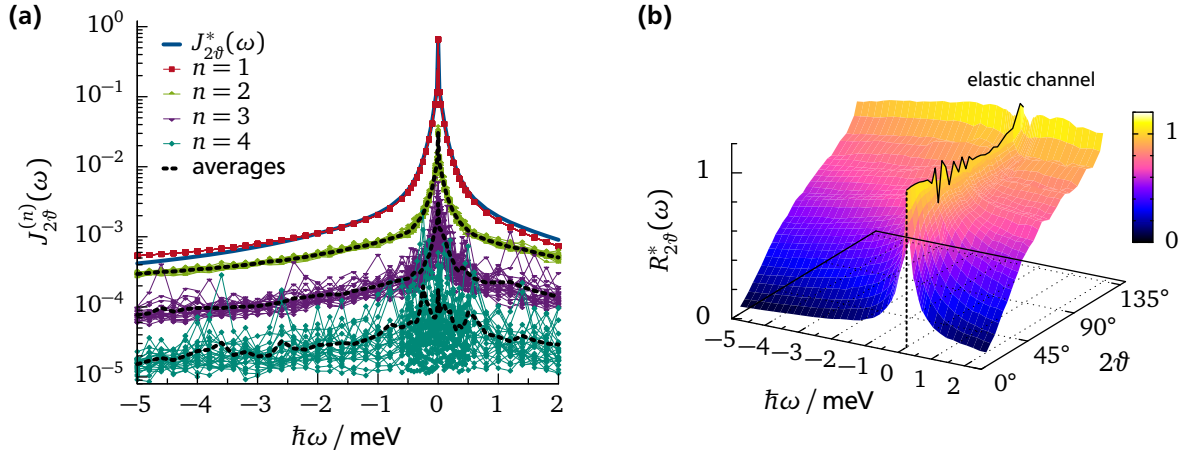


**Figure A.3:** Typical results of the multiple scattering simulation corresponding to the data set analyzed with the non-equivalent sites model shown in Figure 6.4b on page 50. (a) Simulated neutron flux for  $n = 1$  to 4 scattering processes in the sample for scattering angle  $2\vartheta = 49.7^\circ$  ( $Q_{\text{el}} = 1.47 \text{ \AA}^{-1}$ ). Results are shown for each of the 25 independent simulations and their averages (dashed black line). (b) Resulting correction factors  $R_{2\vartheta}^*(\omega)$  for use in the model function. The values of the elastic channel are emphasized by the black line, their apparent strong noise compared to the inelastic channels is due to coherent Bragg peak scattering.

there will be a discontinuity in  $A_0(Q)$  in the extrapolation of these data. However, the multiple scattering correction does neither cause nor can it cure such large inconsistencies between model and data shown in this figure. As will be shown in the next section, the low- $Q$  end is much more affected by the correction factors than the high- $Q$  region.

### A.3 Example of the effect of multiple scattering corrections

A typical example of the resulting hypothetical fluxes  $J_{2\vartheta}^{(n)}(\omega)$  and  $J_{2\vartheta}^*(\omega)$  of a multiple scattering simulation is shown in Figure A.3a. All 25 independent runs for a certain detector and  $n = 1$  to 4 scattering processes in the sample can be seen separately. While the result for  $n = 1$  is highly reproducible in every run, the noise increases significantly with increasing  $n$ . The dashed black lines show the averages which are used for further calculations, and the hypothetical flux  $J_{2\vartheta}^*(\omega)$  is represented by the blue line. It diverges from  $J_{2\vartheta}^{(1)}(\omega)$  with increasing magnitude of energy transfer, primarily due to the increasing differences between the value of  $Q_{\text{el}}$  and the actual  $\omega$ -dependent  $Q$  value. This divergence is much stronger at smaller scattering angles than the one shown in Figure A.3a.

Figure A.3b shows the final correction factors  $R_{2\vartheta}^*(\omega)$  calculated according to eq. (A.2) for all 28 detector groups. At low scattering angles  $2\vartheta$ , the  $\omega$  dependence is very pronounced due to the strong constant- $Q$  correction mentioned above. With increasing scattering angle the correction factors increase as well, especially for the last detector groups which are close to the slab direction of the flat sample. While the correction factors are generally a smooth function of energy transfer  $\hbar\omega$  and scattering angle  $2\vartheta$ , they show a discontinuity in the elastic energy channel due to the corresponding discontinuity in the simulated scattering law  $S(Q, \omega)$  at  $\omega = 0$  and its special treatment in the simulation. The correction factors obtained for the elastic channel are emphasized by the black line. Compared to the smooth inelastic energies, the  $2\vartheta$  dependency of the elastic channel seems to contain significant noise. However, the observed oscillations are not a side effect of badly conditioned simulation parameters, but due to strongly localized coherent scattering from Bragg peaks contained in the scattering law  $S(Q, \omega)$ . This

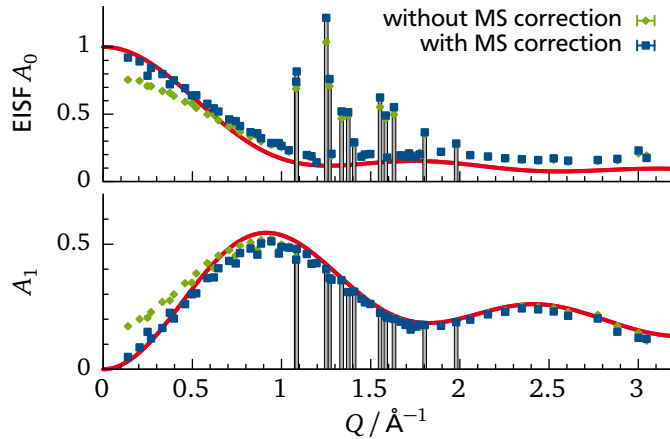


**Figure A.4:** Exemplary comparison of the multiple scattering (MS) corrections on the incoherent structure factors  $A_0(Q)$  and  $A_1(Q)$  obtained for the analysis of IN5 data on ferrocene at  $T = 230\text{ K}$  with  $\lambda_{\text{inc}} = 3.6\text{ \AA}$  and  $6.3\text{ \AA}$  using the non-equivalent sites  $2\times 5$ -fold model (cf. Figure 6.4c on page 50). The red line shows the model prediction. A significant effect of multiple scattering corrections is observed at  $Q < 1\text{ \AA}^{-1}$ . Grey boxes show channels contaminated by Bragg peak scattering, which affects only the obtained values of  $A_0(Q)$ .

leads to discontinuities in the  $2\theta$  dependency of the elastic scattering and consequently to the observed discontinuities of the elastic correction factors and is not an artifact of the calculation.

Figure A.4 shows an example of the influence of the multiple scattering corrections on the obtained values of the incoherent structure factors  $A_0(Q)$  and  $A_1(Q)$ . The Monte-Carlo simulation has been performed in both cases in order to correct for sample self absorption and the transformation of scattering angle to scattering vector, but the maximum number of simulated scattering processes was set to  $n = 1$  (without MS correction) and  $n = 4$  (with MS correction). In contrast to all figures showing EISFs in the main part of this work, the data points in  $A_0(Q)$  containing Bragg peaks have not been removed for visualization in Figure A.4 and are emphasized by gray bars. It can clearly be seen that Bragg peaks lead to outliers with significantly increased intensity in  $A_0(Q)$ , but as expected no influence on  $A_1(Q)$  is observable. The multiple scattering correction has a significant influence on the obtained structure factors for  $Q < 1\text{ \AA}^{-1}$ . The localized influence on the low- $Q$  part can be explained as follows: Already after two scattering processes, the contribution from multiple scattering is essentially isotropic and quasielastic. At low  $Q$ , where the scattering is expected to be essentially elastic as  $A_1(Q)$  tends to zero, the multiple scattering contribution is more important than at larger  $Q$  where it superimposes with the already existing quasielastic scattering. The figure shows that this correction is significant and must be considered to be an important part of the data evaluation process.

Finally, Figure A.5 shows a typical evolution of parameters during the iterative analysis process described in section 5.3. In the zeroth iteration, the initial guess for the correction factors is used (sample self absorption only, no multiple scattering or constant- $Q$  correction). From the first iteration on, the Monte-Carlo simulation is used to obtain the correction factors, by limiting the maximum number of scattering processes to  $n = 1$  (without MS correction) and  $n = 4$  (with MS correction). It can be seen that the multiple scattering correction not only affects the above mentioned structure factors, but also the linewidth  $\tau_1^{-1}$  of quasielastic scattering by more than 10%. In the bottom right graph in Figure A.5, the reduced sum of squared residuals  $\chi_{\text{red}}^2$  between data and model is shown. The significance of the absolute value is not immediately clear and probably differs slightly from the usual meaning of  $\chi_{\text{red}}^2$ , as the model function itself contains small statistical noise from the Monte-Carlo simulation and from the convolution with the experimental model function. This noise has not been accounted for in



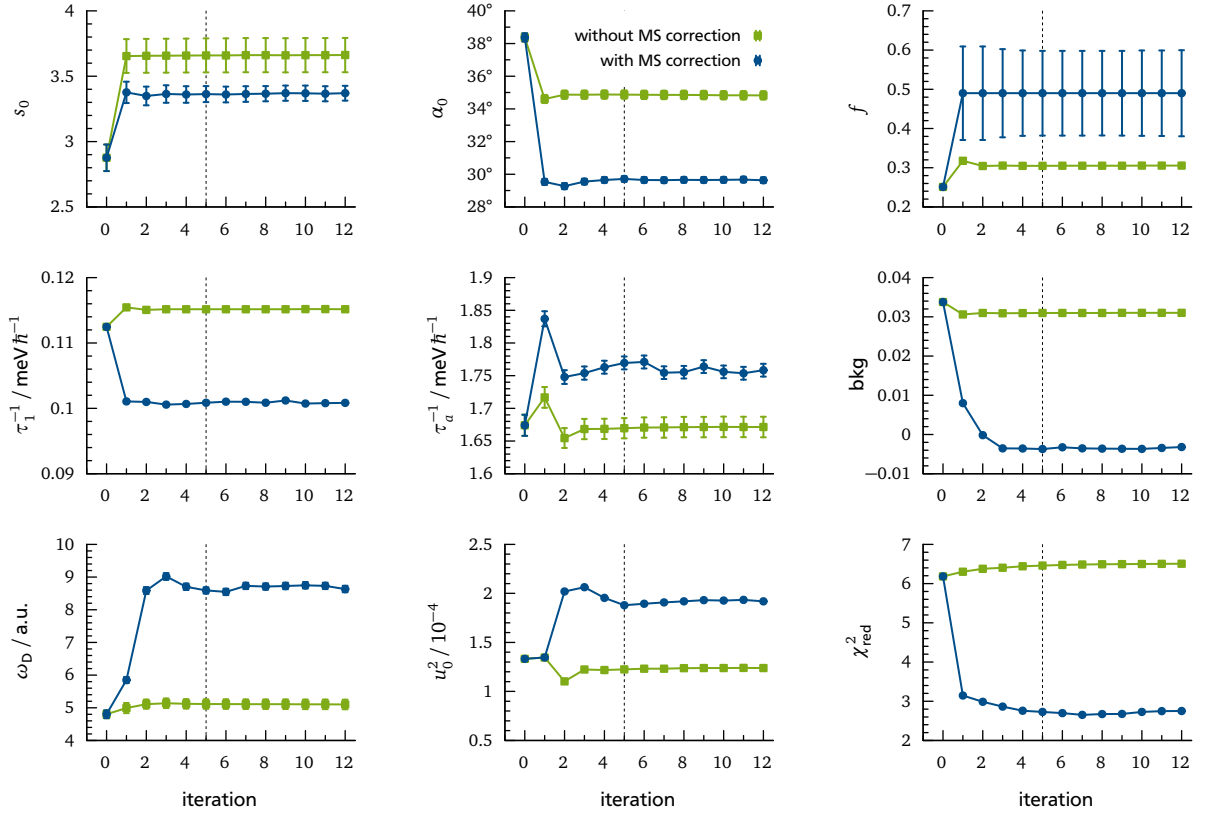


**Figure A.5:** Typical evolution of model parameter values during the iterations of the analysis process when considering up to four scattering events in the simulation (with MS correction) compared to consideration of only one scattering event (without MS correction). The shown data set corresponds to the one in Figure A.4. For the nomenclature of parameters, see chapter 3 and chapter 6. In the lower right, the normalized sum of squared residuals  $\chi_{\text{red}}^2$  of the fit is shown (see text for details). The analysis process is usually run only up to five iterations (dashed line).

the calculation of  $\chi_{\text{red}}^2$ , but the difference between  $\chi_{\text{red}}^2 > 6$  without MS correction and  $\chi_{\text{red}}^2 < 3$  with MS correction clearly underlines the improvement of consistency in the data description when multiple scattering processes are properly accounted for.

## B Raw data correction

The raw data which is collected on all instruments is treated by standard methods prior to any further evaluation, partly using data reduction scripts in the software LAMP<sup>[86]</sup> and the program SQW<sup>[87]</sup> provided at the ILL, and self-written, similar reduction scripts in GNU/Octave.<sup>[59]</sup> The latter have been used for the instruments IN16B and IN1-Lagrange where experiments have been performed shortly after or even during the commissioning phase and a standardized treatment was not established yet. Here, a brief description of the manipulations performed on the raw data is given for ToF, backscattering and polarized diffraction experiments. Data handling for the vibrational spectroscopy on IN1-Lagrange is straightforward and contained in [chapter 9](#).

### ToF data reduction

For the IN5 and IN6 ToF instruments, spectra from different detectors are added or integrated over the multidetector to obtain a set of spectra for different scattering angles. On IN5, the flight time differences due to the cylindrical detector geometry are being corrected for as well. Normalization to a beam monitor then corrects for fluctuations in the incident intensity. The neutrons which are counted in the detector have different kinetic energies, such that another correction is made for energy dependent detector efficiency using an analytical formula. An empty sample cell background measurement was always performed and subtracted from the measured intensity  $I_{\text{meas}}$  as follows:

$$I_{\text{corr}} = I_{\text{meas}} - T I_{\text{empty}} \quad (\text{B.1})$$

with the angular dependent transmission factors of the sample  $T$  that are calculated analytically for flat samples using

$$T = \frac{1}{2} \left\{ \exp \left[ -\frac{\Sigma_T d}{\cos(2\vartheta_0 - \pi/2 - 2\vartheta)} \right] + \exp \left[ -\frac{\Sigma_T d}{\cos(2\vartheta_0 - \pi/2)} \right] \right\} \quad (\text{B.2})$$

where  $d$  is the thickness of the sample,  $2\vartheta_0$  the direction of the slab and  $\Sigma_T$  the macroscopic cross section corresponding to the attenuation coefficient of the sample as defined in [eq. \(A.1\)](#). In this formula, it is assumed that the scattering on the sample cell is caused in equal parts by the first and by the second wall as sketched in [Figure B.1](#). In [eq. \(B.2\)](#), the average attenuation along the red paths by the sample in the cell is calculated, and in [eq. \(B.1\)](#) the measured empty cell intensity is scaled by this attenuation before being subtracted from the sample data. For hollow cylindrical sample geometry, the values of  $T$  are approximated by a modified version of the Monte Carlo simulation described in [Appendix A](#) where the sample attenuation is averaged over randomized trajectories by assuming scattering on every sample boundary in equal parts. This approach assumes that all background scattering from  $I_{\text{empty}}$  is attenuated by the sample. On IN5, additional measurements with Cadmium inside the sample holder were performed to further separate the background scattering. Cadmium is a strong absorber (see [Table 2.1](#) on [page 17](#)) and allows to measure the background  $I_{\text{Cd}}$  which did not pass through the sample volume. [Equation \(B.2\)](#) is then extended to

$$I_{\text{corr}} = (I_{\text{meas}} - I_{\text{Cd}}) - T(I_{\text{empty}} - I_{\text{Cd}}) \quad (\text{B.3})$$

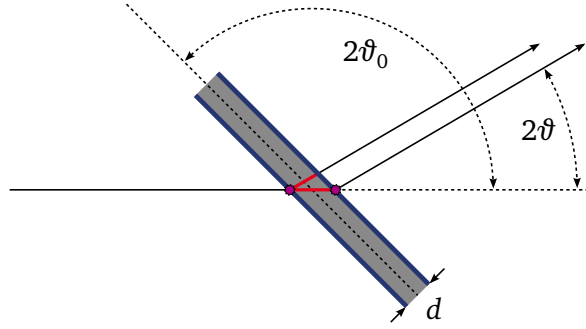


**Figure B.1:** Sketch to estimate the attenuation of scattering from the cell (blue) by the sample (grey) for infinite slab geometry.

To correct for varying detector efficiency and achieve relative and possibly absolute normalization of the energy spectra, a normalization measurement on a vanadium sheet is indispensable in every experiment. Vanadium is a good incoherent isotropic scatterer, and easy to obtain in a well defined thickness. The empty cell scattering is subtracted from the vanadium measurement similar to the method above, and moreover it is corrected for self absorption by using correction factors from a multiple scattering simulation as described in [Appendix A](#). Finally, the sample measurement can be transformed into a differential cross section by

$$\frac{d^2\sigma}{d\Omega dE_f} = \frac{I_{\text{corr;sample}}}{I_{\text{corr;vana}}} \times \frac{\sigma_{\text{inc}}^{\text{vana}}}{4\pi} \times \frac{m_{\text{vana}} M_{\text{sample}}}{M_{\text{vana}} m_{\text{sample}}}$$

where  $m$  is the total vanadium and sample mass, and  $M$  the weight per formula unit. The data then enters the data analysis process described in [chapter 5](#). Correction for sample self absorption has been intentionally omitted here, because it is a part of the multiple scattering corrections during data analysis.

### BS data reduction

Raw data from all IN16 experiments was treated using the program `SQW`, which in principle performs corrections as described above, but uses more elaborate formulas for the subtraction of the empty cell scattering. For the backscattering instruments IN16 and IN16B, no energy dependent detector efficiency needs to be corrected as all neutrons have the same energy selected by the analyzer. Also, they possess a much smaller number of detectors (around 20), such that no grouping was performed. The fact that some neutrons pass through the sample a second time after reflection from the analyzer crystals has been ignored.

### Polarized neutron diffraction data reduction

The polarized neutron diffraction experiment on D7 is in principle treated similar to the above method of empty cell subtraction and normalization, with an additional correction for the efficiency of the beam polarizer and analyzer. The latter is achieved by additional measurement of a quartz glass standard ( $\text{SiO}_2$ ), a material that scatters purely coherent leading to only non-spinflip scattering. The measured and normalized spinflip and non-spinflip intensities of the sample corrected for empty cell scattering and polarizing efficiency are then transformed into coherent and incoherent cross sections using

$$\frac{d^2\sigma_{\text{inc}}}{d\Omega dE_f} = \frac{3}{2} \left( \frac{d^2\sigma_{\uparrow\downarrow}^{\perp}}{d\Omega dE_f} \right) \quad \text{and} \quad \frac{d^2\sigma_{\text{coh}}}{d\Omega dE_f} = \left( \frac{d^2\sigma_{\uparrow\uparrow}^{\perp}}{d\Omega dE_f} \right) - \frac{1}{2} \left( \frac{d^2\sigma_{\uparrow\downarrow}^{\perp}}{d\Omega dE_f} \right)$$

what follows from [eq. \(2.35\)](#) on [page 15](#).

## C Debye Waller factor temperature dependence

The temperature dependent form of the Debye Waller factor used in the model function in eq. (5.3) on page 37 is

$$\exp(-2W) = \exp\left(-\frac{1}{3}Q_{\text{el}}^2 u_0^2 T\right) .$$

For analysis of data at a single or multiple temperatures,  $u_0^2$  is used as free parameter together with the scaling factor  $s_0$  in eq. (5.3) to normalize the sum of the amplitudes  $A_l(Q)$  in the circular jump diffusion models. In order to estimate the accuracy of the linear temperature dependence of the exponent and possibly give a better modeling for low temperatures, the measured density of states  $G(\omega)$  can be used to calculate the Debye Waller factor. The shape of  $G(\omega)$  was extracted from IN6 ToF data at  $T = 80\text{K}$  by standard methods and is shown in Figure C.1a. The temperature dependence of the Debye Waller factor is then calculated numerically from eq. (2.31) on page 14 by using  $Z(\omega) \mapsto G(\omega)$ , where  $\hbar\omega_m = 20\text{meV}$  is the maximum phonon energy considered. The result is then put into the form

$$\exp(-2W) = \exp\left[-\frac{1}{3}Q_{\text{el}}^2 \tilde{u}_0^2 \nu(T)\right]$$

where  $\tilde{u}_0^2$  is used as free parameter to compensate for missing absolute intensity normalization and for another important approximation which is made by this method: The density of states  $G(\omega)$  in eq. (2.31) should be the vibrational density of states of the hydrogen atoms in the sample, while the one actually used is the measured generalized density of states containing the sum over all species (C, H and Fe) weighted by the ratio of neutron scattering cross section and mass. However, due to the strong dominance of scattering from hydrogen, both densities can be assumed to be of comparable shape in the relevant energy range. This approximation is considered sufficient for the present purpose.

The resulting function  $\nu(T)$  describing the temperature dependence of the mean square displacement in Fc is shown in Figure C.1b, and it can be seen that the linear approximation holds well above circa 50 K.

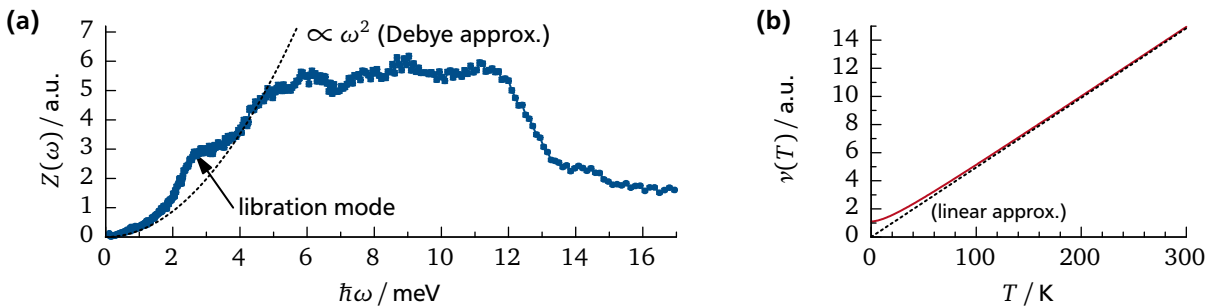


**Figure C.1:** (a) Generalized phonon density of states  $Z(\omega)$  of triclinic ferrocene obtained at 80 K using neutron ToF spectroscopy on IN6. A possible Debye approximation of the low energy region is shown. (b) Resulting  $\nu(T)$  from numerical integration of  $Z(\omega)$  with approximation of linear temperature dependence at higher  $T$ .

## D Spin-1/2 system in external magnetic field

Here, the magnetic neutron scattering cross section for a spin-1/2 system in an external magnetic field will be calculated for the experiments in [chapter 10](#). The magnetic field lifts the degeneracy between the spin up  $|\uparrow\rangle$  and the spin down state  $|\downarrow\rangle$ , and the magnetic moment can be flipped in an inelastic scattering process. The starting point for the calculation is the inelastic cross section for magnetic moments from ref. [39, eq. (7.27)], where only the self part of the correlation is considered:<sup>1</sup>

$$\begin{aligned} \frac{d^2\sigma}{d\Omega dE_f} = r_0^2 \frac{k_f}{k_i} \left[ \frac{1}{2} g F(\mathbf{Q}) \right]^2 \sum_{\alpha, \beta} (\delta_{\alpha\beta} - \tilde{Q}_\alpha \tilde{Q}_\beta) \\ \times \sum_{\nu_i, \nu_f} p_{\nu_i} \langle \nu_i | \hat{S}_\alpha | \nu_f \rangle \langle \nu_f | \hat{S}_\beta | \nu_i \rangle \delta(\hbar\omega + E_{\nu_i} - E_{\nu_f}) \end{aligned} \quad (\text{D.1})$$

where

$r_0^2$  is the basic magnetic cross section defined in [section 2.6](#),

$g$  is the Landé factor of the magnetic moments,

$F(\mathbf{Q})$  is the form factor of the magnetic moments,

$\alpha, \beta$  are summation indices over spatial directions  $\{x, y, z\}$ ,

$\tilde{Q}_\alpha$  are the components of the normalized scattering vector  $\tilde{\mathbf{Q}} = \mathbf{Q}/Q$ ,

$\nu_i, \nu_f$  are the possible initial and final sample spin states  $\uparrow$  or  $\downarrow$ ,

$p_{\nu_i}$  is the thermal population of the initial state,

$\hat{S}_\alpha$  are the components of the sample spin operator  $\hat{\mathbf{S}}$ ,

$E_{\nu_i}, E_{\nu_f}$  are the energies of the initial and final sample spin state.

The energy difference between the spin states in an external magnetic field of strength  $B$  is

$$\Delta E = E_\downarrow - E_\uparrow = g\mu_B B$$

with the Bohr magneton  $\mu_B$ . The next step is the explicit calculation of all terms of the sum in eq. (D.1). As stated in [section 10.1](#), the observed scattering was approximately perpendicular to the external field. Therefore, when the  $z$ -direction is chosen as magnetic field direction and the incident beam is along  $x$ , the direction of the scattering vector lies in the  $xy$ -plane as can be parametrized as

$$\tilde{\mathbf{Q}} = \begin{pmatrix} \cos \eta \\ \sin \eta \\ 0 \end{pmatrix} .$$

<sup>1</sup> The self correlation is extracted from ref. [39, eq. (7.27)] by setting  $l = l'$  and  $d = d'$ .

With the common definition of the ladder operators

$$\begin{aligned}\hat{S}_x &= \frac{1}{2}(\hat{S}_+ + \hat{S}_-) \\ \hat{S}_y &= \frac{1}{2i}(\hat{S}_+ - \hat{S}_-)\end{aligned}$$

and their effect on the spin states  $\hat{S}_+|\downarrow\rangle = |\uparrow\rangle$ ,  $\hat{S}_+|\uparrow\rangle = 0$ , etc., all matrix elements in eq. (D.1) can easily be calculated. The result is then simplified to

$$\frac{d^2\sigma}{d\Omega dE_f} = r_0^2 \frac{k_f}{k_i} \left[ \frac{1}{2} g F(\mathbf{Q}) \right]^2 \frac{1}{4} \left[ \delta(\hbar\omega) + p_\uparrow \delta(\hbar\omega + \Delta E) + p_\downarrow \delta(\hbar\omega - \Delta E) \right] . \quad (\text{D.3})$$

The thermodynamic population of both states is

$$\begin{aligned}p_\uparrow &= \frac{1}{Z} \exp\left(\frac{\Delta E}{2k_B T}\right) = \left[ 1 + \exp\left(-\frac{\Delta E}{k_B T}\right) \right]^{-1} \\ p_\downarrow &= \frac{1}{Z} \exp\left(-\frac{\Delta E}{2k_B T}\right) = \left[ 1 + \exp\left(\frac{\Delta E}{k_B T}\right) \right]^{-1}\end{aligned}$$

where the partition function is

$$Z = 2 \cosh\left(\frac{\Delta E}{2k_B T}\right) .$$

In the notation of section 10.2, the neutron energy gain part (i.e.  $\hbar\omega \leq 0$ ) of eq. (D.3) can be rewritten as

$$\frac{d^2\sigma}{d\Omega dE_f} = \frac{\sigma_{\text{mag}}}{4\pi} \left\{ \delta(\hbar\omega) + \delta(\hbar\omega + \Delta E) \left[ 1 + \exp\left(-\frac{\Delta E}{k_B T}\right) \right]^{-1} \right\} \quad (\text{D.4})$$

where the  $\delta$ -shaped inelastic contribution is ultimately replaced by a Gaussian to allow for finite width of the experimentally observed excitation in section 10.2.

---

# Bibliography

- [1] T. KEALY and P. PAUSON. "A new type of organo compound". In: *Nature* **168** (1951), pp. 1039–40.
- [2] S. A. MILLER, J. A. TEBBOTH, and J. F. TREMAINE. "114. Dicyclopentadienyliron". In: *Journal of the Chemical Society* (1952), pp. 632–5.
- [3] E. O. FISCHER and W. PFAB. "Cyclopentadien-Metallkomplexe, ein neuer Typ metallorganischer Verbindungen". In: *Zeitschrift für Naturforschung B* **7** (1952), p. 377.
- [4] G. WILKINSON, M. ROSENBLUM, M. C. WHITING, and R. B. WOODWARD. "The Structure of Iron bis-cyclopentadienyl". In: *Journal of the American Chemical Society* **74** (1952), pp. 2125–6.
- [5] J. D. DUNITZ and L. E. ORGEL. "Bis-cyclopentadienyl Iron - A Molecular Sandwich". In: *Nature* **171** (1953), pp. 121–2.
- [6] P. F. EILAND and R. PEPINSKY. "X-ray Examination of Iron bis-cyclopentadienyl". In: *Journal of the American Chemical Society* **74** (1952), p. 4971.
- [7] H. WERNER. "At Least 60 Years of Ferrocene: The Discovery and Rediscovery of the Sandwich Complexes". In: *Angewandte Chemie International Edition* **51** (2012), pp. 6052–8.
- [8] M. A. C. STUART, W. T. S. HUCK, J. GENZER, M. MÜLLER, C. OBER, M. STAMM, G. B. SUKHORUKOV, I. SZLEIFER, V. V. TSUKRUK, M. URBAN, F. WINNIK, S. ZAUSCHER, I. LUZINOV, and S. MINKO. "Emerging applications of stimuli-responsive polymer materials". In: *Nature Materials* **9** (2010), pp. 101–13.
- [9] M. NAKAHATA, Y. TAKASHIMA, H. YAMAGUCHI, and A. HARADA. "Redox-responsive self-healing materials formed from host-guest polymers". In: *Nature Communications* **2** (2011), p. 511.
- [10] J. ELBERT, M. GALLEI, C. RÜTTIGER, A. BRUNSEN, H. DIDZOLEIT, B. STÜHN, and M. REHAHN. "Ferrocene Polymers for Switchable Surface Wettability". In: *Organometallics* **32** (2013), pp. 5873–8.
- [11] J. ELBERT, F. KROHM, C. RÜTTIGER, S. KIENLE, H. DIDZOLEIT, B. N. BALZER, T. HUGEL, B. STÜHN, M. GALLEI, and A. BRUNSEN. "Polymer-Modified Mesoporous Silica Thin Films for Redox-Mediated Selective Membrane Gating". In: *Advanced Functional Materials* **24** (2013), pp. 1591–601.
- [12] P. SEILER and J. D. DUNITZ. "The structure of triclinic ferrocene at 101, 123 and 148 K". In: *Acta Crystallographica B* **35** (1979), pp. 2020–32.
- [13] K. MOMMA and F. IZUMI. "VESTA3 for three-dimensional visualization of crystal, volumetric and morphology data". In: *Journal of Applied Crystallography* **44** (2011), pp. 1272–6.
- [14] J. D. DUNITZ. "Phase-changes and Chemical-reactions In Molecular-crystals". In: *Acta Crystallographica B* **51** (1995), pp. 619–31.
- [15] D. BRAGA. "Dynamical Processes In Crystalline Organometallic Complexes". In: *Chemical Reviews* **92** (1992), pp. 633–65.
- [16] D. D. BRAGA and F. GREPIONI. "Crystal Construction and Molecular Interplay In Solid Ferrocene, Nickelocene, and Ruthenocene". In: *Organometallics* **11** (1992), pp. 711–8.
- [17] G. CALVARIN and J. F. BERAR. "Etude par diffraction des rayons X sur poudre de la transition ordre-désordre du ferrocène  $\text{Fe}(\text{C}_5\text{H}_5)_2$ ". In: *Journal of Applied Crystallography* **8** (1975), pp. 380–5.

- [18] P. SEILER and J. D. DUNITZ. "New Interpretation of the Disordered Crystal-structure of Ferrocene". In: *Acta Crystallographica B* **35** (1979), pp. 1068–74.
- [19] F. TAKUSAGAWA and T. KOETZLE. "A Neutron Diffraction Study of the Crystal Structure of Ferrocene". In: *Acta Crystallographica B* **35** (1979), pp. 1074–81.
- [20] C. P. BROCK and Y. G. FU. "Rigid-body disorder models for the high-temperature phase of ferrocene". In: *Acta Crystallographica B* **53** (1997), pp. 928–38.
- [21] K. OGASAHARA, M. SORAI, and H. SUGA. "New Finding of A Stable Low-temperature Phase In Ferrocene Crystal". In: *Chemical Physics Letters* **68** (1979), pp. 457–60.
- [22] J.-F. BÉRAR, G. CALVARIN, D. WEIGEL, K. CHHOR, and C. POMMIER. "New low-temperature crystalline phase of ferrocene: Isomorphous to orthorhombic ruthenocene". In: *Journal of Chemical Physics* **73** (1980), pp. 438–41.
- [23] P. SEILER and J. D. DUNITZ. "Low-temperature crystallization of orthorhombic ferrocene: structure analysis at 98 K". In: *Acta Crystallographica B* **38** (1982), pp. 1741–5.
- [24] J. W. EDWARDS and G. L. KINGTON. "Thermodynamic properties of ferrocene. Part 2. — Vapour pressure and latent heat of sublimation at 25°C by the effusion and thermistor manometer methods". In: *Transactions of the Faraday Society* **58** (1962), pp. 1323–33.
- [25] M. NARUSE, M. SORAI, and M. SAKIYAMA. "Disintegration Energy of Ferrocene Crystal In Triclinic Phase and Kinetic-study On Monotropic Transition From Monoclinic To Orthorhombic Phase". In: *Molecular Crystals and Liquid Crystals* **101** (1983), pp. 219–34.
- [26] K. OGASAHARA, M. SORAI, and H. SUGA. "Thermodynamic Properties of Ferrocene Crystal". In: *Molecular Crystals and Liquid Crystals* **71** (1981), pp. 189–211.
- [27] A. HAALAND and J. E. NILSSON. "Determination of Barriers To Internal Rotation By Means of Electron Diffraction. Ferrocene and Ruthenocene". In: *Acta Chemica Scandinavica* **22** (1968), pp. 2653–70.
- [28] C. H. HOLM and J. A. IBERS. "NMR Study of Ferrocene, Ruthenocene, and Titanocene Dichloride". In: *Journal of Chemical Physics* **30** (1959), pp. 885–8.
- [29] A. J. CAMPBELL, C. A. FYFE, D. HAROLD-SMITH, and K. R. JEFFREY. "An Investigation of the Dynamic Structures of Ferrocene, Ruthenocene and Dibenzenechromium in the Solid State and in Solution". In: *Molecular Crystals and Liquid Crystals* **36** (1976), pp. 1–23.
- [30] A. KUBO, R. IKEDA, and D. NAKAMURA. "Motion of C<sub>5</sub>H<sub>5</sub> Rings In Three Crystalline Modifications of Ferrocene As Studied By <sup>1</sup>H NMR". In: *Chemistry Letters* **10** (1981), pp. 1497–500.
- [31] E. MAVERICK and J. D. DUNITZ. "Rotation Barriers In Crystals From Atomic Displacement Parameters". In: *Molecular Physics* **62** (1987), pp. 451–9.
- [32] D. C. LEVENDIS and J. C. A. BOEYENS. "Analysis of the Molecular-conformation and Rotational Disorder In Crystalline Ferrocene and Nickelocene". In: *Journal of Crystallographic and Spectroscopic Research* **15** (1985), pp. 1–17.
- [33] K. CHHOR, G. LUCAZEAU, and C. SOURISSEAU. "Vibrational Study of the Dynamic Disorder In Nickelocene and Ferrocene Crystals". In: *Journal of Raman Spectroscopy* **11** (1981), pp. 183–98.
- [34] A. GARDNER, J. HOWARD, T. WADDINGTON, R. RICHARDSON, and J. TOMKINSON. "The dynamics of ring rotation in ferrocene, nickelocene and ruthenocene by incoherent quasi-elastic neutron scattering". In: *Chemical Physics* **57** (1981), pp. 453–60.



- [35] M. BÉE. “Quasielastic Neutron Scattering”. Adam Hilger, 1988.
- [36] M. HMYENE, A. YASSAR, M. ESCORNE, A. PERCHERON-GUEGAN, and F. GARNIER. “Magnetic Properties of Ferrocene-Based Conjugated Polymers”. In: *Advanced Materials* **6** (1994), pp. 564–8.
- [37] Y. ANDO, T. HIROIKE, T. MIYASHITA, and T. MIYAZAKI. “Magnetic properties of ferrocenylmethylacrylate-N-dodecylacryl-amide copolymer Langmuir-Blodgett films”. In: *Thin Solid Films* **350** (1999), pp. 232–7.
- [38] S. W. LOVESEY. “Theory of neutron scattering from condensed matter”. Vol. 1. Clarendon Press, 1984.
- [39] S. W. LOVESEY. “Theory of neutron scattering from condensed matter”. Vol. 2. Clarendon Press, 1984.
- [40] P. J. MOHR, B. N. TAYLOR, and D. B. NEWELL. *The 2010 CODATA Recommended Values of the Fundamental Physical Constants*. This database was developed by J. Baker, M. Douma, and S. Kotochigova. National Institute of Standards and Technology. 2011. URL: <http://physics.nist.gov/constants>
- [41] V. F. SEARS. “Neutron scattering lengths and cross sections”. In: *Neutron News* **3** (1992), pp. 26–37.
- [42] J. D. BARNES. “Inelastic neutron scattering study of the ‘rotator’ phase transition in n-nonadecane”. In: *Journal of Chemical Physics* **58** (1973), pp. 5193–201.
- [43] O. SCHÄRPF and H. CAPELLMANN. “The XYZ-difference Method With Polarized Neutrons and the Separation of Coherent, Spin Incoherent, and Magnetic Scattering Cross-sections In A Multidetector”. In: *Physica Status Solidi A* **135** (1993), pp. 359–79.
- [44] E. KEMNER, M. DE SCHEPPER, A. SCHMETS, H. GRIMM, A. OVERWEG, and R. VAN SANTEN. “Molecular Motion of Ferrocene in a Faujasite-Type Zeolite: A Quasielastic Neutron Scattering Study”. In: *Journal of Physical Chemistry B* **104** (2000), pp. 1560–62.
- [45] D. R. LIDE, ed. “CRC Handbook of Chemistry and Physics”. CRC Press, Boca Raton, FL, 2005.
- [46] *Disk Chopper Time of Flight Spectrometer IN5*. Institut Laue Langevin. URL: [www.ill.eu/YellowBook/IN5](http://www.ill.eu/YellowBook/IN5)
- [47] *Cold Neutron Time Focussing Time of Flight Spectrometer IN6*. Institut Laue Langevin. URL: [www.ill.eu/YellowBook/IN6](http://www.ill.eu/YellowBook/IN6)
- [48] B. ALEFELD, M. BIRR, and A. HEIDEMANN. “Ein neues hochauflösendes Neutronenkristallspektrometer und seine Anwendung”. In: *Naturwissenschaften* **56** (1969), pp. 410–2.
- [49] M. BIRR, A. HEIDEMANN, and B. ALEFELD. “A neutron crystal spectrometer with extremely high energy resolution”. In: *Nuclear Instruments and Methods* **95** (1971), pp. 435–439.
- [50] B. FRICK. “Neutron Backscattering Spectroscopy”. In: *Neutron and X-ray Spectroscopy*. Ed. by F. HIPPERT, E. GEISLER, J. HODEAU, E. LELIÈVRE-BERNA, and J.-R. REGNARD. Springer Netherlands, 2006, pp. 483–527.
- [51] *Backscattering Spectrometer IN16B*. Institut Laue Langevin. URL: [www.ill.eu/YellowBook/IN16B](http://www.ill.eu/YellowBook/IN16B)
- [52] *Backscattering Spectrometer IN16*. Institut Laue Langevin. URL: [www.ill.eu/YellowBook/IN16](http://www.ill.eu/YellowBook/IN16)
- [53] *Hot Neutron Three-Axis Spectrometer IN1-TAS/Lagrange*. Institut Laue Langevin. URL: [www.ill.eu/fr/instruments-support/instruments-groups/instruments/in1-taslagrange](http://www.ill.eu/fr/instruments-support/instruments-groups/instruments/in1-taslagrange)
- [54] *Diffuse Scattering Spectrometer D7*. Institut Laue Langevin. URL: [www.ill.eu/YellowBook/D7](http://www.ill.eu/YellowBook/D7)
- [55] S. PERTICAROLI, J. D. NICKELS, G. EHLERS, H. O’NEILL, Q. ZHANG, and A. P. SOKOLOV. “Secondary structure and rigidity in model proteins”. In: *Soft Matter* **9** (2013), pp. 9548–56.

- [56] V. F. SEARS. "Slow-neutron multiple scattering". In: *Advances in Physics* **24** (1975), pp. 1–45.
- [57] R. ZORN, B. FRICK, and L. J. FETTERS. "Quasielastic neutron scattering study of the methyl group dynamics in polyisoprene". In: *Journal of Chemical Physics* **116** (2002), pp. 845–53.
- [58] M. W. JOHNSON. *DISCUS – a computer program for the calculation of multiple scattering effects in inelastic neutron scattering experiments*. Tech. rep. Harwell: United Kingdom Atomic Energy Research Establishment, 1974.
- [59] THE OCTAVE COMMUNITY. *GNU/Octave*. URL: [www.octave.org](http://www.octave.org)
- [60] F. CALVARIN, J. F. BERAR, and G. CLECH. "Study of Static Disorder In A Ferrocene Crystal - Molecular-configuration and Packing, By X-ray-diffraction and Lattice-energy Calculations". In: *Journal of Physics and Chemistry of Solids* **43** (1982), pp. 791–6.
- [61] F. FUJARA, W. PETRY, W. SCHNAUSS, and H. SILLESCU. "Reorientation of Benzene In Its Crystalline State - A Model Case For the Analogy Between Nuclear Magnetic-resonance Spin Alignment and Quasielastic Incoherent Neutron-scattering". In: *Journal of Chemical Physics* **89** (1988), pp. 1801–6.
- [62] T. BERNSTEIN and F. H. HERBSTEIN. "Crystal Structure Ferricinium Triiodide (C<sub>5</sub>H<sub>5</sub>)<sub>2</sub>FeI<sub>3</sub>". In: *Acta Crystallographica B* **24** (1968), pp. 1640–5.
- [63] E. W. NEUSE and M. S. LOONAT. "Ferricenium Polyiodides". In: *Journal of Organometallic Chemistry* **286** (1985), pp. 329–41.
- [64] K. F. TEBBE and R. BUCHEM. "The most iodine-rich polyiodide yet: Fc<sub>3</sub>I<sub>29</sub>". In: *Angewandte Chemie International Edition* **36** (1997), pp. 1345–6.
- [65] J. W. EDWARDS, G. L. KINGTON, and R. MASON. "The thermodynamic properties of ferrocene. Part 1. — The low-temperature transition in ferrocene crystals". In: *Transactions of the Faraday Society* **56** (1960), pp. 660–7.
- [66] Hitherto unpublished density functional theory (DFT) calculations on an isolated molecule in collaboration with Mohamed Zbiri (ILL) result in a sine shaped, 5-fold rotational potential barrier of 2.4 kJ mol<sup>-1</sup> to 3.1 kJ mol<sup>-1</sup> for Fc and 0.7 kJ mol<sup>-1</sup> to 1.6 kJ mol<sup>-1</sup> for Fc<sup>+</sup>, depending on the used basis sets and functionals. The potential minimum is in both cases obtained for the eclipsed D<sub>5h</sub> configuration..
- [67] A. J. TINKER, J. A. BARRIE, and M. H. GEORGE. "The thermal properties of polyvinylferrocene". In: *Journal of Polymer Science: Polymer Letters Edition* **13** (1975), pp. 487–92.
- [68] M. H. GEORGE and G. F. HAYES. "Free-radical polymerization of vinylferrocene. II. Spectroscopic and physical properties". In: *Journal of Polymer Science: Polymer Chemistry Edition* **14** (1976), pp. 475–88.
- [69] J. COLMENERO, A. J. MORENO, and A. ALEGRÍA. "Neutron scattering investigations on methyl group dynamics in polymers". In: *Progress in Polymer Science* **30** (2005), pp. 1147–84.
- [70] A. CHAHID, A. ALEGRIA, and J. COLMENERO. "Methyl Group Dynamics in Poly(vinyl methyl ether). A Rotation Rate Distribution Model". In: *Macromolecules* **27** (1994), pp. 3282–8.
- [71] M. GALLEI, R. KLEIN, and M. REHAHN. "Silacyclobutane-Mediated Re-Activation of Sleeping Polyvinylferrocene Macro-Anions: A Powerful Access to Novel Metalloblock Copolymers". In: *Macromolecules* **43** (2010), pp. 1844–54.
- [72] F. ALVAREZ, J. COLMENERO, R. ZORN, L. WILLNER, and D. RICHTER. "Partial Structure Factors of Polyisoprene: Neutron Scattering and Molecular Dynamics Simulation". In: *Macromolecules* **36** (2003), pp. 238–48.
- [73] I. IRADI, F. ALVAREZ, J. COLMENERO, and A. ARBE. "Structure factors in polystyrene: a neutron scattering and MD-simulation study". In: *Physica B: Condensed Matter* **350** (2004). Proceedings of the Third European Conference on Neutron Scattering, E881 –E884.

- 
- [74] C. KLONINGER and M. REHAHN. “1,1-Dimethylsilacyclobutane-Mediated Living Anionic Block Copolymerization of [1]Dimethylsilaferrocenophane and Methyl Methacrylate”. In: *Macromolecules* **37** (2004), pp. 1720–7.
- [75] V. A. DU and I. MANNERS. “Poly(ferrocenylmethylsilane): An Unsymmetrically Substituted, Atactic, but Semicrystalline Polymetallocene”. In: *Macromolecules* **46** (2013), pp. 4742–53.
- [76] E. KEMNER, M. DE SCHEPPER, G. KEARLEY, and U. JAYASOORIYA. “The vibrational spectrum of solid ferrocene by inelastic neutron scattering”. In: *Journal of Chemical Physics* **112** (2000), pp. 10926–29.
- [77] L. JAYES, A. P. HARD, C. SÉNÉ, S. F. PARKER, and U. A. JAYASOORIYA. “Vibrational Spectroscopic Analysis of Silicones: A Fourier Transform-Raman and Inelastic Neutron Scattering Investigation”. In: *Analytical Chemistry* **75** (2003), pp. 742–6.
- [78] A. P. HARD, S. F. PARKER, and U. A. JAYASOORIYA. “Vibrational Spectroscopic Analysis of Chlorosilanes and Siloxane Oligomers: Implications for the Spectra of Polydimethylsiloxanes”. In: *Applied Spectroscopy* **61** (2007), pp. 314–20.
- [79] A. HEIDEMANN. “Bestimmung des inneren Magnetfeldes in  $V_2O_3$  mit Hilfe der inelastischen Spin-Flip-Streuung von Neutronen”. In: *Zeitschrift für Physik* **238** (1970), pp. 208–20.
- [80] T. CHATTERJI, B. FRICK, and H. S. NAIR. “Magnetic ordering in double perovskites  $R_2CoMnO_6$  ( $R = Y, Tb$ ) investigated by high resolution neutron spectroscopy”. In: *Journal of Physics: Condensed Matter* **24** (2012), p. 266005.
- [81] R. PRINS. “Electronic structure of the ferricenium cation”. In: *Molecular Physics* **19** (1970), pp. 603–20.
- [82] S. E. ANDERSON and R. RAI. “Mechanism of spin delocalization and nature of the ground state in ferricenium cations”. In: *Chemical Physics* **2** (1973), pp. 216–25.
- [83] P. J. BROWN. “Magnetic form factors”. In: *International Tables for Crystallography*. Vol. C. John Wiley & Sons, Ltd, 2006. Chap. 4.4.5, pp. 454–61.
- [84] Z.-F. XU, Y. XIE, W.-L. FENG, and H. F. SCHAEFER. “Systematic Investigation of Electronic and Molecular Structures for the First Transition Metal Series Metallocenes  $M(C_5H_5)_2$  ( $M = V, Cr, Mn, Fe, Co, and Ni$ )”. In: *Journal of Physical Chemistry A* **107** (2003), pp. 2716–29.
- [85] R. B. FIRESTONE. “Table of Isotopes”. 8. Edition August 1999. Wiley-VCH, Berlin, 1999.
- [86] *LAMP, the Large Array Manipulation Program*. Institut Laue Langevin.  
URL: [www.ill.eu/data\\_treat/lamp/the-lamp-book/](http://www.ill.eu/data_treat/lamp/the-lamp-book/)
- [87] *SQW Data Transformation Programme*. Institut Laue Langevin.  
URL: [www.ill.eu/instruments-support/instruments-groups/groups/tof/software/sqw/](http://www.ill.eu/instruments-support/instruments-groups/groups/tof/software/sqw/)



---

# Danksagung

Ich bedanke mich bei allen Menschen, die mich bei meiner Doktorarbeit unterstützt haben und mir zur Seite standen.

Da dieses Projekt eine Kooperation zwischen der TU Darmstadt und dem ILL Grenoble war, sind es gleich zwei Doktorväter, die mir die Möglichkeit zu dieser Arbeit eröffneten und auf die ich mich Jahr für Jahr verlassen konnte. Sowohl Professor Dr. Bernd Stühn in Darmstadt als auch Dr. Bernhard Frick in Grenoble hatten für meine Fragen, Ideen und Probleme immer ein offenes Ohr und nahmen sich viel Zeit für ausführliche Diskussionen mit mir.

Einen besonderen Dank verdient auch Dr. Tinka Spehr-Bechmann, die meinen Wunsch zu einem Kooperationsprojekt mit dem ILL Grenoble aufnahm und viel Arbeit und Mühe in seine erfolgreiche Realisierung steckte.

Für unsere wissenschaftliche Zusammenarbeit bedanke ich mich bei Dr. Markus Gallei und Johannes Elbert, ohne die viele meiner Experimente nicht möglich gewesen wären. Ebenso gilt mein Dank Haiko Didzoleit, Andreas Weber und Christina Lederle, die den weiten Weg von Darmstadt nach Grenoble auf sich nahmen, um mir tatkräftig bei der Durchführung einiger Neutronenstreuexperimente zu helfen.

Auch am ILL in Grenoble konnte ich auf die Unterstützung vieler Leute bauen. Ich möchte Professor Dr. Helmut Schober für das Interesse an meiner Arbeit danken, und insbesondere Dr. Michael Marek Koza, Dr. Jacques Ollivier und Dr. Alexandre Ivanov für viele Stunden fruchtbarer Diskussionen sowie Hilfe bei Experimenten.

Einen letzten, besonderen Dank möchte ich meinen Eltern, Großeltern und Marina Khanefit aussprechen für ihre langjährige Unterstützung, die meinen Weg in vieler Hinsicht vereinfacht.



---

# Erklärung zur Dissertation

Hiermit versichere ich, die vorliegende Dissertation ohne Hilfe Dritter nur mit den angegebenen Quellen und Hilfsmitteln angefertigt zu haben. Alle Stellen, die aus Quellen entnommen wurden, sind als solche kenntlich gemacht. Diese Arbeit hat in gleicher oder ähnlicher Form noch keiner Prüfungsbehörde vorgelegen.

Darmstadt, den 24. Juli 2014

---

(Markus Appel)





---

# Curriculum vitæ

Markus Andreas Appel

born 23 May 1985  
in Hanau, Germany

- 2011–present Post-graduate student,  
*Institut Laue-Langevin Grenoble, France & TU Darmstadt, Germany*
- 03/2011 Master of Science (Physics), *TU Darmstadt, Germany*
- 04/2009–07/2009 Internship, *Institut Laue-Langevin Grenoble, France*
- 08/2008–03/2009 Physics studies, *Institut National Polytechnique, Grenoble, France*
- 08/2008 Bachelor of Science (Physics), *TU Darmstadt, Germany*
- 2005–2011 Physics studies, *TU Darmstadt, Germany*
- 2004–2005 Basic military service, *Germany*
- 06/2004 Abitur, *Einhardschule Seligenstadt, Germany*

## List of publications

- M. APPEL, B. FRICK, T. L. SPEHR, and B. STÜHN.  
“Molecular ring rotation in solid ferrocene revisited”.  
In: *The Journal of Chemical Physics* **142** (2015), p. 114503.
- M. APPEL, B. FRICK, J. ELBERT, M. GALLEI, and B. STÜHN.  
“Direct observation of electronic and nuclear ground state splitting in external magnetic field by inelastic neutron scattering on oxidized ferrocene and ferrocene containing polymers”.  
In: *EPJ Web of Conferences* **83** (2015), p. 02001.
- M. APPEL, B. FRICK, A. IVANOV, J. ELBERT, M. REHAHN, M. GALLEI, T. L. SPEHR, and B. STÜHN.  
“Vibrational spectra of ferrocene, ferrocene-containing polymers and their oxidized compounds”.  
In: *Journal of Physics: Conference Series* **554** (2014), p. 012008.
- M. APPEL, T. L. SPEHR, R. WIPF, C. MOERS, H. FREY, and B. STÜHN. “Micellar interactions in water-AOT based droplet microemulsions containing hydrophilic and amphiphilic polymers”.  
In: *Journal of Chemical Physics* **139** (2013), p. 184903.
- M. APPEL, T. L. SPEHR, R. WIPF, and B. STÜHN. “Water-AOT-alkylbenzene microemulsions: Influence of alkyl chain length on structure and percolation behavior”.  
In: *Journal of Colloid and Interface Science* **376** (2012), pp. 140–5.
- L. VAN EIJCK, B. FRICK, T. SPEHR, and M. APPEL. “Are the Glass Forming Properties of Glycerol Changed when Disrupting the Hydrogen Bond Network by Addition of Silica Nanospheres?”  
In: *Zeitschrift für Physikalische Chemie* **224** (2010), pp. 101–7.